MULTIMODAL AND MULTISCALE CHARACTERIZATION OF BONE

MULTIMODAL AND MULTISCALE CHARACTERIZATION OF BONE AND BONE INTERFACES IN HEALTH AND DISEASE

By Chiara Micheletti, B.Eng., M.A.Sc., M.Sc.Eng.

A Thesis Submitted to the School of Graduate Studies in Partial Fulfilment of the Requirements for the Degree Doctor of Philosophy

McMaster University

Doctor of Philosophy (Materials Science & Engineering)

McMaster University (2023)

Hamilton, ON, Canada

TITLE: Multimodal and multiscale characterization of bone and bone interfaces in health and disease

AUTHOR: Chiara Micheletti, B.Eng., M.A.Sc., M.Sc.Eng. (McMaster University)

SUPERVISOR: Prof. Dr. Kathryn Grandfield (McMaster University)

CO-SUPERVISORS: Prof. Dr. Anders Palmquist, Dr. Furqan A. Shah (University of Gothenburg)

NUMBER OF PAGES: xvi, 182

Thesis in cotutelle with the University of Gothenburg,
Department of Biomaterials, Institute of Clinical Sciences, Sahlgrenska Academy
Gothenburg, Sweden

Lay abstract

Bone is a hierarchical material, meaning that smaller components are progressively organized into larger structures. This multi-level architecture is hard to visualize because different techniques are required to obtain information at different length scales. However, as the proverb says, "seeing is believing", and our understanding of things is often better accomplished by looking at images. This thesis applies a characterization approach more typical of materials science to study the structure, composition, and repair of bone across multiple length scales. This characterization approach is multimodal because it uses different techniques, and multiscale because it targets different length scales in bone. In particular, this thesis focuses on bone in compromised conditions, namely osteoporosis, diabetes, and medication-related osteonecrosis, to understand the impact of disease-induced changes in bone properties. It also examines how bone organizes itself at a fundamental level, which is a critical aspect to understand since bone is built from the bottom-up.

Abstract

Seeing is believing. Our understanding of phenomena often involves their direct observation. However, bone architecture is challenging to visualize given its multi-level hierarchical organization. In this thesis, bone and bone interfaces are characterized via multimodal and multiscale platforms, combining different techniques across several length scales. Imaging techniques across the micro-nano continuum are complemented by spectroscopy methods to explore, respectively, the structure and composition of bone and bone interfaces, using both light and electron probes. By applying a characterization methodology more typical of materials science, this thesis aims to unveil structural and compositional abnormalities of bone induced by disease [Papers I-II], and bone response to functionalized biomaterials in compromised conditions [Papers III-IV]. Additionally, it expands three-dimensional (3D) characterization opportunities at the nanoscale in both native and peri-implant bone [Papers V-VI].

This characterization approach uncovered changes in bone quality (structure and/or composition) in the compromised conditions under investigation in this thesis, i.e., leptin receptor (LepR) deficiency and medication-related osteonecrosis of the jaw (MRONJ) [Papers I-II]. In a preclinical model of LepR deficiency for type 2 diabetes/obesity, multimodal characterization of bone at the microscale showed structural abnormalities indicative of delayed skeletal development, despite unaffected bone matrix composition [Paper I]. A combination of multiscale imaging and spectroscopy techniques spanning the micro-to-nanoscale enabled a detailed study of the interface between necrotic bone and bacteria in a case of MRONJ, shedding light on possible mechanisms of bone degradation. When applied to bone-biomaterial interfaces, the application of a multimodal and multiscale characterization workflow informed perspectives on bone response to novel biomaterial solutions aimed to promote osseointegration in osteoporotic conditions via local drug delivery of phytoestrogens [Paper III] or anabolic agents [Paper IV]. This highlighted the importance of studying peri-implant bone at the mesoscale [Paper III] and of confirming biomaterial behaviour *in vivo* in the presence of surface functionalization [Paper IV]. Lastly, this thesis emphasized the importance of 3D imaging at the nanoscale with electron tomography to resolve bone ultrastructure at biomaterial interfaces [Paper V] and in native conditions [Paper VI]. Specifically, in Paper VI, artifact-free on-axis electron tomography resolved some long-debated aspects regarding the organization of mineralized collagen fibrils, the fundamental building block units of bone.

Keywords: *bone; osseointegration; characterization; mineralization; ultrastructure; diabetes; osteoporosis; MRONJ; surface functionalization; local drug delivery; titanium; bioactive glass; imaging; spectroscopy; microscale; nanoscale; micro-computed X-ray tomography; micro-Raman spectroscopy; scanning electron microscopy; transmission electron microscopy; PFIB-SEM tomography; electron tomography.*

Acknowledgements

For the things we have to learn before we can do them,
we learn by doing them.

Aristotle

I have often thought about my PhD as a journey, an analogy also applicable in a literal sense for the several trips back and forth on opposite sides of the Atlantic Ocean. This journey would not have been possible without my three amazing supervisors, who let me fly my own plane, but were always there when I needed them. Thank you to Kathryn, Anders, and Furqan for all the support throughout the years and for emboldening me to fly high. Thank you, Kathryn, for offering me the plane ticket in the first place, for all the research opportunities, and for your encouragement and mentoring beyond the lab. Thank you, Anders, for embarking on this *cotutelle* trip despite all the extra paperwork you had to deal with, for your practical and always on-point advice, and for staying calm during the storms. Thank you, Furqan, for the endless scientific discussions, for sharing your encyclopedic knowledge with me, and for the Friday jokes!

Thank you to all my collaborators, especially Roberta Okamoto and Pedro Gomes-Ferreira at UNESP for taking me aboard very interesting projects. Thank you to Cecilia Larsson Wexell, Le Fu, and Henry Schwarcz for providing me with unique samples to look at. Thank you to Peter Ercius and Alex Lin for hosting me at the Berkeley National Lab in sunny California to take a break from the Hamilton winter with some exciting science. Thank you to Aurélien Gourrier for insightful discussions on bone structure over the years, and to Brian Langelier and Gabe Arcuri for introducing me to the APT world. Thank you to Ariana and Anna for contributing during their summer research internships. A sincere thank you also to Gianluigi Botton for accepting to be a member of my supervisory committee, giving precious feedback on electron microscopy experiments and stimulating ideas to expand my research further.

Thank you to all the technical staff who helped with my research. A special acknowledgement to those at the CCEM – Travis for the great FIB samples, Jhoynner and Chris for SEM advice and help with sample preparation, and Carmen and Natalie for TEM assistance. Thank you to Stefan at CMAL for trusting my microscopy skills. At GU, a special thank you to Lena for sharing her knowledge of bone sample preparation with me, and to Nesrin for thesis writing advice. I am also grateful for all the administrative support received from Samantha and Mary-Anne at McMaster, and from Rosie and Cina at GU.

This journey would have not been the same without my travel companions. Thank you to the GRG team – Alessandra, Joe, Liza, Alyssa, Bryan, Toni, Shane, Jeromy, and all the undergrad students. Covid-19 got in the way for a long time, but we were still able to build memories that I will cherish. Thank you to the fellow PhD travellers at GU – Martina, Paula, Adam, Heithem, Marsel, and Jincy.

Thank you for the group therapy sessions during *fika* and for all the carefree and happy moments (especially with food!) we shared. Thank you to all the other people in the Department of Biomaterials at GU for welcoming me and making me feel like home in Gothenburg – *tack!*

Thank you to my friends outside the lab, especially Dakota and Meghan, for being my first "travel guides" in Canada and for all the memories shared over the years, and Margherita and Federica, with whom I started my journey in the engineering world as first year students. Thank you also to my French family, Elodie, Alex, Lukas, and Myla, for all the fun moments spent together and the meaningful conversations.

An immense thank you to my parents, Emanuela and Renato, and my sister, Elisa, who watched me take off towards far destinations, but never stopped cheering for me, celebrating my achievements along the way. Thank you to my grandma, Delfina, for her unconditional love.

Lastly, thank you to Viktor, my safe harbour during this PhD journey. Thank you for holding my hand during turbulence, for believing in me when I did not, for taking care of me, for encouraging and supporting me even when that brought me away from you. Thank you for listening to my research doubts and ideas, for the occasional Python advice, and for all the proof-reading. Words cannot express how grateful I am to have you as my partner in this journey of life.

Funding acknowledgements. I am grateful for scholarship support from the Ontario Graduate Scholarship, the Blanceflor Foundation, the Mitacs Globalink Research Award, the James F. Harvey and Helen S. Harvey Travel Scholarship, the Yates Scholarship Fund, and the Svenska Sällskapet för Medicinsk Forskning (SSMF). Financial support is also acknowledged from the Swedish Research Council (grant no. 2020-04715), the Swedish state under the agreement between the Swedish government and the county councils (ALF agreement ALFGBG-725641), the Adlerbertska Foundation, the IngaBritt and Arne Lundberg Foundation, the Kungliga Vetenskaps-och Vitterhets-Samhället i Göteborg, the Hjalmar Svensson Foundation, the Västra Götaland Region, the Area of Advance Materials at Chalmers and at the Department of Biomaterials (University of Gothenburg) within the Strategic Research Area initiative launched by the Swedish government, SSMF, the Natural Sciences and Engineering Research Council of Canada (NSERC) (grant no. RGPIN-2020-05722), the Ontario Ministry of Research, Innovation and Science (Early Researcher Award ER17-13-081), the NSERC Alliance International Catalyst Program (grant no. ALLRP 576146-22), the Canada Research Chairs Program, the Academy of Osseointegration, CAPES (Print Project), FINEP (01.12.0530.00 PROINFRA 01/2011), and the São Paulo Research Foundation (FAPESP) (process no. 2015/14688-0, 2017/08187-3, 2021/06849-4, and 2021/13026-4).

Content

List of figures

List of tables

Abbreviations

2D	Two dimensions, two-dimensional
3D	Three dimensions, three-dimensional
4D	Four dimensions, four-dimensional
AGE	Advanced glycation end-product
AM	Additive manufacturing, additively manufactured
APT	Atom probe tomography
BF	Bright-field
BIC	Bone-implant contact
BMD	Bone mineral density
BSE	Backscattered electron
Cp-Ti	Commercially pure titanium
EDX	Energy-dispersive X-ray spectroscopy
EELS	Electron energy loss spectroscopy
FIB	Focused ion beam
HAADF	High-angle annular dark-field
LCN	Lacuno-canalicular network
Lep	Leptin
LepR	Leptin receptor
L-PBF	Laser powder bed fusion
MetS	Metabolic syndrome
Micro-CT	Micro-computed X-ray tomography
MRONJ	Medication related osteonecrosis of the jaw
ORX	Orchiectomy, orchiectomized
OVX	Ovariectomy, ovariectomized
PFIB	Plasma focused ion beam
PTH	Parathyroid hormone
qBEI	Quantitative backscattered electron imaging
ROI	Region of interest
RPI	Reference point indentation
SAED	Selected area electron diffraction
SE	Secondary electron
SEM	Scanning electron microscopy
SIRT	Simultaneous iterative reconstruction technique
STEM	Scanning transmission electron microscopy
T2DM	Type 2 diabetes mellitus
TEM	Transmission electron microscopy
TMD	Tissue mineral density
Z	Atomic number

List of papers

This thesis is based on the following studies, referred to in the text by their Roman numerals.

I. Micheletti C, Jolic M, Grandfield K, Shah FA, Palmquist A. Bone structure and composition in a hyperglycemic, obese, and leptin receptor-deficient rat: Microscale characterization of femur and calvarium. Bone. 2023;172:116747.

II. Micheletti C, DiCecco L-A, Larsson Wexell C, Binkley DM, Palmquist A, Grandfield K, Shah FA. Multimodal and multiscale characterization of the bone-bacteria interface in a case of medication-related osteonecrosis of the jaw. JBMR Plus. 2022;6:e10693.

III. Micheletti C, DiCecco L-A[#], Deering J[#], Chen W, Ervolino da Silva AC, Shah FA, Palmquist A, Okamoto R, Grandfield K. Micro-to-nanoscale characterization of the osseointegration and lacuno-canalicular network at the interface with an additively manufactured implant for local genistein delivery. *Submitted for publication.*
[#]Equal contribution.

IV. Gomes-Ferreira PHS, Micheletti C, Buzo Frigério P, de Souza Batista FR, Monteiro NG, Bim-júnior O, Lisboa-Filho PN, Grandfield K, Okamoto R. PTH 1-34-functionalized bioactive glass improves peri-implant bone repair in orchiectomized rats: Microscale and ultrastructural evaluation. Biomater Adv. 2022;134:112688.

V. Micheletti C, Gomes-Ferreira PHS, Casagrande T, Lisboa-Filho PN, Okamoto R, Grandfield K. From tissue retrieval to electron tomography: Nanoscale characterization of the interface between bone and bioactive glass. J R Soc Interface. 2021;18:20210181.

VI. Micheletti C, Shah FA, Palmquist A, Grandfield K. Shedding light (… electrons) on human bone ultrastructure with correlative on-axis electron tomography and energy-dispersive X-ray spectroscopy tomography. *Submitted for publication.*
Preprint available in *bioRxiv*, DOI: 10.1101/2023.04.20.537681.

Additional publications not included in the thesis:

I. Micheletti C, Hurley A, Gourrier A, Palmquist A, Tang T, Shah FA, Grandfield K. Bone mineral organization at the mesoscale: A review of mineral ellipsoids in bone and at bone interfaces. Acta Biomater. 2022;142:1–13.

II. Grandfield K, Micheletti C, Deering J, Arcuri G, Tang T, Langelier B. Atom probe tomography for biomaterials and biomineralization. Acta Biomater. 2022;148:44–60. *Invited article.*

III. Fu L[#], Williams J[#], Micheletti C, Lee BEJ, Xu G, Huang J, Engqvist H, Xia W, Grandfield K. Three-dimensional insights into interfacial segregation at the atomic scale in a nanocrystalline glass-ceramic. Nano Lett. 2021;21:6898–6906. [#]Equal contribution.

IV. Shah FA, Jolic M, Micheletti C, Omar O, Norlindh B, Emanuelsson L, Engqvist H, Engstrand T, Palmquist A, Thomsen P. Bone without borders – Monetite-based calcium phosphate guides bone formation beyond the skeletal envelope. Bioact Mater. 2023;19:103–114.

Declaration of academic achievement

This thesis comprises six Papers, which are published in peer-reviewed journals, published as preprints, or submitted for publication, as outlined on page xiii.

Author contributions to each of the Papers are as follows:

Paper I. I conceptualized the study with assistance from my supervisors. I conducted most of the experiments, analyzed all the data, prepared figures for publication, wrote the original draft, and revised it following peer review during publication. M. Jolic completed the reference point indentation experiments. A. Palmquist acquired some of the micro-computed X-ray tomography data. Technical staff (not included in the author list) performed the animal work and sample collection. All authors reviewed the manuscript before submission and publication.

Paper II. I conceptualized the study with assistance from my supervisors. I conducted most of the experiments, analyzed all the data, prepared figures for publication, wrote the original draft, and revised it following peer review during publication. L.-A. DiCecco completed some of the transmission electron microscopy experiments. D.M. Binkley prepared the sample for transmission electron microscopy experiments. C. Larsson-Wexell performed the sample collection. F.A. Shah completed resin cast etching experiments and relative imaging by scanning electron microscopy. All authors reviewed the manuscript before submission and publication.

Paper III. I conceptualized the study with assistance from my supervisors. I conducted most of the experiments, analyzed all the data, prepared figures for publication, and wrote the original draft. L.-A. DiCecco and J. Deering designed the implants. J. Deering completed implant acid etching, some preliminary scanning electron microscopy imaging, and all plasma focused ion beam-scanning electron microscopy tomography acquisition and reconstruction. W. Chen completed resin cast etching experiments and relative imaging by scanning electron microscopy, under my supervision. A.C. Ervolino da Silva performed the animal work and sample collection. All authors reviewed the manuscript before submission.

Paper IV. I designed and conducted all the electron microscopy experiments, analyzed the relative data, and wrote the relative sections in the original draft. P.H.S. Gomes-Ferreira and R. Okamoto conceptualized the main aspects of the study. P.H.S. Gomes-Ferreira performed the animal work and sample collection, and the other experiments included in the study (with assistance from the other co-authors), prepared figures for publication, and wrote the original draft. All authors reviewed the manuscript before submission and publication.

Paper V. I conceptualized the study with assistance from my supervisors. I conducted most of the experiments, analyzed all the data, prepared figures for publication, wrote the original draft, and revised it following peer review during publication. P.H.S. Gomes-Ferreira performed the animal work and sample collection. T. Casagrande prepared the sample for transmission electron microscopy and

electron tomography experiments. All authors reviewed the manuscript before submission and publication.

Paper VI. I conceptualized the study with assistance from my supervisors. I conducted all the experiments, analyzed all the data, prepared figures for publication, and wrote the main manuscript. Technical staff (not included in the author list) prepared the samples for transmission electron microscopy and electron tomography experiments. All authors reviewed the manuscript before submission.

Introduction

This chapter introduces relevant background information to the studies in this thesis.

In the first section, the multiscale, hierarchical structure of bone is described, with a focus on the main components (collagen fibrils and mineral) and on the mineralized collagen fibril. Concepts related to how bones form, model, and remodel are also reviewed. Bone repair and regeneration following biomaterial implantation, i.e., osseointegration, are explained especially in relation to the two biomaterials examined in this thesis, i.e., titanium and bioactive glass [Papers III-V]. Some notions on surface functionalization for local drug delivery are also provided, given its relevance to this thesis [Papers III-IV].

In the second section, an introduction to bone density (quantity) and quality is provided, followed by their contextualization in the two diseased conditions relevant to this thesis, i.e., diabetes mellitus and osteoporosis. An overview of the main therapies used in osteoporosis is given, together with some reported side effects, specifically osteonecrosis of the jaw, as these aspects are relevant to Papers II-IV.

In the third and last section, technical information and example applications of the main techniques used in this thesis to characterize bone and bone interfaces are reviewed.

BONE

Bones in the skeletal system of vertebrates play paramount functions in the body, from protecting internal organs, to working in concert with muscles and other connective tissues to allow the body to move; from storing minerals like calcium and phosphorus, to releasing them when needed[1]. To fulfill the requirements set by evolution, bones need to be lightweight, capable to adapt to the external stimuli and self-repair, and at the same time tough and strong[2]. It is this unique combination of strength (i.e., resistance to non-recoverable deformation) and toughness (i.e., resistance to fracture), which is hard to achieve in material design, that has prompted research to unveil structural-functional relationships in bone to learn from nature to inspire biomimetic design[3]. In a sense, nature has "engineered" bones with an exquisite architecture to serve specific structural demands, in addition to key biological functions.

Bone matrix is composed of organic (24 wt%) and inorganic elements (70 wt%), together with water (6 wt%)[4]. The organic phase mostly comprises type I collagen (85-90%), in addition to a small fraction of non-collagenous proteins[5]. The inorganic phase is a calcium phosphate mineral similar to hydroxyapatite [$Ca_{10}(PO_4)_6(OH)_2$], substituted with carbonate [CO_3^{2-}] (up to 6 wt%) and other elements (e.g., magnesium and sodium)[6]. It is the hierarchical organization of the organic and inorganic components across multiple length scales that imparts strength and toughness to the bone matrix[7–9]. Specifically, collagen and mineral contribute to elasticity and stiffness, respectively[10]. Water also plays a role, increasing the deformability of collagen[5] and affecting the viscoelastic behaviour of bone[11]. The interplay between collagen and mineral makes bone a composite material, which has the "mineralized collagen fibril" as its building block unit at the nanoscale[9,12]. The term "bone" may actually be used in reference to a family of materials (more precisely, biogenic minerals) sharing the mineralized collagen fibril as their structural nanoscopic module[7]. Other than bone tissue in the vertebrate skeleton, other members of the bone family are dentin, cementum, and mineralized tendons. In this thesis, the term "bone" is used to indicate skeletal bone tissue, mostly in reference to bone matrix only.

Bone hierarchical structure

As mentioned above, the mineralized collagen fibril is just the building block for a highly complex hierarchical structure, as shown in Figure 1. At the molecular level, three polypeptide chains of type I collagen (two α_1 chains and one α_2 chain) are twisted in a right-handed triple helix, forming tropocollagen molecules that are 1.5 nm in diameter and 300 nm in length[13]. Tropocollagen molecules self-arrange in a quarter-staggered fashion creating a 67 nm-periodicity of alternating gap (40 nm) and overlap regions (27 nm)[14]. Such an assembly, 80-100 nm in diameter but with unspecified length, is commonly referred to as the "collagen fibril"[9,15].

Collagen fibrils are mineralized into what becomes the "mineralized collagen fibril". The exact spatial relationship between mineral and collagen in the mineralized collagen fibrils has been debated over the years, leading to different ultrastructural models being proposed. Overall, it is now accepted that mineralization occurs both inside an individual fibril, mainly in the gap regions (intra-fibrillar mineralization)[16], and on the fibril's outer surface, hence in between neighbouring fibrils (extra- or inter-fibrillar mineralization)[17]. However, while early investigators suggested that most of the mineral

is located within the gap zones, eventually extending into the overlap regions[16,18], others have indicated that mineral is mainly extra-fibrillar[19,20], and it is organized in stacks of plates called "mineral lamellae", which wrap around the fibrils[21]. More recently, the mineral phase has been shown to exceed the dimensions of a single fibril, spanning several fibrils instead (cross-fibrillar mineralization)[22,23]. However, none of the different models for the spatial organization of collagen fibrils and mineral crystals proposed to date has been fully adopted by the entire bone research community. This is studied in this thesis in Paper VI.

Mineral crystals are aligned with their longest dimension, i.e., the *c*-axis of the unit cell, to the long axis of the collagen fibrils[24,25]. The crystals are typically described as plate-shaped, 50 nm in length[26], 25 nm in width[26], and 2-4 nm in thickness[27], but varying dimensions and morphologies, specifically needles/rods instead of plates[23,28–30], have also been reported[6]. Mineral plates aggregate into larger assemblies, becoming themselves a hierarchical structure[23]. At the mesoscale, i.e., at a level connecting the nano- and microscale, mineral aggregates have the geometrical shape of ellipsoids[22,31,32]. Mineral ellipsoids have been only recently identified, but they appear to be ubiquitously found in native bone and at bone interfaces in different species and anatomical locations, as reviewed by the author of this thesis (see reference 33).

At the next levels in bone's multiscale architecture, mineralized collagen fibrils are assembled in bundles, which in turn are organized in arrays whose pattern varies based on the type of bone, i.e., lamellar *vs.* woven *vs.* parallel fibered[9]. In lamellar bone, which is the dominant type in the skeleton of humans and other mammals[8], fibril bundles 1-3 μm in size[34] are organized in 2-6 μm thick sheets called "lamellae"[5]. In addition to lamellae in circumferential lamellar bone, two structural motifs can be identified in lamellar bone, i.e., trabeculae and osteons. Lamellae are organized in packets with slightly different orientations in the trabeculae, while they form concentric layers around blood vessels in the osteons[9]. In particular, secondary osteons, which form as a result of bone remodeling, are also sometimes referred to as the "Haversian system", as the lamellae encircle the Haversian canal, which hosts blood vessels and nerves[5]. Osteonal lamellar bone is commonly described as a twisted/rotated plywood structure, where arrays of mineralized collagen fibrils are oriented at different angles in different (sub)lamellae[35,36]. However, other models have also been proposed[37].

Lastly, at the whole bone level, i.e., macroscopically, compact and trabecular bone can be distinguished. Compact bone is the outer, dense shell that encloses a porous, sponge-like interior, i.e., trabecular bone.

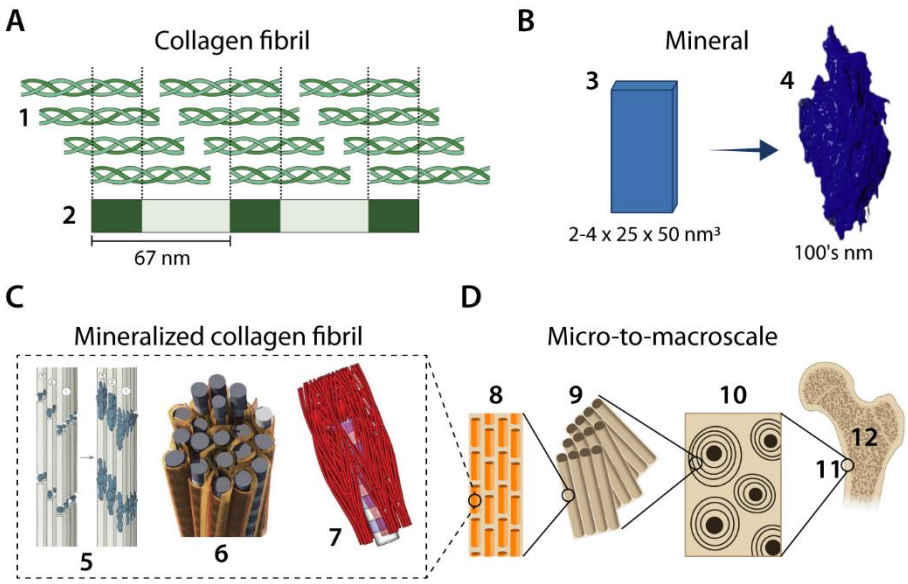

Figure 1. *Schematic representation of bone hierarchical structure, starting from the two main components, i.e., collagen fibrils (A) and mineral (B). In A, arrays of tropocollagen molecules (1) are staggered to form a collagen fibril, characterized by alternating gap (dark-coloured) and overlap (light-coloured) regions with 67 nm periodicity. In B, mineral platelets (3) assemble in ellipsoidal-shaped structures (4). At the mineralized collagen fibril level (C), the collagen-mineral spatial relationship has been proposed to be mostly intra- (5), extra- (6), or cross-fibrillar (7). At the next levels (D), shown in detail for osteonal bone, arrays of fibrils (8) assemble in lamellae (9), which in turn are organized in a twisted/rotated plywood fashion in the osteons (10). At the whole bone level, cortical (11) and trabecular (12) bone can be distinguished. [Images numbered 4 to 7 are reproduced with permission from references 31, 38 (original from 18), 39, and 23, respectively. Images numbered 1-2 and 11-12 are created with icons from BioRender.com].*

Bone formation, modeling, and remodeling

Bones are primarily formed by either endochondral or intramembranous ossification[40–42]. Endochondral ossification proceeds through a cartilage template. As this cartilage matrix grows, it progressively calcifies and is replaced by bone tissue[1]. In intramembranous ossification, bone tissue is laid down directly (*de novo*) without the intervention of the cartilage precursor[40–42]. This ossification route is followed by several bones in the skull[40]. In general, bones grow by apposition of new tissue at the outer surface (periosteum). Long bones formed by endochondral ossification also grow longitudinally at the growth (epiphyseal) plate, which is the cartilage layer separating epiphysis and diaphysis until growth is complete in adulthood[1]. The counterpart of the growth plate in cranial bones formed by intramembranous ossification is represented by cranial sutures. Sutures act as centres of intramembranous bone growth, with new bone being deposited at their edge in response to signals from the expanding cranium[43].

During skeletal development, the size and shape of bones are adjusted through the process of "bone modeling", where bone is formed or removed by two distinct types of bone cells, i.e., osteoblasts (the bone-forming cells) and osteoclasts (the bone-resorbing cells)[40]. Bone formation and resorption during modeling occur independently from each other and are mostly initiated in response to stimuli of a

mechanical nature, ensuring that the overall structure is adapted to the mechanical function[5,40]. This adaptation is exemplified by the fact that both osteons in cortical bone and trabeculae in trabecular bone are oriented along the direction of the principal stresses[1,5]. In the well-known law bearing his name, Wolff observed that the pattern of the trabeculae in the proximal femur is analogous to that of the stress trajectories in the Culmann crane[44]. Analogously, in long bones, osteons are parallel to the long axis of the bone[1].

Osteoblasts and osteoclasts work instead in a coupled manner in the process of "bone remodeling", which is at the basis of bone's dynamic nature. Every year, about 4% and 20% of cortical and trabecular bone, respectively, are replaced to remove microdamaged and old tissue, as well as to maintain bone mass and regulate mineral homeostasis[1]. A remodeling cycle is composed of five phases: i) activation, where osteoclasts are recruited at the remodeling site; ii) resorption, where bone is removed by the osteoclasts; iii) reversal, where the transition from resorption to formation occurs; iv) formation, where new bone is deposited by the osteoblasts, first in the form of an organic matrix, the osteoid, which later becomes mineralized; v) quiescence (resting), where formation stops and bone lining cells cover the quiescent bone surface[40].

Osteocytes and lacuno-canalicular network

Increasing evidence points towards the osteocytes, i.e., the resident bone cells, as having a role as orchestrators of bone remodeling[45]. Osteocytes are the most abundant type of bone cells, constituting over 90% of bone cells in the mature human skeleton[45,46] for an estimated total of 42 billion[47]. Osteocytes differentiate from osteoblasts as these become buried in their own mineralizing matrix[48]. Each osteocyte resides inside within a lens-shaped space called "lacuna" and connects with neighbouring osteocytes through its cell processes, which are housed in narrow channels, the "canaliculi"[5]. In osteonal lamellar bone, lacunae are primarily disposed in concentric layers around the Haversian canal, while canaliculi run in the orthogonal direction, i.e., perpendicular to the Haversian canal[49]. The extensive network of lacunae and canaliculi within the hierarchically structured bone matrix constitutes the so-called "lacuno-canalicular network" (LCN), which is key to the sensing and transmission of mechanical loads[45,50]. Specifically, osteocytes act as mechanotransducers, i.e., they sense mechanical strains to then coordinate the response of osteoblasts and osteoclasts[51]. Hence, osteocytes play an important part in regulating bone metabolism and bone quality[48,50], not just in native bone, but also in bone forming at the interface with biomaterials[52].

Bone repair: biomaterials and osseointegration

Bone tissue is a "smart material" capable of self-repair. Fracture healing and bone repair follow similar steps as embryonic skeletal development, specifically endochondral ossification, where bone formation is preceded by a cartilage matrix[53]. However, to augment or restore lost functions when self-repair is not enough, for example in the case of large and complex defects or compromised healing conditions, biomaterials are often needed. In addition to common biomaterial requirements such as biocompatibility, bone-interfacing biomaterials, such as hearing implants and endosseous dental implants, are selected also based on their ability to osseointegrate. The term "osseointegration" refers to "a direct – on light microscopic level – contact between living bone and implant"[54], although it is

now clear that this contact occurs at the (sub)nanoscale, at a level beyond what light microscopy can resolve[55–57]. Various ultrastructural arrangements of the bone-implant interface have been proposed over the years, but current interpretations emphasize the role of mineralized collagen fibrils as the building blocks of the interface, similarly to native bone[56]. Interestingly, peri-implant bone initially laid down as woven bone is remodeled to closely mimic its native status. The bone-implant interface is thus hierarchical in nature, with intermixing between implant surface elements and bone at the atomic level, and mineralized collagen fibrils oriented parallel to the implant surface at the nanoscale[52,58,59]. At the microscale, osteocytes connect through their processes to the implant surface, establishing a mechanosensing-based communication pathway with the implant itself[60].

The ultimate goal of osseointegration is to close the gap between the implant and native bone with new bone. New bone formation occurs over two fronts: one directed from native bone towards the implant (distance osteogenesis), and the other directed from the implant itself towards native bone (contact osteogenesis), for which it is important that the implant surface displays optimal physicochemical properties to promote formation of bone directly on it[61].

An important distinction should be made between degradable and non-degradable implant materials. In the case of degradable materials, the bone-implant interface is not in a fixed position in the peri-implant compartment, but moves as the implant itself degrades[56]. In this thesis, both non-degradable titanium-based implants and degradable bioactive glass particles are used, hence more background information on these biomaterials are introduced in the following sub-sections.

Titanium-based bone implants

The mechanical properties of titanium, combined with its biocompatibility and corrosion resistance, make it a suitable candidate for load-bearing bone implants[62]. Commercially pure titanium (cp-Ti) and the alloy Ti-6Al-4V are extensively employed in dental and orthopedic applications, respectively[56]. Titanium spontaneously passivates in air forming a 5-10 nm-thick layer of titania (TiO_2)[63]. This surface oxide layer effectively renders the implant a "ceramic" material from the viewpoint of the host environment, and favours osseointegration thanks to its bioactive nature[63].

The physicochemical properties of the implant surface greatly affect osseointegration outcomes[64]. Implant surface topography is often modified to introduce micro- and/or nanoscale features, which are beneficial to osseointegration[61,64–67]. Common surface modification strategies include acid etching to add sub-micron texturing to the implant surface[64]. Micro-rough surface topography can be directly obtained without the need of post-processing by additive manufacturing (AM) via powder bed fusion techniques due to residual microparticles from incomplete melting/sintering of feedstock powders[68]. AM also offers highly customizable solutions, including engineered porous implants with precise control over pore size, volume, and architecture[69,70]. Bone ingrowth can occur within the pores, increasing the area of bone-implant contact (BIC), in turn improving implant stability and osseointegration[71,72].

Bioactive glasses

Bioactive glasses are a class of silica-based bioceramics usually made of SiO_2, Na_2O, CaO, and P_2O_5. Specifically, the first developed bioactive glass, 45S5 Bioglass®, has the following composition by

weight: 45 wt% SiO_2; 24.5 wt% Na_2O; 24.5 wt% CaO; and 6 wt% P_2O_5 [73]. This is analogous to Biogran® used in this thesis [Papers IV-V], which is a bioactive glass commercialized in the form of granules typically 300-360 μm in size. Biogran® granules are used in the clinical practice as fillers to augment bone volume, for example to elevate the sinus floor prior to implant installation in edentulous patients[74].

Bioactive glasses display high surface reactivity *in vivo*, making them chemically bond with bone. On the biomaterial side, five reactions take place: i) leaching, i.e., release of alkali and alkaline elements via ion exchange; ii) dissolution through breaking of –Si–O–Si– bonds; iii) formation of a SiO_2-rich gel; iv) migration of Ca^{2+} and PO_4^{3-} to the SiO_2-rich surface and formation of a CaP-rich outer layer around the Si-rich gel core; v) crystallization of the CaP layer[75]. On the host side, phagocytosing cells reach the Si-rich core through cracks in the CaP-rich outer layer and start resorbing it[76]. Undifferentiated mesenchymal cells also migrate through these cracks and adhere to the CaP surface, which triggers their differentiation into osteoblasts, likely due to its bone-like composition[76]. Osteoblasts then start depositing new bone, promoting osseointegration via contact osteogenesis.

Surface functionalization for local drug delivery

Not only can the surface of biomaterials be modified to optimize its physical and/or chemical properties, but it can also be functionalized to deliver specific molecules and therapeutic agents locally at the implant site[77]. Local drug delivery presents advantages over conventional systemic administration in terms of tuning drug concentration and bioavailability at the site of interest, and avoiding adverse side effects in unaffected parts of the body. Enhancing bone response in the peri-implant space by local release of therapeutics can especially be useful when systemic conditions compromise bone repair and regeneration[78]. For example, in a study by Bai et al., a porous titanium scaffold fabricated by AM was injected with a hydrogel loaded with a common medication to treat osteoporosis, which was released *in vivo* upon hydrogel degradation, in turn improving osseointegration in osteoporotic rabbits[79]. In this thesis, surface functionalization of two different biomaterials (titanium and bioactive glass) for local drug delivery purposes is explored to promote osseointegration in osteoporotic-like conditions [Papers III-IV]. The specific therapeutic agents used in those studies are introduced in the *Osteoporosis* section (see page 11).

BONE QUANTITY AND QUALITY IN DISEASE

The hierarchical organization of bone and its maintenance through modeling and remodeling are essential to the mechanical functioning. Imbalances in bone remodeling, with bone resorption prevailing over formation, or vice versa, can lead to sub-optimal bone mass. A parameter routinely monitored in the clinical practice is bone mineral density (BMD), which represents the amount of bone mass per unit volume (expressed in g/cm^3) and is typically measured by dual-energy X-ray absorptiometry[80]. However, BMD is not the sole determinant of bone fragility. In addition to this quantity-related metric, the concept of "bone quality" has been developed to encompass "the totality of features and characteristics that influence a bone's ability to resist fracture"[81]. These features are mostly bone material properties related to its structure (e.g., shape, micro-architecture, micro-porosity) and composition (e.g., degree of mineralization, properties of bone mineral and/or collagen)[82,83].

The increase in bone fragility that accompanies aging and/or diseases can often be attributed to altered bone turnover, affecting bone quantity, and/or to structural and compositional changes deteriorating bone quality[83,84]. Hereinafter, abnormalities in bone quantity and quality will be reviewed in greater detail for diabetes mellitus, especially type 2, and osteoporosis, which are relevant to this thesis.

Diabetes mellitus

Diabetes mellitus is a "group of metabolic disorders characterized and identified by the presence of hyperglycemia in the absence of treatment"[85]. Chronic hyperglycemia is due to abnormal functioning of pancreatic β-cells, which are responsible for secreting insulin, the hormone controlling blood glucose levels. According to the World Health Organization, 422 million people were affected by diabetes mellitus in 2014[86]. The vast majority (90-95%) of cases are of type 2 diabetes mellitus (T2DM), characterized by insulin resistance[85]. Other common forms of diabetes include type 1 diabetes, which is an autoimmune disease leading to β-cell destruction and insulin deficiency, and gestational diabetes[85].

The number of people with diabetes has been rising over the past three decades. In particular, T2DM is now considered epidemic, as sedentary lifestyles have contributed to an increasing prevalence of obesity, which is a significant risk factor for T2DM[87]. T2DM often co-exists not only with obesity, but also with other metabolic disturbances, creating a cluster of conditions labelled as "metabolic syndrome" (MetS), which increases the susceptibility to cardiovascular disease[88].

The metabolic changes caused by diabetes and/or obesity affect many organs and tissues, including bone. Individuals with T2DM are at greater risk of bone fractures, yet they often display a normal or even higher BMD compared to healthy individuals[89]. While this apparent contradiction could be in part attributed to collateral effects such as a greater likelihood of falls[90], the overall reduction in bone strength can be explained by changes in bone material properties, i.e., bone quality[84,91]. A positive correlation between BMD and body weight, as well as fat and lean mass, is commonly reported[92] and attributed to skeletal adaptation to mechanical stimuli, with increased loading promoting bone formation[93]. This regulation pathway of bone mass related to mechanical loading has been termed as the "mechanostat"[94].

The accumulation of advanced glycation end-products (AGEs) in hyperglycemia is often indicated as one of the main culprits of the increase in skeletal fragility in T2DM[91]. Cross-linking types of AGEs like pentosidine induce non-enzymatic cross-linking of collagen, which causes fibril embrittlement[95]. Together with non-crosslinking types of AGEs, such as carboxymethyl-lysine, the interaction between AGE and its receptor induces oxidative stresses and inflammation[96], with consequences on osteoblastic and osteoclastic activity.

Hyperglycemia and obesity have been associated with a low rate of bone turnover. One of the possible explanations is that adipogenesis is favoured over osteoblastogenesis in obesity due to the preferential differentiation of mesenchymal stem cells in adipocytes rather than osteoblasts[97]. The AGE-AGE receptor axis and oxidative stresses play a role in bone formation, with higher levels of AGEs and oxidative stresses leading to reduced osteoblast proliferation and differentiation[98,99]. It remains controversial whether and how osteoclastic activity is affected by T2DM. Chronic inflammation in obesity appears to increase the production of pro-inflammatory cytokines that stimulate osteoclast-induced bone resorption through the activation of the osteoprotegerin/RANKL (RANK-ligand)/RANK (receptor activator of nuclear factor kappa-B) pathway[100].

Leptin and bone metabolism

Energy and bone metabolism are interconnected through the action of leptin. Leptin is an adipokine, i.e., a cytokine produced by the adipose tissue, responsible for controlling energy storage and appetite[101]. For example, low leptin levels during starvation stimulate appetite. Leptin acts directly on bone cells and indirectly on bone metabolism via the hypothalamus and sympathetic nervous system[102]. Inconsistencies in the indirect effects of leptin on bone mass have been reported. In general, leptin displays an anabolic action through the peripheral pathway and a catabolic effect through the central pathway[103], although deviations from this behaviour have also been reported[104].

Given the effect of leptin on bone metabolism, various animal models employed in T2DM research have mutations in the gene encoding leptin (Lep) or its receptor (LepR). Abnormal leptin signaling results in hyperphagia, hence Lep/LepR-deficient animals become obese, in turn displaying hyperglycemia and impaired glucose tolerance analogously to T2DM conditions[105]. T2DM etiology in humans does not typically involve genetic mutations, but some rare cases of humans with Lep/LepR mutations, causing severe obesity at an early age, have been reported[106–109]. A novel monogenic obese rodent model, the Lund MetS rat[110], is examined in this thesis [Paper I].

Osteoporosis

Osteoporosis, or "porous bone disease", has been defined as a "systemic skeletal disease characterised by low bone mass and microarchitectural deterioration of bone tissue with a consequent increase in bone fragility and susceptibility to fracture"[111]. Osteoporosis is typically associated with aging, although it can also develop as "secondary osteoporosis", for example due to glucocorticoids therapies (steroid-induced osteoporosis)[112]. Osteoporosis-related fragility fractures, i.e., fractures occurring at low-to-moderate levels of trauma, account for around 60% of all bone fractures in individuals above 50 years of age[113]. As the aging population keeps surging across the globe[114], the diagnosis, prevention, and

treatment of osteoporosis become increasingly important for the quality of life of the senior population, as well as the economic burden on the health care system.

Osteoporosis is characterized by low bone mass. In the diagnosis of osteoporosis, BMD is typically expressed as the "T-score" in terms of standard deviation from the mean value in the young healthy population. A T-score below -2.5 is indicative of osteoporosis, between -1 and -2.5 determines osteopenia, and above -1 is considered normal[80]. Loss in bone mass in osteoporosis is due to imbalanced bone remodeling with bone resorption prevailing over bone formation[112]. This naturally occurs with aging due to the decline in hormone levels, especially estrogen, which affect bone metabolism. The effects of aging-related hormone deficiency on bone strength are especially apparent in postmenopausal women, and age-adjusted fracture risk is significantly higher in female than male individuals[113].

Estrogen is the main hormonal regulator of bone metabolism in both sexes[115]. Estrogen has direct effects on various bone cells, specifically decreasing apoptosis of osteocytes and osteoblasts, and, conversely, increasing apoptosis of osteoclasts and decreasing their formation and activity[115,116]. Estrogen appears to modulate strain sensing via the "mechanostat"[94], and it is involved in the intestinal absorption of calcium and its renal conservation[116]. Collectively, direct and indirect effects of estrogen on bone metabolism make bone resorption outweigh bone formation in contexts of estrogen deficiency, such as after menopause[116]. In male individuals, estrogen bioavailability decreases with age[117]. Additionally, androgen levels affect bone remodeling. This is mostly noted in androgen deprivation therapy to treat prostate cancer (chemical/surgical castration), where lower levels of androgen lead to an increased rate of bone loss[118,119].

Because of the role of sex hormones in bone metabolism, widespread animal models used in osteoporosis research are subjected to gonadectomy surgery, i.e., ovariectomy (OVX) in females and orchiectomy (ORX) in males. The OVX rat is especially used to mimic postmenopausal osteoporosis[120,121]. While aged rats represent a more accurate model, mature rats are typically preferred due to their lower cost and greater availability[121]. The male counterpart is the ORX rat, which mimics conditions of androgen deprivation[122].

Not only bone density, but also bone quality is affected by osteoporosis. Deterioration in bone microarchitecture is especially apparent in the trabecular compartment, with reduction in bone volume and trabecular thickness and/or number[121]. Other changes have been reported in both bone structure and composition, e.g., increased cortical porosity, greater mineral crystallinity, and lower mineral heterogeneity[83,84].

Given the altered bone metabolism, it is reasonable to postulate that bone healing at a biomaterial interface may be compromised in osteoporotic individuals. However, there is no clear consensus on the effect of osteoporosis on osseointegration, and osteoporosis is not typically considered a contraindication to the installation of bone implants[123]. On the other hand, it is known that bone quantity and quality are key parameters to successful osseointegration[124]. The systemic alteration in bone metabolism, as well as the deteriorated bone structure, could affect primary implant stability and early biological fixation, in turn compromising osseointegration[125]. Slower osseointegration, higher failure rates and peri-implant bone loss, and lower values of BIC have been reported for implants placed in osteoporotic bone[123,125–127]. Bone healing and osseointegration in OVX/ORX rat models are

studied in this thesis in Papers III-IV, especially to examine the effect of local drug delivery on bone repair using some of the therapeutic agents described below.

Common and emerging therapies

Therapies to counteract bone loss are administered to both osteoporotic individuals and to those deemed at high risk of fracture in order to prevent this from occurring. Commonly used medications are anti-resorptive agents, but anabolic therapies are also available. The therapeutic agents to treat osteoporosis relevant to this thesis [Papers II-IV] are briefly discussed hereinafter.

Anti-resorptive medications are the gold standard in the treatment of osteoporosis, acting to suppress bone resorption. In this group, bisphosphonates are widely used to treat skeletal disorders, not just limited to osteoporosis but also skeletal complications due to metastatic cancer[128]. With a composition similar to that of pyrophosphates, i.e., mineral inhibitors found in the body fluids[129], bisphosphonates can inhibit mineralization and prevent the breakdown of hydroxyapatite crystals when bound to their surface[130,131]. Bisphosphonates also display toxicity towards osteoclasts, and limit their formation and activity[128].

Possible treatment alternatives are based on hormone replacement, specifically of estrogen, as bone loss post-menopause is primarily caused by estrogen deficiency[112]. However, hormone replacement therapy may have significant side effects, as an increased incidence of breast cancer has been reported[132]. Lower breast cancer rates have instead been noted for individuals consuming diets rich in phytoestrogens found, for example, in isoflavones in soybeans[133]. Therefore, phytoestrogens could offer an alternative treatment for osteoporosis while avoiding harmful side effects. An example of isoflavone used in this thesis is genistein [Paper III]. Genistein has shown a positive effect on bone mass on postmenopausal individuals treated in a randomized trial[134]. However, the use of genistein in bone applications has mostly been explored via systemic administration and not locally as investigated in Paper III.

Differently from anti-resorptive medications, anabolic agents act by enhancing bone formation in the remodeling cycle[135]. The 1-34 fragment of parathyroid hormone (PTH), teriparatide (PTH 1-34), was the first anabolic drug approved for clinical use in osteoporosis. Its intermittent use has anabolic effects on bone, for example via promotion of osteoblastogenesis, suppression of sclerostin, and hinderance of osteoclast differentiation[136]. In this thesis, the influence of PTH 1-34 administration on osseointegration in osteoporotic-like conditions is studied in the context of local delivery in the peri-implant space via surface functionalization of bioactive glass [Paper IV].

Side effects of bisphosphonates: osteonecrosis of the jaw

A prolonged or high-dose intake of bisphosphonates has been associated with a greater risk of developing medication-related osteonecrosis of the jaw (MRONJ)[137–140]. According to the American Association of Oral and Maxillofacial Surgeons, MRONJ can be diagnosed when necrotic bone in the jaw does not heal within eight weeks after intervention in an individual without any metastasis or history of radiation therapy in that area[140]. The pathogenesis of MRONJ is still not fully elucidated due to its complexity and multi-factorial nature. Possible causes include the unresponsive status of bone where resorption is suppressed, and the impaired healing due to toxicity of bisphosphonates to cells

of the soft tissue and immune system[141,142]. Bacteria are commonly found at the necrotic sites in the jaw, but the causal/temporal relationship between infection and necrosis is not fully understood[142–144]. This thesis includes a study on the effect of bacteria on bone matrix properties and degradation in a case of MRONJ [Paper II].

MULTISCALE ANALYTICAL TOOLS FOR BONE AND BONE INTERFACES

Owing to its hierarchical architecture spanning from the macro- to the nanoscale, the structure and composition of bone, both native and at biomaterial interfaces, can be examined using a plethora of techniques, each addressing specific features of interest at certain levels in its hierarchy. In other words, comprehensive characterization of bone and bone interfaces is best done by adopting a multiscale approach, correlating information acquired over multiple length scales[55,57,145,146]. This thesis applies a multiscale characterization platform, which is often also multimodal, i.e., different techniques based on dissimilar working principles are used, and sometimes multidimensional, combining two- and three-dimensional (2D and 3D) data. Hereinafter, a review of the technical details of the main characterization tools used in this thesis is provided, together with relevant examples from the literature of their application in the study of bone and bone-biomaterial interfaces. The characterization techniques described are organized based on the nature of the main information provided, i.e., structural or compositional. The typical spatial (lateral) resolution and field of view analyzed are graphically represented in reference to bone structure in Figure 2.

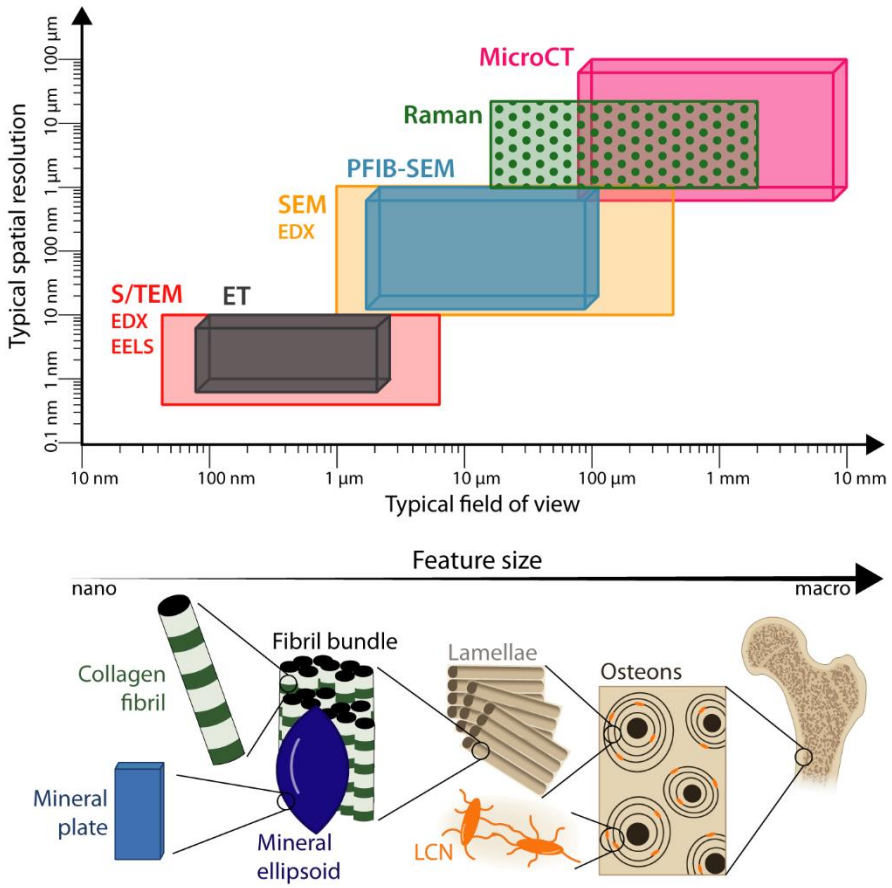

Figure 2. *Graph showing the typical field of view and spatial resolution for the main characterization techniques used in this thesis, in relation to relevant features in bone hierarchical structure. In the graph, the following abbreviations are used: micro-CT (micro-computed X-ray tomography); Raman (micro-Raman spectroscopy); SEM (scanning electron microscopy); PFIB (plasma focused ion beam); S/TEM (scanning/transmission electron microscopy); ET (electron tomography); EDX (energy-dispersive X-ray spectroscopy); and EELS(electron energy loss spectroscopy). 2D and 3D techniques are shown as rectangles and cuboids, respectively. A dotted pattern is used for the purely spectroscopy technique to differentiate it from the imaging techniques used for structural characterization (unless combined with spectroscopy as in SEM/STEM-EDX or STEM-EELS).*

Characterization of bone structure

Light probes: optical microscopy and micro-CT

Visible light microscopy

The most immediate tool to produce magnified images of bone structure is the optical microscope, or, more precisely, the visible light microscope. Imaging of bone with light microscopy dates back to the 17th century where some structural elements now known as lamellae and osteons were visualized[9]. In the 1960s, Brånemark's discovery that bone can form a direct contact with titanium was based on light microscopy observations, and in fact the term osseointegration was first defined "on light microscopic level"[54]. Light microscopy remains the primary tool used in histology to examine bone tissue, including at biomaterial interfaces, both quantitatively and qualitatively. Quantitatively, bone histomorphometry provides information on four types of measurements, i.e., area, length (perimeter or boundary), distance between points/lines, and number of some features of interest (e.g., cells)[147]. Qualitatively, histological sections provide information on the general morphology and structural patterns (e.g., woven *vs.* lamellar bone), the state of the tissue (e.g., signs of necrosis), and which cells are present in it (e.g., bone cells, but also from nearby tissues other than bone), especially when specific features can be enhanced by appropriate stains[57].

Micro-computed X-ray tomography

Bone histomorphometry is performed on 2D sections, and inferring 3D information using stereology has limitations[147]. A solution is offered by micro-computed X-ray tomography (micro-CT). Micro-CT is based on X-ray absorption imaging, where images, i.e., radiographs, are formed by the X-rays transmitted through an object, which are attenuated based on absorption and density differences within the object itself and its thickness. In micro-CT experiments, the sample is mounted on a rotating stage. The stage is rotated typically over 180°-360°, and a radiograph is acquired at each rotation step. These radiographs represent 2D projections of the object at different angular positions of the stage[148]. The projections are reconstructed by specific algorithms (e.g., back-projection) to obtain a 3D representation of the object. The term "topography" (*tomos*, "section", and *graphe*, "to write") refers to this specific type of imaging based on 2D slices (projections) that are then combined to reproduce the original 3D object[55]. Some important parameters that determine the quality and resolution of the micro-CT reconstruction include the X-ray energy, intensity, and tube potential, the voxel size (pixel size in x, y, z), the duration of each projection (integration time), the number of repeated acquisitions at each step (frame averaging), and the number of projections collected, which is related to the rotation steps[149].

Micro-CT reconstructions provide an accurate 3D representation of the overall geometry and microstructure of bone or bone-biomaterial interfaces[55,57,146]. In addition to qualitative observations, various morphometry parameters can be quantified in 3D. These parameters can characterize relevant structural properties of cortical bone, such as cortical thickness, cortical bone area, and cortical area fraction, as well as properties of the trabecular compartment, such as bone volume fraction, trabecular thickness, trabecular separation, and trabecular number[149]. In micro-CT volumes of a bone sample

interfacing with a biomaterial, BIC can be quantified. However, metal implants typically induce artifacts in the reconstruction, especially at the bone-implant interface, due to beam hardening and scattering[150], in turn challenging the reliability of BIC measurements[151]. While micro-CT primarily provides structural information, by using standards of hydroxyapatite of known density, it is possible to obtain a liner correlation between grey-levels and density, which can be used to estimate the tissue mineral density (TMD) of bone samples acquired with the same settings as the standard[149].

Electron probes: SEM, FIB-SEM tomography, S/TEM, and electron tomography

Resolution in light microscopy is diffraction-limited, as first theorized by Abbe. In electron microscopy, thanks to the much smaller wavelength of electrons compared to light, a higher spatial (lateral) resolution can be achieved. The interaction between an electron beam and the atoms of a sample generates multiple signals that can provide several information, both of structural and compositional nature. This section focuses on electron signals used to obtain structural information, while signals employed in spectroscopy techniques are reviewed in the *Characterization of bone composition* section (see page 23). Despite focused ion beam-scanning electron microscopy (FIB-SEM) also involves the use of an ion beam, as explained below, this technique is included in this section as imaging is accomplished by the electron probe.

Scanning electron microscopy

SEM is based on the rastering of a finely focused electron beam across the surface of a sample placed in a high-vacuum chamber ($<10^{-3}$-10^{-4} Pa) (Figure 3A). Some instruments can also be operated in higher pressure regimes (1-2000 Pa), for example by supplying water vapour. This type of SEM is known as low-vacuum or variable pressure SEM, or sometimes environmental SEM in the high pressure range, and it is especially useful to image insulating samples without any conductive coatings, otherwise necessary to reduce charging[152].

The interaction of the incident electron beam with the sample generates several signals (Figure 3B). Two of these signals, secondary electrons (SEs) and backscattered electrons (BSEs), are used to form SEM images. SEs are inelastically scattered electrons, corresponding to weakly bound electrons in the outer atomic shell that are ejected due to the energy transferred by the incident beam (i.e., the primary beam, hence the term "secondary" electron). BSEs are elastically scattered electrons, corresponding to the electrons in the incident beam that are deflected "back" out of the sample due to the interaction with the atomic electric fields. If BSEs have high enough energy to eject weakly bound outer shell electrons, they can also generate SEs when interacting with the atoms of the sample. SEs have low energy, hence only those produced close to the sample surface (few nanometers) can escape and reach the detector. On the other hand, BSEs come from deeper within the sample, up to hundreds-to-thousands of nanometers below the surface[152].

The collection of SEs or BSEs by appropriate detectors produces an image of the sample surface. As the SEs that escape from the sample are those generated up to few nanometers below its surface, the contrast, i.e., the difference in intensity between two adjacent areas[153], in SE-SEM images provides

information on the surface morphology and topography. By optimizing the acquisition conditions, 3D-like images with high depth of focus can be obtained. The number of BSEs produced (BSE coefficient) increases with the atomic number (Z), thus contrast in BSE-SEM images reflects variations in composition, with heavier elements appearing brighter, and, conversely, lighter elements appearing darker. This type of contrast is referred to as "Z-contrast" or "compositional contrast"[152].

SEM is widely used to characterize bone structure, especially in BSE mode as this allows for the easy identification of regions with dissimilar composition, for example, bone *vs.* embedding resin or bone *vs.* implant (Figure 3C). Other features like osteons and lamellae, as well as osteocyte lacunae within the bone matrix, can also be imaged[154]. Thanks to Z-contrast, areas with heterogenous levels of mineralization can be readily visualized. Specifically, if the grey-levels of BSE-SEM images are calibrated using a standard of known Z, it is possible to convert grey-levels into mineral content, expressing it as calcium content (wt% Ca). This technique, termed "quantitative backscattered electron imaging" (qBEI), can be used to map the BMD distribution. Standards for qBEI are typically made of carbon (Z = 6) and aluminum (Z = 13) and their average grey-levels are set to 25 and 225, respectively, during image acquisition to ensure a linear correlation between grey-level and calcium content in the compositional range relevant to bone[155].

SE-SEM images of bone are mostly useful when surface topography provides valuable information, for example in the case of fracture surfaces or when selected tissue components are removed, such as to examine marquise-shaped mineral aggregates post-deproteinization[156]. SE-SEM imaging can also be used to visualize the LCN after resin cast etching (Figure 3D), a treatment that removes both the inorganic and organic components of bone matrix, while preserving the resin-infiltrated LCN[157].

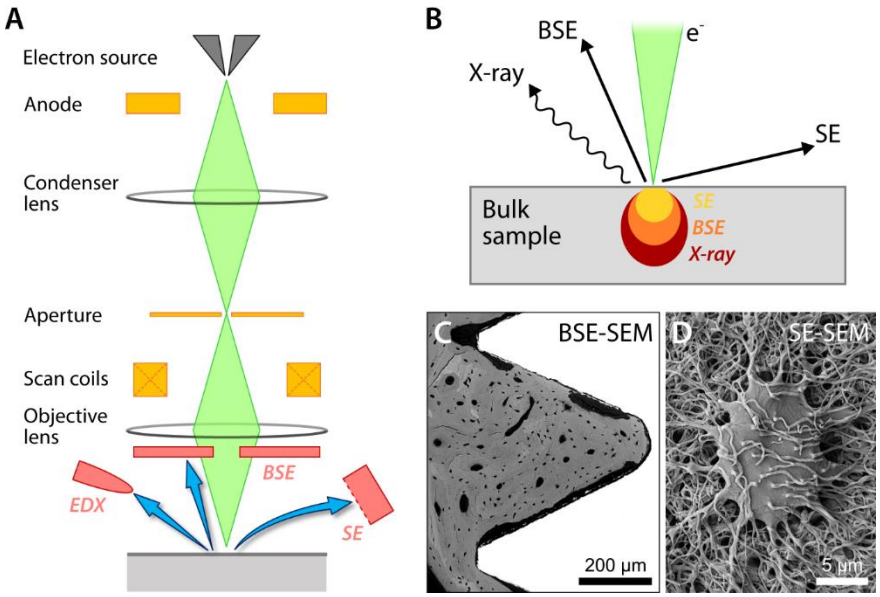

Figure 3. *Schematic representation of an SEM instrument (A) and signals generated of interest to this thesis with relative interaction volumes (B). The use of X-rays is discussed in the "Characterization of bone composition" section on page 23. Examples of SEM images in bone research: BSE-SEM image of a bone-implant interface (C) and SE-SEM image of an osteocyte lacuna after resin cast etching (D). [A is adapted with permission from reference [154], courtesy of Dr. Shah. C and D are reproduced with permission from references 158 and 157, respectively].*

Focused ion beam-scanning electron microscopy tomography

Although SEM is a powerful tool in bone research, SEM images are 2D and provide information on the sample surface only. On the other hand, by collecting a stack of 2D SEM images at successive intervals, it is possible to generate a 3D dataset. This is the working principle of FIB-SEM tomography, sometimes also referred to as "serial surface view", "serial slice-and-view", or "serial sectioning"[159]. This technique requires instruments equipped with two beams, i.e., an electron beam for imaging and an ion beam for milling. After milling with the ion beam a thin slice of material, typically in the 10 nm-range, the exposed cross-section is imaged with the electron beam, and the SE/BSE signal is collected. This sequence of milling and imaging is repeated in alternating steps until a stack of 2D SEM images is obtained. This stack is then assembled to generate a 3D image of the area examined, i.e., where the sequence milling-imaging took place[159]. Conventional dual-beam instruments are equipped with a Ga^+ ion column, but other ions can also be used offering different advantages and limitations. For example, instruments with a Xe^+ ion column, like that used in this thesis [Paper III], also called plasma FIB (PFIB), allows for higher removal rates, yielding volumes hundreds of micrometers in size, as opposed to tens of micrometers for Ga^+ FIB[160].

In bone research, FIB-SEM has been widely used to analyze the hierarchical organization of lamellar bone in relation to the arrangement of collagen fibril bundles[161,162]. Other applications relevant to this thesis include the examination of mineral ellipsoids at the mesoscale, accomplished using both PFIB-SEM[31] and conventional Ga^+ FIB-SEM instruments[22]. FIB-SEM has also been used to probe nanochannels, i.e., a network of nanopores thought to transport ions and small molecules within

bone[163,164]. In the study of bone-implant interfaces, FIB-SEM tomography was first applied in 2005 to visualize bone growing into the pores of a dental implant[165]. FIB-SEM can be especially valuable to evaluate osseointegration in 3D to bridge the length scales probed by micro-CT and electron tomography[55].

Dual-beam instruments can be used not just for 3D tomography, but also for site-specific and minimally destructive preparation of electron transparent samples of bone and bone-biomaterial interfaces for transmission electron microscopy (TEM)[166]. As this is not a characterization-intended application, but a method for advanced sample preparation, it is more fitting to describe its working principle and use in this thesis in the *Materials and methods* chapter (see page 28).

Scanning/transmission electron microscopy

In TEM, an ultrathin sample (<100-200 nm) is illuminated by a (nearly) parallel electron beam, and, conversely from SEM, the signal used to form images is that transmitted through the sample. Various signals are generated from the electron beam-sample interaction, which are both back-scattered or forward-scattered, i.e., transmitted (Figure 4A). A dominant imaging mode in TEM is bright-field (BF), where images are formed by the direct electron beam that is transmitted, undeviated, through the sample. In BF-TEM images, the contrast originates from mass/thickness variations and diffraction. If only certain scattered electrons are selected, then a dark-field TEM image is obtained. Selection of a set of elastically scattered electrons to form dark-field TEM images can be done by placing an aperture (the objective aperture) over specific diffraction spots, instead of over the direct beam like in BF-TEM. The diffraction spots are visible when operating the TEM in diffraction mode, i.e., when imaging the back focal plane of the objective lens (reciprocal space). These diffraction patterns provide information on the crystal structure of the sample. Typically, electron diffraction is performed by illuminating a specific area in the sample using an aperture to collect diffraction information only from that region, hence the term "selected area electron diffraction" (SAED)[153].

Instead of a parallel beam like in traditional TEM, it is also possible to form a convergent electron probe. The convergent beam is rastered across the sample, and scattered electrons are collected at each point (pixel) on the sample. Due to the scanning nature of the probe, this imaging mode is called scanning TEM (STEM). Electrons used for STEM images are typically those incoherently scattered at high angles (Rutherford scattering), which are collected using high-angle annular dark-field (HAADF) detectors (Figure 4B). HAADF-STEM images are formed by Z-contrast, and the scattering intensity is roughly proportional to Z^2 [167].

As electrons have smaller wavelength at higher energies, resolution achievable in S/TEM, with typical accelerating voltages ranging from 80 to 300 kV, is higher than in SEM. This makes S/TEM a powerful tool to image bone and bone interfaces with (sub)nanoscale resolution. BF-TEM has been extensively used to study the ultrastructure of bone, i.e., its nanoscale organization, for example to visualize the characteristic banding pattern of collagen fibrils and the spatial relationship between collagen fibrils and mineral, as well as the orientation of the mineral when combined with electron diffraction[145]. Since the pioneering work of Robinson, TEM has also been employed to study the shape and size of bone mineral[26]. Especially relevant to this thesis [Paper VI] was the use of BF-TEM and

HAADF-STEM to reveal distinct organizational motifs in bone sections based on the orientation of the collagen fibrils with respect to the image plane, i.e., parallel *vs.* perpendicular[23,168–170], as shown in Figure 4C-E. In the context of bone implants, TEM imaging, often completed in HAADF-STEM mode, clearly demonstrated that osseointegration with several biomaterials, such as titanium[58,65,171] and hydroxyapatite[172], occurs at the nanoscale, redefining it as "nano-osseointegration".

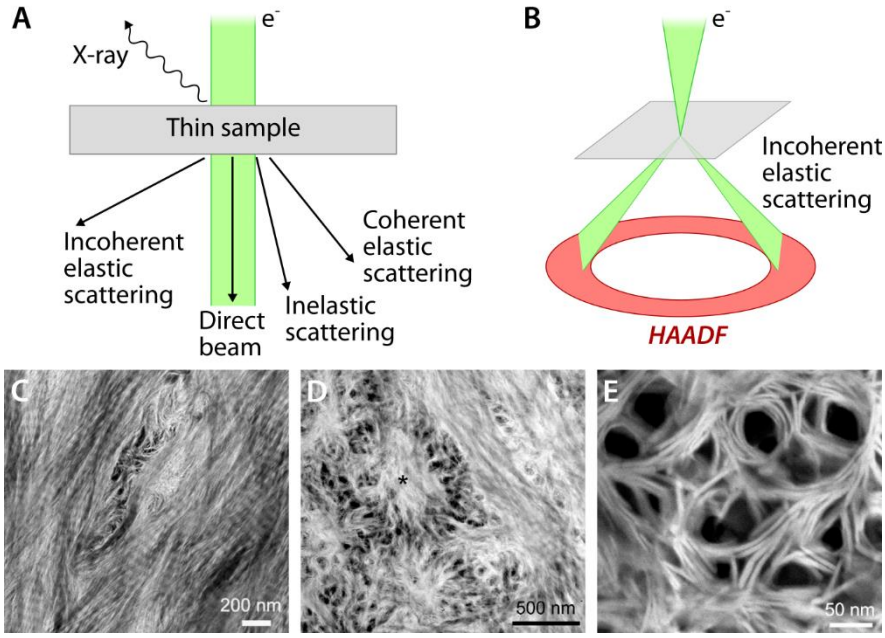

Figure 4. *Schematic representation of the signals generated in S/TEM of interest to this thesis (A), with a focus on HAADF-STEM (B). Characteristic HAADF-STEM images of sections of human femoral cortical bone oriented parallel (C) and perpendicular (D-E) to the long axis of the femur [reproduced with permission from reference 170].*

Electron tomography

While S/TEM images can provide structure-related information with nanoscale resolution, they suffer from the significant drawback of being 2D projection images of a 3D sample. In other words, all features along the sample thickness are projected onto the same plane, hence understanding their arrangement in 3D is not possible and can lead to misinterpretations of the spatial relationship between different components, for example, collagen fibrils and mineral in bone. Such a limitation can be overcome by electron tomography, which is based on the acquisition of S/TEM images at successive tilt angles, typically every 1-2°. This series of images, commonly referred to as "tilt series" in the field, is then aligned, e.g., by cross-correlation, and reconstructed into a 3D representation of the original object thanks to mathematical algorithms, such as simultaneous iterative reconstruction technique (SIRT)[173,174].

The quality of the 3D reconstruction is highly influenced by the number of projections, i.e., images acquired at different tilt angles. However, in conventional (single-tilt) electron tomography, shadowing of the sample holder and reduced size of the instrument chamber limit the tilt range typically to ±70°,

producing an unsampled region, called "the missing wedge" due to its shape, where no projections can be acquired[173,174]. Specialized holders allowing for ±90° tilt or even full 360° rotation exist to overcome this limitation when used in conjunction with rod-shaped samples. This technique is called "on-axis electron tomography" and eliminates missing wedge artifacts in the final reconstruction, leading to improved quality and fidelity[175] (Figure 5).

Electron tomography can be carried out in both TEM and STEM mode. An essential requirement is that the image intensity at every tilt angle is a monotonic function of a certain property in the sampled volume, as stated in the "projection theorem". It follows that BF-TEM tomography cannot be used for crystalline samples, as diffraction contrast violates this theorem. On the other hand, samples containing crystalline phases, such as bone, can be successfully imaged using Z-contrast electron tomography, based on the acquisition of tilt series in HAADF-STEM mode[176].

In bone research, electron tomography has been a primary tool to probe collagen-mineral relationships in 3D and aid the formulation of the main ultrastructural models proposed to date[18,23,177]. Z-contrast electron tomography has also been applied to the study of osseointegration, demonstrating contact between bone and titanium at the nanoscale in 3D[178]. The use of Z-contrast tomography in osseointegration research has also encompassed on-axis electron tomography[179]. Moreover, by removing missing wedge artifacts, on-axis electron tomography presents several advantages for further elucidating bone ultrastructure at the nanoscale, especially collagen-mineral relationships, as demonstrated in this thesis in Paper VI.

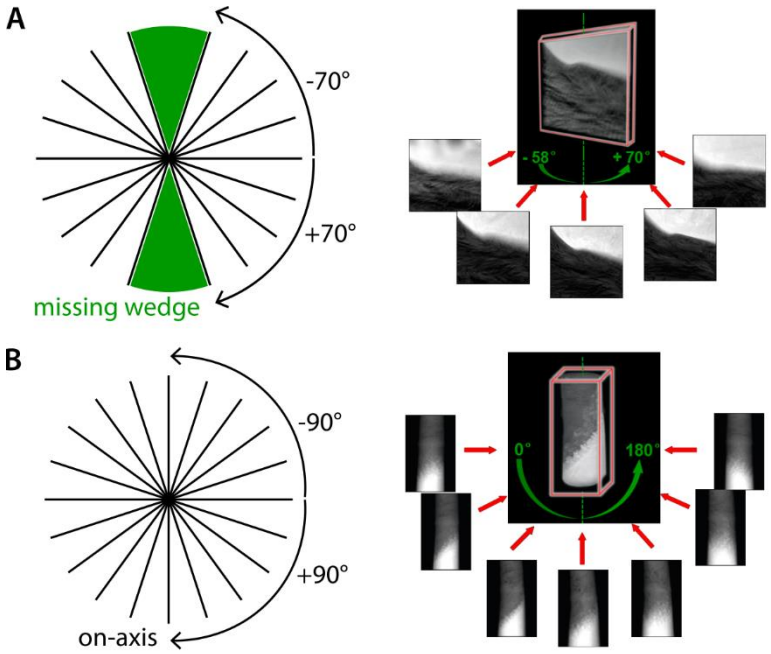

Figure 5. *Tilt range and examples of acquired projection images and final 3D reconstruction of a bone-implant interface in conventional (single-tilt) (A) and on-axis electron tomography (B). [Right images are adapted with permission from reference 179, courtesy of Dr. Wang].*

Characterization of bone composition

Despite BSE-SEM and HAADF-STEM images offering some insights into composition, they cannot determine which elements/compounds are present. Therefore, structural characterization should be complemented with spectroscopy techniques to determine compositional information in qualitative and/or quantitative terms. In this thesis, three spectroscopy techniques are employed, where the signals of interest are produced either using a light probe in the red range (micro-Raman spectroscopy) or an electron probe (energy-dispersive X-ray spectroscopy, EDX; and electron energy loss spectroscopy, EELS).

Micro-Raman spectroscopy

Raman spectroscopy is based on the Raman effect, i.e., the inelastic scattering of photons by matter. When photons of a single quantum energy (e.g., from a laser source) interact with the atoms of a sample, some photons (~1 in 10^7) experience a shift in quantum energy with respect to the source due to the transfer of part of their energy to molecules in the sample that become excited in vibrational states. The shift in energy, i.e., the Raman shift (expressed as frequency/wavenumber in cm^{-1}) can be used to identify the molecular compounds in the sample, as the vibrational states are characteristic of each molecule. After the laser source has interacted with the sample, backscattered photons are collected by a spectrometer where a diffraction grating "splits" them in different components based on their energy. The signal intensity of each component is then recorded by a detector[180].

A schematic representation of the standard set-up of an instrument for Raman spectroscopy is given in Figure 6A. When a Raman spectrometer is integrated with an optical microscope, e.g., a confocal system, the technique is more precisely labelled as "micro-Raman spectroscopy". Raman spectra can be acquired in specific points of interest on the sample surface, but hyperspectral mapping can also

be accomplished. This is done by recording a Raman spectrum at constant steps (pixels) over an area of interest, and then using a specific spectral parameter (e.g., peak intensity) to map its distribution and variation in the examined region. With transparent samples, hyperspectral mapping can be extended in the third dimension, i.e., the sample depth, to produce 3D maps[180].

Micro-Raman spectroscopy can provide information regarding bone quality, both in native and peri-implant bone. The typical Raman spectrum of bone is shown in Figure 6B. Bone matrix composition is often expressed in terms of mineral-to-matrix ratio to evaluate the degree of mineralization[181]. This ratio is obtained from integral areas of bands characteristic of the mineral phase, i.e., the phosphate peaks, and of the organic phase, e.g., the amide peaks, which are mostly representative of collagen[182]. Another compositional metric is the carbonate-to-phosphate ratio, from which the extent of carbonate substitution, typically increasing with age, can be inferred[181]. Lastly, structure-related information can also be obtained, as the full width at half maximum of the phosphate band at ~959 cm^{-1} is related to the mineral crystallinity, with higher crystallinity yielding sharper peaks[181].

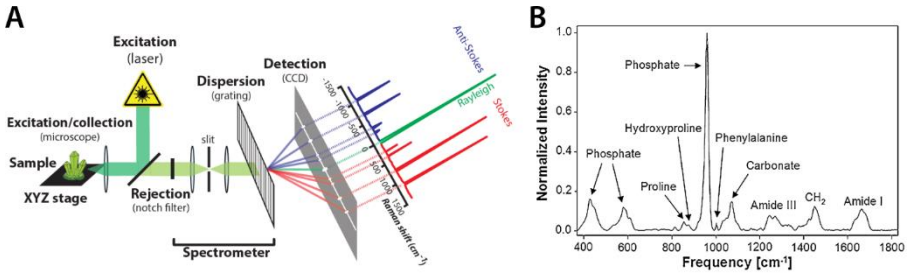

Figure 6. *Schematic representation of the typical configuration of a Raman spectrometer (A) and typical Raman spectrum of bone (B). [A and B are reproduced with permission from references 180 and 181, respectively].*

Energy-dispersive X-ray spectroscopy

The interaction of an electron beam with the atoms of a sample generates not only electron signals, but also X-rays. When the incident electron beam has a high enough energy, above the critical ionization energy, it can cause a core electron, i.e., an electron from an inner shell, to be ejected from the atom, leaving behind a vacancy. This hole can be filled by an electron from a higher energy shell. When this occurs, the excess energy is emitted as a photon, more precisely, an X-ray. These X-rays are called "characteristic" because their energy is unique to each element in the periodic table. This phenomenon is at the basis of EDX, where characteristic X-rays are detected to determine the elemental composition of the sample, also allowing for (semi)quantitative analysis[152]. EDX analyses can be completed in both SEM and TEM instruments if equipped with X-ray detectors. In TEM, EDX is carried out in STEM mode to acquire EDX spectra in specific points, across a line, or also over an entire region of the sample (spectral imaging)[153].

SEM-EDX can be used in bone research to examine bone matrix mineralization, for example in terms of the calcium-to-phosphorus ratio, or to evaluate trends in elemental variation across interfaces[154]. This can be especially applicable to the study of bone-biomaterial interfaces. STEM-EDX can have

similar applications, but offers a greater spatial resolution than SEM-EDX as the interaction volume is reduced compared to bulk SEM samples[153]. Some examples include the quantification of intra- and extra-fibrillar mineralization in native bone[169], or the determination of chemical gradients within the interface between bone and metallic or ceramic implants[171,172,183]. Notably, this thesis includes a novel application of STEM-EDX in bone research, i.e., in tomography mode [Paper VI].

Electron energy loss spectroscopy

In S/TEM, some of the incident electrons lose part of their energy due to inelastic scattering and are slightly deviated from their trajectory as they traverse the sample. These electrons, together with the unscattered ones (direct beam), can be collected by a spectrometer to generate a plot of the signal intensity (electron count) as a function of the energy loss. This type of spectroscopy, called EELS, can provide different information based on the region of the EELS spectrum considered, i.e., the zero-loss, corresponding to the unscattered beam, low-loss, or high-loss region. The high-loss spectrum, also termed "core-loss", which is employed in this thesis, corresponds to electrons scattered inelastically due to the interaction with tightly bound core electrons of the atoms of the sample. Hence, the energy loss in this region represents ionization edges that can be used for elemental fingerprinting. EELS is mostly coupled with STEM to acquire spectral images, where each pixel in the image corresponds to an EELS spectrum. EELS offers higher energy and spatial resolution than EDX, but it has strict requirements in terms of sample thickness as the signal collected is that transmitted through the sample[153,184].

The high spatial resolution of EELS has been employed to probe the chemical composition of nanoscale features in bone, specifically of low Z-contrast circular spaces that are interpreted as cross-sectional views of collagen fibrils by some authors, who corroborated their hypothesis using EELS mapping of carbon and nitrogen as markers for collagen[185,186]. In the study of bone-implant interfaces, a notable application of EELS involved the acquisition of EELS data in tomography mode, i.e., collecting a spectral image together with a HAADF-STEM image at each tilt angle in the tomography experiment[187]. This made it possible to reconstruct the bone-implant interface in four dimensions (4D), i.e., combining 3D structural and compositional information, with nanoscale resolution.

Aim

The overarching goal of this thesis is to apply multimodal and multiscale characterization approaches typical of materials science to understand abnormalities in the structure, composition, and repair of compromised bone, and to advance nanoscale analyses to elucidate bone ultrastructure.

The specific aims are:

1. To determine the structure and composition of bones formed by endochondral (femur) and intramembranous (calvarium in the parietal region) ossification in the Lund MetS rat, a novel animal model for LepR deficiency, obesity, and hyperglycemia (T2DM-like) [Paper I].
2. To resolve the interface between bone and bacteria from the micro- to the nanoscale in MRONJ to inform perspectives on the eventual role played by bacteria in the necrosis of the jaw [Paper II].
3. To examine the bone-implant interface and the LCN in peri-implant bone for a novel AM implant with engineered porosity and genistein functionalization for local drug delivery, in particular bridging micro- and nanoscale considerations via development of mesoscale analyses [Paper III].
4. To evaluate the effect of the local delivery of PTH 1-34, administered via surface-functionalized bioactive glass, on bone repair and osseointegration in ORX rats [Paper IV].
5. To demonstrate a micro-to-nanoscale characterization workflow for bone-bioactive glass interfaces, including 3D high-resolution imaging with electron tomography to resolve and understand the interface and the ultrastructure of bone in its proximity [Paper V].
6. To shed light on bone ultrastructure, specifically the low-contrast spaces characteristic of the lacy pattern and the morphology and organization of the extra-fibrillar mineral, using correlative on-axis Z-contrast electron tomography and EDX tomography [Paper VI].

Materials and methods

BONE MODELS AND BIOMATERIALS

Samples from human [Papers II, VI] and rat bone [Papers I, III-V] were examined in both healthy, i.e., without any known bone disease [Papers V-VI, plus control groups in Papers I-II, IV], and compromised conditions [Papers I-IV]. Different preclinical rat models were used, as described in the following section [Papers I, III-V]. This thesis includes samples from both male and female humans/rats, but both sexes were not evaluated in a same study. Bone samples were collected either from native tissue [Papers I-II, VI] or from the peri-implant compartment [Papers III-V].

Table 1 summarizes the main information on bone samples in terms of species, anatomical location, and sex, as well as eventual compromised conditions and biomaterials present. The use of human tissues and the animal studies were approved by the following committees:

- Animal Research Ethics Committee of Gothenburg, Sweden (Dnr. 14790/2019) [Paper I].
- Regional Ethical Review Board of Gothenburg, Sweden (Dnr. 424-08) [Paper II].
- Ethics Committee on the Use of Animals (CEUA) at UNESP, Brazil (approval no. 00733-2020) [Paper III].
- Ethics Committee on the Use of Animals (CEUA) at UNESP, Brazil (approval no. 00199-2017) [Papers IV-V].
- Hamilton Integrated Research Ethics Board (HIREB) at McMaster University, ON, Canada (approval no. 12-085-T) [Paper VI].

Experimental animal models

LepR-deficient model

In Paper I, 20-week-old Lund MetS male rats were studied. Due to a LepR genetic mutation, these rats are a monogenic model of obesity with potential applications in T2DM research[110,188]. While $LepR^{+/+}$ rats are lean and euglycemic, $LepR^{-/-}$ rats display severe obesity and hyperglycemia. Both $LepR^{+/+}$ and $LepR^{-/-}$ animals were considered by analyzing structure and composition of their femurs and calvaria in the parietal region.

Osteoporotic models

In Paper III, 3-month-old OVX Wistar female rats were used. At 30 days after OVX surgery, the animals received Ti-6Al-4V implants in their tibia and were sacrificed 28 days after implant installation.

In Paper IV, 6-month-old ORX Wistar male rats were used. Non-ORX rats, subjected to sham surgery, were also included as healthy controls. At 30 days after ORX/sham surgery, a defect was

created in the tibia of the animals and filled with bioactive glass (Biogran®), without and with PTH 1-34 functionalization, prior to installation of a cp-Ti implant. Animals were sacrificed at 30 days after implant installation for electron microscopy experiments, and 60 days after implant installation for all the other analyses. One of the rats from the control group in Paper IV was used for the experiments completed in Paper V.

Clinical samples

In Paper II, necrotic and non-necrotic bone samples were retrieved from the upper and lower jaws of a 73-year-old female individual diagnosed with osteoporosis and MRONJ. The sampling procedure occurred 1.5 years after the interruption of a 23-year-long oral therapy with bisphosphonates (alendronate tablets).

In Paper VI, cortical bone prepared from the femur of a 68-year-old male individual without any known bone diseases was examined.

Biomaterials

In Paper III, a Ti-6Al-4V implant with a porous mid-section (45% porosity, 500 μm pore size) was manufactured by laser powder bed fusion (L-PBF). The implant surface was acid-etched with sulfuric acid (H_2SO_4) and functionalized with genistein by an electrochemical layer-by-layer method [patent application BR 10 2021 019134 1, Instituto Nacional da Propriedade Industrial, Brazil].

In Papers IV-V, particles of Biogran®, a commercially available bioactive glass, were used to fill a surgical defect in the rat tibia prior to the installation of a cp-Ti (grade IV) implant. In Paper IV, some animals received Biogran® previously functionalized with PTH 1-34 by sonochemistry following the protocol described by Gomes-Ferreira et al.[189].

Table 1. *Information on the bone samples used in this thesis in terms of species, anatomical locations, and sex. Implanted biomaterials and the type of compromised condition present are also reported when applicable (otherwise stated as not applicable, N/A).*

Paper	Species	Anatomical location	Sex	Biomaterial(s)	Compromised condition
I	Rat (Lund MetS)	Femur Calvarium	Male	N/A	LepR deficiency, obesity, hyperglycemia
II	Human	Maxilla Mandible	Female	N/A	Osteoporosis MRONJ
III	Rat (Wistar)	Tibia	Female	Ti-6Al-4V implant (porous, acid-etched, genistein-coated)	OVX
IV	Rat (Wistar)	Tibia	Male	Bioactive glass (without and with PTH 1-34) Cp-Ti implant	ORX
V	Rat (Wistar)	Tibia	Male	Bioactive glass Cp-Ti implant [not studied]	N/A
VI	Human	Femur	Male	N/A	N/A

SAMPLE PREPARATION

Retrieval, preservation, and preparation of *bulk* samples

In Paper I, femurs and calvaria were retrieved at 20 weeks of age, fixed, and dehydrated. Femurs were cut transversally to separate proximal and distal sections, which were then cut longitudinally. Longitudinal femur sections and calvaria were resin-embedded in LR White and polished. After embedding, the calvaria were cut along the coronal plane to have a cross-sectional view of the parietal region and the sagittal suture.

In Paper II, samples were retrieved from the upper (left side: non-necrotic; right side: necrotic) and lower (right side: necrotic) jaws of a human subject. Samples were fixed, dehydrated, resin-embedded in LR White, and processed for a central histological ground-section stained with toluidine blue. Leftover blocks were polished.

In Papers III-V, implants and peri-implant tissues were retrieved *en bloc*, fixed, dehydrated, and resin-embedded in polymethyl methacrylate [Paper III] or Technovit [Papers IV-V]. Embedded blocks were sectioned longitudinally along the implant and polished. Sections for immunohistochemistry in Paper IV did not follow this preparation route, but were instead demineralized in 10% EDTA (ethylenediaminetetraacetic acid) after fixation, dehydrated, diaphanized in xylol, embedded in paraffin, and cut to a thickness of 5 μm.

For samples in Papers I-V, fixation was done in 10% neutral buffered formalin, and dehydration took place in a graded ethanol series (steps differ in length and concentration in the Papers).

In Paper VI, a section of human femur was fixed in 4% glutaraldehyde in a 0.1 M cacodylate buffer for one week, cut transversally, dehydrated in a graded ethanol series, resin-embedded in Embed812, and polished.

Electron transparent samples for S/TEM

Electron transparent samples for S/TEM experiments were prepared by *in situ* lift-out in dual-beam FIB instruments equipped with a 30 kV Ga^+ ion column, a gas injection system to deposit a protective layer of carbon and/or tungsten over the region of interest (ROI), and a micromanipulator to lift-out and manoeuvre the sample. A schematic representation of a typical dual-beam instrument is provided in Figure 7A.

In Papers II-VI, electron transparent samples were prepared in the conventional form of wedge-shaped lamellae following existing protocols[190], as schematically shown in Figure 7B-C. In short, after depositing a layer of carbon and/or tungsten over the ROI, typically 12×2 μm^2, coarse trenches were milled around it at 30 kV and currents in the 6.5-65 nA range (lower currents closer to the ROI). The sample was then lifted-out using the micromanipulator, attached to a copper grid for TEM holders, and thinned to electron transparency at 30 kV and progressively lower currents (from at most 0.79 nA down to 40 pA), with a final step at low voltage (5-10 kV) and current (60-80 pA) to limit Ga^+ implantation and amorphization damage.

In Paper VI, one sample was lifted-out in a *plan-view* fashion[191]. A large ROI, 15 × 15 μm^2, was coated with a tungsten deposit. Similarly to the lift-out protocol described above, after coarse milling around the ROI, the sample was lifted-out and attached to a copper grid for TEM holders, which had been previously mounted horizontally in a specialized stub (described by Huang et al.[192]). Thanks to its design with two orthogonal pins, the stub was removed from the holder and re-inserted after a 90° rotation so that the copper grid became oriented vertically. Thinning to electron transparency then proceeded normally.

In Paper VI, two rod-shaped samples were also prepared. The lift-out process was analogous to that for wedge-shaped samples, the main differences being the size of the ROI selected (3 × 3 μm^2) and the use 1 mm cylindrical posts for TEM rotation holders, instead of conventional copper grids. Thinning to electron transparency was completed by annular milling at 30 kV and 40-150 pA (Figure 7D).

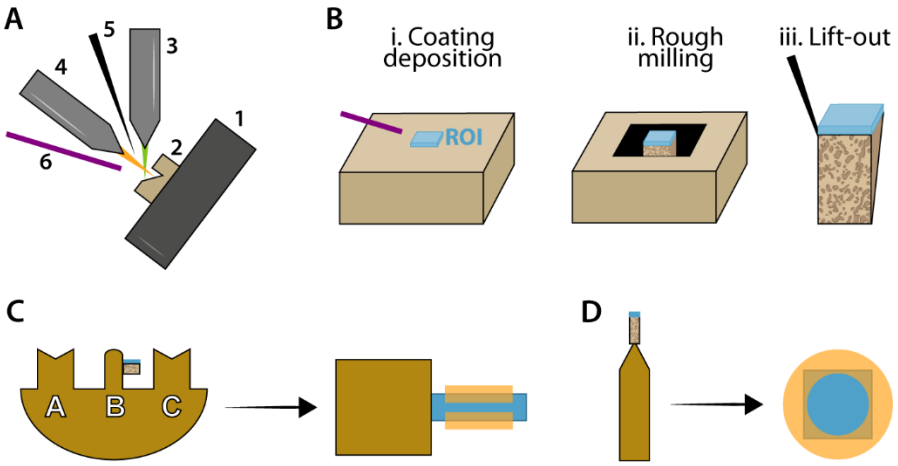

Figure 7. *Schematic representation of the main components of a dual-beam instrument (A): stage (1); sample (2); electron beam column (electron beam is shown in green) (3); ion beam column (ion beam is shown in orange) (4), typically oriented at 52-54° with respect to the electron beam column; micromanipulator (5); and gas injection system (6) [Note: detectors are not shown for simplicity]. Main steps of sample preparation for S/TEM experiments (B-D): after depositing a protective coating (light blue) over the ROI via the gas injection system (step i in B) and milling coarse trenches around it (step ii in B), the sample is lifted-out with the micromanipulator and attached to a copper grid for conventional wedge-shaped samples (C) or to a cylindrical post for rod-shaped samples (D). Thinning to electron transparency is performed by milling on both sides in C, or by annular milling in D.*

Resin cast etching

Resin cast etching was used in Papers II-III to expose resin-infiltrated elements below the surface such as the LCN, as well as bacteria in Paper II. In Paper II, samples were immersed in 9% phosphoric acid (H_3PO_4) for 30 s, while in Paper III a shorter immersion time (10 s) was employed, but in a more concentrated acid solution (37%). In both studies, after rinsing with deionized water, samples were immersed in 5% sodium hypochlorite (NaOCl) for 5 min, then rinsed again and let air-dry overnight.

The steps in phosphoric acid and sodium hypochlorite remove the inorganic and organic components in bone, respectively[157].

X-RAY, ELECTRON, AND ION MICROSCOPY

Micro-CT

Micro-CT was completed in Papers I and IV, prior to resin embedding, to evaluated bone morphometry in 3D. In Paper I, micro-CT scans were acquired for femurs and calvaria to obtain 3D reconstructions of the overall bone geometry, as well as to gain microstructural information. Specifically, in the femurs, various morphometry metrics were quantified in cortical bone (cortical thickness, cortical bone area, total cross-sectional area inside the periosteal envelope, and cortical area fraction) and trabecular bone (bone volume fraction, trabecular thickness, trabecular separation, and trabecular number), together with TMD in both regions. In the calvaria, the analyses focused on the parietal region to measure its thickness and on the sagittal suture to evaluate its thickness and length. In Paper IV, micro-CT was used to assess various morphometry parameters in peri-implant bone (bone volume fraction, trabecular thickness, trabecular separation, and trabecular number), and to measure BIC in order to evaluate osseointegration.

SEM

Polished samples for SEM experiments were mounted on aluminum stubs using conductive tapes (silver/carbon) and/or paint (silver/nickel). In Papers II-VI, these samples were coated with either carbon or gold (~10-20 nm-thick) for imaging in high-vacuum conditions.

BSE-SEM

All the Papers in this thesis included the use of SEM imaging in BSE mode. In Papers III-VI, BSE-SEM images were acquired in high-vacuum conditions, while in Papers I-II the SEM instrument was operated in low-vacuum regime (water vapour pressure of 1 Torr). Accelerating voltage ranged from 5 to 20 kV.

In the Papers, BSE-SEM imaging mainly served the following aims:

- Examination of bone microstructure and differently mineralized areas [Papers I-II].
- Assessment of bone growth in the peri-implant space, e.g., to identify distance and contact osteogenesis and regions of bone-biomaterial contact [Papers III-V].
- Selection of ROIs for STEM sample preparation [Papers II-VI].
- Identification of ROIs for other analyses, i.e., SEM-EDX [Papers II, IV] and micro-Raman spectroscopy [Papers I-II].

qBEI

In Paper I, qBEI was completed to convert grey-levels in BSE-SEM images into mineral content (wt% Ca). The experimental set-up followed published protocols[155], using a standard made of carbon and aluminum and adjusting the brightness and contrast in the BSE-SEM images of the standard to have average grey-levels equal to 25 and 225 in the carbon and aluminum regions, respectively. The following metrics were evaluated: weighted mean calcium concentration; peak height of the

distribution; peak position of the most frequent calcium concentration; full width at half maximum of the calcium peak; spread of the distribution on the low concentration side; and spread of the distribution on the high concentration side.

SE-SEM

In Papers II-III, SE-SEM images were acquired for bone samples after resin cast etching to visualize bone cells [Papers II-III] and bacteria [Paper II]. For the acquisition of SE-SEM images, microscopes were operated in high-vacuum conditions at 3-7 kV.

S/TEM imaging and electron diffraction

STEM

Except for Paper I, all the other Papers included the use of HAADF-STEM imaging. This was completed to resolve bone ultrastructure [Papers II-VI] and/or the interface between bone and biomaterials [Papers III-V] at the nanoscale. The S/TEM instruments were operated at 200-300 kV.

BF-TEM and SAED

In Paper II, a S/TEM instrument was operated at 200 kV in TEM mode to acquire BF images and complete SAED experiments in a region of necrotic bone interfacing with bacteria-invaded resin. The insertion of the aperture illuminated an area of the sample approximately 250 nm in width from which the diffraction pattern was collected.

STEM tomography

In Paper V, conventional (single-tilt) Z-contrast electron tomography using a wedge-shaped electron transparent sample was completed to reconstruct the interface between bone and bioactive glass in 3D, as well as the ultrastructure of bone at said interface. HAADF-STEM images were collected over a tilt range from -60° to +74° with 2° tilt steps. The S/TEM instrument was operated at 300 kV.

In Paper VI, on-axis Z-contrast electron tomography using rod-shaped samples was completed. A specialized holder for rotation tomography was used to extend the tilt range compared to single-tilt electron tomography. Four tilt series were acquired in total: two over a ±90° tilt range, and two over a ±85° tilt range. The tilt step was equal to 2° in one tilt series, and 5° in the other three. In all tilt series, HAADF-STEM images were collected. In one tilt series, BF-STEM images were also acquired alongside HAADF-STEM images. In three tilt series, EDX maps were also collected at each tilt angle, as reported in more detail in the *EDX* section (see page 34). For all acquisitions, the instrument was operated at 200 kV. During the tilt series collection, focusing and image shifting were done automatically in the tomography acquisition software. Tilt series were aligned by cross-correlation and reconstructed using SIRT with 25 iterations.

PFIB-SEM tomography

In Paper III, 3D imaging of a volume of implant and peri-implant bone was accomplished by PFIB-SEM tomography using a dual-beam FIB instrument equipped with a Xe^+ ion column. Ion milling was carried out at 30 kV and 4 nA, with a slice thickness of 30 nm. Imaging with the electron beam was done in BSE mode at 1.2 kV. The stack of BSE-SEM images was aligned to generate a 3D volume, which was mainly used to investigate mineral ellipsoids and the LCN in peri-implant bone.

SPECTROSCOPY

Micro-Raman spectroscopy

Micro-Raman spectroscopy was applied in Papers I-II to gain information on bone quality, primarily in relation to bone matrix composition. Specifically, in Paper I, Raman spectra were collected at each pixel over a rectangular area, in fact obtaining hyperspectral maps. In Paper II, line scans across the bone-resin interface were acquired instead. Raman spectra were acquired with varying step size (1 μm in Papers I-II; 10 μm in Paper I), exposure time (1 s in Paper I; 3 s in Paper II), and accumulations (2 in Paper I; 5 in Paper II) using an instrument equipped with a 633 nm laser and 1800 g mm^{-1} grating. Spectra were baseline subtracted, cleaned of cosmic rays, and denoised. In Paper I, compositional measures, i.e., mineral-to-matrix ratio and carbonate-to-phosphate ratio, and crystallinity of bone mineral were evaluated in different ROIs in femurs and calvaria. In Paper II, only the mineral-to-matrix ratio was measured.

EDX

Both SEM-EDX [Papers II, IV] and STEM-EDX [Papers III, VI] were completed in some of the studies included in this thesis. In particular, EDX was done in tomography mode in Paper VI.

SEM-EDX

In Paper II, SEM-EDX was used to compare mineralization gradients at the bone-resin interface in necrotic and non-necrotic bone, specifically evaluating trends in calcium, phosphorus, and carbon in line scans acquired across the interface. EDX acquisition was carried out in an SEM instrument operated at 20 kV in low-vacuum conditions (water vapour pressure of 1 Torr). In Paper IV, SEM-EDX was used to evaluate compositional gradients within bioactive glass particles after ionic exchange and degradation taking place *in vivo*. This was done by mapping the amount of calcium, phosphorus, and silicon in bioactive glass particles, and extracting line profiles across them. For this analysis, a microscope operated at 10 kV in high-vacuum mode was used.

STEM-EDX

In Paper III, STEM-EDX was used to examine the compositional gradients across the bone-implant interface with nanoscale resolution, mapping the content in implant elements (titanium, aluminum, vanadium, oxygen) and bone elements (calcium, phosphorus). Maps were acquired with a pixel dwell time of 10 μs, integrating over 1000 frames. The microscope was operated at 200 kV, and the EDX signal was acquired using a Super-X detector, which is composed of four in-column silicon drift detectors.

STEM-EDX tomography

In Paper VI, STEM-EDX was coupled with tomography acquisition, i.e., EDX maps were acquired at each angle in the tilt series at the same time as HAADF-STEM images. Elemental maps were acquired for carbon and nitrogen as markers of type I collagen, and calcium and phosphorus as

markers of bone mineral. Maps were acquired with a pixel dwell time of 50 μs, integrating over 10 frames. The tilt series of EDX maps of each element were aligned and reconstructed by SIRT (25 iterations) based on the HAADF signal. Similarly to Paper III, EDX signal acquisition was carried out in a S/TEM instrument equipped with a Super X-detector and operated at 200 kV.

EELS

In Paper II, EELS was completed at the bone front interfacing with the bacteria-invaded resin space to assess mineralization gradients at the nanoscale. EELS spectral images were acquired at 300 kV, with 0.5 eV/channel energy dispersion, 5 nm pixel size, and 0.05 s exposure time per pixel. After background subtraction, elemental maps for calcium, phosphorus, and carbon were obtained from the EELS spectra by extracting the signal in the energy loss window characteristic of each element.

OTHER ANALYTICAL TECHNIQUES

This section briefly summarizes methodological details for the complementary analytical techniques used in this thesis, beyond the main characterization tools previously reviewed.

Reference point indentation

In Paper I, reference point indentation (RPI) measurements were completed on the periosteal surface of the proximal femurs using a microindenter to evaluate the following parameters: 1st cycle indentation distance; 1st cycle unloading slope; 1st cycle creep indentation distance; total indentation distance; indentation distance increase; average creep indentation distance; average energy dissipated; and average unloading slope. These measures are related to the resistance to indentation, hence they provide information on bone mechanical properties.

Static/dynamic histology and immunohistochemistry

In Paper II, histology was used to assess the presence of necrosis and bacterial infection, as well as other relevant cells (e.g., multinucleated cells). Ground sections stained with toluidine blue were imaged in a light microscope with ×4, ×10, ×20, and ×40 objectives.

In Paper IV, dynamic histology was carried out by injection of fluorochromes during the animal study (calcein and alizarin red at 14 and 42 days after implant installation, respectively). Sections obtained from longitudinal cuts in correspondence of the third-to-fifth implant thread were imaged by confocal laser microscopy with a ×10 objective to measure fluorochrome area, daily bone mineral apposition rate, and neoformed bone area.

In Paper IV, immunohistochemistry using TRAP (tartrate-resistant acid phosphatase) staining was performed to assess osteoclast activity. Immunolabelling was classified based on the percentage of positive immunolabels within the ROI as mild (25%), moderate (50%), or intense (75%).

Removal torque

In Paper IV, removal torque measurements were performed to quantify implant anchorage from a biomechanical perspective. Removal torque was applied counter-clockwise with increasing values until disruption of the bone-implant interface occurred. The maximum reverse torque value registered in this process was the one considered for inter-group statistical comparison.

Gene expression

In Paper IV, after the disruption of the bone-implant interface during removal torque measurements, bone tissue in the peri-implant compartment was collected, flash-frozen, and stored at -80 °C until further processing. Total RNA was extracted using a spin-column method, quantified with

spectrophotometry, and cDNA synthesized. qPCR (quantitative polymerase chain reaction) was performed to quantify the relative gene expression of alkaline phosphatase and osteocalcin.

IMAGE ANALYSIS

Images were analyzed not just in qualitative terms, but segmentation of features of interest was also performed for quantification purposes or to identify specific ROIs for subsequent analyses.

In Paper I, micro-CT data were analyzed using the ORS Dragonfly software. Femurs were evaluated with the "Bone Analysis" plug-in, where trabecular and cortical bone were segmented using the Buie algorithm[193] to assess morphometry parameters in each compartment. In the parietal region, bones and sagittal suture were segmented to then evaluate their thickness using the "Volume thickness map" operation. Slice analysis in 2D was performed to evaluate sagittal suture length. Hyperspectral Raman maps were segmented by a clustering algorithm (K-means) using the "sklearn.cluster" library in Python 3.8.10 to separate different ROIs (mineralized cartilage islands in the femurs and highly mineralized bone in the calvaria). Different Raman measures were then evaluated in each region separately.

In Paper II, nanosized particles in HAADF-STEM images were segmented using Fiji[194] to evaluate their average dimensions. Intensity profiles were also extracted from HAADF-STEM images to measure the periodicity of the banding pattern characteristic of collagen fibrils.

In Paper VI, electron tomograms were visualized and analyzed using the ORS Dragonfly software. Data were segmented mostly based on grey-level thresholding to label both dark nanosized spaces within bone and the mineral phase to evaluate feature size and connectivity. EDX tomograms were also segmented to quantify the content of different elements within the segmented nanosized spaces. Manual segmentation followed by slice analysis in 2D was completed to measure the dimensions of the mineral plates.

Segmentation was also carried out for visualization purposes, such as in Paper III where the LCN was segmented to better examine its organization within peri-implant bone. In Paper V, qualitative segmentation was completed by adjusting colour-levels and opacity in the 3D volume rendering to assess collagen fibrils orientation at the interface with bioactive glass. The ORS Dragonfly and Avizo software programs were used in Papers III and V, respectively.

STATISTICAL ANALYSIS

In Papers I-II, two groups were compared, hence statistical significance was evaluated with the Student's *t*-test or Welch's *t*-test, or, alternatively, the non-parametric Mann-Whitney U test with small sample size and/or violation of normality distribution. Specifically, statistical significance of micro-CT data in Paper I was assessed with the Student's *t*-test (in the case of equal variance) or the Welch's *t*-test (in the case of unequal variance or sample size) after verifying normality and homoscedasticity with the Shapiro-Wilk test and the Brown-Forsythe test, respectively. Micro-Raman spectroscopy results were compared with the Mann-Whitney U test in Papers I-II. This test was also used to evaluate statistical significance in qBEI and RPI data in Paper I, and SEM-EDX data in Paper II.

In Paper IV, six different groups were compared, hence statistical significance was evaluated using a one-way ANOVA (analysis of variance) with a Tukey's post-hoc test for data obtained from micro-CT, removal torque, gene expression, and dynamic histology (mineral apposition rate and neoformed bone area). Fluorochrome area in dynamic histology was compared using a two-way ANOVA.

For all statistical tests, significance level was set at $\alpha = 0.05$. In Papers I-II, statistical analysis was completed in Python 3.8.10 using the "scipy.stats" library, while GraphPad Prism 8.1.1 was used in Paper IV. In all the Papers, data are reported as mean ± standard deviation.

Results

PAPER I

In this work, the structure and composition of bone in a novel preclinical model for LepR deficiency, hyperglycemia, and obesity, the Lund MetS rat, was characterized, focusing on bone material properties of femurs and calvaria at the microscale. A graphical summary of the main findings is found below in Figure 8.

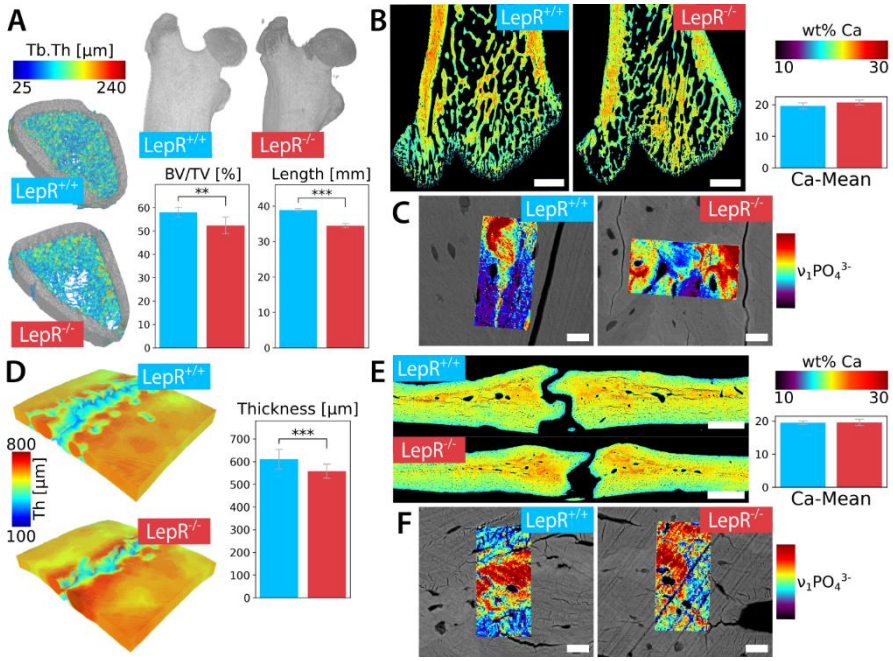

Figure 8. *Micro-CT reconstructions of the trabecular compartment in the distal femurs, coloured based on trabecular thickness (Tb.Th) and of proximal femurs (right), together with bar plots of bone volume fraction (BV/TV) and femur length (A). qBEI images of the femurs where pixel intensity corresponds to mineral concentration (wt% Ca), with relative bar plots of mean calcium concentration (Ca-Mean) (B). BSE-SEM images of areas with mineralized cartilage islands with superimposed Raman maps of the $\nu_1PO_4^{3-}$ peak intensity (C). Micro-CT reconstructions of parietal bones in the calvarium coloured based on bone thickness (Th), with relative bar plot (D). qBEI images of calvaria in the parietal region, where pixel intensity corresponds to mineral concentration (wt% Ca), with relative bar plots of Ca-Mean (E). BSE-SEM images of areas with highly mineralized bone with superimposed Raman maps of the $\nu_1PO_4^{3-}$ peak intensity (F). Healthy (LepR$^{+/+}$) and LepR-deficient (LepR$^{-/-}$) animals are colour-coded in blue and red, respectively. Scale bars are 1 mm in B, 20 µm in C and F, and 500 µm in E. ** and *** denote statistical significance ($p < 0.01$ and $p < 0.001$, respectively). [Adapted with permission from Paper I].*

Results summary: Paper I

LepR-deficient animals ($LepR^{-/-}$) displayed severe obesity and hyperglycemia compared to the healthy control group ($LepR^{+/+}$), as indicated by their statistically significant higher weight and blood glucose levels, respectively ($p < 0.001$).

From the 3D micro-CT reconstruction of the proximal femurs, it was apparent that the femoral head and neck were incompletely developed in the $LepR^{-/-}$ animals. Caliper measurements of the entire femur showed that the bone was significantly shorter in the $LepR^{-/-}$ animals ($p < 0.001$). Morphometry analysis in the distal portion of the femurs revealed that the microstructure was altered in both cortical and trabecular regions of the $LepR^{-/-}$ rodents. Specifically, $LepR^{-/-}$ animals had thinner trabeculae ($p > 0.05$) and cortices ($p < 0.001$) than their healthy counterparts. The trabecular compartment was overall more porous in the $LepR^{-/-}$ group ($p < 0.01$), with fewer trabeculae ($p < 0.05$) and an increased trabecular separation ($p < 0.01$). Cortical bone area and area fraction were also smaller in the $LepR^{-/-}$ animals ($p < 0.001$ and $p < 0.01$, respectively). Calvaria also displayed altered morphology in the $LepR^{-/-}$ rats, which had thinner parietal bones ($p < 0.001$), while the sagittal suture was found to have a reduced length ($p < 0.01$) and width ($p < 0.001$).

On the other hand, no differences in bone matrix composition between $LepR^{-/-}$ and $LepR^{+/+}$ animals were detected in neither femur nor calvarium in the parietal region ($p > 0.05$). This similarity was consistently found regardless of the compositional metrics considered, i.e., TMD in micro-CT, BMD distribution in qBEI, and mineral-to-matrix and carbonate-to-phosphate ratios in micro-Raman spectroscopy. Resistance to indentation measured by RPI on the periosteal surface of the proximal femurs also displayed comparable results in $LepR^{-/-}$ and $LepR^{+/+}$ animals ($p > 0.05$), indicating analogous mechanical properties of the bone matrix.

Due to the compositional nature of the contrast in BSE-SEM images, some relevant microstructural features were noted in both femurs and parietal bones. These structures were identified as islands of mineralized cartilage in the femurs, given their appearance as more highly mineralized, osteocyte-free areas surrounded by "normal" bone matrix. In the cross-sectional views of the parietal bones, areas with a greater degree mineralization were mostly located in the central portion of the section and in the regions close to the sagittal suture. The higher mineral content of both mineralized cartilage islands in the femurs and highly mineralized bone in the parietal bones was confirmed by high-resolution Raman maps (1 μm), although the increase in mineral content compared to bone matrix was not statistically significant ($p > 0.05$). Moreover, the composition of these microstructural features did not display any differences when comparing $LepR^{-/-}$ and $LepR^{+/+}$ animals ($p > 0.05$). qBEI data were examined in distinct intervals of wt% Ca to determine whether mineralized cartilage islands in the femurs and highly mineralized bone in the calvaria were differently distributed in the two animal groups. However, no differences were found ($p > 0.05$), indicating a comparable amount of these microstructural features.

PAPER II

This study examined the interface between bone and bacteria in a case of MRONJ developed by an osteoporotic female individual after 23 years of treatment with alendronate, a common bisphosphonate. The interface was characterized using different techniques spanning from the micro- to the nanoscale. Figure 9 shows the main results, summarized in the following page.

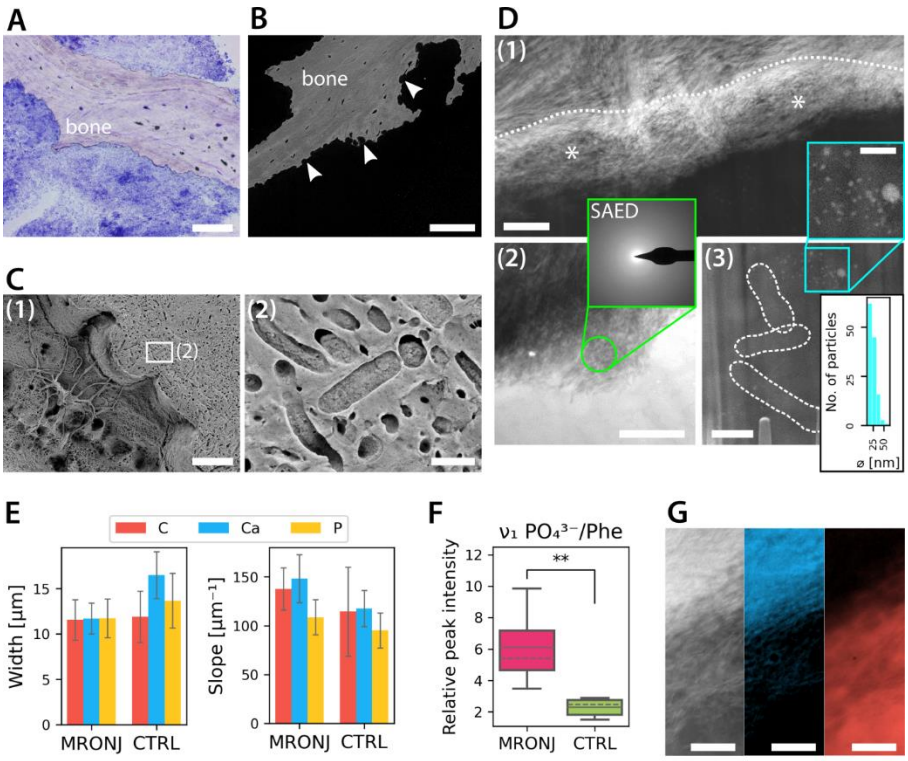

Figure 9. *Histological section (A) and BSE-SEM image (B) of necrotic bone, showing a ragged surface (arrowheads in B). SE-SEM images of necrotic bone after resin cast etching (C), where bacteria are clearly visible in the resin space (magnified in C-2). HAADF-STEM image of the bone-bacteria interface (D), demonstrating the presence of a hyper-mineralized band (dotted line in D-1) fading into a region of high disorder lacking crystallinity (marked by * in D-1), as confirmed by SAED (D-2). In the resin space, bacteria (dashed contour) and nanosized particulate can be observed (D-3). SEM-EDX indicates that the interface is narrower and more abrupt in necrotic bone ("MRONJ" label) (E), which micro-Raman spectroscopy confirms having a higher mineral content than non-necrotic bone ("CTRL" label), as shown by the higher mineral-to-matrix ratio ($\nu_1PO_4^{3-}$/Phenylalanine, Phe) (F). EELS corroborates that calcium (blue) decreases across the bone bacteria-interface (G; left to right: HAADF image and EELS maps for calcium, in blue, and carbon, in red). Scale bars are 100 µm in A and B, 10 µm in C-1, 1 µm in C-2, 500 nm in D, and 200 nm in the blue inset in D-3 and G. ** denotes statistical significance ($p < 0.01$). [Adapted with permission from Paper II].*

Results summary: Paper II

Bone samples were retrieved from both non-necrotic and necrotic areas in the jaw of the individual diagnosed with MRONJ. Toluidine blue-stained histological sections confirmed the necrotic status of bone tissue sampled from the regions deemed necrotic in the oral cavity, while no signs of necrosis were evident in the non-necrotic sample. Bacterial colonization was also evident in the histological sections throughout the regions interfacing with necrotic bone.

Bacteria were imaged at higher resolution in SE mode in SEM after resin cast etching. Rod-shaped bacteria like those identified by the microbial swab (Prevotella and *Haemophilus*-like rods) were found in significant amounts in the outer space surrounding necrotic bone, which was filled with resin during sample embedding. Conversely, bacteria were absent in the resin region surrounding non-necrotic bone. In this case, bone cells like osteoblasts and bone lining cells were instead found at the bone-resin interface, while no such cells were noted in necrotic bone.

While already visible in histological sections examined by visible light microscopy, BSE-SEM images better highlighted differences in the morphology of the bone surface in the necrotic *vs.* non-necrotic samples. Specifically, the surface profile was irregular and jagged in necrotic bone, but had a rather smooth appearance in non-necrotic bone. Some mineral nodules resembling magnesium whitlockite were sometimes noted in the osteocyte lacunae in necrotic bone.

The degree of mineralization in bone close to the resin region was compared in necrotic and non-necrotic samples through the mineral-to-matrix ratio measured in micro-Raman spectroscopy. A higher ratio was found in necrotic bone, indicating a higher mineral content of the bone matrix ($p < 0.01$). Variations in calcium, phosphorus, and carbon were measured across the bone-resin interface by SEM-EDX, which revealed a more abrupt and narrower interface for the necrotic samples, although not in statistically significant terms ($p > 0.05$).

A region of necrotic bone interfacing with resin was resolved at the nanoscale by HAADF-STEM imaging. This made it possible to observe bacteria in the resin space, together with some high Z-contrast particulate located in their proximity or interior. This particulate had dimensions in the nanometer range, with an average size of 24 ± 8 nm. Away from the interface with the bacteria-filled resin space, bone displayed a normal ultrastructure, indicated by the characteristic banding pattern of in-plane collagen fibrils. The interface itself consisted of two main areas, i.e., a hyper-mineralized band (towards the bone side) and a highly disordered region (towards the bacteria side). The lack of crystallinity in this disordered region, where mineral appeared loosely organized, was confirmed by the absence of diffraction spots/rings in SAED patterns. EELS maps of calcium and phosphorus confirmed the decrease in mineral content from the hyper-mineralized band towards the resin region.

PAPER III

In this study, a multimodal and multiscale (micro-to-nano) characterization approach was applied to evaluate the bone response to a novel implant manufactured by L-PBF and designed to combine internal porosity, surface topography modification by acid etching, and surface functionalization with genistein for use in osteoporosis. Figure 10 summarizes the main observations.

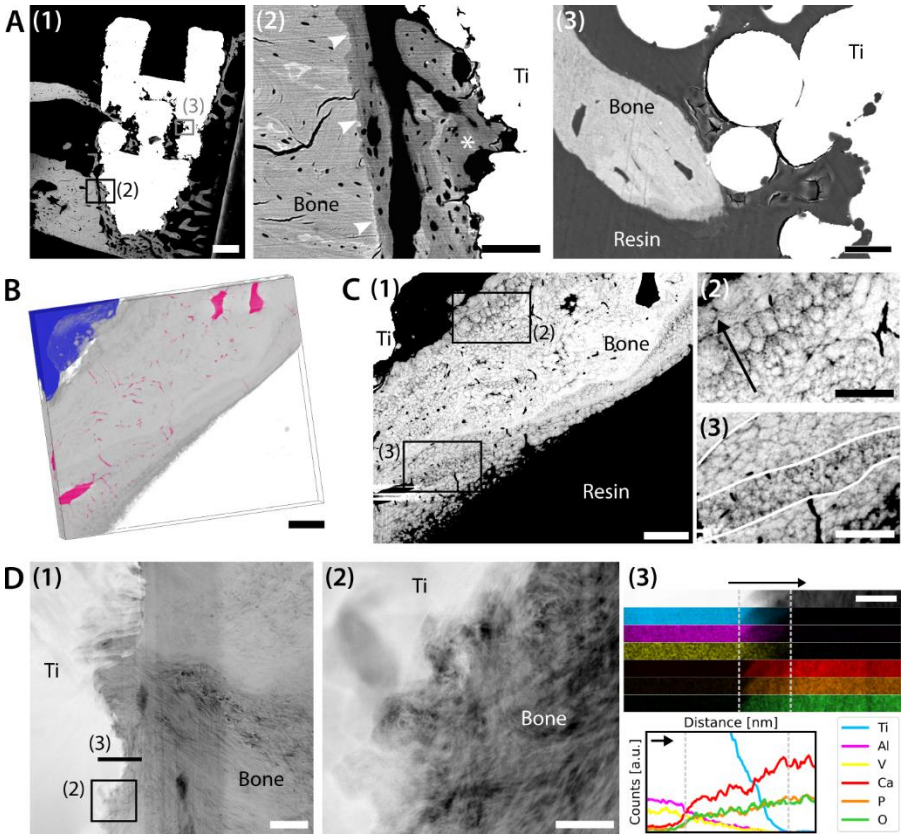

Figure 10. *BSE-SEM image showing new bone growth in the peri-implant space (A-1), and examples of distance osteogenesis (A-2, where arrowheads mark the boundary between native cortical bone and new bone) and contact osteogenesis (A-2, marked by *) also within the implant pores in contact with surface microparticles (A-3). PFIB-SEM 3D tomogram where an extensive LCN (pink) is present in peri-implant bone (bone is grey and implant is blue) (B) and an individual slice (C-1) where mineral ellipsoids display varying size (C-2; ellipsoids become larger in the direction of the arrow) and orientation (C-3; similarly oriented ellipsoids are enclosed by white lines). HAADF-STEM demonstrates osseointegration at the nanoscale (D-1, magnified in D-2) and STEM-EDX corroborates the gradual nature of the interface (D-3). Scale bars are 500 μm in A-1, 100 μm in A-2, 20 μm in A-3, 10 μm in B and C-1, 5 μm in C-2 and C-3, 1 μm in D-1, and 200 nm in D-2 and D-3.*

Results summary: Paper III

Instances of both distance and contact osteogenesis were observed in BSE-SEM survey images in the peri-implant compartment. Distance osteogenesis was especially apparent thanks to the compositional-contrast of BSE-SEM, making it possible to distinguish older bone in the native cortices from newer bone formed as part of the osseointegration process. The most significant example of contact osteogenesis was provided by bone ingrowth in the internal porosity of the implant. Bone in contact with the implant was also noted in correspondence of surface microparticles characteristic of parts manufactured by L-PBF.

Osseointegration was confirmed at the nanoscale by HAADF-STEM imaging and STEM-EDX. Specifically, bone and implant formed a continuous and gradual interface, where implant elements and bone elements intermixed. Such an intimate contact was mediated by the TiO_2 passivation layer that spontaneously forms on titanium, as oxygen was also detected within the bone-implant interface.

Bone regeneration in the peri-implant space was also assessed by examining the LCN. Despite a thin layer of resin or cracks being sometimes present at the bone-implant interface, SE-SEM images after resin cast etching demonstrated canaliculi extending towards the implant surface. This was better shown over a larger field of view and in 3D with PFIB-SEM tomography. Several osteocyte lacunae were present in the implant space, mostly co-aligned with each other and with their longest dimension parallel to the implant surface. Their canaliculi ran in the perpendicular direction, i.e., reaching towards the implant surface.

Some high Z-contrast features resembling cell membranes enclosing intracellular bodies were also noted in the PFIB-SEM image stack. When these features were close to the bone front, they could offer insights into the direction of the mineralization front. Two fronts were noted, one directed towards the implant, and one away from it. One lacuna becoming progressively enclosed by the bone matrix was also observed, likely indicating that an osteoblast-to-osteocyte transition was taking place as osteoid mineralization proceeded.

Mesoscale bone structure imaged by PFIB-SEM tomography revealed the presence of mineral ellipsoids with heterogenous sizes and orientations, as abrupt transitions from regions where they were cross-sectioned transversally *vs.* longitudinally were present throughout the 3D volume. Differing orientations were also confirmed at the nanoscale in HAADF-STEM images, where collagen fibrils transitioned from in-plane to out-of-plane views.

PAPER IV

This work examined the effect of bioactive glass (Biogran®) functionalized with PTH 1-34 on bone repair and osseointegration in ORX rats (abbreviated as ORQ in the Paper). Both the biological response and the micro-to-nanoscale characteristics of peri-implant bone were studied. Figure 11 shows some of the relevant findings.

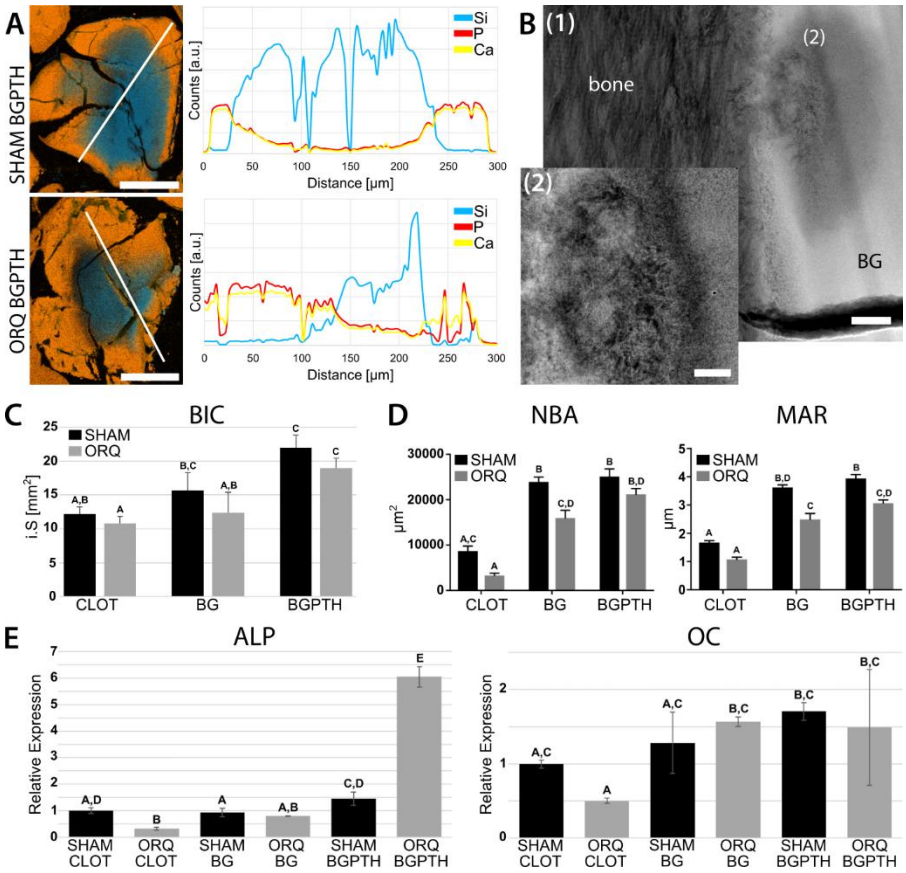

Figure 11. *SEM-EDX maps of silicon (blue), phosphorus (red), and calcium (yellow) for Biogran® particles functionalized with PTH 1-34 placed in the control (SHAM BGPTH) and ORX groups (ORQ BGPTH), and relative line scans across the particles (white lines) (A). HAADF-STEM images of the bone-Biogran® (BG) interface for particles functionalized with PTH 1-34 in an ORX animal (B), where dissolution/reprecipitation can be observed, together with bone formation within the particle (magnified in B-2). Bar plots summarizing the measurements obtained for: BIC (C); neoformed bone area (NBA) and mineral apposition rate (MAR) (D); and gene expression of alkaline phosphatase (ALP) and osteocalcin (OC) (E). Labels indicate: SHAM - healthy animals; ORQ - ORX animals; CLOT - animals receiving no Biogran®; BG and BGPTH - animals receiving Biogran® without and with PTH 1-34 functionalization, respectively. Scale bars are 100 μm in A, 500 nm in B-1, and 200 nm in B-2. Different letters denote statistical significance ($p < 0.05$). [Adapted with permission from Paper IV].*

Results summary: Paper IV

Rats were subjected to ORX or placebo surgery (SHAM). In both ORX and SHAM groups, one sub-group did not receive Biogran® (CLOT group), while the surgical defect was filled with Biogran® without and with PTH 1-34 functionalization in the sub-groups labelled as BG and BGPTH, respectively, prior to implant installation.

Contrast differences between the inner and outer portions of the Biogran® particles in the peri-implant space were often noted in BSE-SEM images. Compositional gradients were confirmed by SEM-EDX maps, showing that the particles were richer in silicon in their core, and in calcium and phosphorus towards their exterior. This was observed for both functionalized and non-functionalized particles. The silicon-rich core appeared more extended in the healthy animals than in the ORX ones, but sample size did not allow for statistical comparisons.

The formation of a gradual interface between bone and Biogran® was confirmed at the nanoscale by HAADF-STEM imaging, demonstrating the presence of an interfacial layer created by dissolution and reprecipitation ranging from 150 nm to 900 nm in width. In two samples, SHAM BG and ORX BGPTH, bone ingrowth in cavities within the biomaterial was also noted. Regarding bone ultrastructure, collagen fibrils mostly oriented parallel to the Biogran® surface were observed in all groups. In the ORX samples, mineral ellipsoids were also distinguished.

Micro-CT revealed higher bone volume in the animals receiving Biogran®, both with and without PTH 1-34 functionalization, accompanied by a lower trabecular separation and higher trabecular number than in the animals with implant only ($p < 0.05$). On the other hand, trabecular thickness was comparable in all groups ($p > 0.05$). Removal torque was overall lower in ORX than healthy animals, while higher values were measured in BG and BGPTH groups compared to CLOT for both healthy and ORX animals, especially in the SHAM BGPTH group ($p < 0.05$). Similar trends were found in BIC measurements. In this case, the use of functionalized Biogran® led to a statistically significant increase in BIC in both ORX and healthy animals compared to those receiving the implant only ($p < 0.05$). In both removal torque and BIC measurements, values in the ORX BGPTH group were comparable to those of the SHAM BG group ($p > 0.05$). This trend was also identified in the fluorochrome (calcein and alizarin red) analyses in terms of fluorochrome area, neoformed bone area, and mineral apposition rate. Additionally, values of neoformed bone area did not show any statistically significant difference between healthy and ORX animals that received functionalized Biogran® ($p > 0.05$).

ORX animals that received functionalized Biogran® had a significantly higher expression of alkaline phosphatase compared to all the other groups ($p < 0.05$). Osteocalcin expression was greater in the ORX animals receiving Biogran®, regardless of the presence of PTH 1-34, compared to those with the implant only ($p < 0.05$). In ORX animals, TRAP (tartrate-resistant acid phosphatase) immunolabelling was discrete in the CLOT group, discrete-to-moderate in the BG group, and moderate in the BGPTH group. In the healthy controls, discrete-to-moderate labelling was found in the sub-groups receiving Biogran®.

PAPER V

This study provided a workflow for the characterization of the interface between bone and bioactive glass (Biogran®), as well as for the ultrastructure of newly formed bone, going from 2D microscale imaging to 3D reconstruction with electron tomography at the nanoscale. The main results are graphically summarized below (Figure 12).

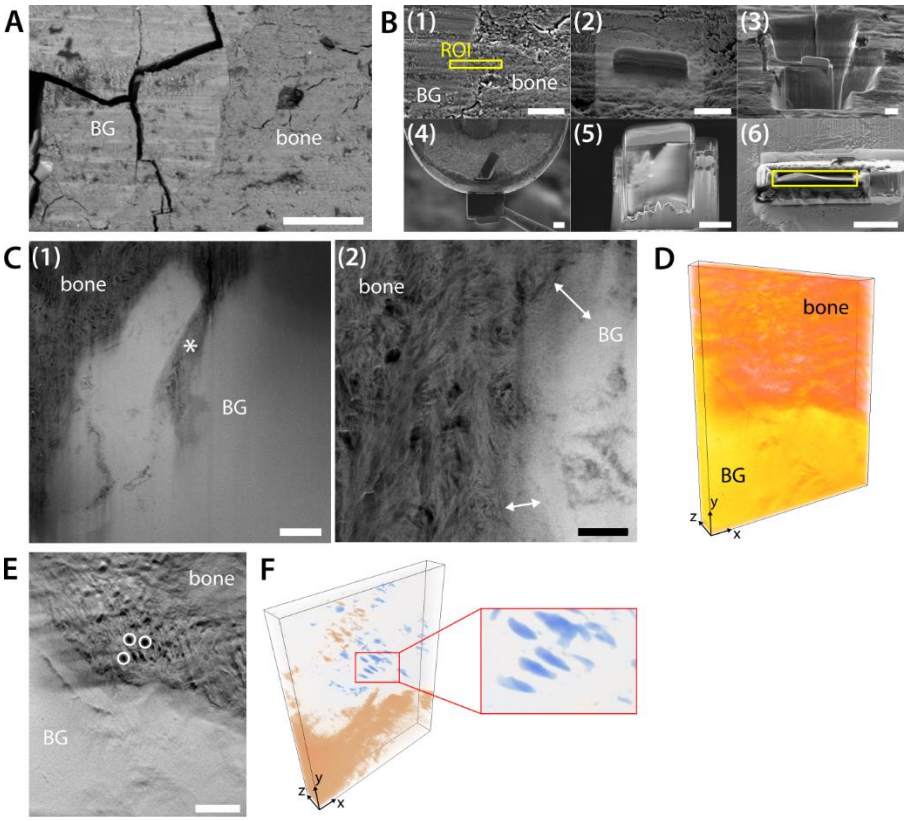

Figure 12. *Area of new bone growing in close contact with a Biogran® (BG) particle (A; BSE-SEM image), where a ROI was selected to prepare a STEM sample by FIB in situ lift-out (B-1, yellow rectangle). The main sample preparation steps involved depositing a protective coating over the ROI (B-2), milling coarse trenches around it (B-3), lifting-out and attaching the sample to a copper grid (B-4), and thinning to electron transparency (B-5; final sample is marked by the yellow rectangle in B-6). HAADF-STEM images show bone-Biogran® contact at the nanoscale with bone ingrowth within Biogran® cavities (* in C-1) and the formation of a 120-200 nm-wide interfacial layer (C-2, white arrows). Nano-osseointegration is confirmed in 3D by electron tomography (D). Collagen fibrils can be seen out-of-plane in individual reconstructed slices (E, white circles), and 3D rendering clearly shows they are parallel to the Biogran® surface (F; blue rods represent collagen fibrils). Scale bars are 20 μm in A, 5 μm in B, 1 μm in C-1, 200 nm in C-2, and 250 nm in E. The dimensions (x, y, z) of the 3D volume in E and F are 1231 × 1494 × 161 nm³. [Adapted with permission from Paper V].*

Results summary: Paper V

After the retrieval *en bloc* of the implant together with its peri-implant space, which included both new and native bone, as well as Biogran® particles, samples were prepared by embedding, sectioning, and polishing for electron microscopy experiments. A thin layer of conductive coating (carbon) was applied to minimize charging in high-vacuum imaging conditions.

BSE-SEM imaging was completed to identify areas of new bone forming in contact with Biogran® particles. Bone and biomaterial displayed a similar contrast, as they both contain calcium and phosphorus. Bone was easily identified by the presence of osteocyte lacunae, while cracks were often observed running through the Biogran® particles. Compositional gradients within the Biogran® particles could be inferred from BSE-SEM images due to the presence of a darker core surrounded by a brighter outer layer.

From the BSE-SEM survey, an area of bone-Biogran® contact on the microscale level was selected for the preparation of an electron transparent sample for STEM experiments. This was accomplished following a FIB *in situ* lift-out protocol in a dual-beam instrument, which allowed for the preservation of an intact interface, despite the different milling behaviour of bone and Biogran® posed some technical challenges.

HAADF-STEM imaging confirmed that the contact between new bone and Biogran® was continuous at the nanoscale, beyond what could be resolved by BSE-SEM. The Z-contrast in HAADF-STEM images also made it possible to better visualize the compositional gradients present in such a gradual interface, for which the term "biointerphase" is perhaps more appropriate. This was further corroborated in 3D by Z-contrast electron tomography, especially when examining individual slices of the reconstructed volume.

Nanoscale imaging in both 2D and 3D also provided information on the ultrastructure of bone forming in contact with Biogran®. Overall, new bone did not appear highly organized, but some distinct collagen fibrils could be distinguished. The fibrils appeared out-of-plane in HAADF-STEM images, but were better visualized and segmented in the 3D electron tomogram. This analysis confirmed that the collagen fibrils were oriented parallel to the biomaterial surface.

PAPER VI

In this work, a correlative characterization approach combining on-axis Z-contrast electron tomography and EDX tomography was used to resolve nanoscale features in human bone, with a focus on the low-contrast nanosized spaces (termed "holes" in the Paper) typical of the lacy pattern of bone, and on the morphology and spatial organization of bone mineral, especially the extra-fibrillar component. Figure 13 provides an overview of the main results.

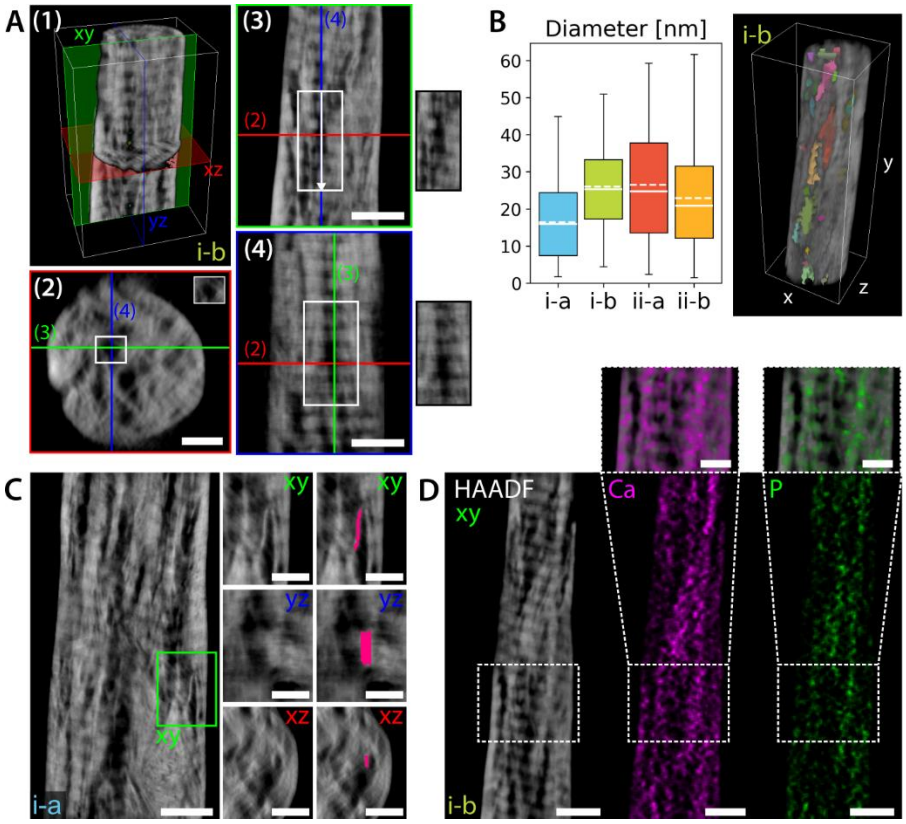

Figure 13. *3D reconstruction (A-1) showing three representative mutually orthogonal slices where a "hole" in the xz plane (A-2, red) corresponds to banding pattern in the xy (A-3, green) and yz (A-4, blue) planes, demonstrating correspondence between "holes" and collagen fibrils. "Holes" have an average diameter going from 16.4 nm to 26.4 nm in the four tomograms (B, box plot) and are disconnected from each other (B, 3D rendering). Mineral structures appear plate-shaped when viewed in three mutually orthogonal planes (C). EDX reconstructed maps demonstrate presence of calcium and phosphorus both in the intra- and extra-fibrillar regions, although the signal appears stronger in the latter (D). The labels "i-a" and "i-b" refer to the naming convention used for the tomograms in the Paper. Scale bars are 100 nm in A-2, C (right magnified panels), and D (top magnified panels), and 200 nm in A-3, A-4, C (left image), and D (bottom images). The dimensions (x, y, z) of the white boxes in the 3D reconstructions are 555.55 × 865.10 × 457.15 nm³ in A-1 and 555.55 × 1611.30 × 457.15 nm³ in B.*

Results summary: Paper VI

Two rod-shaped samples were prepared from individual osteonal lamellae in the femoral cortex by FIB annular milling. The samples were almost cylindrical, with a diameter going from 200-300 nm at the top to 700 nm at the bottom. In one of the samples, the banding pattern of collagen fibrils was observed along the rod length at all tilt angles, confirming collagen fibrils oriented in-plane. In the other sample, the banding pattern was noted only at certain tilt angles, while disordered or more mineral-rich regions, resembling rosettes, were present at other orientations. These features, i.e., collagen banding pattern and rosettes, were also identified in three conventional wedge-shaped samples prepared by FIB *in situ* lift-out. These samples, having known orientations with respect to the osteonal axis, confirmed the characteristic longitudinal and lacy motifs observed in bone in mutually orthogonal sections. Correspondence between the longitudinal and lacy motifs was confirmed by the electron tomography 3D reconstructions when reslicing along representative orthogonal planes. This demonstrated the reciprocity between the "holes" in the lacy motif and the collagen banding pattern in the longitudinal motif. In particular, "holes" appeared to mostly match the overlap regions of the collagen fibrils.

Segmentation of the "holes" in 3D over the entire tomograms showed that their shape is approximately that of rods. These rods were mostly disconnected from each other, and aligned with their long axis in the direction orthogonal to the banding pattern, i.e., in the same direction as the collagen fibrils. The average diameter of the "holes" in the four datasets examined varied from 16.4 nm to 26.4 nm. In one tomogram where a partial mineral ellipsoid was observed, the 3D segmentation of the "holes" showed that these features were mostly located outside the ellipsoid around its periphery.

Simultaneously to Z-contrast electron tomography acquisition, EDX tomography was completed to acquire elemental maps of calcium and phosphorus, representative of the mineral phase, and carbon and nitrogen, representative of the organic phase (type I collagen). EDX maps of carbon and nitrogen appeared quite noisy due to the overall weak signal, hence they proved to be inconclusive in determining the composition of the "holes". Nonetheless, the intersection analysis between the segmented "holes" and the reconstructed EDX maps showed higher spatial correspondence of the "holes" with the maps of carbon and nitrogen over those of calcium and phosphorus.

From the reconstructed EDX maps it was possible to observe the presence of calcium and phosphorus in the gap zones of the collagen fibrils, demonstrating intra-fibrillar mineralization. However, the signals of these two elements appeared more intense in correspondence with the extra-fibrillar component. In the extra-fibrillar space, some individual mineral structures were segmented, showing that bone mineral is in the form of plates with dimensions around 5-9 × 33-43 × 100 nm^3. The extra-fibrillar mineral also seemed to be mostly interconnected and spanning over multiple collagen fibrils.

Discussion

Two conditions affecting bone quantity and/or quality were subject of study in this thesis: LepR deficiency, associated with hyperglycemia (T2DM-like) and obesity in the Lund MetS rat model[110,188] [Paper I]; and osteopenia/osteoporosis, typical of the aging population and mimicked by hormone deficiency in OVX/ORX animal models[120,121] [Papers III-IV]. An extreme case of impaired bone metabolism, i.e., necrotic bone, resulting from anti-resorptive therapy (MRONJ) was also examined [Paper II].

Abnormalities in the overall energy metabolism, such as in the combination of hyperglycemia, obesity, and LepR deficiency[102], or more specifically in bone metabolism, such as imbalanced bone remodeling in osteoporosis[112], can impact not just biological functions, but also structural and compositional properties of the bone matrix. These changes in material properties can be reflected at various levels of bone's architecture, in turn affecting bone strength[83,84]. In the studies included in this thesis, a characterization approach typical of materials science was thus adopted, often combining different tools (multimodal characterization) to access information across several length scales (multiscale characterization), with a focus on the micro-nano continuum. The need for such a multimodal and multiscale approach stems from the trade-off between the volume of material that can be analyzed and the spatial resolution achievable[159,195,196]; the higher the resolution required, the smaller the volume that can be analyzed, especially when acquisition time matters.

The following sections discuss in more detail the application of multimodal and multiscale tools in probing bone quality-related aspects in compromised conditions affecting native bone (first section of this chapter) and osseointegration (second section of this chapter). A discussion on advanced characterization techniques and their implications on our understanding of bone ultrastructure concludes this chapter.

MULTIMODAL AND MULTISCALE CHARACTERIZATION OF DISEASED BONE

An example of multimodal characterization applied to bone is offered by Paper I. Therein, such an approach was selected to determine structural and compositional properties of bone matrix at the microscale in a novel preclinical model for T2DM/MetS, the Lund MetS rat[110,188]. To this author's knowledge, this is the first study examining skeletal attributes of the Lund MetS rat, originally investigated for diabetic vascular complications[110,197,198]. Rat models are frequently employed in preclinical research due to their low cost and good availability, although some dissimilarities in bone metabolism compared to human bone exist, such as the lack of Haversian remodeling[199]. Hence, when a new model is developed, a better understanding of its bone structure and composition is necessary to understand potential translation into human bone research. Interestingly, the LepR-deficient Lund MetS animals examined in Paper I displayed similar microstructural alterations to those commonly reported in widespread monogenic models of obesity with LepR deficiency, i.e., the Zucker fatty and Zucker diabetic fatty rat[200–202]. A deteriorated architecture in the trabecular compartment has also been reported in humans with T2DM[203]. The structural changes observed in the LepR-deficient animals encompassed both the overall bone geometry, with shorter femurs and thinner parietal bones, and the microstructure, with thinner cortices and fewer trabeculae, as well as shorter and less interdigitated sagittal sutures. All these alterations point towards a delayed skeletal development in the LepR-deficient rodents, independently on the ossification mechanism, i.e., endochondral in the femur and intramembranous in the parietal bones of the calvarium. Humans with congenic Lep/LepR deficiency also display severe obesity and delayed growth[107–109], hence suggesting that the Lund MetS rat could find applications in this translational research context.

Regarding the characterization of bone structure, the use of micro-CT in Paper I confirmed the advantages of quantitative morphometry in 3D over 2D, as microstructural differences between groups were not apparent in BSE-SEM images. On the other hand, the greater resolution of SEM compared to micro-CT, combined with the compositional- contrast in BSE-SEM, made it possible to attest to the presence of mineralized cartilage islands in the femurs and highly mineralized bands in the parietal bones. Mineralized cartilage islands, in particular, are a relevant structural feature in rat bone, but are absent in larger mammals, including humans, as they are likely removed by Haversian remodeling[204,205]. Hence, more attention should be paid to better characterize these islands in the future.

In both Paper I and Paper II, direct imaging to qualitatively/quantitatively probe structural aspects was combined with compositional analyses, primarily using spectroscopy, but also based on calibration of BSE-SEM images using a qBEI approach in Paper I. Specifically, in Paper I, characterization of bone composition was accomplished in a truly multimodal way, combining three techniques with different probes (red light, X-rays, electrons) and targeting progressively smaller fields of view at increasingly smaller pixel/voxel size, exemplifying the compromise between volume analyzed and resolution. This helped confirm the comparable bone matrix composition in LepR-deficient and healthy animals, ruling out technique-dependent limitations in capturing eventual differences. Not surprisingly, the comparable composition was reflected by analogous resistance to indentation, as RPI is more sensitive to local structural/compositional properties of the bone matrix[206].

Paper II expands the multimodal characterization approach by encompassing length scales from the micro- to the nano-level. Specifically, nanoscale imaging provided valuable insights into the impact of MRONJ on bone, beside the necrosis already apparent on a "macroscopic" level in the oral cavity. In a sense, necrotic bone can be considered as an extreme case of diseased bone. In this context, it is relevant to shed light on what happens where the necrotic bone front interfaces with the surrounding environment, where biofilm formation is commonly observed[142–144]. Bacterial colonization in necrotic bone in Paper II was confirmed by histology, a more traditional examination, as well as by SE-SEM imaging after resin cast etching. Treatments to remove or preserve specific elements can provide additional information compared to what an embedded and polished bone sample can reveal[154,157]. For example, in Paper II, resin cast etching was used, for the first time, to expose bacteria in a case of MRONJ. This confirmed the extensive bacterial colonization at a much higher resolution than that of visible light microscopy, allowing for a better visualization of the rod shape of the bacteria, while excluding the presence of mineralized bacteria seen instead in dental calculus[207]. Moreover, after resin cast etching, the presence of osteoblasts and bone lining cells in non-necrotic bone, or better, their absence in necrotic bone, could be noted, indicating no ongoing mineralization at the necrotic bone front. This qualitative observation was supported by the determination of compositional gradients across the interface between bone and resin (filled with bacteria in MRONJ) using SEM-EDX, and of bone mineral content close to said interface using micro-Raman spectroscopy.

A multiscale imaging approach similar to that used for bone-biomaterial interfaces, involving microscale imaging with BSE-SEM followed by nanoscale analyses with HAADF-STEM[57], was applied to probe the interface between necrotic bone and the bacteria-invaded resin in Paper II. This nanoscale resolution of the interface provided new insights into the role of bacteria in MRONJ. The structure and composition of the interface, consisting of both a hyper-mineralized band and a disordered and amorphous region, together with particulates around and within the bacteria, suggests that bacteria may have an active role in degrading bone *in vivo*. It is especially relevant for this discussion section to point out that, while SEM-EDX and micro-Raman spectroscopy indicated mineralization abnormalities in necrotic bone, only direct imaging at higher resolution by HAADF-STEM made it possible to determine the nature of the bone-bacteria interface, further corroborating the importance of multiscale characterization.

MULTIMODAL AND MULTISCALE CHARACTERIZATION OF BONE INTERFACES

An intriguing possibility is that of using bone implants as drug-eluting platforms to promote osseointegration and/or suppress undesired phenomena such as inflammation and infection. Currently, clinical applications are limited, but *in vitro* and preclinical research on the subject is quite extensive[77]. In this thesis, two different systems for local drug delivery aiming to counteract the increased bone resorption in osteoporosis, which may affect osseointegration[125], were investigated: an AM Ti-6Al-4V implant functionalized with genistein, a phytoestrogen [Paper III]; and particles of bioactive glass (Biogran®) functionalized with PTH 1-34, an anabolic agent [Paper IV]. Both these drugs offer an alternative to bisphosphonates, for which side affects like MRONJ have been reported[137–140], as also highlighted in Paper II.

Bone response to the biomaterial solutions for local drug delivery proposed in Papers III-IV was evaluated with a multiscale and multimodal characterization approach to examine osseointegration in a comprehensive way across several length scales of interest. This characterization workflow is well exemplified by Paper III, where analyses focused on both the bone-implant interface and the LCN in peri-implant bone going from the micro- to the nanoscale. At the microscale, BSE-SEM images provided information on new bone formation in the peri-implant space, especially in regard to the osseointegration "direction", i.e., distance *vs.* contact osteogenesis[61]. Beyond the microscale, HAADF-STEM images and STEM-EDX confirmed nano-osseointegration. Although these analyses are not routinely performed in osseointegration studies, their application has been demonstrated before[171,172,183]. The main element of novelty in Paper III lies within bridging these two length scales with examinations targeting the mesoscale. This was enabled by PFIB-SEM tomography, a relatively new tool in bone research with limited applications to date[31,208]. Compared to traditional FIB-SEM tomography using a Ga^+ ion beam, bigger volumes of material can be probed with Xe^+ PFIB-SEM, while preserving a good spatial resolution[31,160]. At the bone-implant interface, this means being able to examine the peri-implant space at greater distances from the implant surface and over bigger depths (where "depth" refers to the direction perpendicular to the image plane). In Paper III, seven osteocyte lacunae and relative canaliculi were distinctly visualized in the PFIB-SEM volume. As osteocytes have an important function in mechanotransduction, including when connected to the implant surface[60], PFIB-SEM tomography can find applications in the study of their organization in newly formed bone, offering complementary information, and an additional dimensionality, to 2D SEM images after resin cast etching.

The advent of P/FIB-SEM tomography in bone research has also opened possibilities in the 3D characterization of bone hierarchical structure at the mesoscale, where features are smaller than those resolved with micro-CT and span a larger field of view than those available with electron tomography. Recent studies using this technique have shown that bone mineral forms ellipsoidal aggregates[22,31], which tessellate the collagen matrix in a cross-fibrillar pattern[22]. These features were identified and reviewed by the author of this thesis in HAADF-STEM images of both native and peri-implant bone (see reference 33). Hence, given their increased recognition, examination of mineral ellipsoids was undertaken in Paper III. Therein, the mineral ellipsoids showed varying sizes, in some instances displaying transverse cross-sections larger than those reported in previous studies[22,31]. This could be

due to the systemic impairment in bone regeneration in OVX rats and/or to the local release of genistein. Sudden changes in ellipsoid orientation from longitudinal to transverse views within the image plane were also noted, confirming what was found in the only other PFIB-based work examining ellipsoids in peri-implant bone to date[208]. The origins and implications of size and orientation variations of the mineral ellipsoids are not known, hence P/FIB-SEM tomography should increasingly be implemented in the osseointegration characterization workflow. Transverse cross-sectional views of mineral ellipsoids, i.e., rosettes, were also observed in HAADF-STEM images of the bone-bioactive glass interface in Paper IV, providing yet further evidence of their ubiquitous nature.

A similar approach to that presented in Paper III was applied in Paper V, which placed additional emphasis on nanoscale characterization using electron tomography to resolve the bone-biomaterial interface in the third dimension, limiting overlapping artifacts in 2D S/TEM projection images. Two very dissimilar biomaterials, i.e., a permanent Ti-6Al-4V implant and a degradable bioactive glass, were studied in Paper III and Paper V, respectively, showcasing the versatility of multiscale characterization workflows for bone-biomaterial interfaces. However, these investigations were limited one/two samples, which is often the case in osseointegration studies, in particular when targeting the nanoscale. This workflow can be used as a first approach to minimize the number of animals required when gaining insights into bone response to specific biomaterials, for example for novel implant designs such as that in Paper III. However, the biological response to biomaterials should also be determined in a more quantitative way. In Paper IV, the micro-to-nanoscale evaluation of the bone-implant interface was implemented in a broader characterization context to assess biomechanics, mineralization dynamics, bone resorption, and gene expression. From these analyses, it emerged that Biogran® functionalized with PTH 1-34 could be a promising solution to improve osseointegration in osteoporotic conditions. In fact, ORX rats receiving the functionalized particles often displayed a similar behaviour as the control group receiving non-functionalized Biogran®. Conversely, PTH 1-34 functionalization did not seem to play any additional role in promoting bone repair in healthy animals. A similar preclinical investigation should be conducted for the genistein-functionalized implant in Paper III, although a pilot study (*unpublished*) demonstrated improvements in bone repair.

Despite its wide clinical use, there are not many studies focusing on the bone-Biogran® interface at the nanoscale. This lack was compensated for by Paper V, where both 2D STEM and 3D electron tomography experiments were completed. Compared to previous work where the interface between bone and bioactive glass was resolved in BF-TEM[209], Z-contrast in HAADF-STEM better captured the compositional gradients at the interface. Individual cross-sectional slices in the reconstructed electron tomogram corroborated that the dissolution/reprecipitation layer is characteristic of this type of interface, and not an artifact arising from feature overlap in 2D HAADF-STEM images. By using electron tomography, it was also possible to better visualize collagen fibrils and their orientation relative to the biomaterial surface in 3D. Nanoscale resolution of the bone-Biogran® interface by HAADF-STEM was also employed in Paper IV. This confirmed that the formation of a gradual interface was not affected by the functionalization with PTH 1-34, nor by systemic changes induced by ORX.

The effects of biomaterial implantation are not limited to the host, but changes also occur in the biomaterial itself[210]. In Paper V, these changes were evident in BSE-SEM images of Biogran® particles

where compositional gradients from the core to the outer regions and extensive cracks were observed in the particles, overall confirming known mechanisms of ion exchange and dissolution of bioactive glasses[75,76]. In Paper IV, SEM-EDX showed that neither PTH 1-34 functionalization nor hormone deficiency due to ORX altered the behaviour of Biogran® *in vivo*. Interestingly, ion exchange appeared slightly enhanced in the ORX rats. Further analyses, e.g., involving a greater sample size, should be completed to confirm this enhancement and determine eventual causes, possibly related to differences in local pH or availability of calcium and phosphorus.

EXTENDING THE FRONTIERS OF NANOSCALE CHARACTERIZATION IN BONE RESEARCH

A powerful prospect in multiscale/multimodal characterization stems from the possibility of correlating structural and composition information in 3D, opening avenues into "4D characterization", where the fourth dimension refers to the chemistry[55]. At the nanoscale, 4D characterization can be accomplished by combining S/TEM electron tomography to acquire images and resolve structural details, with spectroscopy tomography, using energy-filtered TEM, STEM-EDX, or STEM-EELS to obtain elemental maps in 3D[211,212]. In bone research, the correlative use of Z-contrast electron tomography and EELS tomography has been applied at the interface between human bone and a dental cp-Ti implant, revealing nanoscale integration between bone elements and the TiO_2 surface oxide[187]. In this thesis, on-axis Z-contrast electron tomography was instead combined with EDX tomography to address some of the debated aspects regarding bone ultrastructure [Paper VI]. Despite EELS typically yielding higher spatial resolution than EDX[184], EDX tomography was chosen over EELS tomography in Paper VI to simplify the acquisition workflow, as well as to avoid the strict limitations in sample thickness in EELS. In fact, the rod-shaped samples used in Paper VI were thicker than common electron transparent bone samples (e.g., 100-200 nm in Papers III-V), with diameters up to 700 nm. This made it possible to reconstruct more information in the direction perpendicular to the image plane (z direction), while preserving the nanoscale resolution typical of electron tomography. Resolution in Paper VI was further improved due to the on-axis nature of the electron tomography acquisition, where rod-shaped samples are mounted on a specialized holder that allows to access the missing wedge region forbidden in conventional single-tilt experimental set-ups (i.e., beyond $\pm 70°$)[173,175]. Previous electron tomography work on bone-implant interfaces showed that extending the tilt range to encompass high tilt angles, up to $\pm 90°$, led to a greater fidelity and quality in the final reconstruction[179]. This was confirmed in Paper VI, despite the larger diameter of the rod-shaped samples used. Improvements in the reconstruction in on-axis electron tomography *vs.* conventional electron tomography were also observed when comparing Paper VI with Paper V, where elongation artifacts typical of the missing wedge were present.

Overall, Paper VI showcased a new technique to expand the characterization toolbox for bone research where artifact-free 3D reconstructions of structure and composition can be obtained for relatively thick samples. Most importantly, this technique also offered new insights into bone ultrastructure. This is especially significant considering the essential role of the mineralized collagen fibrils as building block units not only of native bone[9], but also of bone-biomaterial interfaces[56]. The spatial organization of collagen fibrils and mineral, together with the morphology of the mineral phase, can indeed influence the mechanical properties of bone[213], but also determine diffusion pathways within the bone matrix.

One key aspect investigated in Paper VI was the nature of low-contrast regions, the "holes", characteristic of the lacy pattern of out-of-plane collagen fibrils[169]. It is worth pointing out that these "holes" were deemed to be cross-sectional views of collagen fibrils in Papers IV-V (chronologically antecedent to Paper VI), adopting the interpretation proposed by several authors[21,168–170,177,214]. However, this correspondence is not universally accepted in the bone research community, and other authors have identified the "holes" as nanochannels[163,164], intra-fibrillar unmineralized spaces hosting

macromolecules[215], or provided no clear explanation other than their unlikely correspondence to collagen fibrils[23]. Thanks to on-axis electron tomography in Paper VI, direct confirmation of the fact that most "holes" are collagen fibrils seen in cross-section was obtained. Dissimilarly from previous work assessing this relationship in a more global way through the reciprocity of longitudinal and lacy motifs[169,170], Paper VI provided direct evidence of the collagenous nature of the "holes" in a nearly point-specific manner by slicing the electron tomography reconstructions in mutually orthogonal planes. This demonstrated that the "holes" correspond to dark bands, i.e., overlap zones, in the banding pattern of in-plane fibrils. Interestingly, the rod-like appearance of "holes" segmented in 3D can also be observed in the visualization/segmentation of the electron tomogram in Paper V. However, the more optimal orientation of the samples in Paper VI and their rod shape, together with the removal of missing wedge artifacts thanks to on-axis electron tomography, allowed for more detailed analyses of the "holes".

In Paper VI, EDX tomography proved to be more suited to the analysis of bone mineral rather than of the organic phase. By considering individual 2D slices in the 3D reconstructed maps of calcium and phosphorus and correlating them to the corresponding HAADF-STEM slices, it was possible not only to confirm intra-fibrillar mineralization, but also to reveal higher signal intensity for the extra-fibrillar mineral. Conversely, reconstructed maps of carbon and nitrogen appeared rather noisy and could not be well correlated to specific structural features such as the "holes". A 4D characterization tool not explored in this thesis which could overcome this limitation is atom probe tomography (APT), where compositional information is spatially resolved in 3D by exploiting field ion microscopy and mass spectrometry[216]. APT combines ppm (parts per million) chemical sensitivity with nanoscale spatial resolution[216], making it possible to study individual collagen fibrils, as demonstrated by Lee et al. in leporine bone[217]. Other uses of APT in bone research have focused on resolving bone-implant interfaces at the atomic scale[187,218,219]. These and other applications of APT in bone and other biominerals were reviewed by the author of this thesis and co-workers (see reference 196).

Conclusions

Overall, the multimodal and multiscale characterization approach applied in this thesis revealed structural and compositional changes of bone in the compromised conditions examined, informed perspectives on biomaterial functionalization strategies to improve bone response in the presence of disease, and shed light on the ultrastructure of bone in both native tissue and at biomaterial interfaces.

In Paper I, the multimodal characterization of bone structure and composition highlighted geometrical and microstructural abnormalities in LepR-deficient Lund MetS rats, indicating a delay in their skeletal development which did not seem to affect bone matrix composition.

In Paper II, the multiscale investigation of the bone-bacteria interface in a case of MRONJ, especially when considering nanoscale information, demonstrated the existence of a hyper-mineralized band fading into an amorphous and disordered region. This suggests that, together with uncontrolled precipitation of calcium and phosphorus from the surrounding environment, bacteria actively degrade bone in MRONJ.

In Paper III, micro-to-nanoscale characterization of the interface between bone and an AM porous implant, acid-etched, and functionalized with genistein, showed a promising bone response despite the compromised bone repair in OVX rats. Moreover, Paper III highlighted the importance of including mesoscale analyses to investigate the LCN in 3D and the organization of mineral ellipsoids in peri-implant bone.

In Paper IV, microscopy-based analyses of the interface between bone and bioactive glass confirmed nano-osseointegration and unaffected dissolution/reprecipitation mechanisms in the presence of PTH 1-34 functionalization and altered bone metabolism in ORX rats. Quantitative evaluation of the biological response showed promising results in terms of bone repair in ORX rats when using bioactive glass functionalized with PTH 1-34.

In Paper V, a workflow to characterize the bone-bioactive glass interface was demonstrated, introducing 3D analyses at the nanoscale with electron tomography that further corroborated the gradual nature of the interface and highlighted that collagen fibrils are oriented parallel to the interface.

In Paper VI, on-axis Z-contrast electron tomography and EDX tomography were combined for the first time to resolve bone structure and composition at the nanoscale. This provided a direct identification of the low-contrast nanosized spaces seen in the lacy pattern as collagen fibrils. Additionally, it showed the extra-fibrillar mineral to be made of thin platelets merging in larger aggregates spanning over several fibrils.

Future perspectives

The multiscale and multimodal approach adopted in this thesis captured relevant information on bone structure and/or composition in the cases under investigation. However, many of the studies lacked quantitative investigations and statistical comparisons. This was mostly due to the small sample size (n = 1-2) especially in electron microscopy experiments (PFIB-SEM tomography, S/TEM, and electron tomography) [Papers II-VI]. Restrictions in sample size are indirectly related to high experimental costs, as well as lengthy protocols. Automating at least part of the experimental workflow could mitigate these limitations. For example, tools for automating STEM sample preparation by FIB lift-out have already been developed, demonstrating high sample quality and throughput[220]. However, they have yet to be tested on more complex materials like bone and bone-biomaterial interfaces. In the future, it would be interesting to implement these procedures to afford a higher sample size. For example, this would make it possible to examine broader records of MRONJ-affected individual to corroborate the observations in Paper II.

Even with the implementation of automated sample preparation workflows for S/TEM experiments, technical challenges would persist due to the electron beam sensitivity of biological samples like bone. These challenges become especially relevant when high beam doses are required such as in EDX or EELS, and in long experiments such as electron tomography. The compromise between resolution and exposure is exemplified by Paper VI, where large tilt increments and short dwell times were selected for EDX tomography to limit sample damage, albeit leading to sub-optimal EDX maps. Reconstruction algorithms like compressed sensing could be explored in future work, as they allow for under-sampling, requiring fewer projection images to produce high-quality 3D reconstructions[221]. Faster and more sensitive detectors could also mitigate challenges in electron tomography of beam-sensitive materials. As the acquisition of HAADF-STEM tilt series in ~360 s has been shown[222], it would be interesting to apply this fast electron tomography approach to bone.

There are also opportunities to improve tools for image analysis. Deep learning has emerged as a powerful aid to examine features of interest in large/multidimensional datasets, (semi)automating image segmentation to extract quantitative information[223]. However, complex structures like that found in bone at the nanoscale are difficult to be accurately segmented by algorithms. For example, in Paper VI, it was necessary to segment individual mineral plates manually. Improvements in machine learning algorithms could make it possible to analyze features with greater complexity and to examine larger amount of data, while also limiting operator bias in feature selection.

A main limitation of the characterization tools used in Papers III-IV stems from the inability to visualize the biomaterial surface functionalization, i.e., the layer of genistein or PTH 1-34. At this time, it is not possible to determine how much of the drug coating is still present at the time of retrieval, or if it has all been released in the peri-implant space. This could not be determined by EDX due to the similar elements present in both the drugs under investigation and bone, as well as the embedding resin. Other approaches should then be explored. In a previous study, ^{14}C radiolabelling was used to assess the release of bisphosphonates by autoradiography *ex vivo*, correlating the autoradiographs with

BSE-SEM images[224]. Hence, similar methodologies based on tagging the therapeutics used in Papers III-IV with easily identifiable signals could be tested.

Apart from technical limitations, some biology-related questions remain unanswered in this thesis, calling for further investigations. In Paper I, mechanistic insights into the origins of the altered microstructure in the LepR-deficient animals are needed, especially to decouple LepR deficiency, obesity, and hyperglycemia, as well as to study bone remodeling, with a specific focus on mineralized cartilage islands. These features should also be examined at smaller length scales, for example by P/FIB-SEM tomography and S/TEM, in particular to highlight how type I and type II collagen interface. In Paper I, structure-function relationships should also be better confirmed, for example by mechanical testing on whole bones. In Paper III, a preclinical study involving a greater sample size should be undertaken to quantify the effect of genistein functionalization on osseointegration, combining microscopy with other analytical techniques as done in Paper IV (e.g., biomechanics, mineralization dynamics, and gene expression).

This thesis mainly focused on assessing changes in bone structure and composition in the presence of disease [Papers I-IV]. In Paper V, a characterization workflow encompassing electron tomography was highlighted, and an advanced electron tomography approach was demonstrated in Paper VI. The high-resolution, artifact-free, 3D reconstruction of bone ultrastructure offered by on-axis electron tomography, especially when correlated with compositional information using EDX tomography, could find broader applications in bone research, for example to probe disease-induced changes in bone quality at the nanoscale.

Lastly, the multimodal and multiscale characterization approach adopted in this thesis only involved *ex situ* analyses. While developments in electron microscopy are aiming to get closer to native and dynamic conditions with liquid imaging[225], they still lack clinical relevance. More work needs to be done to implement materials science characterization workflows in clinically relevant contexts, for example identifying metrics that correlate to those measurable *in vivo*.

References

1. Tortora GJ, Derrickson B. The skeletal system: Bone tissue. In: Principles of anatomy and physiology. Hoboken, NJ: John Wiley & Sons; 2009. p. 175–97.
2. Huiskes R. If bone is the answer, then what is the question? J Anat. 2000;197:145–56.
3. Ritchie RO. The conflicts between strength and toughness. Nat Mater. 2011;10:817–22.
4. Skinner HCW. Biominerals. Mineral Mag. 2005;69:621–41.
5. Currey JD. Bones: Structure and mechanics. Princeton, NJ: Princeton University Press; 2002.
6. Glimcher MJ. Bone: Nature of the calcium phosphate crystals and cellular, structural, and physical chemical mechanisms in their formation. Rev Mineral Geochem. 2006;64:223–82.
7. Weiner S, Wagner HD. The material bone: Structure-mechanical function relations. Annu Rev Mater Sci. 1998;28:271–98.
8. Weiner S, Traub W, Wagner HD. Lamellar bone: Structure-function relations. J Struct Biol. 1999;126:241–55.
9. Reznikov N, Shahar R, Weiner S. Bone hierarchical structure in three dimensions. Acta Biomater. 2014;10:3815–26.
10. Ritchie RO, Buehler MJ, Hansma P. Plasticity and toughness in bone. Phys Today. 2009;62:41–7.
11. Sasaki N, Enyo A. Viscoelastic properties of bone as a function of water content. J Biomech. 1995;28:809–15.
12. Weiner S, Traub W. Bone structure: From ångstroms to microns. FASEB J. 1992;6:879–85.
13. Hulmes DJS. Collagen diversity, synthesis and assembly. In: Fratzl P, editor. Collagen: Structure and mechanics. New York, NY: Springer; 2008. p. 1–13.
14. Hodge AJ, Petruska JA. Recent studies with the electron microscope on ordered aggregates of the tropocollagen macromolecule. In: Ramachandran GN, editor. Aspects of protein structure. New York, NY: Academic Press; 1963. p. 289–300.
15. Orgel JPRO, Miller A, Irving TC, Fischetti RF, Hammersley AP, Wess TJ. The in situ supermolecular structure of type I collagen. Structure. 2001;9:1061–9.
16. Weiner S, Traub W. Organization of hydroxyapatite crystals within collagen fibrils. FEBS Lett. 1986;206:262–6.
17. Landis WJ, Hodgens KJ, Song MJ, Arena J, Kiyonaga S, Marko M, et al. Mineralization of collagen may occur on fibril surfaces: Evidence from conventional and high-voltage electron microscopy and three-dimensional imaging. J Struct Biol. 1996;117:24–35.
18. Landis WJ, Song MJ, Leith A, McEwen L, McEwen BF. Mineral and organic matrix interaction in normally calcifying tendon visualized in 3D by HV EM tomography and graphic image reconstruction. J Struct Biol. 1993;110:39–54.
19. Lees S, Prostak KS, Ingle VK, Kjoller K. The loci of mineral in turkey leg tendon as seen by atomic force microscope and electron microscopy. Calcif Tissue Int. 1994;55:180–9.
20. Pidaparti RMV, Chandran A, Takano Y, Turner CH. Bone mineral lies mainly outside collagen fibrils: Predictions of a composite model for osteonal bone. J Biomech. 1996;29:909–16.
21. Schwarcz HP. The ultrastructure of bone as revealed in electron microscopy of ion-milled sections. Semin Cell Dev Biol. 2015;46:44–50.
22. Buss DJ, Reznikov N, McKee MD. Crossfibrillar mineral tessellation in normal and Hyp mouse bone as revealed by 3D FIB-SEM microscopy. J Struct Biol. 2020;212:107603.
23. Reznikov N, Bilton M, Lari L, Stevens MM, Kröger R. Fractal-like hierarchical organization of bone begins at the nanoscale. Science. 2018;360:eaao2189.
24. Traub W, Arad T, Weiner S. Three-dimensional ordered distribution of crystals in turkey tendon collagen fibers. Proc Natl Acad Sci USA. 1989;86:9822–6.
25. Landis WJ, Hodgens KJ, Arena J, Song MJ, McEwen BF. Structural relations between collagen and mineral in bone as determined by high voltage electron microscopic tomography. Microsc Res Tech. 1996;33:192–202.
26. Robinson RA. An electron-microscopic study of the crystalline inorganic component of bone and its relationship to the organic matrix. J Bone Joint Surg Am. 1952;34-A:389–434.
27. Bocciarelli DS. Morphology of crystallites in bone. Calcif Tissue Res. 1970;5:261–9.
28. Arsenault AL. Crystal-collagen relationships in calcified turkey leg tendons visualized by selected-area dark field electron microscopy. Calcif Tissue Int. 1988;43:202–12.
29. Lees S, Prostak K. The locus of mineral crystallites in bone. Connect Tissue Res. 1988;18:41–54.
30. Fratzl P, Schreiber S, Klaushofer K. Bone mineralization as studied by small-angle X-ray scattering. Connect Tissue Res. 1996;34:247–54.

31. Binkley DM, Deering J, Yuan H, Gourrier A, Grandfield K. Ellipsoidal mesoscale mineralization pattern in human cortical bone revealed in 3D by plasma focused ion beam serial sectioning. J Struct Biol. 2020;212:107615.
32. Buss DJ, Kröger R, McKee MD, Reznikov N. Hierarchical organization of bone in three dimensions: A twist of twists. J Struct Biol X. 2022;6:100057.
33. Micheletti C, Hurley A, Gourrier A, Palmquist A, Tang T, Shah FA, et al. Bone mineral organization at the mesoscale: A review of mineral ellipsoids in bone and at bone interfaces. Acta Biomater. 2022;142:1–13.
34. Boyde A. Electron microscopy of the mineralizing front. Metab Bone Dis Rel Res. 1980;2:69–78.
35. Weiner S, Arad T, Sabanay I, Traub W. Rotated plywood structure of primary lamellar bone in the rat: Orientations of the collagen fibril arrays. Bone. 1997;20:509–14.
36. Wagermaier W, Gupta HS, Gourrier A, Burghammer M, Roschger P, Fratzl P. Spiral twisting of fiber orientation inside bone lamellae. Biointerphases. 2006;1:1–5.
37. Mitchell J, van Heteren AH. A literature review of the spatial organization of lamellar bone. C R Palevol. 2016;15:23–31.
38. Stock SR. The mineral-collagen interface in bone. Calcif Tissue Int. 2015;97:262–80.
39. Schwarcz HP, McNally EA, Botton GA. Dark-field transmission electron microscopy of cortical bone reveals details of extrafibrillar crystals. J Struct Biol. 2014;188:240–8.
40. Allen MR, Burr DB. Bone modeling and remodeling. In: Allen MR, Burr DB, editors. Basic and applied bone biology. London, UK: Academic Press; 2014. p. 75–90.
41. Galea GL, Zein MR, Allen S, Francis-West P. Making and shaping endochondral and intramembranous bones. Dev Dyn. 2021;250:414–49.
42. Hall BK. Bone. In: Bones and cartilage. London, UK: Academic Press; 2015. p. 17–42.
43. Opperman LA. Cranial sutures as intramembranous bone growth sites. Dev Dyn. 2000;219:472–85.
44. Wolff J. The law of bone transformation. Berlin, Germany: Hirschwald; 1892.
45. Bonewald LF. The amazing osteocyte. J Bone Miner Res. 2011;26:229–38.
46. Buckwalter JA, Glimcher MJ, Cooper RR, Recker R. Bone biology – Part I: Structure, blood supply, cells, matrix and mineralization. J Bone Joint Surg Am. 1995;77:1256–75.
47. Buenzli PR, Sims NA. Quantifying the osteocyte network in the human skeleton. Bone. 2015;75:144–50.
48. Dallas SL, Bonewald LF. Dynamics of the transition from osteoblast to osteocyte. Ann NY Acad Sci. 2010;1192:437–43.
49. Pacureanu A, Langer M, Boller E, Tafforeau P, Peyrin F. Nanoscale imaging of the bone cell network with synchrotron X-ray tomography: Optimization of acquisition setup. Med Phys. 2012;39:2229–38.
50. Robling AG, Bonewald LF. The osteocyte: New insights. Annu Rev Physiol. 2020;82:485–506.
51. Li MCM, Chow SKH, Wong RMY, Qin L, Cheung WH. The role of osteocytes-specific molecular mechanism in regulation of mechanotransduction – A systematic review. J Orthop Transl. 2021;29:1–9.
52. Shah FA, Wang X, Thomsen P, Grandfield K, Palmquist A. High-resolution visualization of the osteocyte lacuno-canalicular network juxtaposed to the surface of nanotextured titanium implants in human. ACS Biomater Sci Eng. 2015;1:305–13.
53. Einhorn TA, Gerstenfeld LC. Fracture healing: Mechanisms and interventions. Nat Rev Rheumatol. 2015;11:45–54.
54. Albrektsson T, Brånemark PI, Hansson HA, Lindström J. Osseointegrated titanium implants: Requirements for ensuring a long-lasting, direct bone-to-implant anchorage in man. Acta Orthop Scand. 1981;52:155–70.
55. Grandfield K. Bone, implants, and their interfaces. Phys Today. 2015;68:40–5.
56. Shah FA, Thomsen P, Palmquist A. Osseointegration and current interpretations of the bone-implant interface. Acta Biomater. 2019;84:1–15.
57. Palmquist A. A multiscale analytical approach to evaluate osseointegration. J Mater Sci Mater Med. 2018;29:60.
58. Grandfield K, Palmquist A, Engqvist H. Three-dimensional structure of laser-modified Ti6Al4V and bone interface revealed with STEM tomography. Ultramicroscopy. 2013;127:48–52.
59. Shah FA, Nilson B, Brånemark R, Thomsen P, Palmquist A. The bone-implant interface – Nanoscale analysis of clinically retrieved dental implants. Nanomedicine. 2014;10:1729–37.
60. Shah FA, Thomsen P, Palmquist A. A review of the impact of implant biomaterials on osteocytes. J Dent Res. 2018;97:977–86.
61. Davies JE. Understanding peri-implant endosseous healing. J Dent Educ. 2003;67:932–49.
62. Niinomi M. Mechanical properties of biomedical titanium alloys. Mater Sci Eng. 1998;243:231–6.
63. Kasemo B. Biocompatibility of titanium implants: Surface science aspects. J Prosthet Dent. 1983;49:832–7.
64. Bauer S, Schmuki P, von der Mark K, Park J. Engineering biocompatible implant surfaces. Part I: Materials and surfaces. Prog Mater Sci. 2013;58:261–326.
65. Palmquist A, Lindberg F, Emanuelsson L, Brånemark R, Engqvist H, Thomsen P. Biomechanical, histological, and ultrastructural analyses of laser micro- and nano-structured titanium alloy implants: A study in rabbit. J Biomed Mater Res A. 2010;92A:1476–86.

66. Davies JE, Ajami E, Moineddin R, Mendes VC. The roles of different scale ranges of surface implant topography on the stability of the bone/implant interface. Biomaterials. 2013;34:3535–46.
67. Davies JE, Mendes VC, Ko JCH, Ajami E. Topographic scale-range synergy at the functional bone/implant interface. Biomaterials. 2014;35:25–35.
68. Pyka G, Burakowski A, Kerckhofs G, Moesen M, van Bael S, Schrooten J, et al. Surface modification of Ti6Al4V open porous structures produced by additive manufacturing. Adv Eng Mater. 2012;14:363–70.
69. Heinl P, Müller L, Körner C, Singer RF, Müller FA. Cellular Ti-6Al-4V structures with interconnected macro porosity for bone implants fabricated by selective electron beam melting. Acta Biomater. 2008;4:1536–44.
70. Palmquist A, Jolic M, Hryha E, Shah FA. Complex geometry and integrated macro-porosity: Clinical applications of electron beam melting to fabricate bespoke bone-anchored implants. Acta Biomater. 2023;156:125–45.
71. Koschwanez HE, Reichert WM. Textured and porous materials. In: Ratner BR, Hoffman AS, Schoen FJ, Lemons JE, editors. Biomaterials science: An introduction to materials in medicine. Oxford, UK: Academic Press; 2013. p. 321–31.
72. Wang Z, Wang C, Li C, Qin Y, Zhong L, Chen B, et al. Analysis of factors influencing bone ingrowth into three-dimensional printed porous metal scaffolds: A review. J Alloy Compd. 2017;717:271–85.
73. Hench LL. The story of Bioglass®. J Mater Sci Mater Med. 2006;17:967–78.
74. Tadjoedin ES, de Lange GL, Lyaruu DM, Kuiper L, Burger EH. High concentrations of bioactive glass material (BioGran®) vs. autogenous bone for sinus floor elevation. Clin Oral Impl Res. 2002;13:428–36.
75. Hench LL, Andersson Ö. Bioactive glasses. In: Hench LL, Wilson J, editors. An introduction to bioceramics. Singapore: World Scientific; 1993. p. 41–62. (McLaren M, Niesz DE, editors. Advanced series in ceramics; vol. 1).
76. Schepers E, de Clercq M, Ducheyene P, Kempeneers P. Bioactive glass particulate material as a filler for bone lesions. J Oral Rehabil. 1991;18:439–52.
77. Kunrath MF, Shah FA, Dahlin C. Bench-to-bedside: Feasibility of nano-engineered and drug-delivery biomaterials for bone-anchored implants and periodontal applications. Mater Today Bio. 2023;18:100540.
78. Kyllönen L, D'Este M, Alini M, Eglin D. Local drug delivery for enhancing fracture healing in osteoporotic bone. Acta Biomater. 2015;11:412–34.
79. Bai H, Cui Y, Wang C, Wang Z, Luo W, Liu Y, et al. 3D printed porous biomimetic composition sustained release zoledronate to promote osteointegration of osteoporotic defects. Mater Design. 2020;189:108513.
80. Kanis JA, McCloskey EV, Johansson H, Oden A, Melton LJ, Khaltaev N. A reference standard for the description of osteoporosis. Bone. 2008;42:467–75.
81. Bouxsein ML. Bone quality: Where do we go from here? Osteoporos Int. 2003;14:118–27.
82. Seeman E, Delmas PD. Bone quality – The material and structural basis of bone strength and fragility. N Engl J Med. 2006;354:2250–61.
83. Boskey AL, Imbert L. Bone quality changes associated with aging and disease: A review. Ann NY Acad Sci. 2017;1410:93–106.
84. Muñoz A, Docaj A, Ugarteburu M, Carriero A. Poor bone matrix quality: What can be done about it? Curr Osteoporos Rep. 2021;19:510–31.
85. World Health Organization. Classification of diabetes mellitus. 2019.
86. World Health Organization. Global report on diabetes. 2016.
87. Zimmet P, Alberti KGMM, Shaw J. Global and societal implications of the diabetes epidemic. Nature. 2001;414:782–7.
88. Eckel RH, Grundy SM, Zimmet PZ. The metabolic syndrome. Lancet. 2005;365:1415–28.
89. Vestergaard P. Discrepancies in bone mineral density and fracture risk in patients with type 1 and type 2 diabetes—a meta-analysis. Osteoporos Int. 2007;18:427–44.
90. Schwartz AV, Vittinghoff E, Sellmeyer D, Feingold K, de Rekeneire N, Strotmeyer ES, et al. Diabetes-related complications, glycemic control, and falls in older adults. Diabetes Care. 2008;31:391–6.
91. Lekkala S, Taylor EA, Hunt HB, Donnelly E. Effects of diabetes on bone material properties. Curr Osteoporos Rep. 2019;17:455–64.
92. Reid IR. Fat and bone. Arch Biochem Biophys. 2010;503:20–7.
93. Harada S, Rodan GA. Control of osteoblast function and regulation of bone mass. Nature. 2003;423:349–55.
94. Frost HM. Bone's mechanostat: A 2003 update. Anat Rec. 2003;275A:1081–101.
95. Saito M, Kida Y, Kato S, Marumo K. Diabetes, collagen, and bone quality. Curr Osteoporos Rep. 2014;12:181–8.
96. Yamagishi S. Role of advanced glycation end products (AGEs) and receptor for AGEs (RAGE) in vascular damage in diabetes. Exp Gerontol. 2011;46:217–24.
97. Cao JJ. Effects of obesity on bone metabolism. J Orthop Surg Res. 2011;6:30.
98. Yamamoto M, Sugimoto T. Advanced glycation end products, diabetes, and bone strength. Curr Osteoporos Rep. 2016;14:320–6.
99. Hamada Y, Fujii H, Fukagawa M. Role of oxidative stress in diabetic bone disorder. Bone. 2009;45:S35–8.

100. Halade GV, Jamali AE, Williams PJ, Fajardo RJ, Fernandes G. Obesity-mediated inflammatory microenvironment stimulates osteoclastogenesis and bone loss in mice. Exp Gerontol. 2011;46:43–52.
101. Tartaglia LA. The leptin receptor. J Biol Chem. 1997;272:6093–6.
102. Reid IR, Baldock PA, Cornish J. Effects of leptin on the skeleton. Endocr Rev. 2018;39:938–59.
103. Burguera B, Hofbauer LC, Thomas T, Gori F, Evans GL, Khosla S, et al. Leptin reduces ovariectomy-induced bone loss in rats. Endocrinology. 2001;142:3546–53.
104. Bartell SM, Rayalam S, Ambati S, Gaddam DR, Hartzell DL, Hamrick M, et al. Central (ICV) leptin injection increases bone formation, bone mineral density, muscle mass, serum IGF-1, and the expression of osteogenic genes in leptin-deficient ob/ob mice. J Bone Miner Res. 2011;26:1710–20.
105. King A, Austin A. Animal models of type 1 and type 2 diabetes mellitus. In: Conn PM, editor. Animal models for the study of human disease. London, UK: Academic Press; 2017. p. 245–65.
106. Montague CT, Farooqi IS, Whitehead JP, Soos MA, Rau H, Wareham NJ, et al. Congenital leptin deficiency is associated with severe early-onset obesity in humans. Nature. 1997;387:903–8.
107. Clément K, Vaisse C, Lahlou N, Cabrol S, Pelloux V, Cassuto D, et al. A mutation in the human leptin receptor gene causes obesity and pituitary dysfunction. Nature. 1998;392:398–401.
108. Farooqi IS, Wangensteen T, Collins S, Kimber W, Matarese G, Keogh JM, et al. Clinical and molecular genetic spectrum of congenital deficiency of the leptin receptor. N Engl J Med. 2007;356:237–47.
109. Farooqi IS, O'Rahilly S. 20 years of leptin: Human disorders of leptin action. J Endocrinol. 2014;223:T63–70.
110. Gomez MF, Åkesson L, Lernmark Å. A new rat model for diabetic vascular complications. Patent application WO-2015044339-A1.
111. Consensus development conference. Diagnosis, prophylaxis, and treatment of osteoporosis. Am J Medicine. 1993;94:646–50.
112. Ettinger MP. Aging bone and osteoporosis: Strategies for preventing fractures in the elderly. Arch Intern Med. 2003;163:2237–46.
113. Amin S, Achenbach SJ, Atkinson EJ, Khosla S, Melton LJ. Trends in fracture incidence: A population-based study over 20 years. J Bone Miner Res. 2014;29:581–9.
114. World Health Organization. Ageing and health [Internet]. 2022. Available from: https://www.who.int/news-room/fact-sheets/detail/ageing-and-health
115. Khosla S, Oursler MJ, Monroe DG. Estrogen and the skeleton. Trends Endocrinol Metab. 2012;23:576–81.
116. Riggs BL, Khosla S, Melton LJ. Sex steroids and the construction and conservation of the adult skeleton. Endocr Rev. 2002;23:279–302.
117. Khosla S, Melton LJ, Atkinson EJ, O'Fallon WM, Klee GG, Riggs BL. Relationship of serum sex steroid levels and bone turnover markers with bone mineral density in men and women: A key role for bioavailable estrogen. J Clin Endocrinol Metab. 1998;83:2266–74.
118. Daniell HW, Dunn SR, Ferguson DW, Lomas G, Niazi Z, Stratte PT. Progressive osteoporosis during androgen deprivation therapy for prostate cancer. J Urol. 1999;163:181–6.
119. Preston DM, Torréns JI, Harding P, Howard RS, Duncan WE, Mcleod DG. Androgen deprivation in men with prostate cancer is associated with an increased rate of bone loss. Prostate Cancer Prostatic Dis. 2002;5:304–10.
120. Kalu DN. The ovariectomized rat model of postmenopausal bone loss. Bone Miner. 1991;15:175–91.
121. Bonucci E, Ballanti P. Osteoporosis – Bone remodeling and animal models. Toxicol Pathol. 2014;42:957–69.
122. Wakley GK, Schutte HD, Hannon KS, Turner RT. Androgen treatment prevents loss of cancellous bone in the orchidectomized rat. J Bone Miner Res. 1991;6:325–30.
123. Giro G, Chambrone L, Goldstein A, Rodrigues JA, Zenobio E, Feres M, et al. Impact of osteoporosis in dental implants: A systematic review. World J Orthop. 2015;6:311–5.
124. Javed F, Ahmed HB, Crespi R, Romanos GE. Role of primary stability for successful osseointegration of dental implants: Factors of influence and evaluation. Interv Med Appl Sci. 2013;5:162–7.
125. Franchi M, Fini M, Giavaresi G, Ottani V. Peri-implant osteogenesis in health and osteoporosis. Micron. 2005;36:630–44.
126. Dereka X, Calciolari E, Donos N, Mardas N. Osseointegration in osteoporotic-like condition: A systematic review of preclinical studies. J Periodontal Res. 2018;53:933–40.
127. de Medeiros FCFL, Kudo GAH, Leme BG, Saraiva PP, Verri FR, Honório HM, et al. Dental implants in patients with osteoporosis: A systematic review with meta-analysis. Int J Oral Maxillofac Surg . 2018;47:480–91.
128. Russell RGG. Bisphosphonates: The first 40 years. Bone. 2011;49:2–19.
129. Reznikov N, Steele JAM, Fratzl P, Stevens MM. A materials science vision of extracellular matrix mineralization. Nat Rev Mater. 2016;1:16041.
130. Russell RGG, Mühlbauer RC, Bisaz S, Williams DA, Fleisch H. The influence of pyrophosphate, condensed phosphates, phosphonates and other phosphate compounds on the dissolution of hydroxyapatite in vitro and on bone

resorption induced by parathyroid hormone in tissue culture and in thyroparathyroidectomised rats. Calcif Tissue Res. 1970;6:183–96.
131. Fleisch H. Diphosphonates: History and mechanisms of action. Metab Bone Dis Relat Res. 1981;3:279–87.
132. Million Women Study Collaborators. Breast cancer and hormone-replacement therapy in the Million Women Study. Lancet. 2003;362:419–27.
133. Adlercreutz H. Phytoestrogens: Epidemiology and a possible role in cancer protection. Environ Health Perspect. 1995;103:103–12.
134. Marini H, Minutoli L, Polito F, Bitto A, Altavilla D, Atteritano M, et al. Effects of the phytoestrogen genistein on bone metabolism in osteopenic postmenopausal women: A randomized trial. Ann Intern Med. 2007;146:839.
135. Hodsman AB, Bauer DC, Dempster DW, Dian L, Hanley DA, Harris ST, et al. Parathyroid hormone and teriparatide for the treatment of osteoporosis: A review of the evidence and suggested guidelines for its use. Endocr Rev. 2005;26:688–703.
136. Canalis E. Management of endocrine disease: Novel anabolic treatments for osteoporosis. Eur J Endocrinol. 2018;178:R33–44.
137. Bilezikian JP. Osteonecrosis of the jaw – Do bisphosphonates pose a risk? N Engl J Med. 2006;335:2278–81.
138. Reid IR. Osteonecrosis of the jaw – Who gets it, and why? Bone. 2009;44:4–10.
139. Ruggiero SL. Bisphosphonate-related osteonecrosis of the jaw (BRONJ): Initial discovery and subsequent development. J Oral Maxillofac Surg. 2009;67:13–8.
140. Ruggiero SL, Dodson TB, Aghaloo T, Carlson ER, Ward BB, Kademani D. American Association of Oral and Maxillofacial Surgeons' position paper on medication-related osteonecrosis of the jaw – 2022 update. J Oral Maxillofac Surg. 2022;80:920–43.
141. Drake MT, Clarke BL, Khosla S. Bisphosphonates: Mechanism of action and role in clinical practice. Mayo Clin Proc. 2008;83:1032–45.
142. Reid IR, Cornish J. Epidemiology and pathogenesis of osteonecrosis of the jaw. Nat Rev Rheumatol. 2012;8:90–6.
143. Allen MR, Burr DB. The pathogenesis of bisphosphonate-related osteonecrosis of the jaw: So many hypotheses, so few data. J Oral Maxillofac Surg. 2009;67:61–70.
144. Hinson AM, Smith CW, Siegel ER, Stack BC. Is bisphosphonate-related osteonecrosis of the jaw an infection? A histological and microbiological ten-year summary. Int J Dent. 2014;2014:452737.
145. Georgiadis M, Müller R, Schneider P. Techniques to assess bone ultrastructure organization: Orientation and arrangement of mineralized collagen fibrils. J R Soc Interface. 2016;13:20160088.
146. Binkley DM, Grandfield K. Advances in multiscale characterization techniques of bone and biomaterials interfaces. ACS Biomater Sci Eng. 2017;4:3678–90.
147. Dempster DW, Compston JE, Drezner MK, Glorieux FH, Kanis JA, Malluche H, et al. Standardized nomenclature, symbols, and units for bone histomorphometry: A 2012 update of the report of the ASBMR Histomorphometry Nomenclature Committee. J Bone Miner Res. 2013;28:2–17.
148. Orhan K, editor. Micro-computed tomography (micro-CT) in medicine and engineering. Cham, Switzerland: Springer Nature; 2020.
149. Bouxsein ML, Boyd SK, Christiansen BA, Guldberg RE, Jepsen KJ, Müller R. Guidelines for assessment of bone microstructure in rodents using micro-computed tomography. J Bone Miner Res. 2010;25:1468–86.
150. Li JY, Pow EHN, Zheng LW, Ma L, Kwong DLW, Cheung LK. Quantitative analysis of titanium-induced artifacts and correlated factors during micro-CT scanning. Clin Oral Impl Res. 2014;25:506–10.
151. Palmquist A, Shah FA, Emanuelsson L, Omar O, Suska F. A technique for evaluating bone ingrowth into 3D printed, porous Ti6Al4V implants accurately using X-ray micro-computed tomography and histomorphometry. Micron. 2017;94:1–8.
152. Goldstein JI, Newbury DE, Michael JR, Ritchie NWM, Scott JHJ, Joy DC. Scanning electron microscopy and X-ray microanalysis. New York, NY: Springer; 2018.
153. Williams DB, Carter CB. Transmission electron microscopy. New York, NY: Springer; 2009.
154. Shah FA, Ruscsák K, Palmquist A. 50 years of scanning electron microscopy of bone – A comprehensive overview of the important discoveries made and insights gained into bone material properties in health, disease, and taphonomy. Bone Res. 2019;7:15.
155. Roschger P, Fratzl P, Eschberger J, Klaushofer K. Validation of quantitative backscattered electron imaging for the measurement of mineral density distribution in human bone biopsies. Bone. 1998;23:319–26.
156. Shah FA, Ruscsák K, Palmquist A. Transformation of bone mineral morphology: From discrete marquise-shaped motifs to a continuous interwoven mesh. Bone Rep. 2020;13:100283.
157. Sato M, Shah FA. Contributions of resin cast etching to visualising the osteocyte lacuno-canalicular network architecture in bone biology and tissue engineering. Calcif Tissue Int. 2023;112:525–542.

158. Shah FA, Johansson ML, Omar O, Simonsson H, Palmquist A, Thomsen P. Laser-modified surface enhances osseointegration and biomechanical anchorage of commercially pure titanium implants for bone-anchored hearing systems. PLOS One. 2016;11:e0157504.
159. Cantoni M, Holzer L. Advances in 3D focused ion beam tomography. MRS Bull. 2014;39:354–60.
160. Burnett TL, Kelley R, Winiarski B, Contreras L, Daly M, Gholinia A, et al. Large volume serial section tomography by Xe Plasma FIB dual beam microscopy. Ultramicroscopy. 2016;161:119–29.
161. Reznikov N, Almany-Magal R, Shahar R, Weiner S. Three-dimensional imaging of collagen fibril organization in rat circumferential lamellar bone using a dual beam electron microscope reveals ordered and disordered sub-lamellar structures. Bone. 2013;52:676–83.
162. Reznikov N, Shahar R, Weiner S. Three-dimensional structure of human lamellar bone: The presence of two different materials and new insights into the hierarchical organization. Bone. 2014;59:93–104.
163. Tang T, Landis W, Raguin E, Werner P, Bertinetti L, Dean M, et al. A 3D network of nanochannels for possible ion and molecule transit in mineralizing bone and cartilage. Adv Nanobiomed Res. 2022;2:2100162.
164. Tang T, Landis W, Blouin S, Bertinetti L, Hartmann MA, Berzlanovich A, et al. Subcanalicular nanochannel volume is inversely correlated with calcium content in human cortical bone. J Bone Miner Res. 2023;38:313–25.
165. Giannuzzi LA, Giannuzzi NJ, Capuano MJ. FIB, SEM, and TEM of bone/dental implant interfaces. Microsc Microanal. 2005;11:998–9.
166. Grandfield K, Engqvist H. Focused ion beam in the study of biomaterials and biological matter. Adv Mater Sci Eng. 2012;2012:1–6.
167. Pennycook SJ. Z-contrast STEM for materials science. Ultramicroscopy. 1989;30:58–69.
168. Jantou V, Turmaine M, West GD, Horton MA, McComb DW. Focused ion beam milling and ultramicrotomy of mineralised ivory dentine for analytical transmission electron microscopy. Micron. 2009;40:495–501.
169. McNally EA, Schwarcz HP, Botton GA, Arsenault AL. A model for the ultrastructure of bone based on electron microscopy of ion-milled sections. PLOS One. 2012;7:e29258.
170. Grandfield K, Vuong V, Schwarcz HP. Ultrastructure of bone: Hierarchical features from nanometer to micrometer scale revealed in focused ion beam sections in the TEM. Calcif Tissue Int. 2018;103:606–16.
171. Palmquist A, Grandfield K, Norlindh B, Mattsson T, Brånemark R, Thomsen P. Bone-titanium oxide interface in humans revealed by transmission electron microscopy and electron tomography. J R Soc Interface. 2012;9:396–400.
172. Grandfield K, Palmquist A, Ericson F, Malmström J, Emanuelsson L, Slotte C, et al. Bone response to free-form fabricated hydroxyapatite and zirconia scaffolds: A transmission electron microscopy study in the human maxilla. Clin Implant Dent Relat Res. 2012;14:461–9.
173. Bals S, van Aert S, van Tendeloo G. High resolution electron tomography. Curr Opin Solid State Mater Sci. 2013;17:107–14.
174. Ercius P, Alaidi O, Rames MJ, Ren G. Electron tomography: A three-dimensional analytic tool for hard and soft materials research. Adv Mater. 2015;27:5638–63.
175. Kawase N, Kato M, Nishioka H, Jinnai H. Transmission electron microtomography without the "missing wedge" for quantitative structural analysis. Ultramicroscopy. 2007;107:8–15.
176. Midgley PA, Weyland M. 3D electron microscopy in the physical sciences: The development of Z-contrast and EFTEM tomography. Ultramicroscopy. 2003;96:413–31.
177. McNally E, Nan F, Botton GA, Schwarcz HP. Scanning transmission electron microscopic tomography of cortical bone using Z-contrast imaging. Micron. 2013;49:46–53.
178. Grandfield K, Palmquist A, Engqvist H. High-resolution three-dimensional probes of biomaterials and their interfaces. Philos Trans A Math Phys Eng Sci. 2012;370:1337–51.
179. Wang X, Shah FA, Palmquist A, Grandfield K. 3D characterization of human nano-osseointegration by on-axis electron tomography without the missing wedge. ACS Biomater Sci Eng. 2017;3:49–55.
180. Pasteris JD, Beyssac O. Welcome to Raman spectroscopy: Successes, challenges, and pitfalls. Elements. 2020;16:87–92.
181. Morris MD, Mandair GS. Raman assessment of bone quality. Clin Orthop Relat Res. 2011;469:2160–9.
182. Gamsjaeger S, Masic A, Roschger P, Kazanci M, Dunlop JWC, Klaushofer K, et al. Cortical bone composition and orientation as a function of animal and tissue age in mice by Raman spectroscopy. Bone. 2010;47:392–9.
183. Grandfield K, Gustafsson S, Palmquist A. Where bone meets implant: The characterization of nano-osseointegration. Nanoscale. 2013;5:4302–8.
184. Egerton RF. Electron energy-loss spectroscopy in the electron microscope. New York, NY: Springer; 2011.
185. Jantou-Morris V, Horton MA, McComb DW. The nano-morphological relationships between apatite crystals and collagen fibrils in ivory dentine. Biomaterials. 2010;31:5275–86.
186. Lee BEJ, Luo L, Grandfield K, Andrei CM, Schwarcz HP. Identification of collagen fibrils in cross sections of bone by electron energy loss spectroscopy (EELS). Micron. 2019;124:102706.

187. Wang X, Langelier B, Shah FA, Korinek A, Bugnet M, Hitchcock AP, et al. Biomineralization at titanium revealed by correlative 4D tomographic and spectroscopic methods. Adv Mater Interfaces. 2018;5:1800262.
188. Janvier Labs. Lund MetS rat [Internet]. 2019. Available from: https://janvier-labs.com/en/fiche_produit/lund-mets_rat/
189. Gomes-Ferreira PHS, Lisboa-Filho PN, da Silva AC, Bim-júnior O, de Souza Batista FR, Silva ACE, et al. Sonochemical time standardization for bioactive materials used in perimplantar defects filling. Ultrason Sonochem. 2019;56:437–46.
190. Jarmar T, Palmquist A, Brånemark R, Hermansson L, Engqvist H, Thomsen P. Technique for preparation and characterization in cross-section of oral titanium implant surfaces using focused ion beam and transmission electron microscopy. J Biomed Mater Res A. 2008;87A:1003–9.
191. Li C, Habler G, Baldwin LC, Abart R. An improved FIB sample preparation technique for site-specific plan-view specimens: A new cutting geometry. Ultramicroscopy. 2018;184:310–7.
192. Huang J, Wang X, Grandfield K. FIB preparation of bone-implant interfaces for correlative on-axis rotation electron tomography and atom probe tomography. Microsc Microanal. 2014;20:352–3.
193. Buie HR, Campbell GM, Klinck RJ, MacNeil JA, Boyd SK. Automatic segmentation of cortical and trabecular compartments based on a dual threshold technique for in vivo micro-CT bone analysis. Bone. 2007;41:505–15.
194. Schindelin J, Arganda-Carreras I, Frise E, Kaynig V, Longair M, Pietzsch T, et al. Fiji: An open-source platform for biological-image analysis. Nat Methods. 2012;9:676–82.
195. Möbus G, Inkson BJ. Nanoscale tomography in materials science. Mater Today. 2007;10:18–25.
196. Grandfield K, Micheletti C, Deering J, Arcuri G, Tang T, Langelier B. Atom probe tomography for biomaterials and biomineralization. Acta Biomater. 2022;148:44–60.
197. Gomez MF, Silvola J, Berglund LM, Kiugel M, Åkesson L, Knuuti J, et al. Cardiac hypertrophy and oxidative metabolism in novel congenic leptin receptor deficient BBDR.cg-lepr.cp rats. FASEB J. 2014;28:1155.10.
198. Berglund L, Åkesson L, Garcia-Vaz E, Zetterqvist A, Kotova O, Andersson AD, et al. Diabetes complications in congenic leptin receptor deficient BBDR.cg-lepr.cp rats. FASEB J. 2014;28:1072.6.
199. Wancket LM. Animal models for evaluation of bone implants and devices. Vet Pathol. 2015;52:842–50.
200. Reinwald S, Peterson RG, Allen MR, Burr DB. Skeletal changes associated with the onset of type 2 diabetes in the ZDF and ZDSD rodent models. Am J Physiol Endocrinol Metab. 2009;296:E765–74.
201. Tamasi JA, Arey BJ, Bertolini DR, Feyen JH. Characterization of bone structure in leptin receptor-deficient Zucker (fa/fa) rats. J Bone Miner Res. 2003;18:1605–11.
202. Zeitoun D, Caliaperoumal G, Bensidhoum M, Constans JM, Anagnostou F, Bousson V. Microcomputed tomography of the femur of diabetic rats: Alterations of trabecular and cortical bone microarchitecture and vasculature – A feasibility study. Eur Radiol Exp. 2019;3:17.
203. McCabe L, Zhang J, Raehtz S. Understanding the skeletal pathology of type 1 and 2 diabetes mellitus. Crit Rev Eukaryot Gene Expr. 2011;21:187–206.
204. Shipov A, Zaslansky P, Riesemeier H, Segev G, Atkins A, Shahar R. Unremodeled endochondral bone is a major architectural component of the cortical bone of the rat (Rattus norvegicus). J Struct Biol. 2013;183:132–40.
205. Bach-Gansmo FL, Irvine SC, Brüel A, Thomsen JS, Birkedal H. Calcified cartilage islands in rat cortical bone. Calcif Tissue Int. 2013;92:330–8.
206. Allen MR, McNerny EM, Organ JM, Wallace JM. True gold or pyrite: A review of reference point indentation for assessing bone mechanical properties in vivo. J Bone Miner Res. 2015;30:1539–50.
207. Shah FA. Micro-Raman spectroscopy reveals the presence of octacalcium phosphate and whitlockite in association with bacteria-free zones within the mineralized dental biofilm. Microsc Microanal. 2019;25:129–34.
208. Deering J, Chen J, Mahmoud D, Tang T, Lin Y, Fang Q, et al. Characterizing mineral ellipsoids in new bone formation at the interface of Ti6Al4V porous implants. bioRxiv. 2023;2023.01.20.524810.
209. Hench LL, Paschall HA. Direct chemical bond of bioactive glass-ceramic materials to bone and muscle. J Biomed Mater Res. 1973;4:25–42.
210. Puleo DA, Nanci A. Understanding and controlling the bone-implant interface. Biomaterials. 1999;20:2311–21.
211. Möbus G, Doole RC, Inkson BJ. Spectroscopic electron tomography. Ultramicroscopy. 2003;96:433–51.
212. Collins SM, Midgley PA. Progress and opportunities in EELS and EDS tomography. Ultramicroscopy. 2017;180:133–41.
213. Schwarcz HP, Abueidda D, Jasiuk I. The ultrastructure of bone and its relevance to mechanical properties. Front Phys. 2017;5:39.
214. Cressey BA, Cressey G. A model for the composite nanostructure of bone suggested by high-resolution transmission electron microscopy. Mineral Mag. 2003;67:1171–82.
215. Macías-Sánchez E, Tarakina NV, Ivanov D, Blouin S, Berzlanovich AM, Fratzl P. Spherulitic crystal growth drives mineral deposition patterns in collagen-based materials. Adv Funct Mater. 2022;32:2200504.

216. Gault B, Chiaramonti A, Cojocaru-Mirédin O, Stender P, Dubosq R, Freysoldt C, et al. Atom probe tomography. Nat Rev Methods Primers. 2021;1:51.
217. Lee BEJ, Langelier B, Grandfield K. Visualization of collagen-mineral arrangement using atom probe tomography. Adv Biol. 2021;5:2100657.
218. Karlsson J, Sundell G, Thuvander M, Andersson M. Atomically resolved tissue integration. Nano Lett. 2014;14:4220–3.
219. Sundell G, Dahlin C, Andersson M, Thuvander M. The bone-implant interface of dental implants in humans on the atomic scale. Acta Biomater. 2017;48:445–50.
220. Tsurusawa H, Nakanishi N, Kawano K, Chen Y, Dutka M, Leer BV, et al. Robotic fabrication of high-quality lamellae for aberration-corrected transmission electron microscopy. Sci Rep. 2021;11:21599.
221. Leary R, Saghi Z, Midgley PA, Holland DJ. Compressed sensing electron tomography. Ultramicroscopy. 2013;131:70–91.
222. Albrecht W, Bals S. Fast electron tomography for nanomaterials. J Phys Chem C. 2020;124:27276–86.
223. Reznikov N, Buss DJ, Provencher B, McKee MD, Piché N. Deep learning for 3D imaging and image analysis in biomineralization research. J Struct Biol. 2020;212:107598.
224. Karlsson J, Harmankaya N, Allard S, Palmquist A, Halvarsson M, Tengvall P, et al. Ex vivo alendronate localization at the mesoporous titania implant/bone interface. J Mater Sci Mater Med. 2015;26:11.
225. Kelly DF, DiCecco LA, Jonaid GM, Dearnaley WJ, Spilman MS, Gray JL, et al. Liquid-EM goes viral – Visualizing structure and dynamics. Curr Opin Struct Biol. 2022;75:102426.

Paper I

Bone 172 (2023) 116747

Contents lists available at ScienceDirect

Bone

journal homepage: www.elsevier.com/locate/bone

Full length article

Bone structure and composition in a hyperglycemic, obese, and leptin receptor-deficient rat: Microscale characterization of femur and calvarium

Chiara Micheletti [a,b], Martina Jolic [b], Kathryn Grandfield [a,c,d], Furqan A. Shah [b], Anders Palmquist [b,*]

[a] Department of Materials Science and Engineering, McMaster University, Hamilton, ON, Canada
[b] Department of Biomaterials, Sahlgrenska Academy, University of Gothenburg, Gothenburg, Sweden
[c] School of Biomedical Engineering, McMaster University, Hamilton, ON, Canada
[d] Brockhouse Institute for Materials Research, McMaster University, Hamilton, ON, Canada

ARTICLE INFO

Keywords:
Leptin
Bone
Diabetes
Micro-CT
Raman spectroscopy
Electron microscopy

ABSTRACT

Metabolic abnormalities, such as diabetes mellitus and obesity, can impact bone quantity and/or bone quality. In this work, we characterize bone material properties, in terms of structure and composition, in a novel rat model with congenic leptin receptor (LepR) deficiency, severe obesity, and hyperglycemia (type 2 diabetes-like condition). Femurs and calvaria (parietal region) from 20-week-old male rats are examined to probe bones formed both by endochondral and intramembranous ossification. Compared to the healthy controls, the LepR-deficient animals display significant alterations in femur microarchitecture and in calvarium morphology when analyzed by micro-computed X-ray tomography (micro-CT). In particular, shorter femurs with reduced bone volume, combined with thinner parietal bones and shorter sagittal suture, point towards a delay in the skeletal development of the LepR-deficient rodents. On the other hand, LepR-deficient animals and healthy controls display analogous bone matrix composition, which is assessed in terms of tissue mineral density by micro-CT, degree of mineralization by quantitative backscattered electron imaging, and various metrics extrapolated from Raman hyperspectral images. Some specific microstructural features, i.e., mineralized cartilage islands in the femurs and hyper-mineralized areas in the parietal bones, also show comparable distribution and characteristics in both groups. Overall, the altered bone microarchitecture in the LepR-deficient animals indicates compromised bone quality, despite the normal bone matrix composition. The delayed development is also consistent with observations in humans with congenic Lep/LepR deficiency, making this animal model a suitable candidate for translational research.

1. Introduction

Skeletal development generally proceeds via either endochondral or intramembranous ossification [1–3]. The primary difference between these two main ossification mechanisms is whether bone formation is preceded by a cartilaginous intermediate, as in endochondral ossification, or not, as in intramembranous ossification where tissue is laid down directly as bone. Bones serve essential functions to provide the structural framework for the body, protect internal organs, assist locomotion, maintain mineral homeostasis, and support blood cell production [1]. Bone tissue is also an exquisite material, at the same time tough and strong thanks to the hierarchical organization of its components [4].

Bone strength, and in turn its mechanical and biological functioning, relies not only on bone mineral density (BMD), a metric related to bone mass, i.e., bone *quantity*, but also on bone *quality*, defined as the "totality of features and characteristics that influence a bone's ability to resist fracture" [5], encompassing its material properties (structure and composition). Aging and disease can compromise bone quantity and/or quality, leading to an increased fracture risk [6,7]. For example, metabolic changes induced by type 2 diabetes mellitus (T2DM) and often concurrent obesity also affect bone metabolism and remodeling [8–10]. As a consequence, despite normal or even higher BMD than in the healthy population, diabetic subjects have an increased fracture risk as a result of poor bone quality [11,12].

Different mechanisms have been proposed to explain the altered bone quality in T2DM and obesity. Bone fragility in diabetic subjects has

* Corresponding author.
E-mail address: anders.palmquist@biomaterials.gu.se (A. Palmquist).

https://doi.org/10.1016/j.bone.2023.116747
Received 16 January 2023; Received in revised form 3 March 2023; Accepted 21 March 2023
Available online 5 April 2023

often been correlated with the accumulation of advanced glycation end-products (AGEs), both crosslinked, such as pentosidine (PEN), and non-crosslinked, such as carboxymethyl lysine (CML) [13]. Non-enzymatic crosslinking induced by AGEs such as PEN has been associated with an increased brittleness of collagen fibers, likely causing loss in bone strength [14]. It also appears that fat accumulation in hyperglycemic conditions and obesity promotes the differentiation of mesenchymal stem cells in adipocytes rather than osteoblasts, in turn favouring adipogenesis over osteoblastogenesis [10,11]. While the effect of T2DM on osteoclasts remains unclear, osteoclastic activity could be overall stimulated through the RANKL/RANK/OPG pathway due to the increased production of inflammatory cytokines [15].

Animal models to study T2DM are often diet-induced or monogenic/polygenic models of obesity. Monogenic models are mostly based on mutations of the gene encoding leptin (Lep) or of the leptin receptor (LepR) [16]. Leptin, a cytokine-like hormone mainly produced by adipocytes, plays an important role in regulating energy storage and appetite [17]. Several studies have documented that mutations in Lep and LepR impacts bone metabolism, but the underlying mechanisms are still unclear, and contrasting outcomes in terms of bone mass have been observed [18]. Leptin is mediated both by the central nervous system and the sympathetic nervous system, hence skeletal changes are due to the overall balance between central and peripheral mechanisms of action [18]. Leptin has also direct effects on bone cells, as they have a leptin receptor [19]. Reduced bone length and/or mass have been commonly reported in the appendicular skeleton [20–22], while an increased trabecular bone volume is often observed in the spine of Lep/LepR-deficient rodents [23,24]. While some investigators have postulated that leptin is bone anabolic through the peripheral pathway, but catabolic through the central one [25], others have found that central (intracerebroventricular) administration of leptin promotes bone growth [26].

There exist concerns on the translation of Lep/LepR-deficient animal models to diabetes research in humans due to the dissimilar disease etiology [27]. However, it is worth pointing out that congenic Lep/LepR deficiency has been reported, although rarely, also in humans, where it manifests with severe obesity already during childhood [28–31]. The rarity of this condition has impacted bone research in Lep/LepR-deficient human subjects. A clear bone phenotype has not been identified yet, and systemic leptin administration leads to both unchanged and increased BMD in the few studies available [18].

In this work, we examine bone structure and composition in a congenic LepR-deficient rat, the Lund MetS (metabolic syndrome) rat, that displays obesity and hyperglycemia, as well as micro- and macrovascular changes typical of diabetes [32–34]. To our knowledge, this is the first study evaluating the skeleton of this rodent as a potential candidate animal model for LepR deficiency and T2DM-like conditions in bone research. Multiscale characterization was performed on bone tissue from the femur and calvarium (parietal bones and sagittal suture) to probe formation by endochondral and intramembranous ossification, respectively. Bone morphology and microarchitecture were investigated with micro-computed X-ray tomography (micro-CT) and scanning electron microscopy (SEM). Bone mineralization was evaluated as tissue mineral density (TMD) by micro-CT and as BMD distribution (BMDD) by quantitative backscattered electron imaging (qBEI). Bone matrix composition, in terms of degree of mineralization, carbonate substitution, and mineral crystallinity/maturity, was assessed by Raman hyperspectral imaging. Mechanical properties of the femurs were measured by reference point indentation (RPI). Our analyses also probed site-specific microstructural features, including mineralized cartilage islands in the femurs and bands of increased mineral content in the calvaria.

2. Materials and methods

2.1. Animal study, sample retrieval and preparation

Two variants of the male Lund MetS rat, a congenic (Cg) rat with a LepR mutation introduced on a BioBreeding Diabetes Resistant Rat (BBDR) [32], were obtained from Janvier Labs (France) [35]: i) BBDR.Cg-LepR$^{+/+}$ (abbreviated to LepR$^{+/+}$ hereinafter), lean and with normal insulin sensitivity (euglycemia) ($n = 10$); ii) BBDR.Cg-LepR$^{-/-}$ (abbreviated to LepR$^{-/-}$ hereinafter), LepR-deficient, severely obese and with insulin resistance (hyperglycemia) ($n = 11$). The study was approved by the Animal Research Ethics Committee of Gothenburg (Dnr. 14790/2019). At both 16 and 20 weeks of age, LepR$^{-/-}$ animals had a greater weight and blood glucose level than LepR$^{+/+}$ animals ($p < 0.001$) (Tables 1, S1). High blood glucose in the LepR$^{-/-}$ group confirms their hyperglycemic condition (Tables 1, S1). At 20 weeks of age, animals were sacrificed. Their femurs (left and right) and calvaria were retrieved and fixed in 10% neutral buffered formalin. Femur length was measured with a caliper. Micro-CT was performed on unembedded samples, while SEM and micro-Raman spectroscopy were carried out post-resin embedding, as described below.

Femurs. After micro-CT, right femurs were sectioned transversally (with respect to the long axis of the femur) to separate the femur head from the distal to mid-diaphysis portion. The distal to mid-diaphysis portions were sectioned longitudinally (with respect to the long axis of the femur), dehydrated in ethanol and resin embedded (LR White, London Resin Co. Ltd., UK). After embedding, samples were polished with SiC paper (800, 1200, 2000, and 4000 grit; ISO grit designation). Only the half towards the medial side was considered for qBEI and micro-Raman spectroscopy.

Calvaria. After micro-CT, calvaria were dehydrated in ethanol, resin embedded (LR White, London Resin Co. Ltd., UK), and cross-sectioned along the coronal plane in the parietal bone region, approximately at one third of the length of the sagittal suture towards the frontal bone side. Samples were polished with SiC paper (800, 1200, 2000, and 4000 grit; ISO grit designation).

2.2. Micro-CT

For both femurs and calvaria, micro-CT data were acquired with a SkyScan 1172 (Bruker, MA, USA), reconstructed in NRecon (Bruker, Billerica, USA), aligned in DataViewer (Bruker, MA, USA), and visualized and analyzed in Dragonfly 2020.2 (Objects Research Systems, QC, Canada). Standards of hydroxyapatite ($\varnothing = 2$ mm) with known density (0.25 and 0.75 g/cm^3) were used to obtain a calibration line to convert the pixel intensity in micro-CT data into TMD (expressed in g/cm^3) [36].

Femurs. Right and left femurs ($n = 8$/group) were scanned with a 70 kV X-ray beam, Al—Cu filter, 180° rotation range, 0.7° step size, 3 frame averaging, and 13.90 μm pixel size. Morphometry metrics were measured in three dimensions (3D) using the "Bone Analysis" plug-in in Dragonfly 2020.2 (Objects Research Systems, QC, Canada), segmenting trabecular and cortical bone with the Buie algorithm (input guess for trabecular thickness = 125 μm) [37]. For trabecular bone, morphometry parameters (bone volume fraction, BV/TV; trabecular thickness, Tb.Th;

Table 1
Values of weight and blood glucose measured at 16 and 20 weeks of age.

Group	Weight at 16 weeks [g]	Weight at 20 weeks [g]	Blood glucose at 16 weeks [mmol/l]	Blood glucose at 20 weeks [mmol/l]
LepR$^{+/+}$	381 ± 27	422 ± 21	9.7 ± 1.0	9.4 ± 1.5
LepR$^{-/-}$	553 ± 41***	598 ± 48***	24.1 ± 6.6***	24.9 ± 5.0***

*** Denotes statistical significance with respect to the control group ($p < 0.001$).

trabecular separation, Tb.Sp) were evaluated in the distal femur metaphysis, selecting a region with a height equal to 5% of the average femur length in each group (i.e., 1.946 and 1.723 mm in $LepR^{+/+}$ and $LepR^{-/-}$, respectively), at a consistent distance from the growth plate (Fig. S1). Trabecular number (Tb.N) was computed as the reciprocal of the sum of Tb.Th and Tb.Sp (following the guidelines of Skyscan CT-analyser). For cortical bone, morphometry parameters (cortical thickness, Ct.Th; cortical bone area, Ct.Ar; total cross-sectional area inside the periosteal envelope, Tt.Ar; cortical area fraction, Ct.Ar/Tt.Ar) were measured in the femur diaphysis, selecting a region with a height equal to 5% of the average femur length in each group (i.e., with the same height as the region used for trabecular bone analysis) at a consistent distance from the growth plate (Fig. S1). The proximal portion of right and left femurs ($n = 8$/group) was scanned with a 70 kV X-ray beam, Al—Cu filter, 180° rotation range, 0.7° step size, 3 frame averaging, and 26.72 μm pixel size. Morphology of the femoral head and neck was evaluated qualitatively in Dragonfly 2020.2 (Objects Research Systems, QC, Canada).

Calvaria. Calvaria ($n = 8$/group) were scanned with a 49 kV X-ray beam, Al filter, 360° rotation range, 0.7° step size, 5 frame averaging, and 17.90 μm pixel size. Parietal bone thickness was evaluated in a region 285 × 335 px^2 in the axial plane (xy plane), centred at mid-length of the sagittal suture and encompassing the entire calvaria thickness (z direction). In this region, parietal bones were separated from non-bone regions by Otsu thresholding. The sagittal suture was examined using the same region used to examine the parietal bones, but limiting the analyses to 25 px-thick region approximately centred in the mid-point of the calvaria thickness. In this region, the sagittal suture was segmented by Otsu thresholding, followed by a "Process island" operation to remove noise, and manual refinement to remove mis-labelled regions. Parietal bone thickness and sagittal suture width were measured with the "Volume thickness map" operation, taking the average value in the distribution of thickness measurements. Variation in suture length (in the xy plane) along the calvaria thickness (z direction) was evaluated with the "Slice analysis" module by computing the perimeter ($2p$) and thickness (t) of the ROI corresponding to the segmented suture in each xy slice, and estimating the length (l) by subtracting the thickness from the semi-perimeter ($l = p - t$).

2.3. SEM and qBEI

Embedded samples were imaged in backscattered electron (BSE) mode in a Quanta 200 environmental SEM (FEI Company, The Netherlands) operated at 20 kV in low vacuum mode (1 Torr water vapour pressure), with a working distance of 10 mm. For qBEI analyses ($n = 3$/group), image calibration and acquisition were completed following published protocols [38], using a custom-made standard of pure C and pure Al. Briefly, for each imaging session (i.e., for each sample), standard and sample were loaded in the instrument at the same time. Brightness and contrast in BSE-SEM images were adjusted to have an average grey-level of 25 and 225 in the C and Al regions of the standard, respectively [38]. After this calibration, BSE-SEM images of the sample were acquired in a mosaic fashion, and combined into an overview image manually in Photoshop (Adobe, CA, USA) without altering their grey-levels. The overview mosaic images were processed in Python 3.8.10 to convert grey-levels into wt% Ca content. Regions of bone and resin were separated by Otsu thresholding using the "threshold_otsu" module in the "skimage.filters" library. The x-axis of the greyscale histogram of the bone region (upper range of Otsu thresholding) was converted in wt% Ca using pure hydroxyapatite (39.86 wt% Ca) [38] and the C standard [39] as reference points for 39.86 wt% Ca and 0.17 wt% Ca, respectively. The grey-level of these two reference points was computed from the grey-level/atomic number (Z) calibration line [38], obtained by averaging the mean grey-level in the C (Z = 6) and Al (Z = 12) regions for each imaging session. Following established protocols [38], BMDD was evaluated in terms of weighted mean Ca concentration (Ca-Mean), peak height of the distribution (MaxFreq), peak position of the most frequent Ca concentration (Ca-MaxFreq), full-width half maximum (FWHM), spread of the distribution on the low concentration side (SpLow), and spread of the distribution on the high concentration side (SpHigh). Frequency values below 0.001% were excluded from BMDD analysis. FWHM was obtained using the "find_peaks" and "peak_widths" functions in the "scipy.signal" library. SpLow and SpHigh were evaluated by comparing the acquired histogram to an equivalent-area Gaussian curve [38], computing their integral areas with the composite trapezoidal rule using the "numpy.trapz" function. Lastly, the range 10–30 wt% Ca was divided in bins with a width equal to 5 wt% Ca, and the number of pixels in each bin was counted and normalized by the total number of pixels in the 10–30 wt% Ca range.

2.4. Micro-Raman spectroscopy

Micro-Raman spectroscopy was performed in a Renishaw inVia Qontor (Renishaw PLC, UK) equipped with a 633 nm laser and LiveTrack focus-tracking technology. The laser was focused on the surface using a × 100 (0.9 NA) objective. Raman signal was collected using a Peltier cooled CCD deep depletion NIR enhanced detector behind a 1800 g mm^{-1} grating (1.0 ± 0.15 cm^{-1} step size). Spectra were baseline subtracted (intelligent spline fitting with 10 nodes and 1.3 noise level), cleaned of cosmic rays, and denoised by Principal Component Analysis (PCA) with a component auto-correlation limit of 0.7 (default value) in Renishaw WiRE 5.4 (Renishaw PLC, UK). Spectra were analyzed in Python 3.8.10. The following Raman peaks were considered [40]: phosphate (PO_4^3) ν_1 (~930–980 cm^{-1}) and ν_2 (~410–460 cm^{-1}); amide III (~1215–1300 cm^{-1}); carbonate (CO_3^2) (~1050–1100 cm^{-1}); phenylalanine (Phe) (~1000–1005 cm^{-1}). Mineral-to-matrix ratio was obtained from the ratio $\nu_2PO_4^3$/amide III [40] and the ratio $\nu_1PO_4^3$/Phe [41]. Carbonate-to-phosphate ratio was obtained from the ratio CO_3^2 / $\nu_2PO_4^3$ [40]. For all these ratios, integral peak areas were computed with the composite trapezoidal rule using the "numpy.trapz" function. Mineral crystallinity was evaluated as the reciprocal of the FWHM of the $\nu_1PO_4^3$ peak [42], which was computed using the "find_peaks" and "peak_widths" functions in the "scipy.signal" library, after Voigt-fitting of the $\nu_1PO_4^3$ peak using the "curve_fit" function in the "scipy.optimize" library.

2.4.1. Femurs

Maps were acquired with a pixel size of 10 μm, 1 s exposure, and 2 accumulations in both cortical and trabecular bone in 65 × 95 px^2 and 70 × 60 px^2 areas, respectively ($n = 3$/group). When analyzing these maps, resin regions were excluded by setting a threshold at 40% of the $\nu_1PO_4^3$ peak intensity. High-resolution maps with a pixel size of 1 μm were acquired with 1 s exposure and 2 accumulations in specific 50 × 100 μm^2 ROIs in both cortical and trabecular femoral bone, specifically on areas containing bone-mineralized cartilage interfaces ($n = 3$/group). Areas of bone and mineralized cartilage in the Raman maps of the $\nu_1PO_4^3$ peak intensity were segmented using the "Kmeans" function in the "sklearn.cluster" library (4 clusters) in Python 3.8.10. Only data points in the 5% to 95% quantiles of the $\nu_1PO_4^3$ peak intensity were considered for segmentation and analysis.

2.4.2. Calvaria

Maps were acquired with a pixel size of 10 μm, 1 s exposure, and 2 accumulations in 80–90 × 70–85 px^2 areas in the parietal bone in proximity to the sagittal suture ($n = 3$/group). When analyzing these maps, resin regions were excluded by setting a threshold at 25% of the $\nu_1PO_4^3$ peak intensity. High-resolution maps with a pixel size of 1 μm were acquired with 1 s exposure and 2 accumulations in specific 50 × 100 μm^2 ROIs in areas containing bone interfacing with hyper-mineralized bone ($n = 3$/group). Areas of bone and hyper-mineralized bone in the Raman maps of the $\nu_1PO_4^3$ peak intensity were segmented using the "Kmeans" function in the "sklearn.cluster" library (5 clusters) in Python 3.8.10. Only data points in the 5% to 95% quantiles of the

$\nu_1 PO_4^3$ peak intensity were considered for segmentation and analysis.

2.5. RPI

Mechanical properties were evaluated ex vivo by RPI using a BioDent microindenter (Active Life Scientific, CA, USA) in right and left proximal femurs (n = 6/group). Three measurements were acquired in each sample by applying an indentation force of 4 N at a frequency of 2 Hz in 10 cycles using a 90° cono-spherical (≤ 5 μm radius point) test probe and a flat bevel reference probe. The following parameters were assessed: 1st cycle indentation distance (ID 1st); 1st cycle unloading slope (US 1st); 1st cycle creep indentation distance (CID 1st); total indentation distance (TID); indentation distance increase (IDI); average creep indentation distance (Avg CID); average energy dissipated (Avg ED); and average unloading slope (Avg US).

2.6. Statistical analysis

Statistical significance of micro-CT data was evaluated with the Student's t-test ($\alpha = 0.05$), after verifying normality with the Shapiro-Wilk test ($\alpha = 0.05$) and homoscedasticity with the Brown-Forsythe test ($\alpha = 0.05$). In case of homoscedasticity violation, the unequal variance correction was applied to the Student's t-test, i.e., a Welch's t-test was performed instead ($\alpha = 0.05$). Statistical significance of qBEI, micro-Raman spectroscopy, and RPI data was evaluated with the Mann-Whitney U test ($\alpha = 0.05$). Statistical analysis was completed in Python 3.8.10 using the "scipy.stats" library. Data are reported as mean ± standard deviation.

3. Results

3.1. Femurs

3.1.1. Structure

3D reconstructions of micro-CT scans revealed that LepR$^{-/-}$ animals presented not fully developed femoral head and neck (Figs. 1A, S2), as well as overall shorter femurs (caliper measurements) ($p < 0.001$) (Fig. 1B, Table S2). In the trabecular space, LepR$^{-/-}$ animals had thinner trabeculae (Tb.Th), although not significantly with respect to LepR$^{+/+}$ animals ($p > 0.05$), as well as lower BV/TV ($p < 0.01$), higher Tb.Sp ($p < 0.01$), and reduced Tb.N ($p < 0.05$) (Fig. 1C, Table S2). In the cortical region, the LepR$^{-/-}$ group displayed significantly smaller values of Ct.Ar, Tt.Ar, Ct.Ar/Tt.Ar, and Ct.Th ($p < 0.001$ for Ct.Ar, Tt.Ar, and Ct.Th; $p < 0.01$ for Ct.Ar/Tt.Ar) (Fig. 1C, Table S2).

3.1.2. Composition

LepR$^{+/+}$ and LepR$^{-/-}$ animals did not display statistically significant differences in TMD measured in micro-CT data in neither cortical (Ct.TMD) nor trabecular (Tb.TMD) bone ($p > 0.05$) (Table S2). Comparable composition between animal groups was also confirmed by qBEI, as there were no significant differences in any of the metrics evaluated (Ca-Mean, FWHM, MaxFreq, Ca-MaxFreq, SpLow, SpHigh) ($p > 0.05$) (Figs. 2A-B, S3, Table S3). Similarly, the number of pixels in different 5 wt% Ca-wide bins was analogous in the two groups ($p > 0.05$) (Table S4). Raman maps with 10 μm pixel size confirmed the presence of regions with higher mineral content throughout the bone matrix noted in BSE-SEM and qBEI images in both cortical and trabecular bone (Figs. 2C, S4). LepR$^{-/-}$ and LepR$^{+/+}$ animals had statistically comparable mineral-to-matrix ratio, carbonate-to-phosphate ratio, and mineral crystallinity in both cortical and trabecular bone ($p > 0.05$) (Figs. 2C, S5, Table S5),

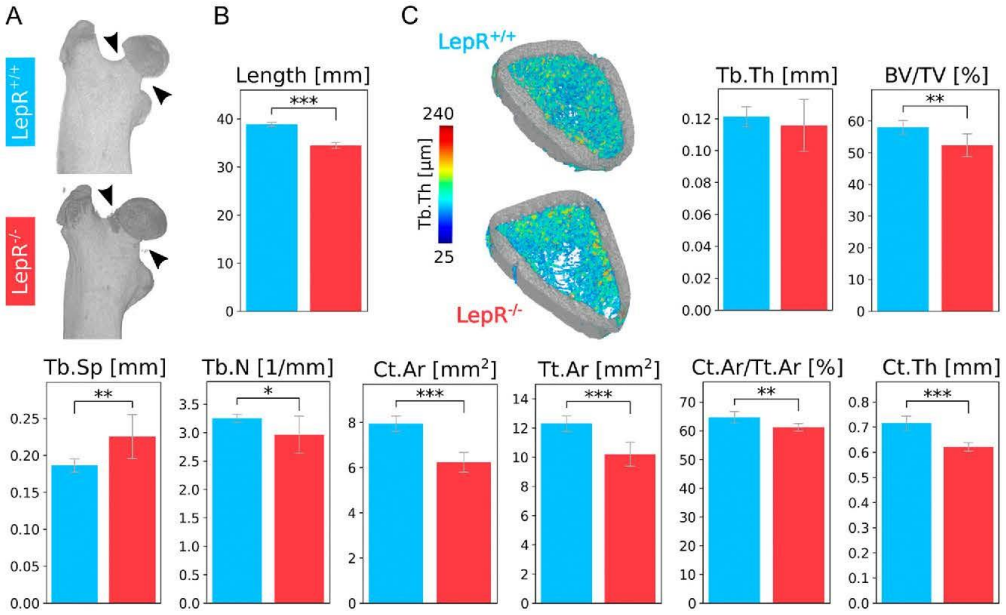

Fig. 1. Femur structure. A) 3D reconstruction of micro-CT scans of representative femur heads. Under-developed head and neck can be noted in the femur of LepR$^{-/-}$ animals (arrowheads). B) Bar plot of femur length obtained by caliper measurements, showing that the LepR$^{-/-}$ group (red bar) has significantly shorter femurs than LepR$^{+/+}$ animals (blue bar). C) 3D reconstruction of a representative femur section with volume thickness map of Tb.Th, and bar plots of morphometry parameters obtained from micro-CT scans. *, **, and *** in the bar plots denote statistical significance ($p < 0.05$, $p < 0.01$, and $p < 0.001$, respectively). (For interpretation of the references to colour in this figure legend, the reader is referred to the web version of this article.)

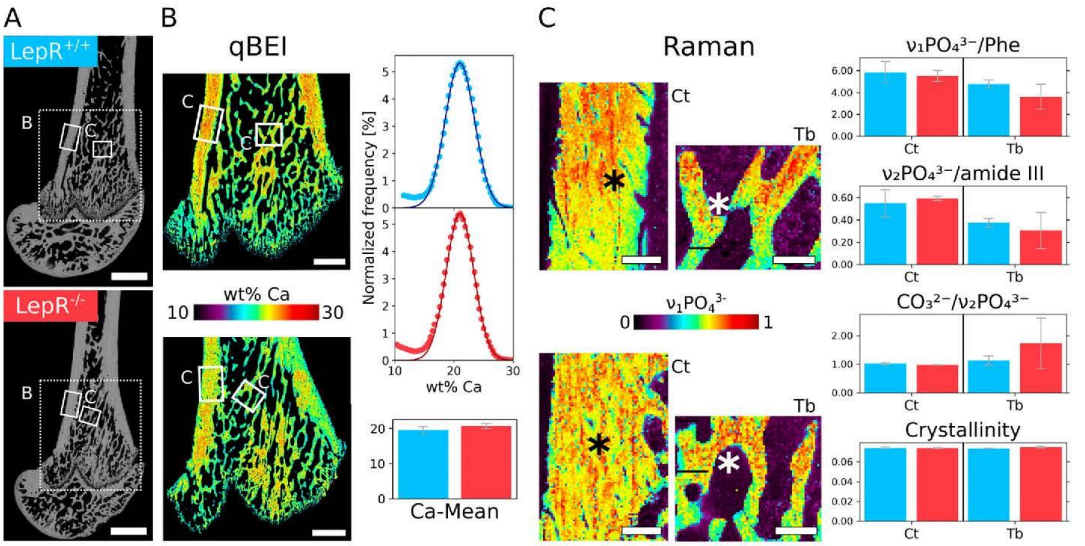

Fig. 2. Femur composition. A) Overview BSE-SEM image of longitudinal sections of a representative femur of LepR$^{+/+}$ (colour-coded in blue) and LepR$^{-/-}$ animals (colour-coded in red), with marked areas indicating the regions where qBEI (dotted border, B) and Raman (solid border, C) analyses were completed. B) qBEI images where pixel intensity corresponds to mineral concentration, expressed as wt% Ca, with corresponding histograms (dots represent the histogram of the acquired data, and continuous line corresponds to the area-equivalent Gaussian curve) and bar plot for Ca-Mean. C) Raman maps (10 μm pixel size) of the $\nu_1PO_4^{3-}$ peak intensity (normalized by the maximum value registered in the map), and bar plots summarizing the values of mineral-to-matrix ratio ($\nu_2PO_4^{3-}$/amide III; $\nu_1PO_4^{3-}$/Phe), carbonate-to-phosphate ratio ($CO_3^{2-}/\nu_2PO_4^{3-}$), and mineral crystallinity (1/FWHM) measured in the maps. In the qBEI images and Raman maps, more mineralized regions (orange-to-red) can be noted throughout the bone matrix in both cortical and trabecular bone. Some of these regions (* in the Raman maps) were examined at higher resolution (1 μm pixel size Raman maps, see Fig. 3). Scale bars are 2 mm in A, 1 mm in B, and 200 μm in C. (For interpretation of the references to colour in this figure legend, the reader is referred to the web version of this article.)

confirming TMD and qBEI observations. Although values of mineral-to-matrix ratio were higher in the LepR$^{+/+}$ animals in both femoral cortical and trabecular bone (with the exception of the ratio $\nu_2PO_4^3$ /amide III in cortical bone), differences failed to reach statistical significance. No statistically significant differences in these metrics were found also when considering high-resolution Raman maps (1 μm pixel size) ($p > 0.05$) (Tables S6, S7).

3.1.3. Notable microstructural features

In BSE-SEM images, areas without osteocytes and with higher contrast than the surrounding bone matrix were observed in both cortical and trabecular regions (Fig. 3A-D). These areas are believed to correspond to islands of mineralized cartilage. High-resolution Raman maps (1 μm pixel size) of the regions where bone interfaces with mineralized cartilage islands confirmed the higher mineral content (i.e., mineral-to-matrix ratio) of mineralized cartilage compared to bone (Figs. 3E-H, S6), although the difference was not statistically significant in either group, both in cortical and trabecular regions ($p > 0.05$). Analogously, carbonate-to-phosphate ratio was higher in the mineralized cartilage islands than in bone in both groups, but not significantly ($p > 0.05$). Values of mineral crystallinity (1/FWHM) were very similar in mineralized cartilage islands and bone ($p > 0.05$) (Figs. 3I-J, S7, Tables S6, S7).

3.1.4. Mechanical properties

Mechanical properties evaluated by RPI revealed no statistically significant differences for any of the metrics assessed (Tables 2, S8).

3.2. Calvaria

3.2.1. Structure

The LepR$^{-/-}$ group displayed significantly thinner parietal bones ($p < 0.001$) than the LepR$^{+/+}$ group (Fig. 4A, Table S9). Sagittal suture was significantly narrower and shorter in the LepR$^{-/-}$ animals ($p < 0.001$ for width; $p < 0.01$ for length) (Fig. 4B, Table S9). In both groups, the suture length increased across the calvaria thickness in the direction from the dura mater side towards the cranium exterior (Fig. 4C).

3.2.2. Composition

LepR$^{+/+}$ and LepR$^{-/-}$ animals did not display statistically significant differences in TMD measured in micro-CT scans ($p > 0.05$) (Table S9). Similarly, qBEI showed no significant difference between LepR$^{-/-}$ and LepR$^{+/+}$ groups for any of the metrics evaluated (Ca-Mean, FWHM, MaxFreq, Ca-MaxFreq, SpLow, SpHigh) ($p > 0.05$) (Figs. 5A, S8, Table S10). Similarly, no differences in the number of pixels in the 5 wt% Ca-wide bins were observed between groups ($p > 0.05$) (Table S11). LepR$^{-/-}$ and LepR$^{+/+}$ animals also had comparable mineral-to-collagen ratio, carbonate-to-phosphate ratio, and mineral crystallinity in the parietal region, as evaluated from 10 μm pixel size Raman maps ($p > 0.05$) (Figs. 5B, S9, S10, Table S12). No statistically significant differences in these metrics were found also when considering high-resolution Raman maps (1 μm pixel size) ($p > 0.05$) (Table S13).

3.2.3. Notable microstructural features

Areas with an increased mineral content, approximately centrally-located in the parietal bones cross-sections, as well as close to the sagittal suture, were noted in BSE-SEM images, where contrast is composition-based, as well as in qBEI and Raman maps with 10 μm pixel size. These areas, herein labelled as hyper-mineralized bone, were better

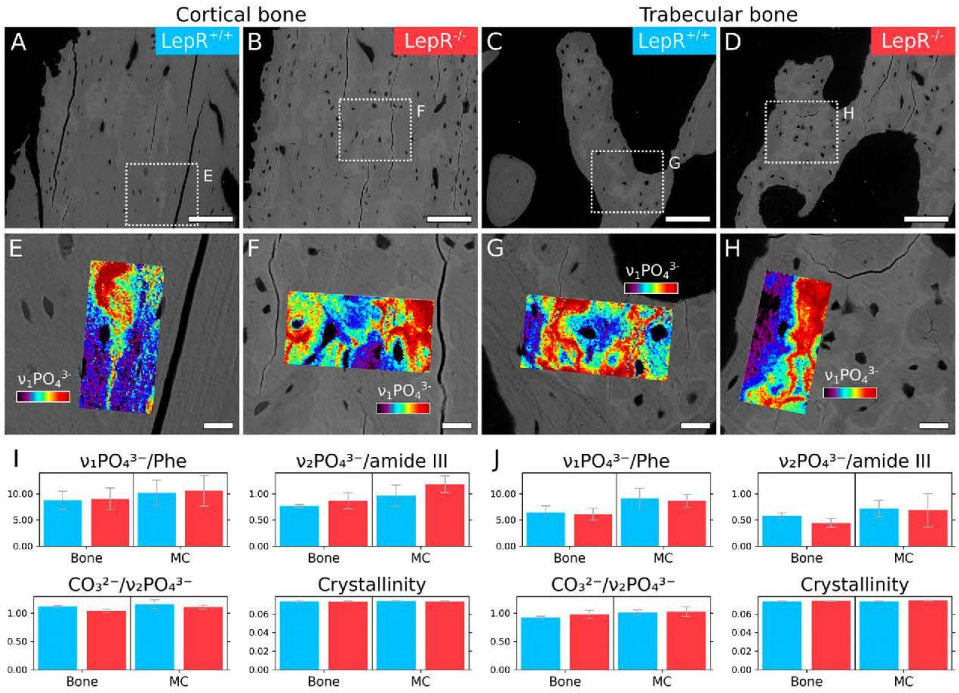

Fig. 3. Mineralized cartilage islands. A-D) Representative BSE-SEM image where mineralized cartilage islands can be distinguished as the lighter grey regions within bone matrix (dark grey) in both cortical (A, B) and trabecular bone (C, D) in both LepR$^{+/+}$ (A, C) and LepR$^{-/-}$ (B, D) animals. E-H) Higher magnification BSE-SEM images (corresponding to A-D, respectively) with superimposed Raman maps (1 μm pixel size) of the $\nu_1PO_4^{2-}$ peak intensity (restricted to 5–95% quantile range). I-J) Bar plots summarizing the values of mineral-to-matrix ratio ($\nu_2PO_4^{2-}$/amide III; $\nu_1PO_4^{2-}$/Phe), carbonate-to-phosphate ratio ($CO_3^{2-}/\nu_2PO_4^{2-}$), and mineral crystallinity (1/FWHM) measured in bone and mineralized cartilage (MC) in the Raman maps acquired in cortical and trabecular bone, respectively. Scale bars are 100 μm in A-D, and 20 μm in E-H.

Table 2
RPI measurements in the proximal femurs.

Parameter	LepR$^{+/+}$	LepR$^{-/-}$
IDI 1st [μm]	42.0 ± 4.2	40.8 ± 4.2
US 1st [N/μm]	0.334 ± 0.040	0.334 ± 0.041
CID 1st [μm]	3.94 ± 0.39	3.78 ± 0.66
TID [μm]	45.0 ± 4.4	43.7 ± 4.3
IDI [μm]	6.11 ± 0.41	5.99 ± 0.36
Avg CID [μm]	1.39 ± 0.27	1.26 ± 0.17
Avg ED [μJ]	9.6 ± 1.1	10.1 ± 1.2
Avg US [N/μm]	0.352 ± 0.047	0.353 ± 0.045

examined in high-resolution Raman maps (1 μm pixel size) (Figs. 6A-D, S11), which confirmed the higher mineral content (mineral-to-matrix ratio) of hyper-mineralized bone compared to bone, although the difference was not statistically significant in either group ($p > 0.05$). Similarly, carbonate-to-phosphate ratio was higher in hyper-mineralized bone than bone in both groups, but not significantly ($p > 0.05$). No differences in mineral crystallinity in hyper-mineralized bone and bone were noted ($p > 0.05$) (Figs. 6E, S12, Table S13).

4. Discussion

We examined the structure and composition of the femur and the calvarium (parietal region) as examples of bones formed by endochondral and intramembranous ossification, respectively, in a novel rodent model with congenic LepR deficiency, the Lund MetS rat [32,35]. Analogously to what has been reported in humans with LepR deficiency [29–31], the LepR$^{-/-}$ rats displayed severe early-onset obesity, with a greater weight than the LepR$^{+/+}$ animals (Table 1). Additionally, elevated blood glucose levels confirmed hyperglycemia (Table 1), pointing towards the co-presence of a diabetic (type 2) condition.

One of the most widespread rat models for obesity-induced T2DM is the LepR-deficient Zucker fatty (fa/fa) rat, together with its sub-strain Zucker diabetic fatty (ZDF) rat [27]. Zucker fatty rats develop obesity at 4 weeks of age [16], similarly to the Lund MetS LepR$^{-/-}$ rats used herein, which are severely obese at 30 days of age [35]. ZDF rats have increased diabetic features than Zucker fatty rats, with overt diabetes at 8–10 weeks of age, but less obesity [16]. On the other hand, Lund MetS LepR$^{-/-}$ male rats are both severely obese and develop diabetes by 145 days of age [35]. Therefore, this rat model can be a promising alternative to combine obese and diabetic characteristics. Moreover, it closely resembles traits of the metabolic syndrome in humans [35], together with diabetes-related vascular complications [32–34].

4.1. Structure

Micro-CT of femurs revealed an abnormal microarchitecture in LepR$^{-/-}$ animals in both cortical and trabecular bone, with reduced cortical and trabecular thickness, lower cortical area, and lower bone mass in the trabecular compartment, given the lower BV/TV and Tb.N, and the increased Tb.Sp. The femurs were also nearly 5 mm shorter in the LepR$^{-/-}$ group. These findings are consistent with the skeletal

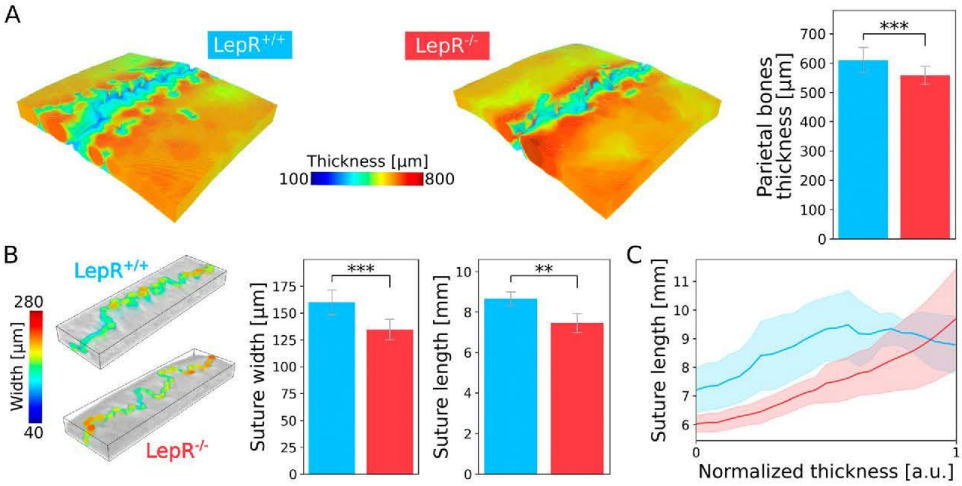

Fig. 4. Calvarium structure. A) Volume thickness map of parietal bones and relative bar plot, showing that the LepR$^{-/-}$ animals (red bar) have significantly thinner parietal bones than the LepR$^{+/+}$ animals (blue bar). B) 3D reconstruction of a representative section of parietal bones with the volume thickness map of the sagittal suture width, and bar plots summarizing the width and length of the sagittal suture. C) Variation in suture length along the calvarium thickness in the parietal region (normalized thickness is 0 towards the dura mater side and 1 towards the cranium exterior). The solid line corresponds to the average, while the faded region represents the standard deviation. ** and *** in the bar plots denote statistical significance ($p < 0.01$ and $p < 0.001$, respectively). (For interpretation of the references to colour in this figure legend, the reader is referred to the web version of this article.)

phenotype commonly identified in other rodent models of either hyperglycemia/T2DM, Lep/LepR deficiency, and obesity. Reduced bone length in femur and tibia [20,43,44] and altered morphological parameters (e.g., lower Ct.Th, Ct.Ar, BV/TV, Tb.Th, Tb.N; higher Tb.Sp) have been reported in both Zucker fatty and ZDF rats [44–46], consistently with what we observed in the LepR$^{-/-}$ animals. Similar results have also been described in the mouse model equivalent to the Zucker fatty rat, the Lep$^{db/db}$ mouse [22], and in a LepR knockout rat developed using CRISPR/Cas9 technology [47]. The greater animal weight in the obese LepR$^{-/-}$ animals also likely plays a role in the dissimilar bone shape and structure, since bone adapts to mechanical loads [48–50]. In particular, increased loading has been associated with reduced body growth and shorter tibia and femur [51]. However, this could be due to LepR deficiency only rather than greater loading due to weight, since leptin-independent regulation of body weight (i.e., the "gravitostat" [52]) has been challenged by studies in micro-gravity [53].

Macroscopically, calvaria were thinner in the parietal region of the LepR$^{-/-}$ rats. In a rat model of streptozotocin (STZ)-induced DM, type 1 DM was also associated with smaller skulls, showing decreased cranial vault length and cranial base length in the neurocranium [54]. The smaller bone size in both calvaria and femurs, which also lacked full development in the femoral head and neck, suggests a delay in skeletal growth. A lower bone formation rate has also been reported in Lep$^{ob/ob}$ and Lep$^{db/db}$ mice compared to age-matched wild type controls [24]. The delayed skeletal growth also appears in agreement with the overall reduced development experienced by Lep/LepR-deficient humans [29–31].

To the best of our knowledge, suture morphology has never been studied in the context of LepR deficiency, diabetes, and obesity. However, sutures play an essential role in the development and morphology of the skull vault, acting as centres of intramembranous bone growth [55,56]. Considering that suture interdigitation increases with age [57], the shorter sagittal suture of the LepR$^{-/-}$ animals further reinforces our hypothesis of delayed skeletal growth. Sutures usually display less interdigitation in the deeper side of the cranium, i.e., towards the dura mater [57]. Our observations on the variation in suture length, which is representative of the degree of interdigitation, along the calvarium thickness confirm this trend. Interestingly, the suture length increases almost linearly across the calvarium thickness in the direction towards the cranium exterior in the LepR$^{-/-}$ group, while it tends to plateau at around one third of the calvarium thickness in the LepR$^{+/+}$ group. This could indicate that, while a sort of equilibrium in the development of suture morphology is reached in the LepR$^{+/+}$ animals, substantial changes are still ongoing in the LepR$^{-/-}$ rodents, given the higher variability in the degree of interdigitation.

The smaller width of the sagittal suture in the LepR$^{-/-}$ animals appears in contrast with the hypothesis of reduced skeletal growth. Although in rodents the sagittal suture remain patent (unfused) throughout their lives [55], the sagittal suture narrows as the parietal bones thickens when the cranial expansion slows down [58,59]. Therefore, as skeletal growth is supposedly delayed in the LepR$^{-/-}$ group, a wider, more patent suture would be expected. A reduction in sutural gap indicates an increased bone apposition at the suture edges operated by the osteoblasts, as bone remodeling has been identified as mechanism controlling suture patency [59]. Fat accumulation in obesity is usually thought to promote adipogenesis at the expense of osteoblastogenesis [10,11,60]. On the other hand, severe obesity appears to mitigate the skeletal changes in Lep$^{ob/ob}$ mice [61]. Lower bone formation rates have often been reported in Lep$^{ob/ob}$ and Lep$^{db/db}$ mice [24,62]. Obesity also appears to stimulate bone resorption thorough the RANK/RANKL pathway in presence of chronic inflammation [15]. Hence, one would expect bone resorption prevailing over bone formation in the LepR$^{-/-}$ group, in turn leaving a wider suture. On the other hand, it is possible that the narrower sagittal suture reflects the lack of expansion of the cranial vault due to the delayed growth, resulting in the two parietal bones remaining closer to each other. Lastly, the width of the sagittal suture could simply be proportioned to the size of the calvaria, which is thinner in the parietal region of LepR$^{-/-}$ animals, as it is known that skull and suture development are strongly linked [56,59]. It is also worth noting that sutures are very complex features to analyze, and, overall, there still is a lack of metrics to capture their complexity in a truly quantitative way [63].

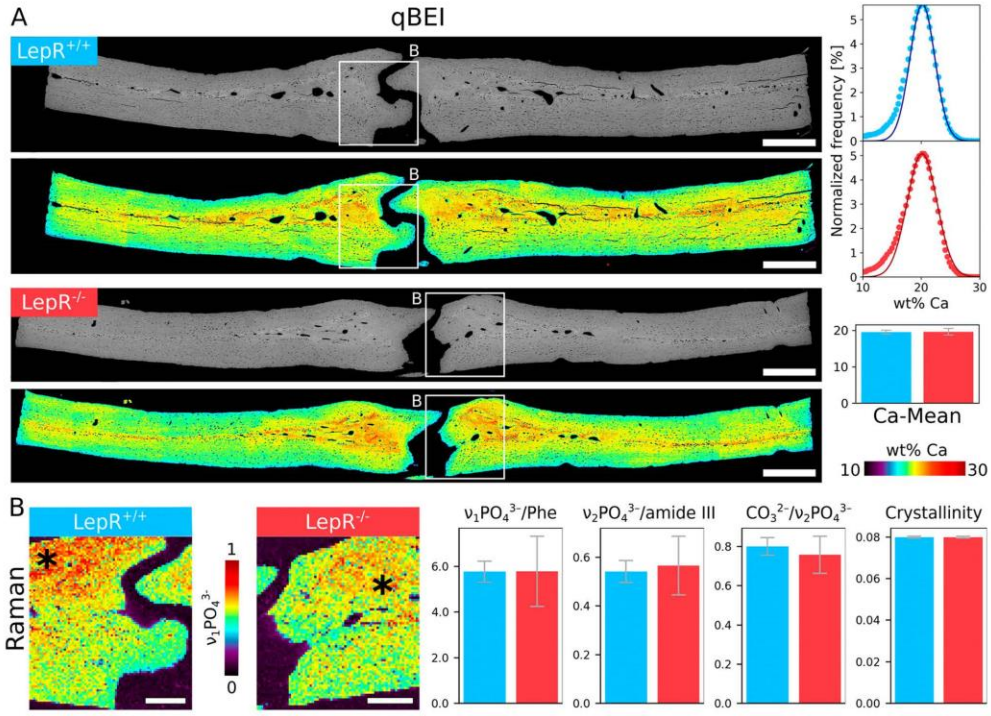

Fig. 5. Calvarium composition. A) Overview BSE-SEM image of cross-sections of representative calvaria (parietal region) of LepR$^{+/+}$ (colour-coded in blue) and LepR$^{-/-}$ animals (colour-coded in red), with corresponding qBEI images where pixel intensity corresponds to mineral concentration, expressed as wt% Ca, histograms (dots represent the histogram of the acquired data, and continuous line corresponds to the area-equivalent Gaussian curve) and bar plot for Ca-Mean. B) Raman maps (10 μm pixel size) of the $\nu_1PO_4^{3-}$ peak intensity (normalized by the maximum value registered in the map), and bar plots summarizing the values of mineral-to-matrix ratio ($\nu_2PO_4^{3-}$/amide III; $\nu_1PO_4^{3-}$/Phe), carbonate-to-phosphate ratio ($CO_3^{2-}/\nu_2PO_4^{3-}$), and mineral crystallinity (1/FWHM) measured in the maps. In the qBEI images and Raman maps, more mineralized regions (orange-to-red) can be noted. Some of these regions (* in the Raman maps) were examined at higher resolution (1 μm pixel size Raman maps, see Fig. 6). Scale bars are 500 μm in A and 200 μm in B. (For interpretation of the references to colour in this figure legend, the reader is referred to the web version of this article.)

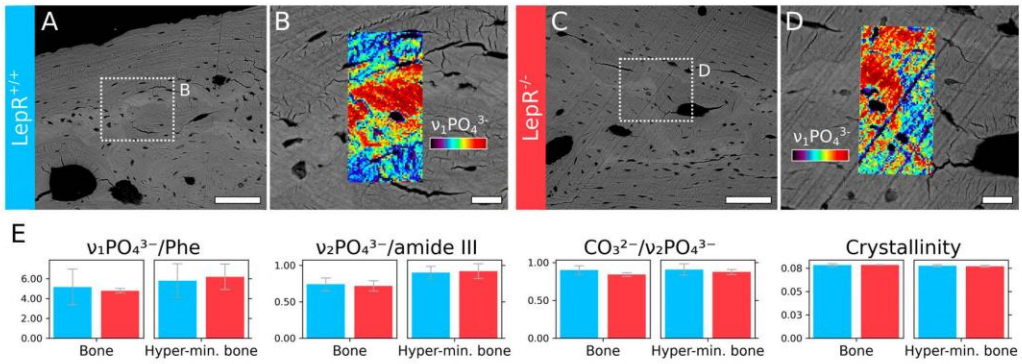

Fig. 6. Hyper-mineralized bone. A) Representative BSE-SEM image where areas of hyper-mineralized bone can be distinguished as the lighter grey regions within bone matrix (dark grey) in a LepR$^{+/+}$ animal. B) Higher magnification BSE-SEM image of the dotted region in A with superimposed Raman map (1 μm pixel size) of the $\nu_1PO_4^{3-}$ peak intensity (restricted to 5–95% quantile range). C) Representative BSE-SEM image where areas of hyper-mineralized bone can be distinguished as the lighter grey regions within bone matrix (dark grey) in a LepR$^{-/-}$ animal. D) Higher magnification BSE-SEM image of the dotted region in C with superimposed Raman map (1 μm pixel size) of the $\nu_1PO_4^{3-}$ peak intensity (restricted to 5–95% quantile range). E) Bar plots summarizing the values of mineral-to-matrix ratio ($\nu_2PO_4^{3-}$/amide III; $\nu_1PO_4^{3-}$/Phe), carbonate-to-phosphate ratio ($CO_3^{2-}/\nu_2PO_4^{3-}$), and mineral crystallinity (1/FWHM) measured in bone and hyper-mineralized (Hyper-min.) bone in the Raman maps. Scale bars are 100 μm in A and C, and 20 μm in B and D.

4.2. Composition and mechanical properties

While microstructure presented substantial alterations in the LepR$^{-/-}$ animals, no significant differences in bone matrix composition were detected in neither femurs nor calvaria. All the different methods to assess composition used in this work confirmed this trend, regardless of the probe used to produce signals (X-rays in micro-CT; electron beam in qBEI; red-light laser in micro-Raman spectroscopy) and the resolution attainable (voxel size of 13.90–17.90 μm in micro-CT; pixel size around 1.3 μm in qBEI; pixel size of 1 μm and 10 μm in micro-Raman spectroscopy).

In a study by Creecy et al., Zucker Diabetic Sprague Dawley (ZDSD) rats displayed no significant differences in Ct.TMD and Tb.TMD in the femur compared to healthy Sprague Dawley rats at different ages (16, 22, and 29 weeks) [64]. Despite ZDSD rats have no LepR mutation [65], we found analogous results, with comparable values of TMD in both femoral cortical and trabecular bone and in the parietal bones of LepR$^{-/-}$ and LepR$^{+/+}$ animals. TMD is a metric for the degree of bone mineralization easily assessed in micro-CT systems, but it differs from the more widely used BMD parameter as TMD does not include the average attenuation from non-bone regions [36]. Patients with T2DM are commonly reported having normal or even higher values of BMD than non-diabetic individuals [11,12]. On the other hand, inconsistent trends in BMD have been observed in Zucker fa/fa rats, with values of BMD both comparable [45] or statistically reduced [21,43] with respect to healthy controls.

The absence of statistically significant differences in bone matrix mineralization expressed as TMD were corroborated by qBEI. In qBEI, the degree of mineralization of the bone matrix corresponds to the BMDD after proper calibration of grey-levels in BSE-SEM images using standards of C and Al [38]. This method was developed by Roschger et al. to mitigate the limitations of BMD measures, where changes in bone volume cannot be differentiated from those in bone matrix mineralization [38]. In our BSE-SEM images acquired post-calibration, no differences in BMDD between LepR$^{-/-}$ and LepR$^{+/+}$ rats were detected in neither femurs nor calvaria. Comparable BMDD was also found between 21-week-old ZDF and non-diabetic rats in qBEI carried out by Hamann et al., where differences were only observed in the femur metaphysis, but not in the epiphysis nor in the cortical mid-shaft [66].

In agreement with TMD and BMDD evaluated by micro-CT and qBEI, respectively, differences in values of mineral-to-matrix ratio assessed micro-Raman spectroscopy were not statistically significant in neither femurs (cortical and trabecular bone) nor calvaria, regardless of the bands considered ($\nu_2PO_4^3$ /amide III; $\nu_1PO_4^3$ /Phe). This is not surprising, as a strong correlation between $\nu_2PO_4^3$ /amide III in micro-Raman spectroscopy and wt% Ca in qBEI has been demonstrated [67]. In the Raman maps with a 10 μm pixel size, the trend of lower mineral-to-matrix ratio in the femurs of LepR$^{-/-}$ animals, indicating reduced mineralization, appeared in agreement with the delayed growth suggested by the altered microarchitecture. However, clear conclusions cannot be drawn, given the absence of statistical significance and the lack of a similar trend in the Raman maps with a 1 μm pixel size. Moreover, carbonate-to-phosphate ratio, which normally increases with tissue age [42,68], and mineral crystallinity were comparable in both animal groups, further suggesting no differences in the degree of skeletal maturity in terms of bone matrix composition. Other authors have reported a similar lack of variation in bone composition (mineral-to-matrix ratio and carbonate substitution) in trabecular bone in the peri-implant space of ZDF and Sprague Dawley rats [69]. Hammond et al. also reported comparable values of carbonate-to-phosphate ratio and mineral crystallinity in ZDSD and Sprague Dawley rats [70]. On the other hand, they found that mineral-to-matrix ratio was higher in the ZDSD animals [70]. However, this discrepancy can be attributed to the different bands used to compute the mineral-to-matrix ratio in the Raman spectra. In a recent study by Monahan et al., Fourier transform infrared (FTIR) spectroscopy revealed comparable mineral-to-matrix ratio and mineral crystallinity in ZDF and control rats at all ages examined (12, 26, and 46 weeks of age), while acid phosphate content and carbonate-to-phosphate ratio showed statistically significant differences in 46-week-old animals (with acid phosphate being different also at 12 weeks) [71].

Parameters related to mechanical properties evaluated by RPI were comparable in the femurs of LepR$^{+/+}$ and LepR$^{-/-}$ rats. In a previous study, Hammond et al. found statistically significant differences in CID 1st and IDI, which the authors concluded to be caused by increased resistance to plastic deformation and reduced fracture toughness due to AGEs crosslinking [70]. Here, the comparable RPI measurements are consistent with the similarity in bone matrix composition. Although microstructural differences are expected to impact mechanical properties, these are likely not captured by RPI, as fracture risk is also determined by trabecular and intracortical properties, which are not assessed by periosteal indentation [72].

4.3. Notable microstructural features

Part of our analyses focused on some specific microstructural features noted in BSE-SEM images, in particular, mineralized cartilage islands in the femurs and more highly mineralized bone areas in the calvaria. Mineralized cartilage islands have been reported in the femoral cortical bone of both mice [73] and rats [39,74]. As these islands are observed also in skeletally mature animals, and not just in those at growing stages, they are believed to be remnants of endochondral ossification due to the little to no Haversian remodeling in rodents [39,74]. Where Haversian remodeling takes place, such as in human bone, mineralized cartilage is not present as islands enclosed by bone, but it is mostly noted at subchondral bone-cartilage interfaces at the growth plates or at the joints [75,76], and in the femoral neck of elderly subjects [77].

Here, mineralized cartilage islands were observed also in the trabecular region, further confirming mineralized cartilage as a characteristic feature of rodent bone, regardless of the type (cortical vs. trabecular). These elements could be easily distinguished from the surrounding bone matrix as they presented a higher degree of mineralization, i.e., they appeared considerably brighter in BSE-SEM images. High-resolution Raman maps (1 μm pixel size) also confirmed the higher mineral content of mineralized cartilage islands compared to bone in both cortical and trabecular regions. This trend was consistent in both LepR$^{-/-}$ and LepR$^{+/+}$ animals, although differences were not statistically significant. A higher sample number could be probed to verify whether the lack of statistical differences corresponds to a true lack of difference, or whether the study is underpowered. In fact, previous work reported a significantly higher degree of mineralization in mineralized cartilage islands than in bone using qBEI [39]. In our work, qBEI was completed to gain global information on the degree of mineralization over large sample areas, hence the magnification and standard used were not suitable to exactly probe compositional differences between mineralized cartilage islands and bone. Nonetheless, we analyzed our qBEI data by dividing them in 5 wt% Ca-wide bins to assess eventual differences in the amount of mineralized cartilage islands in LepR$^{-/-}$ and LepR$^{+/+}$ animals, assuming this would be reflected by a greater pixel count in the bins corresponding to high values of wt% Ca. However, no differences between groups were found. This was expected, as drastic differences in mineralized cartilage islands content would have altered the overall degree of mineralization of bone matrix, which was indeed comparable in the two animal groups for all the compositional analyses completed (TMD by micro-CT, BMDD by qBEI, and mineral-to-matrix ratio by micro-Raman spectroscopy).

In analogy with the mineralized cartilage islands indicating partial remodeling in endochondral bones, we hypothesize that hypermineralized bone in the calvaria is also related to incomplete/ongoing remodeling. From qBEI images and Raman maps (10 μm pixel size), it appears that bone is less mineralized at its surfaces (superior, inferior,

and suture edge). Therefore, it is possible that hyper-mineralized bone corresponds to older, more mineralized bone that will progressively be replaced by new tissue as remodeling takes place. LepR$^{-/-}$ animals had a similar content of hyper-mineralized bone as the LepR$^{+/+}$ group when comparing different 5 wt% Ca bins in qBEI data. This further confirms the comparable bone matrix composition in the two groups examined, regardless of the anatomical location (femur vs. calvarium).

4.4. Limitations and future directions

To the best of our knowledge, this is the first examination of Lund MetS rats addressing skeletal changes, as previous work investigated vasculature complications [32–34]. While the focus of the present study is on microstructure and bone matrix composition, more work is needed to comprehensively characterize the skeletal phenotype of Lund MetS rats, which is especially important in order to establish whether they can constitute a valid alternative to already available LepR-deficient rodent models for diabetes research.

Presently, it is not possible to establish whether the skeletal abnormalities in the Lepr$^{-/-}$ group are due to LepR deficiency, obesity, hyperglycemia, or a combination thereof. While decoupling these variables was out-of-scope in this work, such a task was accomplished in previous studies for example by pair-feeding [61] or bone marrow transplantation [24]. Hence, a similar methodological approach could be applied in the future to gain mechanistic insights on the altered microstructure and reduced bone mass in the trabecular compartment of the Lund MetS rats.

The role of AGEs accumulation in increasing fracture risk has often been emphasized in diabetic individuals. Interestingly, a recent study showed no correlation between mechanical properties and AGEs in ZDF rats [71], while others have observed an increased resistance to indentation in ZDSD animals, which, combined with an altered collagen D-spacing, corroborates the direct effect of AGEs on the mechanical behaviour of collagen fibrils [70]. The amount of AGEs and the eventual correlation with mechanical properties should also be assessed in the Lund MetS rats. The analysis should not be limited to more commonly measured fluorescent AGEs like PEN, but also include non-fluorescent, non-crosslinking AGEs like CML, which is found in greater content than PEN in human cortical bone [78].

Here, insights into mechanical properties were partially gained from indentation-related response through RPI. However, geometrical and microstructural alterations in the femurs of LepR$^{-/-}$ animals are likely to cause an abnormal mechanical behaviour not detected by RPI via periosteal measurements, which we believe to be more influenced by bone matrix composition. Mechanical testing of whole bones with a three-point bend test would be a more fitting approach to confirm loss in bone strength and toughness induced by microstructural alterations.

The similarity in bone matrix composition and features related to remodeling (mineralized cartilage islands and hyper-mineralized bone in femurs and calvaria, respectively) are indicative of comparable bone turnover in the two groups. On the other hand, previous studies showed higher content of mineralized cartilage and lower bone turnover in Lep$^{ob/ob}$ and Lep$^{db/db}$ mice [24,62]. Static and dynamic histomorphometry and evaluation of bone formation/resorption markers (e.g., through serum analysis) are therefore necessary to eventually confirm the differences in bone turnover between LepR$^{-/-}$ and LepR$^{+/+}$ animals. This will also have relevant implications for bone repair and regeneration, for example in the context of osseointegration. Although osseointegration outcomes in patients with T2DM under glycemic control are generally positive, chronic hyperglycemia impairs wound healing, potentially leading to implant failure [79].

Fracture risk in diabetic subjects appears to be correlated with disease duration [80]. As bone strength was shown to worsen with disease progression in ZDF rats [71], a longitudinal study of Lund MetS rats would offer insights into the time-evolution of the skeletal alterations in the LepR$^{-/-}$ animals and their impact on mechanical properties. Lastly, while only male rats were used in this study, female rats should also be investigated in the future. Lund MetS LepR$^{-/-}$ female rats display impaired glucose tolerance and obesity, but do not develop overt T2DM [32,35], similarly to ZDF rats [16]. Nonetheless, given the incidence of obesity in both sexes, together with reports of LepR-deficiency in female individuals [30], such an animal model can still be employed in contexts relevant to human research.

5. Conclusion

Regardless of the ossification route, the LepR$^{-/-}$ animals presented altered morphology and microarchitecture in both femurs and calvaria. On the other hand, bone matrix composition was comparable to that of the control group. Similarly, specific microstructural features like mineralized cartilage islands in the femurs and hyper-mineralized bone in the calvaria also appeared equally distributed in the two groups. Therefore, it seems that the altered metabolic state in the LepR$^{-/-}$ animals affects bone formation macroscopically (e.g., shorter femurs, thinner calvaria) and microscopically (e.g., more porous trabecular region, shorter sagittal suture), leading to a delayed skeletal development. In spite of the analogous composition and RPI measurements, LepR$^{-/-}$ animals are expected to display impaired mechanical functions, given the compromised macro- and microstructure. Overall, our findings are consistent with the delayed development experienced by humans with Lep/LepR congenic mutations [29–31], and with the altered bone microstructure of diabetic subjects [11], making this animal model promising for translational bone research.

CRediT authorship contribution statement

Chiara Micheletti: Conceptualization, Methodology, Formal analysis, Investigation, Visualization, Writing – original draft. **Martina Jolic:** Investigation, Writing – review & editing. **Kathryn Grandfield:** Supervision, Funding acquisition, Writing – review & editing. **Furqan A. Shah:** Conceptualization, Methodology, Investigation, Supervision, Funding acquisition, Writing – review & editing. **Anders Palmquist:** Conceptualization, Methodology, Investigation, Supervision, Funding acquisition, Writing – review & editing.

Declaration of competing interest

The authors declare that they have no known competing financial interests or personal relationships that could have appeared to influence the work reported in this paper.

Data availability

Additional data are available in Supplementary Material.

Acknowledgements

The authors gratefully acknowledge Krisztina Ruscsák, Lena Emanuelsson, and Birgitta Norlindh for performing the animal work and sample collection, and Marie Lagerquist for providing access to the RPI machine. This work was performed in part at the Chalmers Materials Analysis Laboratory (CMAL). C.M. is thankful for the support from the Ontario Graduate Scholarship and the Blanceflor Foundation. K.G. acknowledges funding support from Natural Sciences and Engineering Research Council of Canada (NSERC) (grant no. RGPIN-2020-05722), the Ontario Ministry of Research, Innovation and Science (Early Researcher Award ER17-13-081), and the Canada Research Chairs Program from whom K.G. holds the Tier II Chair in Microscopy of Biomaterials and Biointerfaces. F.A.S. is thankful for the support of the Svenska Sällskapet för Medicinsk Forskning (SSMF), the Adlerbertska Foundation, and the Kungliga Vetenskaps-och Vitterhets-Samhället i Göteborg. A.P. acknowledges funding support from the Swedish

Research Council (grant no. 2020-04715), the Swedish state under the agreement between the Swedish government and the county councils, the ALF agreement (ALFGBG-725641), the IngaBritt and Arne Lundberg Foundation, the Hjalmar Svensson Foundation, and the Area of Advance Materials at Chalmers and at the Department of Biomaterials (University of Gothenburg) within the Strategic Research Area initiative launched by the Swedish government.

Appendix A. Supplementary data

Supplementary data to this article can be found online at https://doi.org/10.1016/j.bone.2023.116747.

References

[1] G.J. Tortora, B. Derrickson, The skeletal system: bone tissue, in: Principles of Anatomy and Physiology, John Wiley & Sons, New York NY, 2009.
[2] M.R. Allen, D.B. Burr, Bone modeling and remodeling, in: Basic and Applied Bone Biology, Academic Press, London, UK, 2014, pp. 75–90.
[3] G.L. Galea, M.R. Zein, S. Allen, P. Francis-West, Making and shaping endochondral and intramembranous bones, Dev. Dyn. 250 (2021) 414–449.
[4] N. Reznikov, R. Shahar, S. Weiner, Bone hierarchical structure in three dimensions, Acta Biomater. 10 (2014) 3815–3826.
[5] M.L. Bouxsein, Bone quality: where do we go from here? Osteoporos. Int. 14 (2003) 118–127.
[6] A.L. Boskey, L. Imbert, Bone quality changes associated with aging and disease: a review, Ann. N. Y. Acad. Sci. 1410 (2017) 93–106.
[7] A. Muñoz, A. Docaj, M. Ugarteburu, A. Carriero, Poor bone matrix quality: what can be done about it? Curr. Osteoporos. Rep. 19 (2021) 510–531.
[8] L.R. McCabe, The diabetes-bone relationship, J. Diabetes Metab. 3 (2012), e001.
[9] W.D. Leslie, M.R. Rubin, A.V. Schwartz, J.A. Kanis, Type 2 diabetes and bone, J. Bone Miner. Res. 27 (2012) 2231–2237.
[10] J.J. Cao, Effects of obesity on bone metabolism, J. Orthop. Surg. Res. 6 (2011) 30.
[11] L. McCabe, J. Zhang, S. Raehtz, Understanding the skeletal pathology of type 1 and 2 diabetes mellitus, Crit. Rev. Eukaryot. Gene Expr. 21 (2011) 187–206.
[12] L.J. Melton, B.L. Riggs, C.L. Leibson, S.J. Achenbach, J.J. Camp, M.L. Bouxsein, E. J. Atkinson, R.A. Robb, S. Khosla, A bone structural basis for fracture risk in diabetes, J. Clin. Endocrinol. Metab. 93 (2008) 4804–4809.
[13] M. Yamamoto, T. Sugimoto, Advanced glycation end products, diabetes, and bone strength, Curr. Osteoporos. Rep. 14 (2016) 320–326.
[14] M. Saito, Y. Kida, S. Kato, K. Marumo, Diabetes, collagen, and bone quality, Curr. Osteoporos. Rep. 12 (2014) 181–188.
[15] G.V. Halade, A.E. Jamali, P.J. Williams, R.J. Fajardo, G. Fernandes, Obesity-mediated inflammatory microenvironment stimulates osteoclastogenesis and bone loss in mice, Exp. Gerontol. 46 (2011) 43–52.
[16] A.J. King, The use of animal models in diabetes research, Br. J. Pharmacol. 166 (2012) 877–894.
[17] L.A. Tartaglia, The leptin receptor, J. Biol. Chem. 272 (1997) 6093–6096.
[18] I.R. Reid, P.A. Baldock, J. Cornish, Effects of leptin on the skeleton, Endocr. Rev. 39 (2018) 938–959.
[19] J. Cornish, K. Callon, U. Bava, C. Lin, D. Naot, B. Hill, A. Grey, N. Broom, D. Myers, G. Nicholson, I. Reid, Leptin directly regulates bone cell function in vitro and reduces bone fragility in vivo, J. Endocrinol. 175 (2002) 405–415.
[20] J. Foldes, M.S. Shih, J. Levy, Bone structure and calcium metabolism in obese zucker rats, Int. J. Obes. Relat. Metab. Disord. 16 (1992) 95–102.
[21] J. Mathey, M.-N. Horcajada-Molteni, B. Chanteranne, C. Picherit, C. Puel, P. Lebecque, C. Cubizoles, M.-J. Davicco, V. Coxam, J.-P. Barlet, Bone mass in obese diabetic zucker rats: influence of treadmill running, Calcif. Tissue Int. 70 (2002) 305–311.
[22] G.A. Williams, K.E. Callon, M. Watson, J.L. Costa, Y. Ding, M. Dickinson, Y. Wang, D. Naot, I.R. Reid, J. Cornish, Skeletal phenotype of the leptin receptor–deficient db/db mouse, J. Bone Miner. Res. 26 (2011) 1698–1709.
[23] P. Ducy, M. Amling, S. Takeda, M. Priemel, A.F. Schilling, F.T. Beil, J. Shen, C. Vinson, J.M. Rueger, G. Karsenty, Leptin inhibits bone formation through a hypothalamic relay a central control of bone mass, Cell 100 (2000) 197–207.
[24] R.T. Turner, S.P. Kalra, C.P. Wong, K.A. Philbrick, L.B. Lindenmaier, S. Boghossian, U.T. Iwaniec, Peripheral leptin regulates bone formation, J. Bone Miner. Res. 28 (2013) 22–34.
[25] B. Burguera, L.C. Hofbauer, T. Thomas, F. Gori, G.L. Evans, S. Khosla, B.L. Riggs, R. T. Turner, Leptin reduces ovariectomy-induced bone loss in rats, Endocrinology 142 (2001) 3546–3553.
[26] S.M. Bartell, S. Rayalam, S. Ambati, D.R. Gaddam, D.L. Hartzell, M. Hamrick, J. She, M.A. Della-Fera, C.A. Baile, Central (ICV) leptin injection increases bone formation, bone mineral density, muscle mass, serum IGF-1, and the expression of osteogenic genes in leptin-deficient ob/ob mice, J. Bone Miner. Res. 26 (2011) 1710–1720.
[27] B. Wang, P. Chandrasekera, J. Pippin, Leptin- and leptin receptor-deficient rodent models: relevance for human type 2 diabetes, Curr. Diabetes Rev. 10 (2014) 131–145.
[28] C.T. Montague, I.S. Farooqi, J.P. Whitehead, M.A. Soos, H. Rau, N.J. Wareham, C. P. Sewter, J.E. Digby, S.N. Mohammed, J.A. Hurst, C.H. Cheetham, A.R. Earley, A. H. Barnett, J.B. Prins, S. O'Rahilly, Congenital leptin deficiency is associated with severe early-onset obesity in humans, Nature 387 (1997) 903–908.
[29] K. Clément, C. Vaisse, N. Lahlou, S. Cabrol, V. Pelloux, D. Cassuto, M. Gourmelen, C. Dina, J. Chambaz, J.-M. Lacorte, A. Basdevant, P. Bougnères, Y. Lebouc, P. Froguel, B. Guy-Grand, A mutation in the human leptin receptor gene causes obesity and pituitary dysfunction, Nature 392 (1998) 398–401.
[30] I.S. Farooqi, T. Wangensteen, S. Collins, W. Kimber, G. Matarese, J.M. Keogh, E. Lank, B. Bottomley, J. Lopez-Fernandez, I. Ferraz-Amaro, M.T. Dattani, O. Ercan, A.G. Myhre, L. Retterstol, R. Stanhope, J.A. Edge, S. McKenzie, N. Lessan, M. Ghodsi, V.D. Rosa, F. Perna, S. Fontana, I. Barroso, D.E. Undlien, S. O'Rahilly, Clinical and molecular genetic Spectrum of congenital deficiency of the leptin receptor, N. Engl. J. Med. 356 (2007) 237–247.
[31] I.S. Farooqi, S. O'Rahilly, 20 years of leptin: human disorders of leptin action, J. Endocrinol. 223 (2014) T63–T70.
[32] M.F. Gomez , L. Åkesson, Å. Lernmark, A new rat model for diabetic vascular complications, Patent Application WO-2015044339-A1.
[33] M.F. Gomez, J. Silvola, L.M. Berglund, M. Kiugel, L. Åkesson, J. Knuuti, A. Roivainen, Å. Lernmark, P. Nuutila, A. Saraste, Cardiac hypertrophy and oxidative metabolism in novel congenic leptin receptor deficient BBDR.Cg-lepr.Cp rats, FASEB J. 28 (2014), 1155.10.
[34] L. Berglund, L. Åkesson, E.G. Vaz, A. Zetterqvist, O. Kotova, A.D. Andersson, M. Johansson, N. Wierup, A. Jönsson-Rylander, Å. Lernmark, M. Gomez, Diabetes complications in congenic leptin receptor deficient BBDR.Cg-lepr.Cp rats, FASEB J. 28 (2014), 1072.6.
[35] Janvier Labs, Lund MetS rat. https://janvier-labs.com/en/fiche_produit/lund-mets_rat/.
[36] M.L. Bouxsein, S.K. Boyd, B.A. Christiansen, R.E. Guldberg, K.J. Jepsen, R. Müller, Guidelines for assessment of bone microstructure in rodents using micro–computed tomography, J. Bone Miner. Res. 25 (2010) 1468–1486.
[37] H.R. Buie, G.M. Campbell, R.J. Klinck, J.A. MacNeil, S.K. Boyd, Automatic segmentation of cortical and trabecular compartments based on a dual threshold technique for in vivo micro-CT bone analysis, Bone 41 (2007) 505–515.
[38] P. Roschger, P. Fratzl, J. Eschberger, K. Klaushofer, Validation of quantitative backscattered electron imaging for the measurement of mineral density distribution in human bone biopsies, Bone 23 (1998) 319–326.
[39] F.L. Bach-Gansmo, S.C. Irvine, A. Brüel, J.S. Thomsen, H. Birkedal, Calcified cartilage islands in rat cortical bone, Calcif. Tissue Int. 92 (2013) 330–338.
[40] S. Gamsjaeger, A. Masic, P. Roschger, M. Kazanci, J.W.C. Dunlop, K. Klaushofer, E. P. Paschalis, P. Fratzl, Cortical bone composition and orientation as a function of animal and tissue age in mice by raman spectroscopy, Bone 47 (2010) 392–399.
[41] J.P. McElderry, G. Zhao, A. Khmaladze, C.G. Wilson, R.T. Franceschi, M.D. Morris, Tracking circadian rhythms of bone mineral deposition in murine calvarial organ cultures, J. Bone Miner. Res. 28 (2013) 1846–1854.
[42] M.D. Morris, G.S. Mandair, Raman assessment of bone quality, Clin. Orthop. Relat. Res. 469 (2011) 2160–2169.
[43] R.D. Prisby, J.M. Swift, S.A. Bloomfield, H.A. Hogan, M.D. Delp, Altered bone mass, geometry and mechanical properties during the development and progression of type 2 diabetes in the zucker diabetic fatty rat, J. Endocrinol. 199 (2008) 379–388.
[44] S. Reinwald, R.G. Peterson, M.R. Allen, D.B. Burr, Skeletal changes associated with the onset of type 2 diabetes in the ZDF and ZDSD rodent models, Am. J. Physiol. Endocrinol. Metab. 296 (2009) E765–E774.
[45] J.A. Tamasi, B.J. Arey, D.R. Bertolini, J.H. Feyen, Characterization of bone structure in leptin receptor-deficient zucker (fa/fa) rats, J. Bone Miner. Res. 18 (2003) 1605–1611.
[46] D. Zeitoun, G. Caliaperoumal, M. Bensidhoum, J.M. Constans, F. Anagnostou, V. Bousson, Microcomputed tomography of the femur of diabetic rats: alterations of trabecular and cortical bone microarchitecture and vasculature—a feasibility study, Eur. Radiol. Exp. 3 (2019) 17.
[47] D. Bao, Y. Ma, X. Zhang, F. Guan, W. Chen, K. Gao, C. Qin, L. Zhang, Preliminary characterization of a leptin receptor knockout rat created by CRISPR/Cas9 system, Sci. Rep. 5 (2015) 15942.
[48] J.D. Wolff, The Law of Bone Transformation, Hirschwald, Berlin, 1892.
[49] J.D. Currey, Bones: Structure and Mechanics, Princeton University Press, Princeton NJ, 2002.
[50] A.G. Robling, C.H. Turner, Mechanical signaling for bone modeling and remodeling, Crit. Rev. Eukaryot. Gene Expr. 19 (2009) 319–338.
[51] J.-O. Jansson, A.D. Gasull, E. Schéle, S.L. Dickson, V. Palsdottir, A. Palmquist, F. F. Gironés, J. Bellman, F. Anesten, D. Hägg, C. Ohlsson, A body weight sensor regulates pre-pubertal growth via the somatotropic axis in male rats, Endocrinology 162 (2021) bqab053-.
[52] J.-O. Jansson, V. Palsdottir, D.A. Hägg, E. Schéle, S.L. Dickson, F. Anesten, T. Bake, M. Montelius, J. Bellman, M.E. Johansson, R.D. Cone, D.J. Drucker, J. Wu, B. Aleksie, A.E. Törnqvist, K. Sjögren, J.-Å. Gustafsson, S.H. Windahl, C. Ohlsson, Body weight homeostat that regulates fat mass independently of leptin in rats and mice, Proc. Natl. Acad. Sci. 115 (2018) 427–432.
[53] R.T. Turner, A.J. Branscum, C.P. Wong, U.T. Iwaniec, E. Morey-Holton, Studies in microgravity, simulated microgravity and gravity do not support a gravitostat, J. Endocrinol. 247 (2020) 273–282.
[54] M.A. Abbassy, I. Watari, K. Soma, Effect of experimental diabetes on craniofacial growth in rats, Arch. Oral Biol. 53 (2008) 819–825.
[55] L.A. Opperman, Cranial sutures as intramembranous bone growth sites, Dev. Dyn. 219 (2000) 472–485.
[56] K.A. Lenton, R.P. Nacamuli, D.C. Wan, J.A. Helms, M.T. Longaker, Cranial suture biology, Curr. Top. Dev. Biol. 66 (2005) 287–328.

[57] T. Miura, C.A. Perlyn, M. Kinboshi, N. Ogihara, M. Kobayashi-Miura, G.M. Morriss-Kay, K. Shiota, Mechanism of skull suture maintenance and interdigitation, J. Anat. 215 (2009) 642–655.
[58] B. Zimmermann, A. Moegelin, P. de Souza, J. Bier, Morphology of the development of the sagittal suture of mice, Anat. Embryol. 197 (1998) 155–165.
[59] H.E. White, A. Goswami, A.S. Tucker, The intertwined evolution and development of sutures and cranial morphology, Front. Cell Dev. Biol. 09 (2021), 653579.
[60] Y. Hamada, H. Fujii, M. Fukagawa, Role of oxidative stress in diabetic bone disorder, Bone 45 (2009) S35–S38.
[61] R.T. Turner, K.A. Philbrick, C.P. Wong, D.A. Olson, A.J. Branscum, U.T. Iwaniec, Morbid obesity attenuates the skeletal abnormalities associated with leptin deficiency in mice, J. Endocrinol. 223 (2014) M1–M15.
[62] K.A. Philbrick, S.A. Martin, A.R. Colagiovanni, A.J. Branscum, R.T. Turner, U. T. Iwaniec, Effects of hypothalamic leptin gene therapy on osteopetrosis in leptin-deficient mice, J. Endocrinol. 236 (2018) 57–68.
[63] H.E. White, J. Clavel, A.S. Tucker, A. Goswami, A comparison of metrics for quantifying cranial suture complexity, J. R. Soc. Interface 17 (2020), 20200476.
[64] A. Creecy, S. Uppuganti, A.R. Merkel, D. O'Neal, A.J. Makowski, M. Granke, P. Voziyan, J.S. Nyman, Changes in the fracture resistance of bone with the progression of type 2 diabetes in the ZDSD rat, Calcif. Tissue Int. 99 (2016) 289–301.
[65] A.N. Wang, J. Carlos, G.M. Fraser, J.J. McGuire, Zucker diabetic-Sprague dawley (ZDSD) rat: type 2 diabetes translational research model, Exp. Physiol. 107 (2022) 265–282.
[66] C. Hamann, C. Goettsch, J. Mettelsiefen, V. Henkenjohann, M. Rauner, U. Hempel, R. Bernhardt, N. Fratzl-Zelman, P. Roschger, S. Rammelt, K.-P. Günther, L. C. Hofbauer, Delayed bone regeneration and low bone mass in a rat model of insulin-resistant type 2 diabetes mellitus is due to impaired osteoblast function, Am. J. Physiol. Endocrinol. Metab. 301 (2011) E1220–E1228.
[67] A. Roschger, S. Gamsjaeger, B. Hofstetter, A. Masic, S. Blouin, P. Messmer, A. Berzlanovich, E.P. Paschalis, P. Roschger, K. Klaushofer, P. Fratzl, Relationship between the v2PO4/amide III ratio assessed by raman spectroscopy and the calcium content measured by quantitative backscattered electron microscopy in healthy human osteonal bone, J. Biomed. Opt. 19 (2014), 065002-065002.
[68] D.B. Burr, Changes in bone matrix properties with aging, Bone 120 (2019) 85–93.
[69] K.D. Anderson, F.C. Ko, S. Fullam, A.S. Virdi, M.A. Wimmer, D.R. Sumner, R. D. Ross, The relative contribution of bone microarchitecture and matrix composition to implant fixation strength in rats, J. Orthop. Res. 40 (2022) 862–870.
[70] M.A. Hammond, M.A. Gallant, D.B. Burr, J.M. Wallace, Nanoscale changes in collagen are reflected in physical and mechanical properties of bone at the microscale in diabetic rats, Bone 60 (2014) 26–32.
[71] G.E. Monahan, J. Schiavi-Tritz, M. Britton, T.J. Vaughan, Longitudinal alterations in bone morphometry, mechanical integrity and composition in Type-2 diabetes in a zucker diabetic fatty (ZDF) rat, Bone 170 (2023), 116672.
[72] M.R. Allen, E.M. McNerny, J.M. Organ, J.M. Wallace, True gold or pyrite: a review of reference point indentation for assessing bone mechanical properties in vivo, J. Bone Miner. Res. 30 (2015) 1539–1550.
[73] V. Ip, Z. Toth, J. Chibnall, S. McBride-Gagyi, Remnant woven bone and calcified cartilage in mouse bone: differences between Ages/Sex and effects on bone strength, PLoS One 11 (2016), e0166476.
[74] A. Shipov, P. Zaslansky, H. Riesemeier, G. Segev, A. Atkins, R. Shahar, Unremodeled endochondral bone is a major architectural component of the cortical bone of the rat (Rattus norvegicus), J. Struct. Biol. 183 (2013) 132–140.
[75] T.R. Oegema, R.J. Carpenter, F. Hofmeister, R.C. Thompson, The interaction of the zone of calcified cartilage and subchondral bone in osteoarthritis, Microsc. Res. Tech. 37 (1997) 324–332.
[76] Y. Zhang, F. Wang, H. Tan, G. Chen, L. Guo, L. Yang, Analysis of the mineral composition of the human calcified cartilage zone, Int. J. Med. Sci. 9 (2012) 353–360.
[77] T. Tang, W. Wagermaier, R. Schuetz, Q. Wang, F. Eltit, P. Fratzl, R. Wang, Hypermineralization in the femoral neck of the elderly, Acta Biomater. 89 (2019) 330–342.
[78] C.J. Thomas, T.P. Cleland, G.E. Sroga, D. Vashishth, Accumulation of carboxymethyl-lysine (CML) in human cortical bone, Bone 110 (2018) 128–133.
[79] F. Javed, G.E. Romanos, Chronic hyperglycemia as a risk factor in implant therapy, Periodontol. 2000 (81) (2019) 57–63.
[80] A.D. Dede, S. Tournis, I. Dontas, G. Trovas, Type 2 diabetes mellitus and fracture risk, Metabolis. 63 (2014) 1480–1490.

SUPPLEMENTARY

Table S1. Values of weight and blood glucose measured at 16 and 20 weeks of age.

Group	Weight at 16 weeks [g]	Weight at 20 weeks [g]	Blood glucose at 16 weeks [mmol/l]	Blood glucose at 20 weeks [mmol/l]
$LepR^{+/+}$	369	424	9.7	10.9
	332	398	10.3	9.0
	350	393	10	7.3
	366	406	10	8.9
	407	455	10.8	10.2
	390	420	11.4	6.8
	407	438	9.2	10.3
	409	449	8.9	9.3
	405	428	8.9	11.7
	374	412	8.1	10.0
Average	**381 ± 27**	**422 ± 21**	**9.7 ± 1.0**	**9.4 ± 1.5**
$LepR^{-/-}$	546	603	23.9	21.5
	579	596	27.8	25.7
	596	668	13.9	19.9
	530	636	23.4	33.2
	501	630	12.1	21.5
	545	611	22.1	23.6
	500	507	33.2	26.2
	524	542	26.4	16.8
	634	635	24.3	24.8
	549	546	32.7	29.5
	576	602	25.5	31.2
Average	**553 ± 41*****	**598 ± 48*****	**24.1 ± 6.6*****	**24.9 ± 5.0*****

*** denotes statistical significance with respect to the control group ($p < 0.001$).

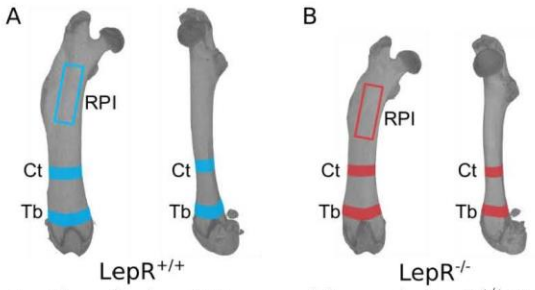

Figure S1. 3D reconstruction of micro-CT scans of femurs in $LepR^{+/+}$ (A) and $LepR^{-/-}$ animals (B), showing the regions where morphometry measurements were completed in both cortical (Ct) and trabecular (Tb) compartments. The areas where RPI measurements were acquired are also shown (marked by rectangles). Two different views (frontal, side) are provided for clarity.

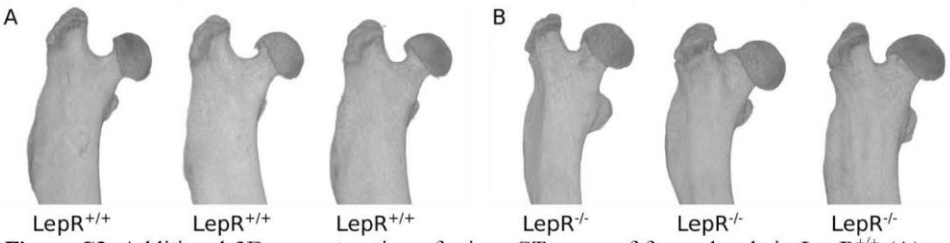

Figure S2. Additional 3D reconstruction of micro-CT scans of femur heads in $LepR^{+/+}$ (A) and $LepR^{-/-}$ animals (B), displaying incompletely developed head and neck.

Table S2. Values of femur length (measured by a caliper), and morphometry parameters and tissue mineral density (TMD) measured in micro-CT data.

Group	Length [mm]	Ct.Ar [mm²]	Tt.Ar [mm²]	Ct.Ar/Tt.Ar [%]	Ct.Th [mm]	BV/TV [%]	Tb.Sp [mm]	Tb.N [1/mm]	Tb.Th [mm]	Ct.TMD [g/cm³]	Tb.TMD [g/cm³]
$LepR^{+/+}$	38.7	8.348	12.967	64.379	0.719	61.046	0.174	3.322	0.127	1.141	0.994
	38.6	7.584	11.603	65.361	0.711	55.840	0.187	3.324	0.114	1.164	0.971
	38.3	7.525	12.180	61.778	0.673	57.136	0.185	3.272	0.120	1.122	1.000
	39.5	8.462	13.122	64.490	0.734	60.946	0.175	3.288	0.129	1.135	0.955
	38.8	7.963	12.410	64.168	0.708	58.009	0.184	3.290	0.120	1.119	0.993
	38.8	7.802	12.286	63.505	0.697	55.737	0.201	3.178	0.113	1.133	0.919
	38.4	7.727	12.035	64.203	0.710	56.358	0.192	3.212	0.119	1.108	0.944
	39.5	8.105	11.749	68.987	0.770	58.620	0.192	3.127	0.128	1.052	0.914
Average	**38.825 ± 0.453**	**7.940 ± 0.345**	**12.294 ± 0.535**	**64.609 ± 2.049**	**0.715 ± 0.028**	**57.961 ± 2.123**	**0.186 ± 0.009**	**3.252 ± 0.072**	**0.121 ± 0.006**	**1.122 ± 0.033**	**0.961 ± 0.034**
$LepR^{-/-}$	35.0	6.802	10.967	62.024	0.658	56.344	0.233	2.697	0.138	1.163	1.006
	34.8	6.504	10.555	61.620	0.630	53.125	0.183	3.488	0.104	1.134	0.818
	34.3	5.945	9.824	60.514	0.602	46.708	0.258	2.840	0.095	1.138	0.930
	33.3	5.548	8.719	63.630	0.615	51.344	0.273	2.475	0.131	1.117	0.953
	34.8	6.739	11.345	59.401	0.625	56.034	0.212	2.949	0.127	1.125	0.971
	35.0	6.315	10.320	61.192	0.620	53.236	0.196	3.309	0.107	1.099	0.909
	34.5	6.127	10.188	60.138	0.608	47.848	0.225	3.086	0.099	1.157	0.926
	34.0	5.931	9.660	61.398	0.613	54.272	0.223	2.869	0.125	1.158	1.015
Average	**34.463 ± 0.585*** **	**6.239 ± 0.433*** **	**10.197 ± 0.816*** **	**61.240± 1.289** **	**0.621 ± 0.017*** **	**52.364 ± 3.540** **	**0.225 ± 0.030** **	**2.964 ± 0.326***	**0.115 ± 0.016**	**1.137 ± 0.022**	**0.941 ± 0.062**

*, **, and *** denote statistical significance with respect to the control group ($p < 0.05$, $p < 0.01$, and $p < 0.001$, respectively).

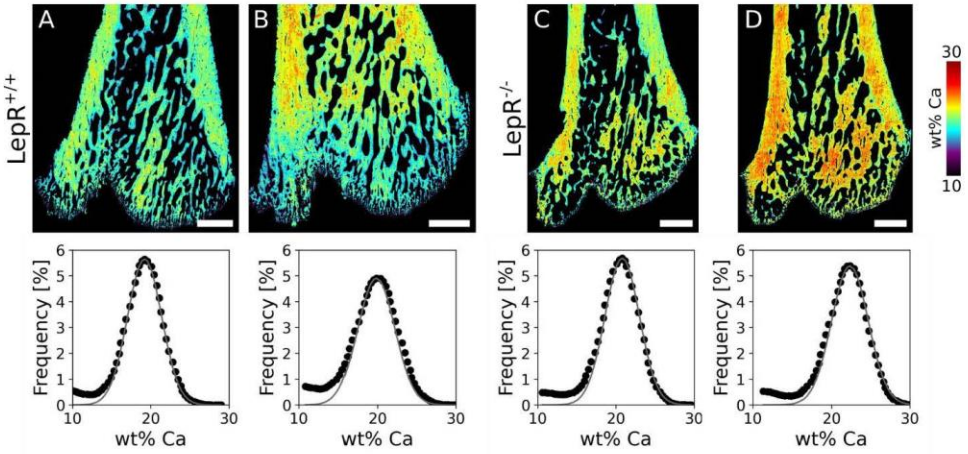

Figure S3. Additional qBEI images (pixel intensity converted in Ca concentration) and relative histograms (black dots correspond to acquired point, and dark grey line corresponds to area-equivalent Gaussian curve) in the femurs of $LepR^{+/+}$ (A-B) and $LepR^{-/-}$ animals (C-D). Scale bars are 1 mm.

Table S3. Parameters expressing bone mineral density distribution (BMDD) evaluated by qBEI in the femurs.

Group	Ca-Mean [wt% Ca]	FWHM [wt% Ca]	MaxFreq. [%]	Ca-MaxFreq. [wt% Ca]	SpLow [wt% Ca × %]	SpHigh [wt% Ca × %]
$LepR^{+/+}$	20.672	5.871	5.320	20.997	1.239	-0.323
	18.705	5.142	5.644	19.212	2.557	0.339
	19.417	5.532	4.910	19.846	3.380	1.327
Average	**19.958 ± 0.996**	**5.515 ± 0.365**	**5.291 ± 0.368**	**20.019 ± 0.905**	**2.392 ± 1.080**	**0.447 ± 0.830**[§]
$LepR^{-/-}$	20.108	5.189	5.678	20.804	3.169	-0.296
	21.569	5.506	5.382	22.342	3.250	-0.459
	20.400	5.527	5.391	21.023	2.504	-0.122
Average	**20.692 ± 0.773**	**5.407 ± 0.189**	**5.484 ± 0.168**	**21.389 ± 0.832**	**2.974 ± 0.409**	**-0.292 ± 0.169**[§]

[§] *SpHigh presented both positive and negative deviation in the area-equivalent Gaussian curve with respect to the acquired histogram, hence the standard deviation is higher than the mean.*

Table S4. Pixel count in qBEI images of the femurs in different Ca concentration ranges, normalized by the total number of pixels in the 10-30 wt% Ca range.

Group	10-15 wt% Ca [%]	15-20 wt% Ca [%]	20-25 wt% Ca [%]	25-30 wt% Ca [%]
$LepR^{+/+}$	4.11	33.54	58.72	3.62
	8.37	54.28	36.78	0.57
	8.61	47.51	41.63	2.25
Average	**7.03 ± 2.53**	**45.11 ± 10.57**	**45.71 ± 11.53**	**2.15 ± 1.53**
$LepR^{-/-}$	5.83	35.42	56.52	2.24
	4.69	18.07	67.17	10.07
	5.87	34.24	56.64	3.25
Average	**5.46 ± 0.67**	**29.24 ± 9.70**	**60.11 ± 6.12**	**5.18 ± 4.26**

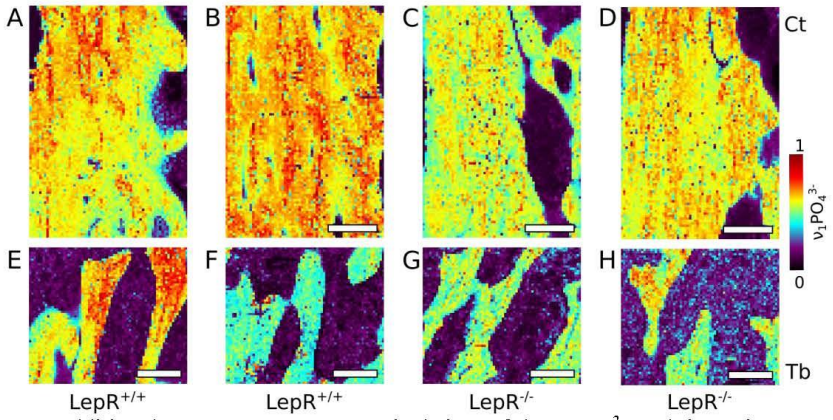

Figure S4. Additional Raman maps (10 µm pixel size) of the $\nu_1PO_4^{3-}$ peak intensity (normalized by the maximum value registered in the map) acquired in femoral cortical (Ct) (A-D) and trabecular (Tb) bone (E-H) in $LepR^{+/+}$ (A-B, E-F) and $LepR^{-/-}$ animals (C-D, G-H). Scale bars are 200 µm.

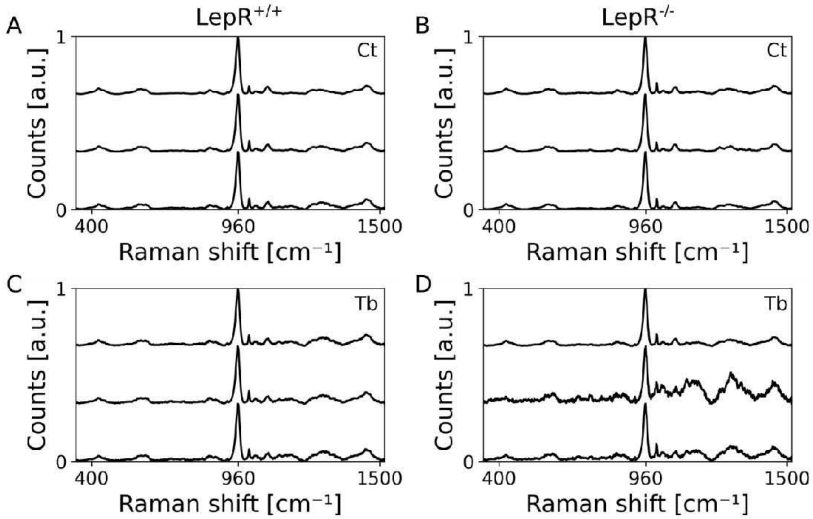

Figure S5. Average spectra of the Raman maps (10 µm pixel size) (resin region excluded, counts normalized by the maximum value registered in the map) acquired in femoral cortical (Ct) (A-B) and trabecular (Tb) bone (C-D) in $LepR^{+/+}$ (A, C) and $LepR^{-/-}$ animals (B, D).

Table S5. Mineral-to-matrix ratio ($\nu_2PO_4^{3-}$/amide III; $\nu_1PO_4^{3-}$/Phe), carbonate-to-phosphate ratio ($CO_3^{2-}/\nu_2PO_4^{3}$) and mineral crystallinity (1/FWHM) computed in the Raman maps with 10 μm pixel size acquired in the femurs.

Group	Region	$\nu_2PO_4^{3-}$/amide III	$\nu_1PO_4^{3-}$/Phe	$CO_3^{2-}/\nu_2PO_4^{3-}$	1/FWHM
$LepR^{+/+}$	Cortical	0.429	5.221	1.067	0.075
		0.545	5.295	0.997	0.074
		0.673	7.001	0.999	0.073
Average		**0.549 ± 0.122**	**5.839 ± 1.007**	**1.021 ± 0.040**	**0.074 ± 0.001**
$LepR^{-/-}$	Cortical	0.597	5.388	0.967	0.075
		0.609	6.080	0.982	0.073
		0.570	5.060	0.972	0.074
Average		**0.592 ± 0.020**	**5.509 ± 0.521**	**0.974 ± 0.007**	**0.074 ± 0.001**
$LepR^{+/+}$	Trabecular	0.328	4.668	1.310	0.074
		0.388	4.460	1.061	0.073
		0.406	5.168	1.015	0.074
Average		**0.374 ± 0.041**	**4.766 ± 0.364**	**1.129 ± 0.159**	**0.074 ± 0.000**
$LepR^{-/-}$	Trabecular	0.274	3.297	1.441	0.075
		0.160	2.653	2.727	0.076
		0.481	4.860	1.027	0.075
Average		**0.305 ± 0.163**	**3.603 ± 1.135**	**1.732 ± 0.887**	**0.075 ± 0.001**

Table S6. Mineral-to-matrix ratio ($\nu_2PO_4^{3-}$/amide III; $\nu_1PO_4^{3-}$/Phe), carbonate-to-phosphate ratio ($CO_3^{2-}/\nu_2PO_4^{3}$) and mineral crystallinity (1/FWHM) computed in Raman maps with 1 μm pixel size acquired in 50 × 100 μm^2 ROIs where bone interfaces with mineralized cartilage (MC) islands in femoral cortical bone. Only data points within the 5-95% quantiles with respect to the $\nu_1PO_4^{3-}$ peak intensity were considered.

Group	ROI	$\nu_2PO_4^{3-}$/amide III	$\nu_1PO_4^{3-}$/Phe	$CO_3^{2-}/\nu_2PO_4^{3-}$	1/FWHM
$LepR^{+/+}$	Entire map	0.735	7.494	1.117	0.075
		0.930	9.336	1.169	0.073
		0.833	11.013	1.121	0.073
Average		**0.832 ± 0.097**	**9.281 ± 1.760**	**1.136 ± 0.029**	**0.074 ± 0.001**
$LepR^{-/-}$	Entire map	1.093	10.235	1.080	0.073
		0.874	12.204	1.100	0.073
		1.061	7.050	1.049	0.074
Average		**1.009 ± 0.119**	**9.830 ± 2.600**	**1.076 ± 0.026**	**0.074 ± 0.000**
$LepR^{+/+}$	Bone	0.728	7.331	1.134	0.075
		0.765	8.350	1.117	0.073
		0.794	10.660	1.099	0.073
Average		**0.762 ± 0.033**	**8.780 ± 1.706**	**1.117 ± 0.018**	**0.074 ± 0.001**
$LepR^{-/-}$	Bone	1.020	9.941	1.054	0.073
		0.720	10.526	1.065	0.073
		0.859	6.659	1.012	0.074
Average		**0.866 ± 0.150**	**9.042 ± 2.084**	**1.044 ± 0.028**	**0.073 ± 0.000**
$LepR^{+/+}$	MC	0.753	7.686	1.069	0.075
		1.156	10.294	1.215	0.073
		0.981	12.586	1.194	0.074
Average		**0.963 ± 0.202**	**10.189 ± 2.451**	**1.159 ± 0.079**	**0.074 ± 0.001**
$LepR^{-/-}$	MC	1.233	11.111	1.108	0.073
		0.998	13.202	1.146	0.073
		1.306	7.419	1.069	0.074
Average		**1.179 ± 0.161**	**10.577 ± 2.928**	**1.108 ± 0.038**	**0.074 ± 0.000**

Table S7. Mineral-to-matrix ratio ($\nu_2PO_4^{3-}$/amide III; $\nu_1PO_4^{3-}$/Phe), carbonate-to-phosphate ratio ($CO_3^{2-}/\nu_2PO_4^{3-}$) and mineral crystallinity (1/FWHM) computed in Raman maps with 1 µm pixel size acquired in 50 × 100 µm^2 ROIs where bone interfaces with mineralized cartilage (MC) islands in femoral trabecular bone. Only data points within the 5-95% quantiles with respect to the $\nu_1PO_4^{3-}$ peak intensity were considered.

Group	ROI	$\nu_2PO_4^{3-}$/amide III	$\nu_1PO_4^{3-}$/Phe	$CO_3^{2-}/\nu_2PO_4^{3-}$	1/FWHM
LepR$^{+/+}$	Entire map	0.566	6.187	0.965	0.073
		0.596	7.775	0.935	0.074
		0.771	9.264	1.002	0.074
Average		**0.644 ± 0.111**	**7.742 ± 1.538**	**0.968 ± 0.034**	**0.073 ± 0.000**
LepR$^{-/-}$	Entire map	0.510	7.750	0.986	0.074
		0.397	8.355	1.096	0.074
		0.752	6.110	0.948	0.075
Average		**0.553 ± 0.181**	**7.405 ± 1.162**	**1.010 ± 0.077**	**0.074 ± 0.000**
LepR$^{+/+}$	Bone	0.543	5.250	0.908	0.073
		0.555	6.348	0.917	0.074
		0.642	7.749	0.950	0.074
Average		**0.580 ± 0.054**	**6.449 ± 1.253**	**0.925 ± 0.022**	**0.073 ± 0.000**
LepR$^{-/-}$	Bone	0.456	6.803	0.948	0.074
		0.351	6.730	1.056	0.074
		0.518	4.809	0.927	0.075
Average		**0.442 ± 0.084**	**6.114 ± 1.130**	**0.977 ± 0.069**	**0.074 ± 0.000**
LepR$^{+/+}$	MC	0.614	7.007	1.034	0.073
		0.638	9.587	0.958	0.074
		0.896	10.755	1.045	0.074
Average		**0.716 ± 0.156**	**9.116 ± 1.918**	**1.012 ± 0.047**	**0.074 ± 0.000**
LepR$^{-/-}$	MC	0.563	8.904	1.029	0.074
		0.448	9.722	1.120	0.075
		1.046	7.368	0.941	0.074
Average		**0.686 ± 0.318**	**8.665 ± 1.196**	**1.030 ± 0.089**	**0.074 ± 0.000**

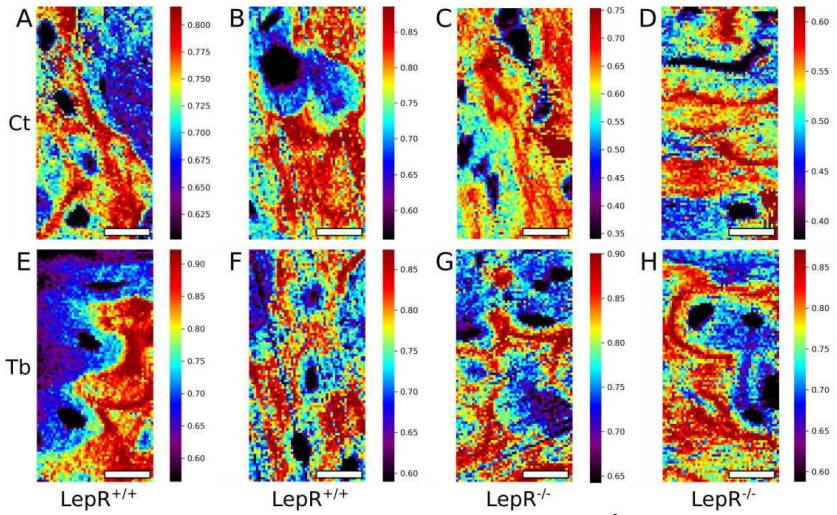

Figure S6. Additional Raman maps (1 µm pixel size) of the $\nu_1PO_4^{3-}$ peak intensity (restricted to 5%-95% quantile range) acquired in femoral cortical (Ct) (A-D) and trabecular (Tb) bone (E-H) in LepR$^{+/+}$ (A-B, E-F) and LepR$^{-/-}$ animals (C-D, G-H). Scale bars are 20 µm.

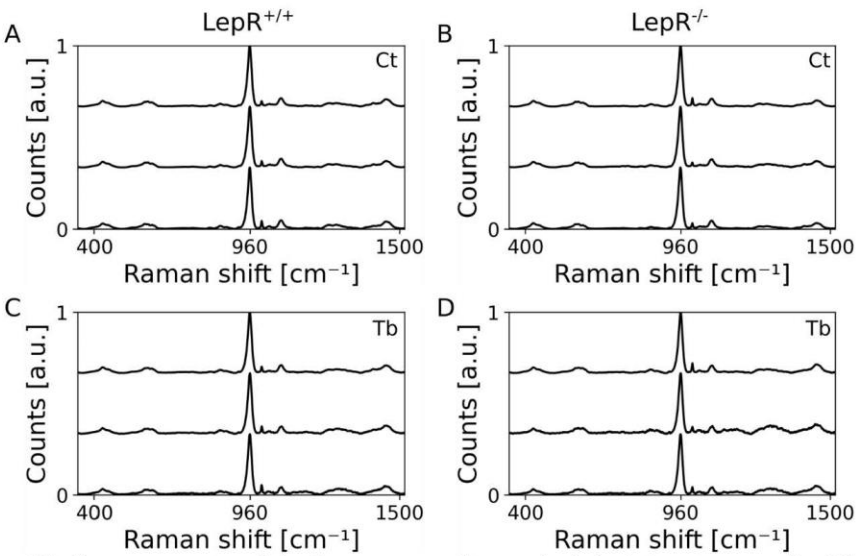

Figure S7. Average spectra of the Raman maps (1 μm pixel size) (counts normalized by the maximum value registered in the map, restricted to 5%-95% quantile range) acquired in femoral cortical (Ct) (A-B) and trabecular (Tb) bone (C-D) in $LepR^{+/+}$ (A, C) and $LepR^{-/-}$ animals (B, D).

Table S8. RPI measurements in the proximal femurs. Each value represents the average of three measurements carried out in each sample.

Group	IDI 1st [µm]	US 1st [N/µm]	CID 1st [µm]	TID [µm]	IDI [µm]	Avg CID [µm]	Avg ED [µJ]	Avg US [N/µm]
$LepR^{+/+}$	37.7	0.357	4.00	40.3	6.40	1.27	8.7	0.377
	40.7	0.373	4.33	43.3	6.27	1.37	8.8	0.410
	37.7	0.373	3.67	40.7	5.60	1.23	8.8	0.387
	48.3	0.277	4.00	51.7	6.40	1.33	10.5	0.287
	43.7	0.307	3.33	46.7	5.57	1.23	9.7	0.320
	44.0	0.320	4.33	47.3	6.43	1.93	11.3	0.330
Average	**42.0 ± 4.2**	**0.334 ± 0.040**	**3.94 ± 0.39**	**45.0 ±4.4**	**6.11 ± 0.41**	**1.39 ± 0.27**	**9.6 ± 1.1**	**0.352 ± 0.047**
$LepR^{-/-}$	35.3	0.400	3.33	38.0	5.73	1.13	9.0	0.427
	37.3	0.350	4.33	40.3	6.20	1.17	8.1	0.363
	43.7	0.307	4.67	46.3	6.30	1.43	10.7	0.360
	41.3	0.290	3.00	44.3	5.50	1.10	10.6	0.293
	47.0	0.307	4.00	50.0	6.40	1.50	10.7	0.320
	40.0	0.350	3.33	43.0	5.80	1.20	11.3	0.357
Average	**40.8 ± 4.2**	**0.334 ± 0.041**	**3.78 ± 0.66**	**43.7 ± 4.3**	**5.99 ± 0.36**	**1.26 ± 0.17**	**10.1 ± 1.2**	**0.353 ± 0.045**

Table S9. Values of parietal bones thickness, sagittal suture width and length, and tissue mineral density (TMD) measured in micro-CT data.

Group	Parietal bones thickness [μm]	Sagittal suture width [μm]	Sagittal suture length [mm]	TMD [g/cm^3]
LepR$^{+/+}$	630.872	148.664	8.157	0.828
	593.808	159.879	8.937	0.919
	593.558	151.256	7.763	0.945
	585.912	167.677	10.006	0.775
	590.832	173.795	8.873	0.969
	604.288	154.978	8.309	0.898
	629.878	153.955	9.289	0.866
	653.443	169.995	7.951	0.824
Average	**610.324 ± 24.582**	**160.025 ± 9.380**	**8.661 ± 0.757**	**0.878 ± 0.066**
LepR$^{-/-}$	548.112	138.922	7.422	0.847
	550.293	133.938	7.357	0.855
	544.443	132.527	6.959	0.866
	549.523	126.912	8.332	0.914
	561.538	131.613	6.745	0.855
	563.577	144.168	7.462	0.869
	570.408	137.640	8.087	0.941
	575.840	130.403	7.301	0.819
Average	**557.967 ± 11.518*** **	**134.515 ± 5.475*** **	**7.458 ± 0.528** **	**0.871 ± 0.039**

** and *** denote statistical significance with respect to the control group ($p < 0.01$ and $p < 0.001$, respectively).

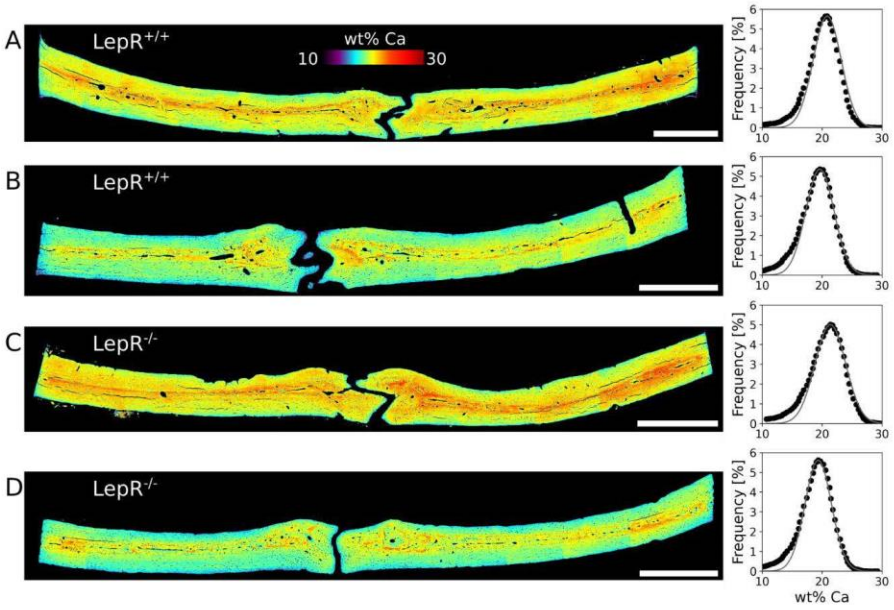

Figure S8. Additional qBEI images (pixel intensity converted in Ca concentration) and relative histograms (black dots correspond to acquired point, and dark grey line corresponds to area-equivalent Gaussian curve) in the calvaria of LepR$^{+/+}$ (A-B) and LepR$^{-/-}$ (C-D) animals. Scale bars are 1 mm.

Table S10. Parameters expressing bone mineral density distribution (BMDD) evaluated by qBEI in the calvaria.

Group	Ca-Mean [wt% Ca]	FWHM [wt% Ca]	MaxFreq. [%]	Ca-MaxFreq. [wt% Ca]	SpLow [wt% Ca × %]	SpHigh [wt% Ca × %]
LepR$^{+/+}$	20.020	5.541	5.653	20.844	3.087	-1.503
	18.967	5.553	5.369	19.628	3.317	-0.468
	19.592	5.007	5.646	20.197	3.696	0.252
Average	**19.526 ± 0.530**	**5.367 ± 0.312**	**5.556 ± 0.162**	**20.223 ± 0.608**	**3.367 ± 0.308**	**-0.573 ± 0.882**[§]
LepR$^{-/-}$	20.588	6.036	5.010	21.377	3.269	-1.001
	18.864	5.210	5.618	19.349	2.992	0.217
	19.413	6.025	5.086	20.140	3.012	-1.014
Average	**19.622 ± 0.880**	**5.757 ± 0.474**	**5.238 ± 0.332**	**20.289 ± 1.022**	**3.091 ± 0.154**	**-0.599 ± 0.707**[§]

[§] *SpHigh presented both positive and negative deviation in the area-equivalent Gaussian curve with respect to the acquired histogram, hence the mean is negative and the standard deviation is higher than the mean.*

Table S11. Pixel count in qBEI images of the calvaria in different Ca concentration ranges, normalized by the total number of pixels in the 10-30 wt% Ca range.

Group	10-15 wt% Ca [%]	15-20 wt% Ca [%]	20-25 wt% Ca [%]	25-30 wt% Ca [%]
$LepR^{+/+}$	4.97	39.00	54.38	1.64
	9.23	50.54	39.63	0.60
	5.45	46.18	47.35	1.02
Average	**6.55 ± 2.33**	**45.24 ± 5.83**	**47.12 ± 7.38**	**1.08 ± 0.53**
$LepR^{-/-}$	5.40	31.32	58.67	4.61
	7.82	55.18	36.58	0.42
	8.39	44.26	46.01	1.33
Average	**7.20 ± 1.59**	**43.59 ± 11.94**	**47.09 ± 11.09**	**2.12 ± 2.20**

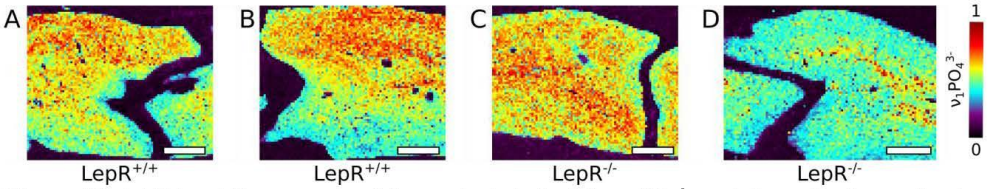

Figure S9. Additional Raman maps (10 µm pixel size) of the $\nu_1PO_4^{3-}$ peak intensity (normalized by the maximum value registered in the map) acquired in the calvaria of $LepR^{+/+}$ (A-B) and $LepR^{-/-}$ animals (C-D). Scale bars are 200 µm.

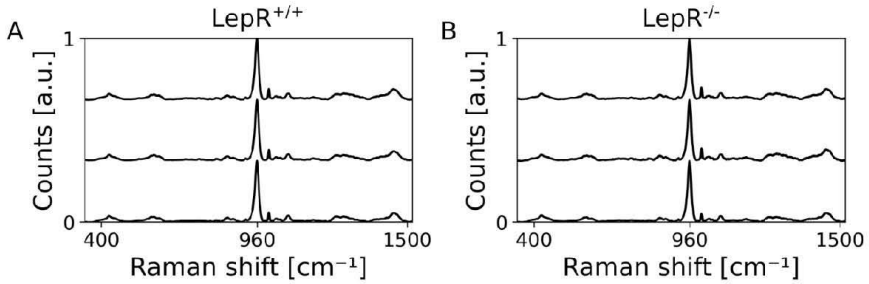

Figure S10. Average spectra of the Raman maps (10 µm pixel size) (resin region excluded, counts normalized by the maximum value registered in the map) acquired in the calvaria of $LepR^{+/+}$ (A) and $LepR^{-/-}$ animals (B).

Table S12. Mineral-to-matrix ratio ($\nu_2PO_4^{3-}$/amide III; $\nu_1PO_4^{3-}$/Phe), carbonate-to-phosphate ratio ($CO_3^{2-}/\nu_2PO_4^{3}$) and mineral crystallinity (1/FWHM) computed in Raman maps with 10 µm pixel size acquired in the calvaria.

Group	$\nu_2PO_4^{3-}$/amide III	$\nu_1PO_4^{3-}$/Phe	$CO_3^{2-}/\nu_2PO_4^{3-}$	1/FWHM
$LepR^{+/+}$	0.588	6.299	0.769	0.079
	0.532	5.457	0.851	0.080
	0.500	5.557	0.779	0.080
Average	**0.540 ± 0.045**	**5.771 ± 0.460**	**0.800 ± 0.045**	**0.080 ± 0.001**
$LepR^{-/-}$	0.704	7.560	0.653	0.079
	0.489	4.819	0.784	0.080
	0.501	4.961	0.836	0.080
Average	**0.565 ± 0.121**	**5.780 ± 1.543**	**0.758 ± 0.095**	**0.080 ± 0.000**

Table S13. Mineral-to-matrix ratio ($\nu_2PO_4^{3-}$/amide III; $\nu_1PO_4^{3-}$/Phe), carbonate-to-phosphate ratio ($CO_3^{2-}/\nu_2PO_4^{3}$) and mineral crystallinity (1/FWHM) computed in Raman maps with 1 μm pixel size acquired in 50 × 100 μm^2 ROIs where bone interfaces with hyper-mineralized (HM) bone in the calvaria. Only data points within the 5-95% quantiles with respect to the $\nu_1PO_4^{3-}$ peak intensity were considered.

Group	ROI	$\nu_2PO_4^{3-}$/amide III	$\nu_1PO_4^{3-}$/Phe	$CO_3^{2-}/\nu_2PO_4^{3-}$	1/FWHM
$LepR^{+/+}$	Entire map	0.880	3.995	0.929	0.079
		0.745	6.937	0.951	0.077
		0.712	4.863	0.843	0.079
Average		**0.779 ± 0.089**	**5.265 ± 1.512**	**0.908 ± 0.057**	**0.078 ± 0.001**
$LepR^{-/-}$	Entire map	0.885	4.699	0.851	0.078
		0.797	5.421	0.836	0.077
		0.709	5.746	0.881	0.078
Average		**0.797 ± 0.088**	**5.289 ± 0.535**	**0.856 ± 0.023**	**0.078 ± 0.001**
$LepR^{+/+}$	Bone	0.803	3.915	0.906	0.079
		0.775	7.235	0.954	0.076
		0.639	4.345	0.838	0.079
Average		**0.739 ± 0.088**	**5.165 ± 1.805**	**0.900 ± 0.058**	**0.078 ± 0.001**
$LepR^{-/-}$	Bone	0.794	4.640	0.841	0.078
		0.705	4.671	0.818	0.078
		0.655	5.039	0.863	0.079
Average		**0.718 ± 0.070**	**4.783 ± 0.222**	**0.841 ± 0.022**	**0.078 ± 0.000**
$LepR^{+/+}$	HM bone	0.993	4.111	0.944	0.079
		0.825	7.533	0.960	0.076
		0.884	5.768	0.821	0.077
Average		**0.901 ± 0.086**	**5.804 ± 1.711**	**0.908 ± 0.076**	**0.077 ± 0.001**
$LepR^{-/-}$	HM bone	0.986	4.721	0.894	0.077
		0.971	7.044	0.839	0.076
		0.802	6.849	0.893	0.078
Average		**0.920 ± 0.102**	**6.205 ± 1.289**	**0.875 ± 0.032**	**0.077 ± 0.001**

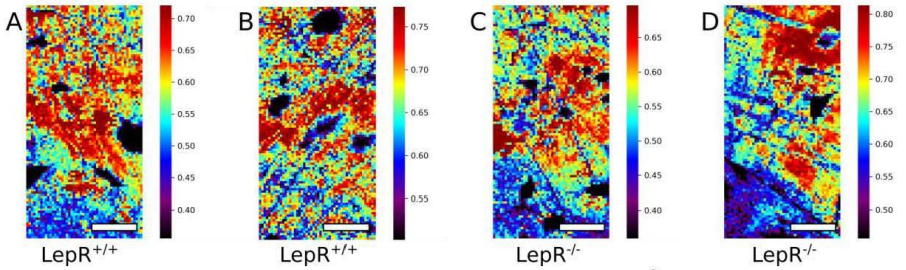

Figure S11. Additional Raman maps (1 μm pixel size) of the $\nu_1PO_4^{3-}$ peak intensity (restricted to 5%-95% quantile range) acquired in the calvaria of $LepR^{+/+}$ (A-B) and $LepR^{-/-}$ animals (C-D). Scale bars are 20 μm.

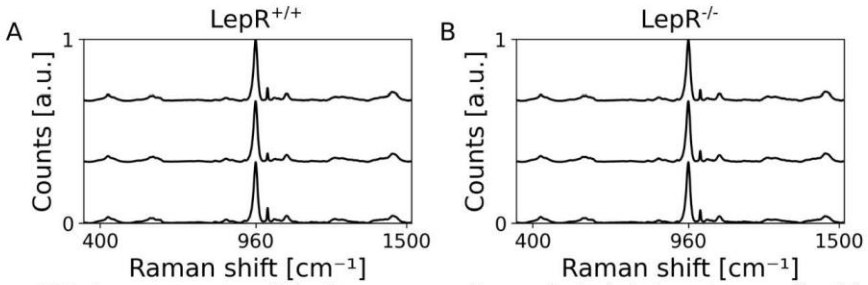

Figure S12. Average spectra of the Raman maps (1 μm pixel size) (counts normalized by the maximum value registered in the map, restricted to 5%-95% quantile range) acquired in the calvaria of $LepR^{+/+}$ (A) and $LepR^{-/-}$ animals (B).

Paper II

RESEARCH ARTICLE

JBMR PLUS Open Access ASBMR

Multimodal and Multiscale Characterization of the Bone-Bacteria Interface in a Case of Medication-Related Osteonecrosis of the Jaw

Chiara Micheletti,[1,2] Liza-Anastasia DiCecco,[1] Cecilia Larsson Wexell,[2,3,4] Dakota M. Binkley,[5] Anders Palmquist,[2] Kathryn Grandfield,[1,5] and Furqan A. Shah[1,2]

[1]Department of Materials Science and Engineering, McMaster University, Hamilton, Ontario, Canada
[2]Department of Biomaterials, Sahlgrenska Academy, University of Gothenburg, Gothenburg, Sweden
[3]Department of Oral and Maxillofacial Surgery, Skåne University Hospital, Lund, Sweden
[4]Department of Oral and Maxillofacial Surgery and Oral Medicine, Malmö University, Malmö, Sweden
[5]School of Biomedical Engineering, McMaster University, Hamilton, Ontario, Canada

ABSTRACT

Medication-related osteonecrosis of the jaw (MRONJ) is a known side effect of bisphosphonates (BPs). Although bacterial infection is usually present, the etiology of MRONJ remains unknown. Here we apply a multimodal and multiscale (micro-to-nano) characterization approach to investigate the interface between necrotic bone and bacteria in MRONJ. A non-necrotic bone sample was used as control. Both necrotic and non-necrotic bone samples were collected from the jaw of a female individual affected by MRONJ after using BPs for 23 years. For the first time, resin cast etching was used to expose bacteria at the necrotic site. The bone–bacteria interface was also resolved at the nanoscale by scanning transmission electron microscopy (STEM). Nanosized particulates, likely corresponding to degraded bone mineral, were often noted in close proximity to or enclosed by the bacteria. STEM also revealed that the bone–bacteria interface is composed of a hypermineralized front fading into a highly disordered region, with decreasing content of calcium and phosphorus, as assessed by electron energy loss spectroscopy (EELS). This, combined with the variation in calcium, phosphorus, and carbon across the necrotic bone–bacteria interface evaluated by scanning electron microscopy (SEM)-energy dispersive X-ray spectroscopy (EDX) and the lower mineral-to-matrix ratio measured by micro-Raman spectroscopy in necrotic bone, indicates the absence of a mineralization front in MRONJ. It appears that the bone–bacteria interface originates not only from uncontrolled mineralization but also from the direct action of bacteria degrading the bone matrix. © 2022 The Authors. *JBMR Plus* published by Wiley Periodicals LLC on behalf of American Society for Bone and Mineral Research.

Introduction

Skeletal disorders such as osteoporosis and cancer-related bone metastasis are often treated with bisphosphonates (BPs) because of their antiresorptive function.[1] By inhibiting osteoclastic activity and by binding to hydroxyapatite crystals, BPs inhibit hydroxyapatite breakdown[2] and alter the balance in bone remodeling by suppressing bone resorption[3] in favor of a net gain in bone mineral density (BMD).[4] However, treatment with BPs for a long period of time or in a high dosage has been associated with a greater risk of developing osteonecrosis of the jaw (ONJ),[5–9] often referred to as medication-related ONJ (MRONJ). The American Association of Oral and Maxillofacial Surgeons (AAOMS) classifies MRONJ as the presence in the jaw of exposed bone or bone that can be probed through an intra- or extraoral fistula that does not heal within 8 weeks after identification and appropriate intervention, in the absence of metastasis or history of radiation therapy to the craniofacial region.[7, 10, 11] Histological examinations of individuals diagnosed with MRONJ confirm the presence of necrotic bone and often show signs of infection.[12] The pathogenesis of MRONJ remains unclear, but preclinical and clinical studies indicate that infection plays an important role, although it is still debated whether MRONJ precedes or follows oral infection.[13–15]

Overall, it appears that several factors contribute to the onset of MRONJ. Infection in the oral cavity can be triggered by dental traumas and procedures, for example, tooth extraction, which are often needed to resolve the damage caused by previous

Received in original form July 18, 2022; revised form August 25, 2022; accepted October 16, 2022.
Address correspondence to: Furqan A. Shah, Department of Biomaterials, Sahlgrenska Academy, University of Gothenburg, Gothenburg, Sweden.
Email: furqan.ali.shah@biomaterials.gu.se
Additional supporting information may be found online in the Supporting Information section.
JBMR® Plus (WOA), Vol. 6, No. 12, December 2022, e10693.
DOI: 10.1002/jbm4.10693

infections (e.g., dental caries) or diseases such as periodontitis.[16] Infection and, consequently, microbial biofilm formation can lead to bone destruction despite the presence of BPs.[15] On the other hand, suppression of bone resorption by BPs may cause a lower bone turnover and a less responsive ("frozen") bone surface incapable of adequately contrasting microbial colonization.[6, 15] High local concentrations of BPs can be toxic to the soft tissue and to cells involved in the local immune response, in turn compromising the healing of the oral mucosa and leading to persistent infection.[15, 17] Wound healing could even be worsened by compromised angiogenesis, which is sometimes reported for BPs.[13] It is unclear whether microbial biofilm pathogens are able to directly resorb bone, but some in vitro and ex vivo work has presented such a possibility.[18] In other diseases of the oral cavity such as periodontitis, microbial biofilms play a critical role in tissue breakdown.[16, 19] The likelihood of developing MRONJ under BP treatment probably depends on a combination of environmental, metabolic, and genetic factors, with impaired general condition, systemic chronic inflammation, diabetes, smoking, and obesity often seen as risk factors.[11, 20, 21]

Here we present a case study of a female individual diagnosed with MRONJ after a 23-year-long treatment with BPs (alendronate) for osteoporosis. Specifically, we focus on examining the interface between necrotic bone and bacteria from a structural and compositional point of view at different length scales, from the micro- to the nanoscale. As appropriate, necrotic bone was also compared to non-necrotic bone retrieved from unexposed areas of the jaw. The materials science approach of multimodal, multiscale analytic characterization applied to a clinically relevant issue presented the opportunity to probe the relationship between MRONJ, bacterial infection, and bone mineralization from a less conventional perspective. This in turn offered new insights into possible events taking place where necrotic bone and bacteria meet, including a potentially direct role of bacteria in degrading the bone matrix, never demonstrated in vivo to date.

Materials and methods

Patient history

Necrotic and non-necrotic bone samples were collected from the jaw of a 73-year-old osteoporotic female with a low body mass index (BMI) (<18 kg/m^2) and 23 years of exposure to BPs (alendronate tablets) administered orally, suffering from MRONJ in both the upper and lower jaws. A schematic timeline of clinically relevant events is presented in Figure 1. Two years before the bone sampling procedures, the upper right second premolar and the upper right canine were extracted (Figure S1). Healing of the area was absent, and the patient was diagnosed with MRONJ at the upper right jaw. MRONJ was also present at both sides of the lower jaw. The patient stopped smoking (after over 50 years) and taking alendronate 1.5 years before the bone sampling procedure.

Sample collection, histology, and microbiology

The patient was treated with 1.6 g phenoxymethylpenicillin orally for 3.5 weeks prior to surgery and sampling. Under general anesthesia, bone samples were collected from the exposed and necrotic areas (upper jaw and lower jaw, right side) ($n = 2$) and from intact/unaffected areas (upper jaw, left side) ($n = 1$)

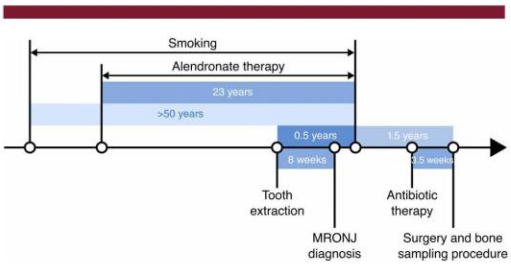

Fig. 1. Timeline (not to scale) of clinically relevant events preceding bone sampling procedure due to medication-related osteonecrosis of the jaw (MRONJ) diagnosis.

(Figure S1). In the upper jaw, a crestal incision was made from the left side close to the midline to the second upper molar on the right side. A large mobile sequester of bone, 2.5 × 2.5 × 2 cm^3, was removed. Swabbing for microbiology analyses was made directly at the bottom of the lesion. A small cortical bone sample was collected from the non-exposed area on the left side of the upper jaw. In the lower jaw, six teeth were extracted. After a crestal incision and uncovering of the jawbone, large areas of necrotic tissue were noted and removed.

The samples were fixed by immersion in 10% neutral buffered formalin, dehydrated, and resin embedded (LR White, London Resin Company, UK). Toluidine blue–stained ground sections were prepared by sawing and grinding to a thickness of 30–40 μm for histological examination in a light microscope (Nikon Eclipse E600) using a condenser with numerical aperture (NA) set to 1 and ×4, ×10, ×20, and ×40 objectives (0.13, 0.3, 0.5, and 0.75 NA, respectively).

The study was approved by the Regional Ethical Review Board of Gothenburg (Dnr 424–08), including sampling from apparently non-necrotic areas, as part of the intervention plan for dental restoration established by the clinician.

Scanning electron microscopy and energy dispersive X-ray spectroscopy

Backscattered electron (BSE) scanning electron microscopy (SEM) images were acquired in an environmental SEM (Quanta 200, FEI Company, The Netherlands) operated at 20 kV accelerating voltage, 1 Torr water vapor pressure, and 10 mm working distance. The same instrument settings were used for energy dispersive X-ray spectroscopy (EDX). Three line scans across the bone–resin interface were acquired for each sample using 20 accumulations per spectrum (AZtec 5.0, Oxford Instruments, UK). The interaction area and volume for the elements considered (C, Ca, and P) were estimated to range between 53–66 μm^2 and 183–257 μm^3, respectively. These values were obtained from the probed radius and volume for non-backscattered electrons (here considered as the range upper limit, as an approximation for C), and P and Ca (here considered as the range lower limit) computed by Howell and Boyde.[22] The interaction area was estimated as the area of a circle using the radius computed by Howell and Boyde.[22] EDX data were smoothed by Savitzky–Golay filtering using the "savgol_filter" function (21 coefficients, fourth-order polynomial) available in the "scipy.signal" library in Python 3.8.10. The width of the region

where C, Ca, and P presented the highest variation was measured as the width of the peak in the first-order derivative of the unsmoothed data, computed using the "savgol_filter" function (21 coefficients, fourth-order polynomial, first-order derivative order). The region of the C, Ca, and P plots where significant variation occurred was fitted with a line using "numpy.polyfit" in Python 3.8.10 in order to obtain the slope of the line.

Micro-Raman spectroscopy

Micro-Raman spectroscopy was performed using a confocal Raman microscope (Renishaw inVia Qontor) equipped with a 633 nm laser and LiveTrack focus-tracking technology. The laser was focused on the surface using a ×100 objective (0.9 NA). Following the definitions of lateral resolution[23] ($\Delta x = 0.61\lambda/NA$) and depth of focus[23, 24] $\left(\Delta z = \pm\frac{4.4n\lambda}{2\pi(NA)^2}\right)$, the lateral ($\Delta x$) and vertical ($2|\Delta z|$) resolutions were determined to be equal to 0.4 and 1.1 μm, respectively, resulting in a probed volume (half-ellipsoid) of 0.7 μm^3. Line scans of 11 points each were acquired at 1 μm step size across the bone–resin interface. Each point measurement was acquired with a 3 s exposure time and five accumulations per spectrum and preceded by a 60 s bleaching. Five line scans per sample were acquired in different locations. Spectra were denoised by fast Fourier transform (FFT) using the "scipy.fft" module available in the "scipy" library in Python 3.8.10. The noise threshold was set as the average signal in the 340–400 cm^{-1} region of the spectrum multiplied by a constant value k ($k = 2.5$ in non-necrotic bone sample; $k = 5$ in necrotic bone samples). Spectra were then truncated (700–1050 cm^{-1}) and baseline-subtracted by fitting a fifth-order polynomial using the "baseline_poly" function available in the "rampy" library in Python 3.8.10. Mineral content in the collagen matrix was estimated as the mineral-to-matrix ratio, taken as the ratio between the peak intensity in the phosphate band (ν_1 PO_4^{3-}, 930–980 cm^{-1}) and in the phenylalanine band (Phe, 1000–1005 cm^{-1}).[25] Mineral-to-matrix ratios computed from spectra acquired in the bone region ($n = 5$) were averaged in each line scan and then averaged for each sample.

Resin cast etching

Samples were immersed in 9% H_3PO_4 for 30 s, quickly rinsed in deionized H_2O (for 2 s), immersed in 5% NaOCl for 5 min, rinsed again in deionized H_2O for 30 s, and allowed to air-dry overnight. After Au sputter coating (~10 nm thickness), secondary electron (SE) imaging was carried out in a high-vacuum SEM (Ultra 55 FEG, Leo Electron Microscopy, UK) operated at 3 kV.

Nano-analytical electron microscopy

An electron transparent sample of necrotic bone interfacing with the bacteria-invaded resin for transmission electron microscopy (TEM) and scanning TEM (STEM) analyses was prepared by in situ lift-out in a dual-beam focused ion beam (FIB) instrument (Zeiss NVision 40, Carl Zeiss AG, Oberkochen, Germany) equipped with a 30 kV Ga ion column, a gas injection system, and a micromanipulator (Kleindiek Nanotechnik GmbH, Reutlingen, Germany), following published protocols.[26] The region of interest for the in situ lift-out was selected by prior BSE-SEM imaging in a high-vacuum SEM (FEI Magellan 400 XHR, Thermo Fisher Scientific, Hillsboro, OR, USA) operated at 10 kV, after the samples were sputter coated with Au (~10 nm thickness).

TEM and STEM imaging were performed at 200 kV (Talos 200X, Thermo Fisher Scientific, Waltham, MA, USA) and 300 kV (FEI Titan 80–300 LB, Thermo Fisher Scientific, Hillsboro, OR, USA), respectively. TEM images were collected in bright field (BF) mode. STEM images were acquired using a high-angle annular dark-field (HAADF) detector.

Particulate analysis

Particles observed in HAADF-STEM images in the bacteria-invaded region were measured using Fiji[27] (NIH, Bethesda, MD, USA) with the "Analyze particles" command after applying a bandpass filter and a threshold. The mean diameter of each particle was obtained by averaging the major and minor axes of the ellipse fitted to the particle by the software. The average particle size was computed by averaging the mean diameter of 127 distinct particles.

Collagen banding measurement

The average D-spacing in the collagen banding pattern was measured from HAADF-STEM images using Fiji[27] (NIH, Bethesda, MD, USA). Five fibrils in different locations were examined. For each fibril, the histogram profile was extracted from a 20-pixel-thick line (0.85–1.19 nm pixel size). The average length of the period (i.e., overlap and gap regions) in each fibril was obtained by dividing the total length between the first and sixth minima in the histogram profile by the number of periods included, that is, five. The average D-spacing was computed as the mean of the values measured for each fibril.

Electron energy loss spectroscopy

Electron energy loss spectroscopy (EELS) was performed in a STEM instrument (FEI Titan 80–300, Thermo Fisher Scientific, Hillsboro, OR, USA) equipped with a Gatan Tridiem spectrometer (Gatan, Inc., Pleasanton, CA, USA). The microscope was operated at 300 kV with an 8 mrad convergence semi-angle and a 25 mrad collection semi-angle. EELS maps across the bone–bacteria interface were acquired with an energy dispersion of 0.5 eV/channel, a 0.05 s exposure time, and a 5 nm step size. EELS spectral images were denoised by principal component analysis (PCA) and background-subtracted in Gatan Microscopy Suite (GMS) 3.4.3 (Gatan, Inc., Pleasanton, CA, USA). Elemental maps for C, Ca, and P were obtained by extracting the signal in the peak energy window of each element. From the elemental maps, variation in elemental concentration across the interface was obtained by considering a 10-pixel-thick line scan.

Selected area electron diffraction

Selected area electron diffraction (SAED) patterns were acquired using a 40 μm aperture (illuminating an area of about 250 nm in the sample) in a TEM instrument (Talos 200X, Thermo Fisher Scientific, Waltham, MA, USA) operated at 200 kV.

Statistical analysis

Final values of average measurements are reported as mean values ± standard deviations. When comparing non-necrotic and necrotic bone, statistical significance was evaluated by a Mann–Whitney U test ($\alpha = 0.05$) in Python 3.8.10 using the "scipy.stats" library.

Results and Discussion

Clinical and microscale manifestation of MRONJ

Histology confirmed the necrosis of the affected areas in the jaw, with most vascular spaces filled with bacteria rather than blood cells, and empty osteocyte lacunae, which is a characteristic histological trait of MRONJ[28] (Figure 2A, B, Figure S2). On the other hand, bone from the unaffected area appears normal, that is, non-necrotic (Figure 2C, Figure S2). Microbial swab demonstrated the abundant growth of *Neisseria* and *Prevotella*, including black pigmented fusiform rods, and the relatively abundant growth of *Haemophilus*-like rods.

As was already visible in histological images, the bone surface resolved in BSE-SEM presented a jagged outline in bone retrieved from necrotic areas (Figures 2D, E, G, H, Figure S3), whereas the contour was generally smooth in non-necrotic bone (Figures 2F, I, Figure S3). The presence of irregular, scalloped borders has often been reported for MRONJ.[12, 14] However, this surface appearance remains poorly understood and rather paradoxical because such irregular edges are usually indicative of ongoing osteoclast-mediated resorption, which should be largely suppressed by BPs.[3] Moreover, if the irregular edges were due to resorption only, this would not explain the difference between the surface appearance of necrotic and non-necrotic bone. Therefore, we propose that it can be explained by an active role of bacteria in the degradation of bone extracellular matrix, as discussed subsequently.

Closer examination by BSE-SEM of some osteocyte lacunae in necrotic bone revealed the presence of mineral inclusions, most likely hydroxyapatite-based. Some rhomboidal nodules, analogous in shape and size to magnesium whitlockite crystals previously reported,[29] were also noted (Figure S4). Although magnesium whitlockite has been described for pathological calcification in various tissues,[30] whether BPs (in)directly contribute to mineralization in whitlockite rather than apatite remains to be determined.

From SE-SEM imaging after resin cast etching, bacteria were clearly visible in the resin region surrounding necrotic bone (Figure 3, Figure S5), corroborating the existence of an extensive biofilm[31] (Figure 3A, B). No evidence of mineralized or mineral-filled bacteria was found. Cocci, bacilli, and filamentous bacteria were observed (Figure 3C), in good agreement with the

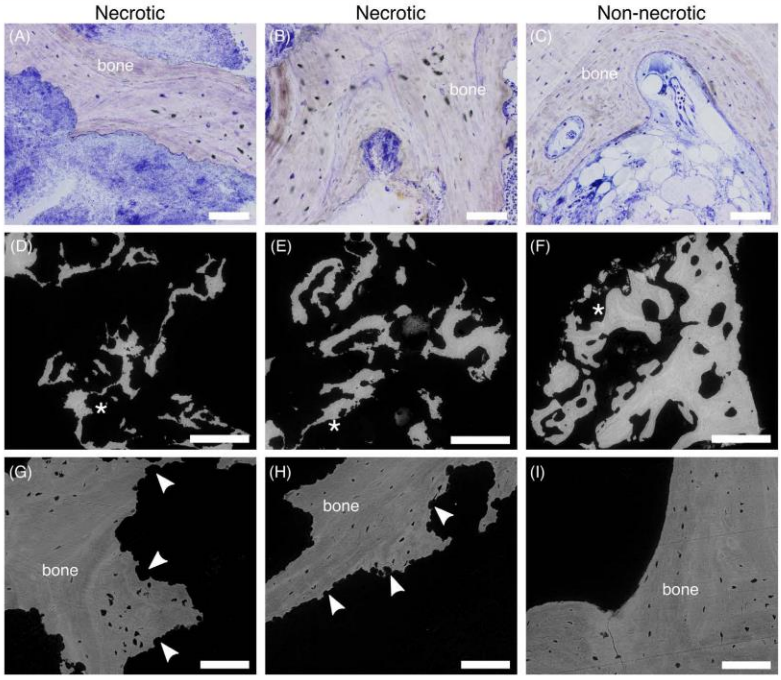

Fig. 2. Histology and BSE-SEM. Histological sections of necrotic (A, B) and non-necrotic (C) bone (images acquired with a ×20 objective). The space interfacing with bone is occupied by an extensive biofilm in necrotic bone, whereas bone marrow surrounds non-necrotic bone. Empty osteocyte lacunae in necrotic bone are indicated by absence of staining. Overview BSE-SEM images of necrotic (D, E) and non-necrotic (F) bone, and higher magnification images (G and H for necrotic bone, I for non-necrotic bone), corresponding to areas indicated by asterisk in images D, E, and F. Necrotic bone displays an irregular surface (G and H, arrowheads), as opposed to the smooth contour of non-necrotic bone (I). Images A, D, and G correspond to necrotic bone in the lower jaw, whereas images B, E, and H correspond to necrotic bone in the upper jaw. Scale bars are 100 μm in A, B, C, G, H, and I, and 1 mm in D, E, and F.

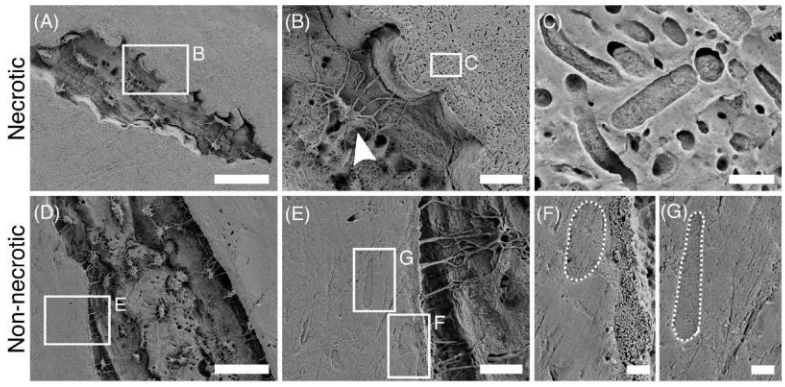

Fig. 3. Resin cast etching. Overview SE-SEM image of necrotic bone after resin cast etching (A), surrounded by an extensive biofilm (B) where several rod-shaped bacteria can be distinguished (C). An osteocyte with "withered" protrusions, which could be indicative of a non-vital cell, can also be observed (arrowhead in B). Overview SE-SEM image of non-necrotic bone after resin cast etching (D). At the bone surface, an osteoblast and a lining cell can be distinguished (E), marked by dotted line in higher magnification views in F and G, respectively. Scale bars are 50 μm in A and D, 10 μm in B and E, 1 μm in C, and 2 μm in F and G.

identification from the microbial swab and compatibly with rod-shaped bacteria commonly present in MRONJ.[14, 32] On the other hand, no bacteria were detected in the resin region in non-necrotic bone (Figure 3D, E), but some osteoblasts (Figure 3F) and lining cells (Figure 3G) were identified instead in proximity to the bone surface, supporting the presence of bone deposition. Neither osteoblasts nor lining cells were spotted in the resin region interfacing with necrotic bone. However, this is not unexpected, since dead tissue is metabolically inactive. Some cells in necrotic bone appeared shrunken and with "withered" retracted protrusions, which could be indicative of non-vital cells[33] (Figure 3B). Little is known about osteocyte death in MRONJ,[34] but it is believed that high intracellular concentrations of BPs can be toxic to bone cells other than osteoclasts.[8, 13]

Ultrastructural considerations

At the necrotic bone–resin interface, HAADF-STEM images revealed the existence of a hypermineralized front, which fades into a region with exaggerated disorder and loosely arranged mineral platelets, and no discernable collagen fibrils, toward the resin space (Figure 4A, B). The hypermineralized front appears as an electron-dense, high-*Z*-contrast band, approximately 100–350 nm in width, without any obvious structural features. Beyond this front, bone tissue displayed a normal structural organization, with in-plane collagen fibrils originating a cross-striated banding pattern with a 68 nm ± 1 nm D-spacing (Figure 4C), compatibly to values commonly reported in the literature for healthy bone (i.e., 67 nm).[35, 36] In the 400–500 nm-wide disordered layer interfacing with the resin region, the complete absence of diffraction rings in SAED patterns suggests that this area is highly amorphous (Figure 4D), as opposed to that with in-plane collagen fibrils exhibiting the characteristic (002) arcs of the *c*-axis of hydroxyapatite (Figure S6).

In the resin region further away from bone, bacteria were observed (Figure 4E, Figure S7), confirming histological findings and SE-SEM images of necrotic bone after resin cast etching. In addition, some high-*Z*-contrast particulate matter, 24 ± 8 nm in size, was noted often enclosed within or in close association with the bacteria (Figure 4E). We hypothesize that these nano-sized particles are remainders of bone mineral recently having been degraded by the bacteria or by phagocytosing cells and, eventually, re-expelled into the outer environment.

Mineralization at the bone–bacteria interface

Trends in C, Ca, and P evaluated from SEM–EDX line scans revealed that all elements, and especially Ca, varied across a narrower region and at a faster rate (i.e., steeper slope of the fitted line) for the bone–resin interface in necrotic bone, although the difference with non-necrotic bone was not statistically significant ($p > 0.05$) (Figure 5A, Table S1). Nonetheless, this appears to be in agreement with the fact that, although a mineralization front exists in non-necrotic bone, and hence a gradual concentration gradient is expected, no such front is present in necrotic bone, which explains the higher abruptness in concentration change.

The mineral-to-matrix ratio was higher in necrotic than in non-necrotic bone ($p < 0.01$), as evaluated from Raman spectra (Figure 5B, Table S2). Again, this can be explained by the lack of a mineralization front in the presence of necrosis, with no newly formed bone or osteoid-rich regions that would contribute to the Phe signal, thereby lowering the mineral-to-matrix ratio. In addition, BP treatment has been associated with an increase in bone mineralization.[4] From HAADF-STEM images of necrotic bone, it is interesting to note that the collagen banding pattern was no longer distinguishable, whereas mineral was still present (albeit in a highly disordered state) at the bone–resin interface. The apparent absence of collagen (and, therefore, most of the organic component of the extracellular matrix) offers an explanation for the higher mineral-to-matrix ratio of necrotic bone.

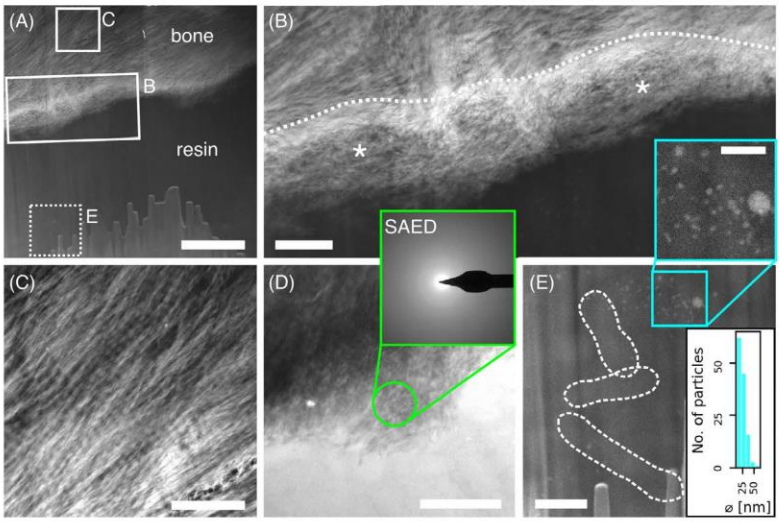

Fig. 4. HAADF-STEM and SAED. Overview HAADF-STEM image of necrotic bone interfacing with bacteria-invaded space (A). The interface appears as an electron-dense band (dotted line) that fades into a loosely organized region (asterisk) toward the resin space (B, corresponding to area marked by rectangle in A). Further from the interface, bone structure appears normal, and the characteristic banding pattern of in-plane collagen can be distinguished (C, corresponding to area marked by square in A). BF-TEM image of disordered region at the interface (D), where bone appears lacking crystallinity, as indicated by absence of diffraction rings in the SAED pattern (inset with a green border, SAED from region marked by green circle in D). In the resin space (E, corresponding to area marked by dotted square in A), bacteria (dotted line, unmarked image available as Figure S7) and nanosized particulate matter (inset with a blue border) can be noted. The histogram in the bottom right corner of E represents the distribution of the particle diameter (ø). Scale bars are 2 μm in A, 500 nm in B, C, D, and E, and 200 nm in the blue inset of E.

It is worth pointing out that the HAADF-STEM images show that only a small region, overall less than 1 μm in width, at the bone–resin interface presented significant structural alterations. SEM–EDX and micro-Raman spectroscopy may be unable to precisely characterize this region due to its limited width, especially in relation to the volume probed by these two techniques (183–257 μm^3 in SEM–EDX and 0.7 μm^3 in micro-Raman spectroscopy), as well as to limitations in lateral and vertical resolution. However, variations in the mineral-to-matrix ratio suggest that compositional changes can occur over a broader area, so compositional analyses by SEM–EDX and micro-Raman spectroscopy could effectively be capturing abnormalities due to the lack of ongoing mineralization and remodeling in MRONJ. Spectroscopy analyses with nanoscale resolution using EELS confirmed the decrease in Ca and P across the necrotic bone–resin interface (Figure 6), as was already evident from the variation in *Z*-contrast in the HAADF-STEM images (Figure 4).

Overall considerations on the bone–bacteria interface in MRONJ

In light of the findings described in the preceding sections, we propose two mechanisms, likely concurrent, responsible for the creation of the hypermineralized and disordered regions at the interface between bone and the bacteria-invaded region in MRONJ: (i) progressive mineralization, where a progressive, excessive mineralization occurs in the absence of cell-mediated regulatory mechanisms; (ii) dissolution and reprecipitation, where bone mineral is, at least partly, degraded and dissolved by the bacteria and subsequently reprecipitates.

Evidence for the first mechanism stems from the fact that, given the necrosis, most cells in the tissue are dead, as seen from histology and resin cast etching. Bone cells play a fundamental regulatory role in coupling bone formation and resorption and in initiating/preventing mineralization.[37] Therefore, the absence of viable cells can lead to the uncontrolled (both in terms of quantity and structural organization) precipitation of Ca and P at the bone–bacteria interface, especially since many body fluids, such as blood and saliva, are supersaturated with respect to calcium phosphate precipitation.[38, 39] That mineralization is thermodynamically and kinematically favored in the absence of specific inhibitors is observed in pathological mineralization contexts such as atherosclerosis,[40] kidney stones,[41] and dental calculus.[42] However, in an apparent contradiction, uncontrolled mineralization in MRONJ should still be prevented by the action of BPs because they are analogs of pyrophosphate (PPi), which are known mineralization inhibitors.[43] On the other hand, an increased mineral content has been associated with MRONJ.[4, 37]

Regarding the second mechanism, although direct degradation of bone by biofilm pathogens is not yet widely recognized, the presence of bacteria at the interface with bone and of mineral-like nanosized particulate matter within and around them (Figure 4E) supports an active role of bacteria in degrading

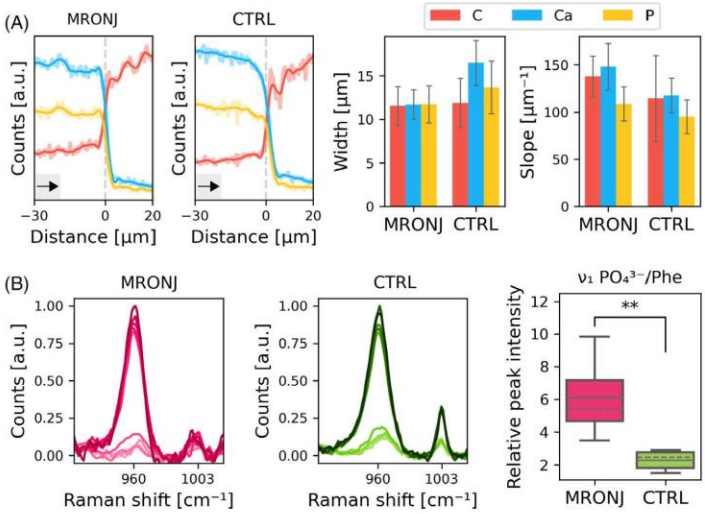

Fig. 5. EDX and micro-Raman spectroscopy. (A) EDX line scans of necrotic (MRONJ) and non-necrotic (CTRL) bone taken across the bone–resin interface and bar graphs comparing the width and slope of the interface for the two groups. The difference was not statistically significant for either. The faded and bold lines in the line scan plots correspond to spectra before and after smoothing, respectively. The vertical dashed line in gray in the line scan plots approximately marks the interface between bone and resin. Black arrows indicate scanning direction, that is, from bone toward resin. (B) Raman spectra of points in line scans across the bone–resin interface for necrotic (MRONJ) and non-necrotic (CTRL) bone and box plots showing mineral-to-matrix ratio (ν_1 PO_4^{3-}/Phe) of the two groups (for points in bone region only). Boxes represent 50% of data, limited by upper and lower quartiles, and vertical lines indicate data range. The mean and median values are marked by continuous and dashed lines, respectively, across each box. ** denotes statistical significance ($p < 0.01$).

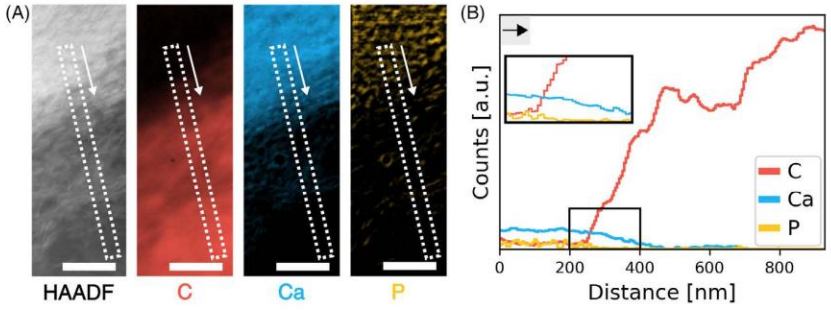

Fig. 6. EELS. (A) HAADF-STEM image and corresponding EELS maps for C, Ca, and P. (B) Variation in C, Ca, and P across the bone–resin interface extracted from the area marked by a dashed rectangle in the HAADF-STEM image and EELS maps in A (white arrow indicates scanning direction, that is, from bone toward resin). The inset in B provides a magnified view of decrease in Ca and P across the interface. Black arrow indicates scanning direction, that is, from bone toward resin. Note that the P map appears "spotty" because the L-edge of P was mostly within the tail of the plasmon peak, and limited signal could be extracted. Scale bars are 200 nm.

bone, especially since osteoclast-mediated resorption should be largely suppressed by BPs. The possibility of biofilm-operated bone destruction has been proved in vitro and ex vivo,[18] as well as post mortem in microbial bioerosion.[44, 45] Gram-negative bacteria, like those identified by microbial swab in this study, can adhere to proteins of the extracellular matrix (ECM), including collagen type I, facilitating further bacterial colonization and host invasion.[46] Moreover, bacterial proteases can degrade ECM proteins, with bacterial collagenases specifically targeting collagen.[47] Some of the disordered mineral at the interface

could also correspond to Ca and P being released in the bone degradation process and reprecipitating. Moreover, Ca and P could also precipitate from the surrounding environment via the first mechanism described, enriching the region at the interface that appears as hypermineralized. BPs are known to inhibit the amorphous-to-crystalline transition of Ca and P precipitates,[48, 49] which could explain the region lacking crystallinity identified by SAED (Figure 4D). Lastly, it cannot be excluded that, together with bacteria, host immune cells secondary to the presence of the pathogens also participate in the degradation of bone ECM. In fact, some multinucleated cells were observed in histological sections of necrotic bone, indicating the presence of inflammation (Figure S8). Additionally, since the administration of alendronate was interrupted 1.5 years before the sampling procedure, the presence of osteoclast-mediated resorption cannot be excluded. However, as alendronate tablets were taken for a very extended period of time (23 years), it is reasonable to assume that osteoclastic activity is still largely suppressed, and some eventual osteoclastic resorption alone could not explain the changes we observed at the bone–bacteria interface. In addition, the absence of a mineralization front excludes the possibility that remodeling is taking place.

Conclusions

As many have previously observed, MRONJ is a highly complex scenario involving multiple actors that may have direct or indirect effects, or both, on its onset and progression. Our structural and compositional analyses, focused on probing the bone–bacteria interface across multiple length scales, point to two main directions, involving nonmediated mineralization or a direct role of the bacteria. No matter the mechanism, it is evident that the necrotic bone is completely passive (after all, it is *dead*!), and the interface with the bacteria-invaded space is a product of the environment outside it, whether that is the biofilm or a supersaturated Ca/P solution. Despite the systemic administration of BPs, a local effect emerges quite clearly, both macroscopically in the oral cavity, and at the micro- and nanoscale levels in bone. Macroscopically, there are areas in the jaw with no signs of necrosis or oral infection. When considering necrotic areas, the effect of MRONJ on bone micro-/nanostructure and composition appears to be localized in a very limited region, smaller than 1 μm in width, right at the interface with the bacteria-invaded region, giving rise to a hypermineralized band (on the bone side) and a highly disordered and amorphous area (on the bacteria-invaded side).

Acknowledgments

The authors gratefully acknowledge Lena Emanuelsson for assistance with sample preparation for histology. The SEM experiments were completed at the Chalmers Materials Analysis Laboratory (CMAL) (Gothenburg, Sweden). FIB in situ lift-outs and TEM and STEM experiments were performed at the Canadian Centre for Electron Microscopy (CCEM) (Hamilton, ON, Canada), a Canadian Foundation for Innovation's Major Science Initiatives–funded facility, also supported by the Natural Sciences and Engineering Research Council of Canada (NSERC) and other government agencies. Chiara Micheletti is thankful for the support from the Mitacs Globalink Research Award and the Blanceflor Foundation. Financial support provided by NSERC for the Vanier Canada Graduate Scholarship for Liza-Anastasia DiCecco and for the Canada Graduate Doctoral Scholarship for Dakota M. Binkley is gratefully acknowledged. Cecilia Larsson Wexell is thankful for the support of the Västra Götaland Region. Anders Palmquist acknowledges funding support from the Swedish Research Council (Grant 2020-04715). Financial support from the IngaBritt and Arne Lundberg Foundation, the Hjalmar Svensson Foundation, and the Area of Advance Materials at Chalmers and at the Department of Biomaterials (University of Gothenburg) within the Strategic Research Area initiative launched by the Swedish government is acknowledged. Kathryn Grandfield acknowledges funding support from NSERC (Grant RGPIN-2020-05722), the Ontario Ministry of Research, Innovation and Science (Early Researcher Award ER17-13-081), and the Canada Research Chairs Program from whom Kathryn Grandfield holds the Tier II Chair in Microscopy of Biomaterials and Biointerfaces. Furqan A. Shah is thankful for the support of the Adlerbertska Foundation and the Kungliga Vetenskaps-och Vitterhets-Samhället i Göteborg. Furqan A. Shah was also supported by a postdoctoral scholarship from the Svenska Sällskapet för Medicinsk Forskning (SSMF).

Author Contributions

Chiara Micheletti: Conceptualization; formal analysis; investigation; methodology; visualization; writing – original draft. **Liza-Anastasia DiCecco:** Investigation; methodology; writing – review and editing. **Cecilia Larsson Wexell:** Conceptualization; resources; writing – review and editing. **Dakota M. Binkley:** Investigation; methodology; writing – review and editing. **Anders Palmquist:** Funding acquisition; supervision; writing – review and editing. **Kathryn Grandfield:** Funding acquisition; supervision; writing – review and editing. **Furqan Shah:** Conceptualization; funding acquisition; investigation; methodology; supervision; writing – review and editing.

Authors' roles

CM: conceptualization, formal analysis, investigation, methodology, visualization, writing—original draft. L-AD: investigation, methodology, writing—review and editing. CLW: conceptualization, resources, writing—review and editing. DMB: investigation, methodology, writing—review and editing. AP: funding acquisition, supervision, writing—review and editing. KG: funding acquisition, supervision, writing—review and editing. FAS: conceptualization, methodology, investigation, funding acquisition, supervision, writing—review and editing.

Conflict of Interest

We declare that we have no conflict of interest.

Peer Review

The peer review history for this article is available at https://publons.com/publon/10.1002/jbm4.10693.

Data Availability Statement

The data used in this work are provided either in the main manuscript or in the supplementary information.

References

1. Russell RGG. Bisphosphonates: the first 40 years bone. *Bone*. 2011;49: 2-19.
2. Russell RGG, Mühlbauer RC, Bisaz S, Williams DA, Fleisch H. The influence of pyrophosphate, condensed phosphates, phosphonates and other phosphate compounds on the dissolution of hydroxyapatite in vitro and on bone resorption induced by parathyroid hormone in tissue culture and in thyroparathyroidectomised rats. *Calcif Tissue Res*. 1970;6:183-196.
3. Flanagan AM, Chambers TJ. Inhibition of bone resorption by bisphosphonates: interactions between bisphosphonates, osteoclasts, and bone. *Calcif Tissue Int*. 1991;49:407-415.
4. Burr DB. Fifty years of bisphosphonates: what are their mechanical effects on bone? *Bone*. 2020;138:115518.
5. Bilezikian JP. Osteonecrosis of the jaw — do bisphosphonates pose a risk? *N Engl J Med*. 2006;335:2278-2281.
6. Drake MT, Clarke BL, Khosla S. Bisphosphonates: mechanism of action and role in clinical practice. *Mayo Clin Proc*. 2008;83:1032-1045.
7. Ruggiero SL et al. American Association of Oral and Maxillofacial Surgeons Position Paper on bisphosphonate-related osteonecrosis of the jaws—2009 update. *J Oral Maxillofac Surg*. 2009;67:2-12.
8. Reid IR. Osteonecrosis of the jaw — who gets it, and why? *Bone*. 2009; 44:4-10.
9. Migliorati CA, Epstein JB, Abt E, Berenson JR. Osteonecrosis of the jaw and bisphosphonates in cancer: a narrative review. *Nat Rev Endocrinol*. 2011;7:34-42.
10. American Association of Oral and Maxillofacial Surgeons. American Association of Oral and Maxillofacial Surgeons Position Paper on bisphosphonate-related osteonecrosis of the jaws. *J Oral Maxillofac Surg*. 2007;65:369-376.
11. Ruggiero SL et al. American Association of Oral and Maxillofacial Surgeons' position paper on medication-related osteonecrosis of the jaws—2022 update. *J Oral Maxillofac Surg*. 2022;80:920-943.
12. Hansen T, Kunkel M, Weber A, Kirkpatrick CJ. Osteonecrosis of the jaws in patients treated with bisphosphonates – histomorphologic analysis in comparison with infected osteoradionecrosis. *J Oral Pathol Med*. 2006;35:155-160.
13. Allen MR, Burr DB. The pathogenesis of bisphosphonate-related osteonecrosis of the jaw: so many hypotheses, so few data. *J Oral Maxillofac Surg*. 2009;67:61-70.
14. Hinson AM, Smith CW, Siegel ER, Stack BC. Is bisphosphonate-related osteonecrosis of the jaw an infection? A histological and microbiological ten-year summary. *Int J Dent*. 2014;2014:452737.
15. Reid IR, Cornish J. Epidemiology and pathogenesis of osteonecrosis of the jaw. *Nat Rev Rheumatol*. 2012;8:90-96.
16. Kinane DF, Stathopoulou PG, Papapanou PN. Periodontal diseases. *Nat Rev Dis Primers*. 2017;3:17038.
17. Reid IR, Bolland MJ, Grey AB. Is bisphosphonate-associated osteonecrosis of the jaw caused by soft tissue toxicity? *Bone*. 2007;41:318-320.
18. Junka A et al. Bad to the bone: on In vitro and ex vivo microbial biofilm ability to directly destroy colonized bone surfaces without participation of host immunity or osteoclastogenesis. *Plos One*. 2017; 12:e0169565.
19. Pihlstrom BL, Michalowicz BS, Johnson NW. Periodontal diseases. *Lancet*. 2005;366:1809-1820.
20. Khamaisi M et al. Possible association between diabetes and bisphosphonate-related jaw osteonecrosis. *J Clin Endocrinol Metabolism*. 2007;92:1172-1175.
21. Dodson TB, Wessel JH, Zavras AI. Zoledronate and other risk factors associated with osteonecrosis of the jaw in cancer patients: a case-control study. *J Oral Maxillofac Surg*. 2008;66:625-631.
22. Howell PGT, Boyde A. Volumes from which calcium and phosphorus X-rays arise in electron probe emission microanalysis of bone: Monte Carlo simulation. *Calcif Tissue Int*. 2003;72:745-749.
23. Gamsjaeger S et al. Cortical bone composition and orientation as a function of animal and tissue age in mice by Raman spectroscopy. *Bone*. 2010;47:392-399.
24. Juang C, Finzi L, Bustamante CJ. Design and application of a computer-controlled confocal scanning differential polarization microscope. *Rev Sci Instrum*. 1988;59:2399-2408.
25. McElderry JP et al. Tracking circadian rhythms of bone mineral deposition in murine calvarial organ cultures. *J Bone Miner Res*. 2013;28:1846-1854.
26. Wang X, Shah FA, Palmquist A, Grandfield K. 3D characterization of human nano-osseointegration by on-axis electron tomography without the missing wedge. *ACS Biomater Sci Eng*. 2017;3:49-55.
27. Schindelin J et al. Fiji: an open-source platform for biological-image analysis. *Nat Methods*. 2012;9:676-682.
28. Franco-Pretto E, Pacheco M, Moreno A, Messa O, Gnecco J. Bisphosphonate-induced osteonecrosis of the jaws: clinical, imaging, and histopathology findings. *Oral Surg Oral Med Oral Pathol Oral Radiol*. 2014;118:408-417.
29. Shah FA et al. Micrometer-sized magnesium whitlockite crystals in micropetrosis of bisphosphonate-exposed human alveolar bone. *Nano Lett*. 2017;17:6210-6216.
30. Shah FA. Magnesium whitlockite – omnipresent in pathological mineralisation of soft tissues but not a significant inorganic constituent of bone. *Acta Biomater*. 2021;125:72-82.
31. Sedghizadeh PP et al. Identification of microbial biofilms in osteonecrosis of the jaws secondary to bisphosphonate therapy. *J Oral Maxillofac Surg*. 2008;66:767-775.
32. Sedghizadeh PP et al. Microbial biofilms in osteomyelitis of the jaw and osteonecrosis of the jaw secondary to bisphosphonate therapy. *J Am Dent Assoc*. 2009;140:1259-1265.
33. Kroemer G et al. Classification of cell death: recommendations of the nomenclature committee on cell death 2009. *Cell Death Differ*. 2009; 16:3-11.
34. Aguirre JI, Castillo EJ, Kimmel DB. Biologic and pathologic aspects of osteocytes in the setting of medication-related osteonecrosis of the jaw (MRONJ). *Bone*. 2021;153:116168.
35. Hodge AJ, Petruska JA. Recent studies with the electron microscope on ordered aggregates of the tropocollagen macromolecule. In Ramachandran G, ed. *Aspects of Protein Structure*, vol. 289–300. Academic Press; 1963.
36. Petruska JA, Hodge AJ. A subunit model for the tropocollagen macromolecule. *Proc Natl Acad Sci U S A*. 1964;51:871-876.
37. Boskey AL. Mineralization of bones and teeth. *Elements*. 2007;3:385-391.
38. Epple M, Lanzer P. How much interdisciplinarity is required to understand vascular calcifications? Formulation of four basic principles of vascular calcification. *Z Kardiol*. 2001;90:III2–III5.
39. Dorozhkin SV, Epple M. Biological and medical significance of calcium phosphates. *Angew Chem Int Ed*. 2002;41:3130-3146.
40. Alexopoulos N, Raggi P. Calcification in atherosclerosis. *Nat Rev Cardiol*. 2009;6:681-688.
41. Wesson JA, Ward MD. Pathological biomineralization of kidney stones. *Elements*. 2007;3:415-421.
42. Akcali A, Lang NP. Dental calculus: the calcified biofilm and its role in disease development. *Periodontol 2000*. 2018;76:109-115.
43. Fleisch H, Russell RGG, Straumann F. Effect of pyrophosphate on hydroxyapatite and its implications in calcium homeostasis. *Nature*. 1966;212:901-903.
44. Jans MME, Nielsen-Marsh CM, Smith CI, Collins MJ, Kars H. Characterisation of microbial attack on archaeological bone. *J Archaeol Sci*. 2004;31:87-95.
45. Jans MME. Microbial bioerosion of bone - a review. In Wisshak M, Tapanila L, eds. *Current Developments in Bioerosion*. Springer; 2008 pp 397-413.
46. Vaca DJ et al. Interaction with the host: the role of fibronectin and extracellular matrix proteins in the adhesion of gram-negative bacteria. *Med Microbiol Immun*. 2020;209:277-299.
47. Watanabe K. Collagenolytic proteases from bacteria. *Appl Microbiol Biot*. 2004;63:520-526.
48. Fleisch H. Diphosphonates: history and mechanisms of action. *Metab Bone Dis Relat Res*. 1981;3:279-287.
49. Akiyama K et al. Calciprotein particles regulate fibroblast growth factor-23 expression in osteoblasts. *Kidney Int*. 2020;97:702-712.

SUPPLEMENTARY

Table S1. Values of width and slope of the bone-resin interface for C, Ca, and P measured from SEM-EDX spectra.

		Width C [µm]	Width Ca [µm]	Width P [µm]	Slope C [µm^{-1}]	Slope Ca [µm^{-1}]	Slope P [µm^{-1}]
Necrotic sample (lower jaw)	line 1	9.876	9.876	9.876	121.278	181.294	127.984
	line 2	12.546	13.741	14.338	130.320	113.090	80.197
	line 3	9.624	10.190	10.190	177.953	157.225	123.629
Necrotic sample (upper jaw)	line 1	9.340	11.416	10.897	142.552	138.464	114.936
	line 2	14.811	11.109	10.491	134.106	166.357	109.572
	line 3	13.014	13.780	14.545	119.835	133.857	95.977
Non-necrotic sample (upper jaw)	line 1	11.911	18.528	15.219	129.955	106.682	90.814
	line 2	14.720	17.318	15.586	63.2193	106.985	79.811
	line 3	9.048	13.572	10.179	150.193	138.915	114.873

Table S2. Values of mineral-to-matrix ratio measured for each of the points in the bone region in the micro-Raman spectroscopy line scan.

		line 1	line 2	line 3	line 4	line 5
Necrotic sample (lower jaw)	point 1	5.431	5.485	4.690	8.679	6.044
	point 2	5.135	3.670	4.978	7.261	4.016
	point 3	4.947	3.192	5.357	7.784	3.976
	point 4	4.525	3.425	4.066	5.821	5.667
	point 5	2.789	1.625	5.736	5.319	1.930
Necrotic sample (upper jaw)	point 1	4.647	11.273	8.668	4.473	6.876
	point 2	4.463	7.569	8.373	6.727	5.053
	point 3	5.388	7.510	11.919	4.638	11.284
	point 4	5.642	10.427	8.531	5.714	6.601
	point 5	6.357	7.330	11.771	5.969	6.361
Non-necrotic sample (upper jaw)	point 1	3.704	3.195	2.208	1.679	3.096
	point 2	3.334	2.678	1.939	1.744	3.056
	point 3	3.082	2.538	1.777	1.488	2.696
	point 4	2.322	2.202	1.583	1.430	2.740
	point 5	1.299	1.724	1.484	1.192	2.800

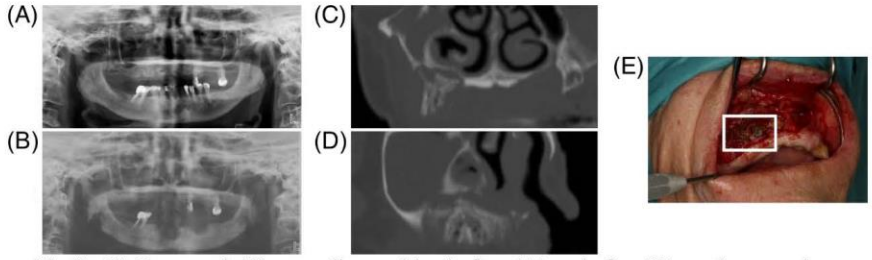

Figure S1. (A, B) Panoramic X-ray radiographies before (A) and after (B) tooth extraction surgery. (C, D) X-ray radiographies corresponding to the frontal (C) and lateral (D) view of the upper jaw and maxillary sinus. (E) Picture of the surgery and bone sampling procedure, where areas of necrotic bone can be noted in the region marked by the white rectangle.

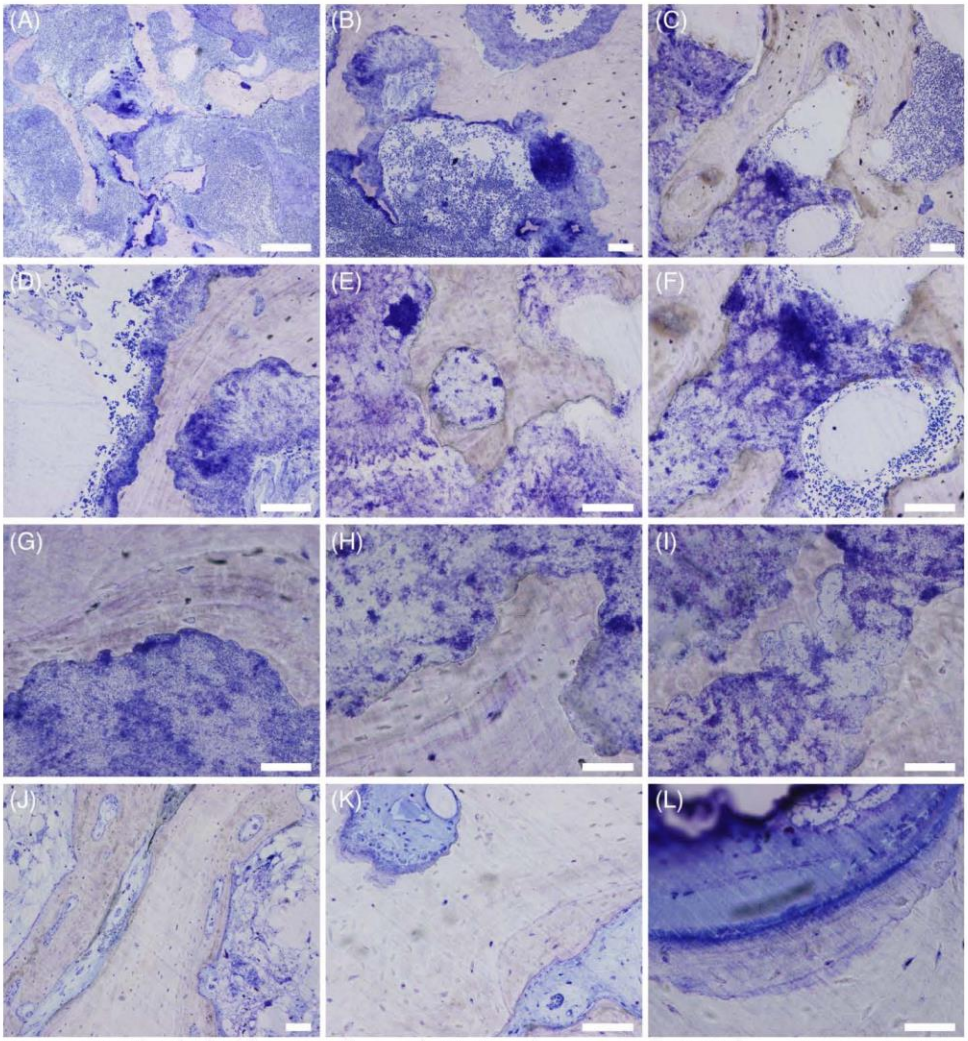

Figure S2. Histological images of necrotic (A-I) and non-necrotic (J-L) bone. Images A, B, D, and G correspond to necrotic bone in the lower jaw; images C, E, F, H, and I correspond to necrotic bone in the upper jaw. Scale bars are 500 μm in A, 100 μm in B, C, D, E, F, J, and K, and 50 μm in G, H, I, and L. The following objectives were used: ×4 for image A; ×10 for images B, C, and J; ×20 for images D, E, F, and K; ×40 for G, H, I, and L.

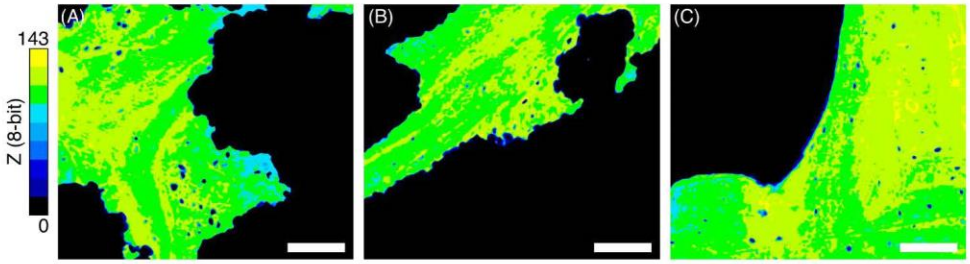

Figure S3. Pseudo-coloured BSE-SEM images of necrotic (A, B) and non-necrotic (C) bone, corresponding to Figure 2G-I. A 16-level lookup table has been applied post median filtering ("ndimage" module using a median filter with size 10 in the "scipy" library in Python 3.8.10). Scale bars are 100 µm.

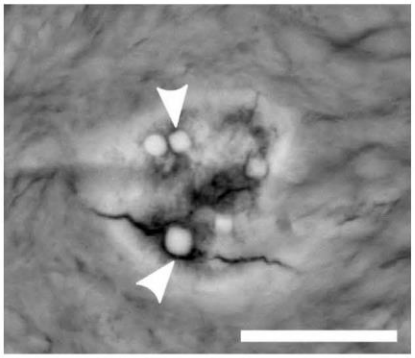

Figure S4. Osteocyte lacuna presenting signs of micropetrosis (BSE-SEM image). Rhomboidal mineral nodules (arrowheads) likely correspond to magnesium whitlockite. Scale bar is 5 µm.

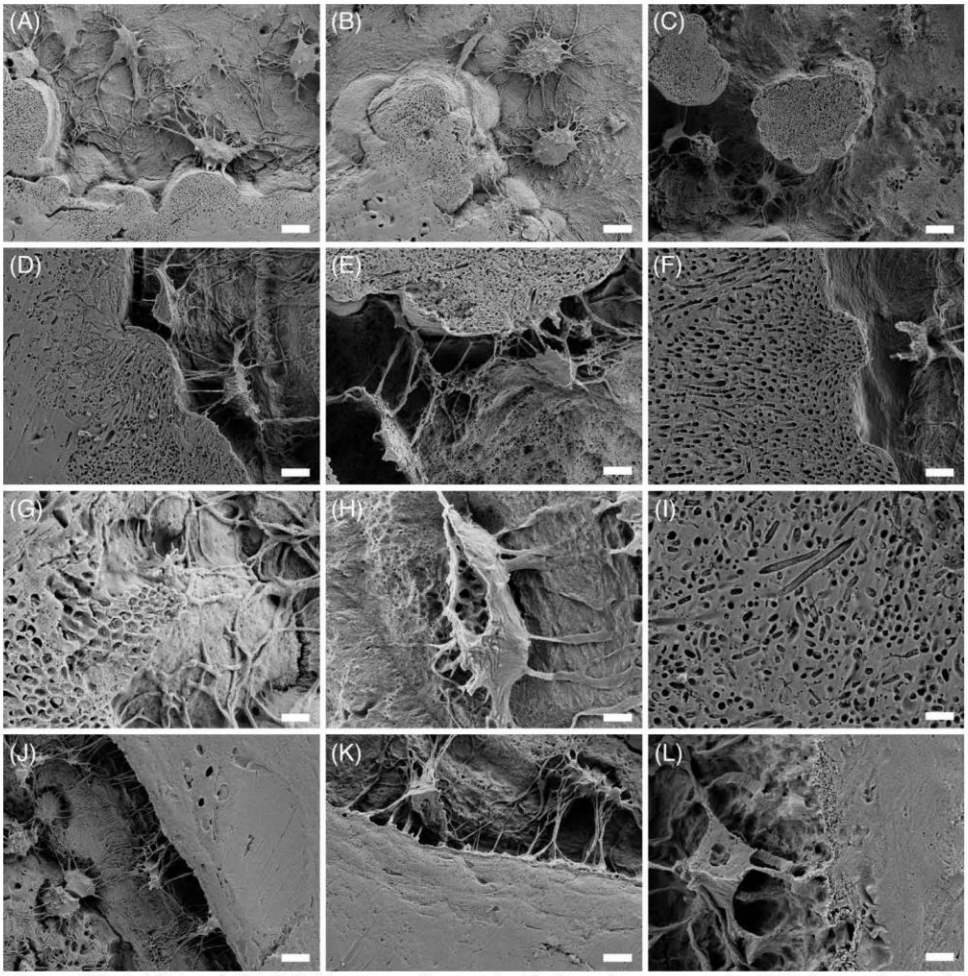

Figure S5. Additional SE-SEM images of necrotic (A-I) and non-necrotic (J-L) bone after resin cast etching. Images A, B, E, G, and H correspond to necrotic bone in the lower jaw; images C, D, F, and I correspond to necrotic bone in the upper jaw. Scale bars are 10 μm in A, B, C, and J, 5 μm in D, E, F, and K, and 2 μm in G, H, I, and L.

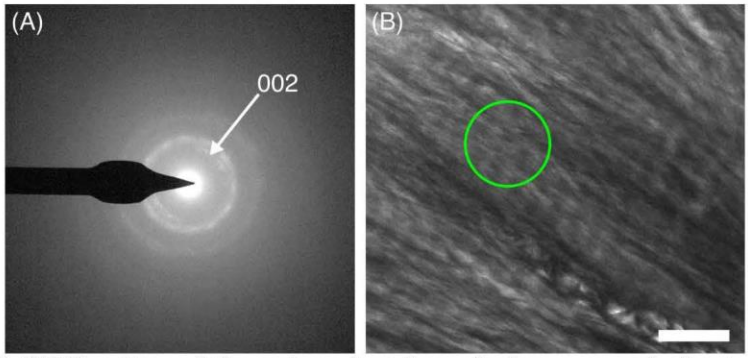

Figure S6. SAED pattern of the region where bone displays a normal ultrastructure (A), corresponding to the area marked by the green circle in the BF-TEM image (B). The characteristic (002) arcs of the *c*-axis of hydroxyapatite are visible, as typically observed where collagen fibrils are in-plane. Scale bar is 200 nm.

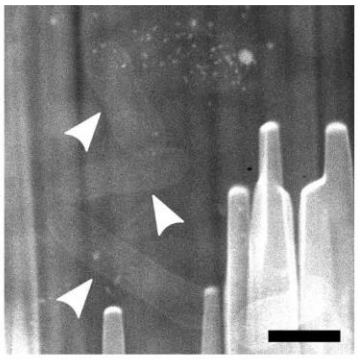

Figure S7. Unmarked HAADF-STEM corresponding to Figure 4e, showing bacteria in the resin region interfacing with necrotic bone. Three bacteria are indicated by arrowheads, and a fourth bacterium can be distinguished where the scale bar is. Scale bar is 500 nm.

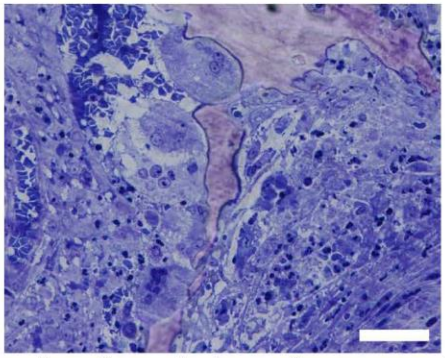

Figure S8. Histological section of necrotic bone where some multinucleated cells can be distinguished. Scale bar is 50 µm.

Paper III

Micro-to-nanoscale characterization of the osseointegration and lacuno-canalicular network at the interface with an additively manufactured implant for local genistein delivery

Chiara Micheletti[1,2*], Liza-Anastasia DiCecco[1#], Joseph Deering[1#], Wanqi Chen[1], Ana Cláudia Ervolino da Silva[3], Furqan A. Shah[2], Anders Palmquist[2], Roberta Okamoto[4,5], Kathryn Grandfield[1,6,7*]

[1] Department of Materials Science and Engineering, McMaster University, Hamilton, ON, Canada
[2] Department of Biomaterials, Sahlgrenska Academy, University of Gothenburg, Gothenburg, Sweden
[3] Department of Diagnosis and Surgery, São Paulo State University, Araçatuba Dental School, Araçatuba, SP, Brazil
[4] Department of Basic Sciences, São Paulo State University, Araçatuba Dental School, Araçatuba, SP, Brazil
[5] Research Productivity Scholarship (Process: 309408/2020-2), Araçatuba, SP, Brazil
[6] School of Biomedical Engineering, McMaster University, Hamilton, ON, Canada
[7] Brockhouse Institute for Materials Research, McMaster University, Hamilton, ON, Canada
[#] Equal contribution.

[*] Corresponding authors:
Chiara Micheletti, Department of Biomaterials, Sahlgrenska Academy, University of Gothenburg, Gothenburg, Sweden, e-mail: chiara.micheletti@biomaterials.gu.se
Prof. Kathryn Grandfield, Department of Materials Science and Engineering, McMaster University, Hamilton, ON, Canada, e-mail: kgrandfield@mcmaster.ca

ABSTRACT

Given the hierarchical nature of bone and bone interfaces, osseointegration, namely the formation of a direct bone-implant contact without interposed soft tissue, is best evaluated using a multiscale and multimodal approach. In this study, we combine established electron microscopy techniques to probe bone-implant interfaces at the microscale and nanoscale with plasma focused ion beam-scanning electron microscopy (PFIB-SEM) tomography to evaluate osseointegration at the mesoscale. Specifically, we examine bone response to a porous Ti-6Al-4V implant designed to locally promote bone healing in osteoporotic conditions. The implant is fabricated by laser powder bed fusion, acid-etched, and coated with a layer of genistein, a phytoestrogen that promotes osteoblastogenesis. The bone-implant interface and peri-implant bone formation are evaluated across the micro-nanoscale in a pre-clinical ovariectomized rat model. SEM demonstrates new bone formation at the peri-implant site, including in the internal implant pores. By imaging a large volume of peri-implant bone, PFIB-SEM tomography highlights the presence of mineral ellipsoids varying in size and orientation, together with a well-developed lacuno-canalicular network and mineralization fronts directed both towards the implant (distance osteogenesis) and away from it (contact osteogenesis). At the nanoscale, scanning transmission electron microscopy and energy-dispersive X-ray spectroscopy confirm the gradual nature of the bone-implant interface.

Keywords: mineral ellipsoid; PFIB-SEM tomography; scanning transmission electron microscopy; resin cast etching; local drug delivery; osteoporosis

1. INTRODUCTION

Bone bonding to titanium implants is a multiscale phenomenon, spanning from a macro-level of anchorage to the microscale where cells interact with the implant surface, all the way down to the nanoscale where the titanium oxide surface layer intermixes with calcium and phosphorus [1]. Originally, bone-implant contact, i.e., "osseointegration", was defined "on the light microscopic level" [2]. The advent of scanning/transmission electron microscopy (S/TEM) imaging of bone-implant interfaces, combined with minimally destructive sample preparation by focused ion beam [3], highlighted that osseointegration is also a nanoscale phenomenon [4–6]. While various ultrastructural models for the bone-implant interface have been proposed (reviewed in [1]), STEM and electron tomography have demonstrated direct bone bonding to nanotextured titanium-based implants in both two dimensions (2D) and three dimensions (3D), respectively [4,7,8]. Over the years, it has thus emerged that a multiscale and multimodal characterization approach is ideal to evaluate osseointegration in a comprehensive manner [6,9].

That bone-implant interfaces are best studied across multiple length scales is not surprising, given the hierarchical nature of bone itself. This multi-level architecture begins with the distinction between cortical and trabecular within the whole bone at the macroscale, and culminates with the mineralized collagen fibrils, and other small proteins and water, at the nanoscale, passing through other levels of organization such as osteons in cortical lamellar bone [10]. While, in the words of Richard Feynman *"there's plenty of room at the bottom"*, a renewed interest in studying bone at the mesoscale has recently emerged [11,12], especially thanks to the implementation of FIB-scanning electron microscopy (SEM) in bone research [13]. FIB-SEM tomography probes relatively large 3D volumes of material, typically in the order of 1000 μm^3 for Ga^+ FIB instruments, with a spatial resolution on the nanoscale level. The volume of material examined can be further expanded by the use of Xe^+ plasma FIB (PFIB) instruments, without compromising the resolution [14]. This opens new avenues to evaluate bone-implant interfaces and the peri-implant space over greater distances from the implant surface.

Herein, multiscale evaluation of osseointegration is applied to bone interfacing with a porous Ti-6Al-4V implant manufactured by laser powder bed fusion (L-PBF) and surface-modified by acid-etching followed by functionalization with a genistein coating. This implant design combines the advantages of engineered porosity in implants with those of local drug delivery to improve osseointegration in osteoporotic conditions. Local release of genistein has demonstrated promising results compared to its systemic administration in a preliminary study conducted in our groups (*unpublished*). While osteoporosis is not considered a contraindication to the installation of bone implants, systemic conditions affecting bone quantity and/or quality can impair osseointegration [15]. Genistein is a natural phytoestrogen capable of promoting osteoblastogenesis [16]. This in turn can stimulate bone repair while avoiding the pitfalls of systemic or local delivery of commonly used antiresorptive medications, which display side effects such as osteonecrosis of the jaw [17]. Additionally, porous implants can promote cell migration and angiogenesis, and stimulate bone ingrowth, which has been shown to increase bone-implant stabilization [18–20]. Additive manufacturing (AM) offers great flexibility in terms of implant design, including pore volume, size, and distribution [21,22]. AM techniques based on PBF produce implants with a micro-rough surface finish due to the presence of partially unmelted/unsintered raw powders [23,24]. Microtopography, especially when combined with nanotopography, has generally been shown to improve osseointegration, as it provides mechanical interlocking between bone and implant, creates a greater surface area for protein adsorption, and favours cell interactions [24–28].

The multiscale and multimodal characterization approach we present aims to examine not only the bone-implant interface, but also peri-implant bone in terms of structure and cellular network. Our characterization platform encompasses SEM, to gain an overview of bone formation in the peri-implant space and cell-implant

interactions, and high-angle annular dark-field (HAADF)-STEM, to resolve the nanoscale bone-implant bonding. Micro- and nanoscale are bridged by PFIB-SEM tomography, to examine both the mesoscale architecture of newly formed bone and the lacuno-canalicular network (LCN) within.

2. MATERIALS AND METHODS

2.1. Implant manufacturing

Ti-6Al-4V implants (diameter = 2 mm, height = 4 mm) were designed with 45% porosity in the mid-section (height = 1 mm) with 500 µm pores, together with a central solid strut for structural support (diameter = 300 µm) (Figure S1). Implants were manufactured by L-PBF with a Renishaw AM 400 laser-modulated system (Renishaw, UK) using a hatch fill strategy with 200 W power, 75 µm point distance, 50 µs exposure time, 30 µm layer thickness, 65 µm hatch distance and 67° hatch increment angle, employing Ti-6Al-4V grade 23 feedstock powders with a particle size of 15-45 µm (AP&C, QC, Canada). Post-manufacturing, implants were cleaned by ultrasonication (15 min in ethanol, 15 min in acetone, and 5 min in deionized water), acid etched in 50% H_2SO_4 in deionized water at approximately 95 °C for 2 h (Figure S2), and functionalized with genistein by an electrochemical layer-by-layer coating technique [patent application BR 10 2021 019134 1, Instituto Nacional da Propriedade Industrial, Brazil].

2.2. Implant placement, and sample retrieval and preparation

The animal experiments were conducted with institutional ethical approval (Ethics Committee on the Use of Animals, UNESP, approval no. 00733-2020). Bilateral ovariectomy (OVX) was performed on 3-month-old female Wistar rats (n = 2) as a model for impaired bone repair analogous to that occurring in osteoporosis [29]. At 30 days after OVX, implants were placed in the tibia. The implant and surrounding tissue were retrieved *en bloc* after 28 days of healing, fixed in 10% neutral buffered formalin, dehydrated in ethanol, and embedded in polymethyl methacrylate resin. The samples were sectioned in half along the longitudinal axis of the implant, polished, and characterized from the micro- to the nanoscale (Figure 1).

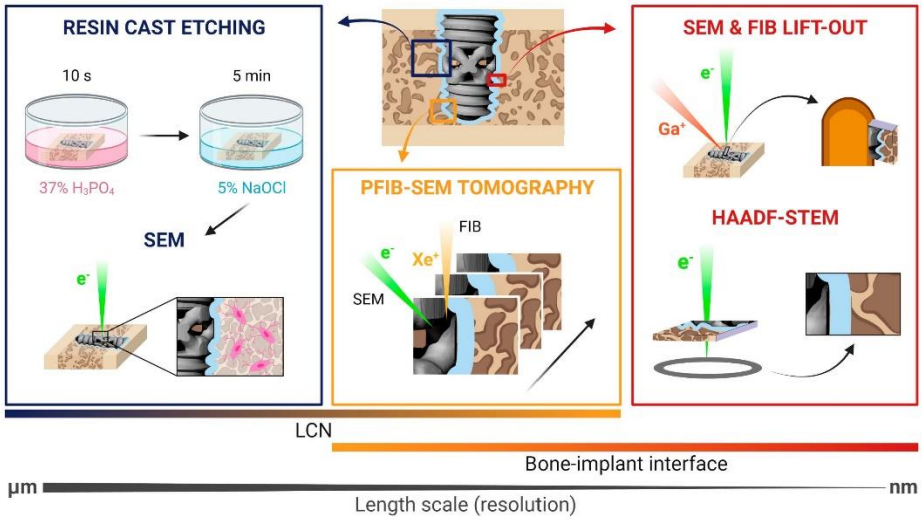

Figure 1. Schematic (not to scale) of the multimodal and multiscale characterization workflow of new bone forming in the peri-implant compartment. The blue border around the porous implant represents the genistein coating. The LCN was examined in 2D by SEM imaging after resin cast etching and in 3D by PFIB-SEM tomography. PFIB-SEM tomography was also used to image the bone-implant interface. Nanoscale resolution was achieved by HAADF-STEM imaging of an electron transparent lamella prepared by the FIB *in situ* lift-out technique.

2.3. SEM survey

Embedded samples were mounted on aluminum stubs using carbon tape and silver paint, and sputter-coated with gold (~20 nm thickness). Backscattered electron (BSE)-SEM images were acquired in a SEM instrument (JEOL 6610LV, JEOL, MA, USA) operated at high vacuum, 15-20 kV accelerating voltage, and a working distance of 10 mm. BSE-SEM images were used to identify areas of direct bone-implant contact for the preparation of the sample for STEM analysis.

2.4. PFIB-SEM tomography

Acquisition. PFIB-SEM tomography was performed in a dual-beam Xe^+ PFIB instrument (Helios G4 UXe, Thermo Fisher Scientific, MA, USA) using a 45° pre-tilt holder. A layer of carbon was deposited over a 70 × 25 μm^2 region of interest (ROI) by ion beam deposition at 12 kV and 20 nA for the first 1 µm-thick layer, and at 65 nA for an additional 12 µm-thick deposit. Trenches were milled on both sides of the ROI using "cleaning cross-section" (CCS) milling patterns (30 kV, 0.20 µA and 15 nA currents) and in front of the ROI (30kV, 0.20 µA and 4 nA currents). Fiducials were milled on the side of the exposed ROI cross-section and on the top of the ROI for tracking during tomography acquisition and for image alignment post-acquisition. The ROI cross-section was prepared for tomography acquisition by final CCS milling at 30 kV and 4 nA. Tomography was acquired in Auto Slice-and-View software, milling 30 nm slices by CCS at 30 kV and 4 nA, preceded by 4° rocking mill to minimize curtaining artifacts. Each slice was imaged by BSE-SEM at 1.2 kV and 0.20 nA at a working distance of 3.4 mm. A total volume of 82.7 × 85 × 29.6 μm^3 was acquired after compensating for sample drift and alignment.

Processing and visualization. Data were reconstructed, processed, and visualized in Dragonfly (ORS, QC, Canada). The image stack was aligned using translation by Optical Flow (smallest step = 0.1%, Gaussian pyramid level = 3) and Linear Drift Compensation (maximum compensation factor), and smoothed by Gaussian blur (3D kernel, size = 7, sigma = 1.5). Osteocyte lacunae and canaliculi were segmented for ease of visualization of the LCN. First, "bone + implant" and "resin + LCN" ROIs were segmented by Otsu thresholding, assigning the "bone + implant" ROI to the upper Otsu range (140.45-255). This ROI was further refined by selecting the 218-255 range to isolate the titanium implant ("implant" ROI). As this operation also included regions corresponding to charging artifacts, these were removed from the "implant" ROI using the "Process islands" operation to keep the largest object in the segmented region (i.e., the implant). The "bone" ROI was obtained by subtracting the "implant" ROI from the "bone + implant" ROI. A separate ROI, hereinafter referred to as "filled bone", was created by adding all the unlabeled pixels within the "bone" ROI using the "Fill inner areas" operation applied in 2D in the x, y, and z direction, with a manual refinement using 2D/3D brushes in the "ROI painter" tool. The LCN was obtained by subtracting the "bone" ROI from the "filled bone" ROI, followed by manual addition/removal of mislabelled pixels/voxels using the 2D/3D brushes in the "ROI painter" tool. The LCN was further refined using the "Process islands" operation to exclude objects with a voxel count below 3000 (value chosen to remove most of the noise and mislabeled voxels while preserving features of interest).

2.5. HAADF-STEM and EDX

An electron-transparent sample (lamella) of the bone-implant interface was prepared in a dual-beam FIB instrument (Helios 5 UC DualBeam, Thermo Fisher Scientific, MA, USA) equipped with a 30 kV Ga^+ ion beam, a gas-delivery system (MultiChem), and a micromanipulator (EasyLift). The lamella was prepared by *in situ* lift-out following existing protocols [30]. Briefly, a 12 × 2 μm^2 ROI was coated with tungsten by electron and ion beam depositions. Rough trenches were milled at 30 kV with 65 nA and 9.3 nA currents. The sample was attached to the micromanipulator with a tungsten deposit, lifted out, and attached to a copper grid. The lamella was thinned to electron transparency (~150 nm thickness) by CCS milling at 30 kV and progressively lower currents (0.79 nA, 0.43 nA, 80 pA, and 40 pA). Lastly, final polishing was completed at 5 kV and 68 pA to limit Ga implantation and amorphization. HAADF-STEM images and energy-dispersive X-Ray spectroscopy (EDX) maps of the lamella

were acquired at 200 kV in a S/TEM instrument (Talos 200X, Thermo Fisher Scientific, MA, USA) equipped with four in-column silicon drift detectors (Super-X detector). EDX maps were acquired on 1000 frames at a dwell time of 10 µs per pixel.

2.6. Resin cast etching and SEM

After BSE-SEM imaging, PFIB-SEM tomography, and *in situ* lift-out, the samples were removed from the aluminum stubs and polished to remove the gold coating. Samples were immersed in 37% phosphoric acid for 10 s, thoroughly rinsed with deionized water, immersed in 5% sodium hypochlorite for 5 min, rinsed with deionized water again, and left to air-dry overnight. The samples were mounted on aluminum stubs using conductive carbon and aluminum tapes, and sputter-coated with gold (~20 nm thickness). Secondary electron (SE)-SEM images were acquired in an SEM instrument (JEOL 6610LV, JEOL, MA, USA) operated at high vacuum, 7 kV accelerating voltage, and a working distance of 10 mm.

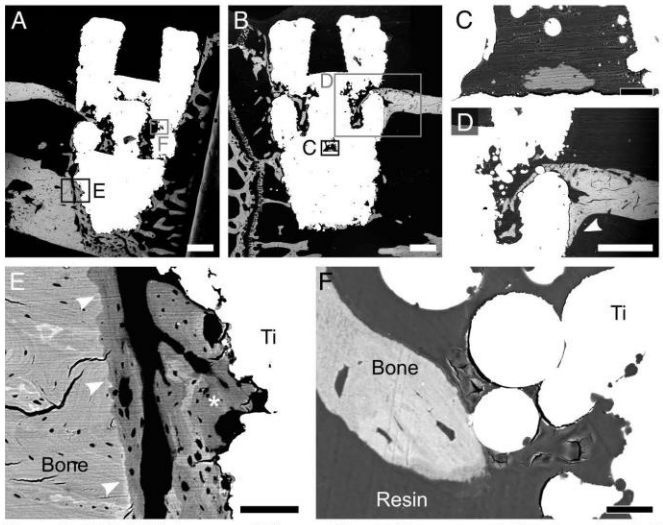

Figure 2. BSE-SEM images of the peri-implant space and the bone-implant interface. A-B) BSE-SEM mosaic images of two genistein-coated Ti-6Al-4V porous implants and their peri-implant space 28 days after implant placement. C) Magnified image of bone within the porous space (corresponding to the internal pore marked by the asterisk in B). D) New bone growing from the native upper cortex down towards the implant (marked by arrowhead). E) New bone growing from pre-existing cortical bone in the lower cortex (marked by arrowheads) and from the implant surface (label "Ti") (marked by the asterisk), indicating distance and contact osteogenesis, respectively. A difference in greyscale level can be noted between old (lighter) and new (darker) bone. F) Bone formed within the porous space in close association with microparticles from L-PBF. Scale bars are 500 µm in A, B, and D, 50 µm in C, 100 µm in E, and 20 µm in F.

3. RESULTS AND DISCUSSION

3.1. Microscale: bone-implant contact and LCN

BSE-SEM imaging provided a general overview of new bone formation in the peri-implant space. New bone was detected both in proximity to the exterior implant surface (Figure 2A-B), as well as inside the porous space (Figure 2C), indicating bone ingrowth facilitated by the porous design. As new bone is continually produced over time, the continuous ingrowth inside the porous space would provide a greater surface area for bone-implant contact and increased interlocking, creating a strong bone-implant interface [19].

Areas of new bone originating at the native cortical bone were noted as lower *Z*-contrast regions connected to higher *Z*-contrast regions, representing new and relatively older tissue, respectively (Fig 2D-E). These areas, together with new bone close to the implant surface and located away from the existing tissue indicates that bone formation proceeds via both distance and contact osteogenesis [25]. Contact osteogenesis is especially apparent within the implant porous space (Figure 2F). Although not possible to chemically confirm its presence *in vivo* in this study, this new bone formation, especially considering the compromised bone repair in the OVX rodent [29], may be in part attributed to the genistein coating, since genistein has a positive effect on osteoblasts [16], hence on bone formation. New bone is also shown adherent to microparticles remaining from L-PBF (Figure 2F), demonstrating interaction with the surface microtopography, as well as the additional

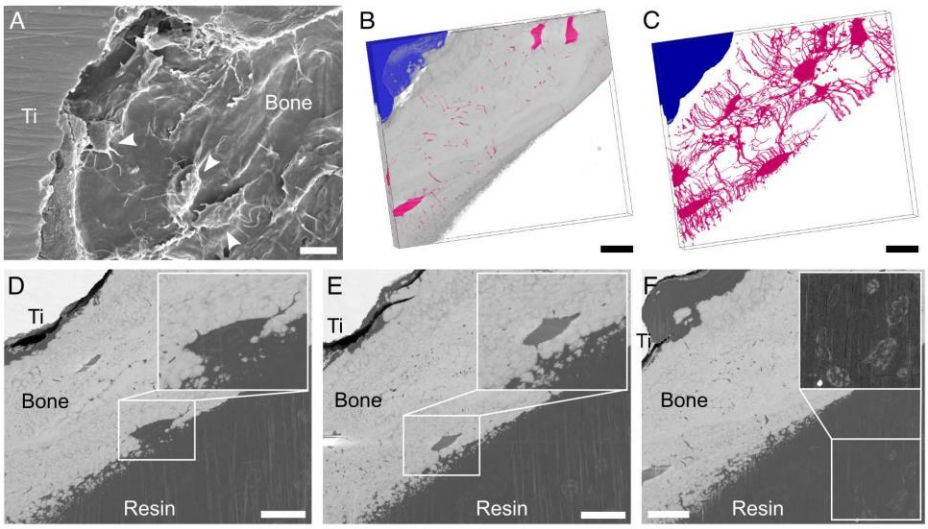

Figure 3. LCN in peri-implant bone. A) SE-SEM image of a sample after resin cast etching, where cells (marked by arrowheads) and their processes are visible in bone juxtaposed to the Ti-6Al-4V implant (indicated by the label "Ti"). B-C) Visualization of the PFIB-SEM tomogram with (B) and without (C) bone (light grey), where implant and LCN are coloured in blue and pink, respectively (resin not shown in the rendering, but available in image B in Figure S3). D-E) Sequence of slices in the PFIB-SEM dataset showing a cell becoming entrapped within mineralizing bone matrix (magnified in insets). While in D part of the lacuna cannot be clearly distinguished from the resin, the same lacuna is fully surrounded by bone matrix in E. The image planes in D and E are approximately 5.8 µm away from each other in the image stack. F) Some brighter features, possibly corresponding to membrane-bound intracellular organelles, can be noted in the resin, especially in the bottom right corner (contrast-enhanced in the inset). Scale bars are 10 µm.

submicron-texturing created by acid etching (Figure S2). This is consistent with several studies showing that surface topography presenting micro-to-nano features favours osseointegration [26,27].

As osteoblasts in the peri-implant compartment become entrapped within the mineralizing matrix, differentiating into osteocytes [31], an extensive LCN develops in newly formed bone. The LCN plays an essential role in mechanosensing [32,33], hence osteocytes are important indicators of bone quality in osseointegration [1]. The formation of an interconnected network of osteocytes was visualized by resin cast etching (Figure 3A), which is a facile method to expose the LCN and directly visualize it by SEM [34–36]. The presence of a well-developed LCN was further confirmed in 3D by PFIB-SEM tomography (Figure 3B-C, Figure S3). Compared to conventional FIB-SEM with Ga^+ ion sources, larger volumes of material can be probed by Xe^+ PFIB-SEM [11,14]. After cropping the collected dataset to remove irrelevant regions (e.g., fiducials, capping layer), a 72.95 × 63.56 × 18.93 μm^3 volume was examined, allowing to visualize peri-implant bone up to 40-50 µm away from the implant surface. A total of 7 osteocyte lacunae with their canaliculi were clearly distinguishable in the dataset. Most lacunae were aligned with their major axes parallel to each other and to the implant surface, with most canaliculi running in the orthogonal direction across the peri-implant bone volume. Cell processes appeared to extend towards the implant surface (Figure 3C), similar to what has been reported by others in osseointegrated implants [35,37].

Interestingly, one lacuna only partly enclosed by bone was noted close to the bone-resin interface (Figure 3D-E). This likely corresponds to a cell transitioning from osteoblast to osteocyte during bone matrix mineralization [31]. Within said lacuna, some brighter features, consisting of a circular/oval line around some globular elements, could be noted. Similar high-contrast features were also present within the resin space (Figure 3F), analogously to what has been reported in previous work [38]. While these features resemble membrane-bound structures such as intracellular organelles, since the sample is not stained it is unclear why they display greyscale

levels higher than resin and closer to mineralized bone.

3.2. Mesoscale: mineralization front and mineral ellipsoids

High *Z*-contrast features resembling cell bodies could be identified in the thin layer of resin between bone and the implant (Figure 4A). These could correspond to either osteoblasts, indicating that in this area bone has grown towards the implant, or bone lining cells, suggesting the presence of an inactive surface. On the other hand, the cell becoming entrapped within the bone matrix (Figure 3D–F) suggests that there is also a mineralization front directed in the opposite direction, i.e., moving away from the implant (Figure 4B). At the bone surface close to this cell lacuna, globular elements of dense bone mineral can be observed (Figure 4B). These features, often termed "mineral foci" or "calcospherulites", have been reported at the mineralization front and in the early stages of mineralization [39–41]. Hence, their presence at the bone surface is a further indication of ongoing mineralization. The same bone surface also presents an area without any mineral foci, where the surface appears mostly smooth instead (Figure 4B). As observed in previous work [38], this location of the bone surface is likely quiescent and not an active formation/mineralization front [47]. Structures similar to mineral foci, referred to as "mineral ellipsoids" or "tesselles", have also been recently reported in mature bone and are recognized as a feature of bone mineral organization at the mesoscale, i.e., at a level bridging micro- and nanoscale [11,12,42–44]. Mineral ellipsoids have largely gone undetected in many studies, but in hindsight, present as "rosettes" [45] and "elliptical motifs", i.e., the 2D transverse and longitudinal cross-sections of mineral ellipsoids, respectively, at bone-biomaterial interfaces [42]. It can be noted that their size and orientation are inconsistent in the bone volume imaged (Figure 4C-D). Ellipsoids are in register with each other only within small areas and change in orientation abruptly from one region to another (Figure 4E). Similar changes in orientation have also been reported in the mouse tibia at the mineralization front of native bone (in absence of an implant) [12]. Another study using PFIB-SEM tomography to investigate new bone at the interface with an AM porous implant in

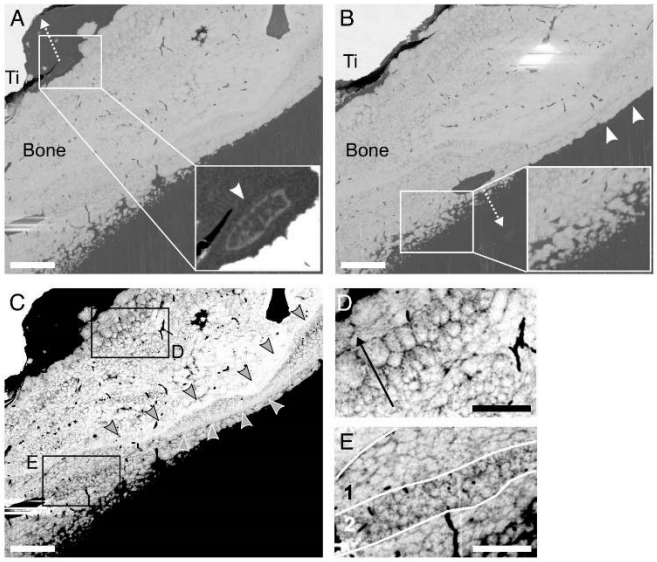

Figure 4. Mineral ellipsoids in newly formed bone in the peri-implant region. A) A high-contrasting feature in the resin region between bone and implant ("Ti" label) marked by the arrowhead in the inset (brightness/contrast-enhanced). If this feature corresponds to a cell (presumably an osteoblast-osteocyte), this suggests that bone is growing towards the implant, as indicated by the dashed arrow. B) A cell (presumably an osteoblastic osteocyte) becoming entrapped by mineralizing bone matrix and the presence of mineral foci (enlarged in the inset) suggest that in this area bone is growing away from the implant, in the direction of the dashed arrow. Away from the cell but along the same bone surface, mineral foci are absent, and the surface appears smoother (arrowheads). C) Contrast/brightness-enhanced version of image A to better visualize the mineral ellipsoids. D) Magnified image showing the size variation of the ellipsoids (becoming larger in the direction of the arrow). E) Magnified image exemplifying an abrupt variation in orientation of the ellipsoids from region 1, where they are predominantly cross-sectioned longitudinally (elliptical motif), to region 2, where they are predominantly cross-sectioned transversally (rosette). Arrowheads indicate two highly-mineralized bands, where no ellipsoids can be distinguished. Scale bars are 10 μm in A, B, and C, and 5 μm in D and E.

the rabbit tibia also identified mineral ellipsoids with alternating orientations, hypothesizing that this architecture contributes to bone toughness analogous to twisted plywood and Bouligand structures [38]. Some ellipsoids were larger (diameter up to 2.5 μm in transverse cross-sections) than what has been reported in past studies (average diameter of 0.6-0.9 μm in transverse cross-sections [11,12,42]) (Figure 4D). This could be related to the mineralization stage and/or the rate at which bone formation proceeds. The dependence of mineral ellipsoid dimensions on mineralization progression has been shown in the tibia of wild type and *Hyp* mice, with ellipsoids enlarging as the distance from the mineralization front increases [12]. Conversely, some of the large mineral ellipsoids observed were relatively close the mineralization front (Figure 4D). It is possible that the altered bone repair due to OVX [29] and/or the local promotion of osteoblastogenesis by genistein [16] influence the formation and maturation of the mineral ellipsoids. More work needs to be done on ellipsoids in peri-implant bone to elucidate size variations, especially in presence of disease. On the other hand, it cannot be excluded that the contour between distinct ellipsoids is not well resolved in the dataset at times, making multiple neighbouring ellipsoids appear as one, large ellipsoid. Some brighter bands, without any ellipsoids distinguishable, were also noted (Figure 4C, arrowheads). These more densely mineralized regions could correspond to cement lines marking the position where different mineralization fronts meet.

3.3. Nanoscale: bone-implant interface and nano-osseointegration

In the PFIB-SEM tomogram, a thin layer of resin and/or cracks were often present between bone and implant, hindering intimate contact between the two. These are mostly artifacts arising from implant retrieval and/or sample preparation. In particular, bone detachment from the implant can occur during retrieval [46,47], while shrinkage during fixation and embedding often results in cracks at the bone-implant interface [48]. Nonetheless, some regions of close bone-implant contact, without any interposed resin or cracks, were identified in BSE-SEM images. An electron transparent lamella was prepared at one of said regions by FIB *in situ* lift-out (Figure S4) and imaged by HAADF-STEM. This confirmed that bone-implant contact existed at the nanoscale (Figure 5A-B). Collagen fibrils appeared to lack long-range registry, especially in proximity to the implant, compatibly with the early retrieval time point. Groups of collagen fibrils co-aligned with each other and displaying the characteristic banding pattern of in-plane collagen were noted (Figure 5C, region 1). Near this area, out-of-plane fibrils were also present (Figure 5C, region 2), confirming the abrupt changes in orientation observed in the PFIB-SEM tomogram in both this study and previous work [38]. EDX validated the gradual nature of the bone-implant interface (Figure 5D-E). A decrease in content for implant elements (Ti, Al, V) was accompanied by an increase in Ca and P (Figure 5F), demonstrating, with nanoscale resolution, the intermixing between the implant oxide surface layer (TiO_2) and newly formed bone. In the top region of the lamella, a brighter area, with not clearly distinguishable collagen fibrils, was observed (Figure 5A, C). While this could correspond to a region with increased mineralization, it is also possible to be an artifact due to a higher thickness in that portion of the lamella as a result of uneven thinning or an exaggerated wedge shape.

In this imaging and elemental analysis, the detection of genistein was not possible. The electrochemical layer-by-layer method produces an extremely thin coating of genistein, and its chemical composition, mostly consisting of hydrocarbons, is not sufficiently distinct from the organic compounds in bone to differentiate it in the EDX spectra and maps. Conversely, the roughened acid-etched surface is visible by HAADF-STEM and contributes to the nanoscale interlocking observed.

4. CONCLUSIONS

A multiscale and multimodal characterization workflow was used to examine bone response to an AM porous implant for local genistein delivery. BSE-SEM showed new bone within the internal pores of the implant, confirming

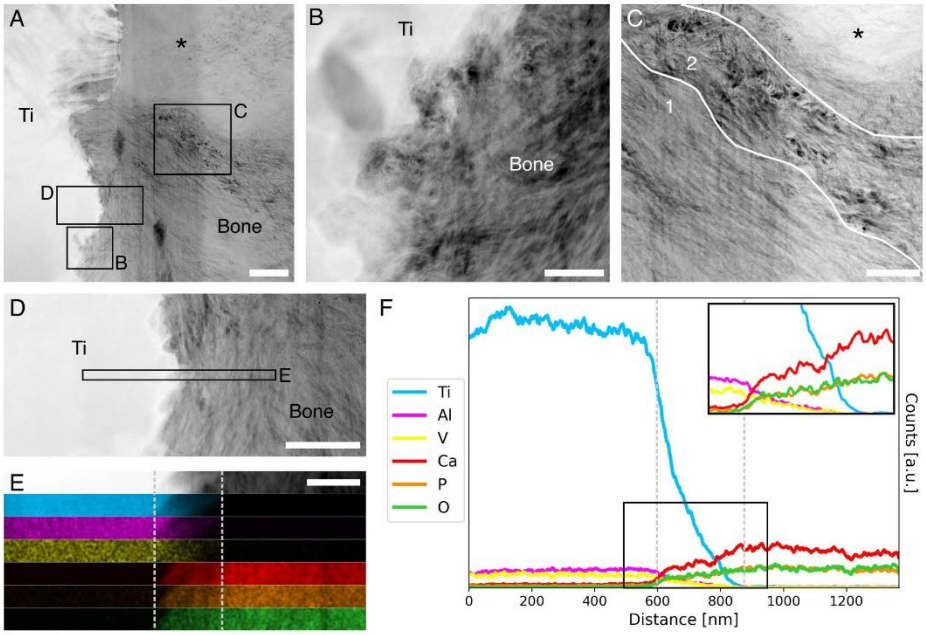

Figure 5. Bone-implant interface at the nanoscale. A) HAADF-STEM overview image of the lamella of a bone-implant ROI prepared by FIB *in situ* lift-out. B) Magnified image of an area of bone-implant contact occurring at the nanoscale, demonstrating nano-osseointegration. C) Collagen fibrils change orientation abruptly from in-plane (region 1) to out-of-plane (region 2). The asterisk in the top region in A and C marks a brighter region, likely due to the higher thickness of the lamella in that area. D) HAADF-STEM image of the bone-implant interface to provide a lower-magnification overview of the area where EDX acquisition was completed (marked by the rectangle). E) From top to bottom, HAADF-STEM image of the area where EDX maps were acquired, and EDX maps of titanium (blue), aluminum (magenta), vanadium (yellow), calcium (red), phosphorous (orange), and oxygen (green). The interfacial area is marked by the grey dotted lines, and measures approximately 250 nm in width. F) Elemental variation along a line directed from the implant towards bone (over the entire area of the maps in E), magnified in the inset. The grey dotted lines indicate the same interfacial zone marked on the maps in E. Oxygen displays a high concentration not just at the interface but also in bone, as it is one of its constituting elements. Scale bars are 1 µm in A, 200 nm in B and E, and 500 nm in C and D.

bone formation and ingrowth facilitated by the porous design. HAADF-STEM and EDX validated that osseointegration occurred at the nanoscale. In the volume of peri-implant bone imaged via PFIB-SEM tomography, mineral ellipsoids were noted throughout newly formed bone and displayed inconsistencies in size and orientation. Cell processes extending towards the implant surface were visible in 2D in SEM images after resin cast etching, and further confirmed in 3D by PFIB-SEM tomography. Overall, information gained across multiple length scales shows a promising bone response despite the impaired bone repair conditions in the OVX pre-clinical rat model. Hence, this innovative implant combining engineered porosity to maximize bone-implant contact and a genistein coating for local drug delivery could be a promising design for applications in osteoporosis. Lastly, multiscale characterization of osseointegration should also encompass the mesoscale, i.e., the level connecting micro- and nanoscale. This could be especially important for a better understanding of mineral ellipsoids in peri-implant bone to determine their eventual role in mechanical functions, and whether they are affected by diseases and/or therapeutic agents.

ACKNOWLEDGEMENTS

Funding was provided by the Academy of Osseointegration and Natural Sciences and Engineering Research Council of Canada (NSERC) Alliance International Catalyst Program (grant no. ALLRP 576146-22). Scholarships for student support are greatly acknowledged from the Ontario Graduate

Scholarship and the Blanceflor Foundation for C.M., the NSERC Vanier Canada Graduate Scholarship for L.-A.D., the NSERC Postgraduate Scholarship – Doctoral for J.D., and the NSERC Undergraduate Student Research Awards (USRA) for W.C. Funding support is also acknowledged from the São Paulo Research Foundation (FAPESP) for A.C.E.S. and R.O. (process no. 2021/06849-4 and 2021/13026-4, respectively), the Svenska Sällskapet för Medicinsk Forskning (SSMF) for F.A.S., and the Swedish Research Council for A.P. (grant no. 2020-04715). The Area of Advance Materials at Chalmers and at the Department of Biomaterials (University of Gothenburg) within the Strategic Research Area initiative launched by the Swedish government is also acknowledged. Implants were manufactured at the Multi-Scale Additive Manufacturing Lab at the University of Waterloo (ON, Canada). Electron microscopy experiments were performed at the Canadian Centre for Electron Microscopy (CCEM) at McMaster University (ON, Canada), a facility supported by the Natural Sciences and Engineering Research Council of Canada (NSERC) and other government agencies. Figure 1 was created with BioRender.com. Authors are thankful to Martina Jolic for fruitful scientific discussions.

AUTHOR CONTRIBUTIONS

Conceptualization: Chiara Micheletti, Liza-Anastasia DiCecco, Joseph Deering, Roberta Okamoto, Kathryn Grandfield. **Formal analysis:** Chiara Micheletti. **Methodology**: Chiara Micheletti, Liza-Anastasia DiCecco, Joseph Deering. **Investigation:** Chiara Micheletti, Liza-Anastasia DiCecco, Joseph Deering, Wanqi Chen, Ana Cláudia Ervolino da Silva. **Visualization:** Chiara Micheletti, Wanqi Chen. **Supervision:** Furqan A. Shah, Anders Palmquist, Roberta Okamoto, Kathryn Grandfield. **Funding acquisition:** Roberta Okamoto, Kathryn Grandfield. **Writing – original draft:** Chiara Micheletti. **Writing – review and editing:** All authors.

CONFLICT OF INTEREST

The authors declare no conflicts of interest.

DATA AVAILABILITY STATEMENT

Data are provided in the main manuscript or in Supplementary Information.

REFERENCES

1. Shah FA, Thomsen P, Palmquist A. Osseointegration and current interpretations of the bone-implant interface. Acta Biomater. 2018;84:1–15.
2. Albrektsson T, Brånemark P-I, Hansson H-A, Lindström J. Osseointegrated titanium implants: Requirements for ensuring a long-lasting, direct bone-to-implant anchorage in man. Acta Orthop Scand. 1981;52:155–70.
3. Engqvist H, Botton GA, Couillard M, Mohammadi S, Malmström J, Emanuelsson L, et al. A novel tool for high-resolution transmission electron microscopy of intact interfaces between bone and metallic implants. J Biomed Mater Res A. 2006;78A:20–4.
4. Palmquist A, Grandfield K, Norlindh B, Mattsson T, Brånemark R, Thomsen P. Bone-titanium oxide interface in humans revealed by transmission electron microscopy and electron tomography. J R Soc Interface. 2012;9:396–400.
5. Grandfield K, Gustafsson S, Palmquist A. Where bone meets implant: The characterization of nano-osseointegration. Nanoscale. 2013;5:4302–8.
6. Grandfield K. Bone, implants, and their interfaces. Phys Today. 2015;68:40–5.
7. Shah FA, Nilson B, Brånemark R, Thomsen P, Palmquist A. The bone-implant interface – Nanoscale analysis of clinically retrieved dental implants. Nanomed Nanotechnol Biol Med. 2014;10:1729–37.
8. Wang X, Shah FA, Palmquist A, Grandfield K. 3D characterization of human nano-osseointegration by on-axis electron tomography without the missing wedge. ACS Biomater Sci Eng. 2017;3:49–55.
9. Palmquist A. A multiscale analytical approach to evaluate osseointegration. J Mater Sci Mater Med. 2018;29:60.
10. Reznikov N, Shahar R, Weiner S. Bone hierarchical structure in three dimensions. Acta Biomater. 2014;10:3815–26.
11. Binkley DM, Deering J, Yuan H, Gourrier A, Grandfield K. Ellipsoidal mesoscale mineralization pattern in human cortical bone revealed in 3D by plasma focused ion beam serial sectioning. J Struct Biol. 2020;212:107615.
12. Buss DJ, Reznikov N, McKee MD. Crossfibrillar mineral tessellation in normal and Hyp mouse bone as revealed by 3D FIB-SEM microscopy. J Struct Biol. 2020;212:107603.
13. Reznikov N, Almany-Magal R, Shahar R, Weiner S. Three-dimensional imaging of collagen fibril organization in rat circumferential lamellar bone using a dual beam electron microscope reveals ordered and disordered sub-lamellar structures. Bone. 2013;52:676–83.
14. Burnett TL, Kelley R, Winiarski B, Contreras L, Daly M, Gholinia A, et al. Large volume serial section tomography by Xe Plasma FIB dual beam microscopy. Ultramicroscopy. 2016;161:119–29.
15. Javed F, Ahmed HB, Crespi R, Romanos GE. Role of primary stability for successful osseointegration of dental implants: Factors of influence and evaluation. Interv Med Appl Sci. 2013;5:162–7.
16. Cepeda SB, Sandoval MJ, Crescitelli MC, Rauschemberger MB, Massheimer VL. The isoflavone genistein enhances osteoblastogenesis: Signaling pathways involved. J Physiol Biochem. 2020;76:99–110.
17. Ruggiero SL, Dodson TB, Aghaloo T, Carlson ER, Ward BB, Kademani D. American Association of Oral and Maxillofacial Surgeons' position paper on medication-related osteonecrosis of the jaw – 2022 update. J Oral Maxil Surg. 2022;80:920–43.
18. Koschwanez HE, Reichert WM. Textured and porous materials. In: Ratner BR, Hoffman AS, Schoen FJ, Lemons JE, editors. Biomaterials science: An introduction to materials in medicine. Oxford, UK: Academic Press; 2013. p. 321–31.

19. Wang Z, Wang C, Li C, Qin Y, Zhong L, Chen B, et al. Analysis of factors influencing bone ingrowth into three-dimensional printed porous metal scaffolds: A review. J Alloy Compd. 2017;717:271–85.
20. Deering J, Grandfield K. Current interpretations on the in vivo response of bone to additively manufactured metallic porous scaffolds: A review. Biomaterials Biosyst. 2021;2:100013.
21. Heinl P, Müller L, Körner C, Singer RF, Müller FA. Cellular Ti–6Al–4V structures with interconnected macro porosity for bone implants fabricated by selective electron beam melting. Acta Biomater. 2008;4:1536–44.
22. Palmquist A, Jolic M, Hryha E, Shah FA. Complex geometry and integrated macro-porosity: Clinical applications of electron beam melting to fabricate bespoke bone-anchored implants. Acta Biomater. 2023;156:125–45.
23. Pyka G, Burakowski A, Kerckhofs G, Moesen M, Van Bael S, Schrooten J, et al. Surface modification of Ti6Al4V open porous structures produced by additive manufacturing. Adv Eng Mater. 2012;14:363–70.
24. Micheletti C, Lee BEJ, Deering J, Binkley DM, Coulson S, Hussanain A, et al. Ti-5Al-5Mo-5V-3Cr bone implants with dual-scale topography: A promising alternative to Ti-6Al-4V. Nanotechnology. 2020;31:235101.
25. Davies JE. Understanding peri-implant endosseous healing. J Dent Educ. 2003;67:932–49.
26. Palmquist A, Lindberg F, Emanuelsson L, Brånemark R, Engqvist H, Thomsen P. Biomechanical, histological, and ultrastructural analyses of laser micro- and nano-structured titanium alloy implants: A study in rabbit. J Biomed Mater Res A. 2010;92A:1476–86.
27. Davies JE, Ajami E, Moineddin R, Mendes VC. The roles of different scale ranges of surface implant topography on the stability of the bone/implant interface. Biomaterials. 2013;34:3535–46.
28. Davies JE, Mendes VC, Ko JCH, Ajami E. Topographic scale-range synergy at the functional bone/implant interface. Biomaterials. 2014;35:25–35.
29. Luvizuto ER, Queiroz TP, Dias SMD, Okamoto T, Domelles RCM, Garcia-Junior IR, et al. Histomorphometric analysis and immunolocalization of RANKL and OPG during the alveolar healing process in female ovariectomized rats treated with oestrogen or raloxifene. Arch Oral Biol. 2010;55:52–9.
30. Jarmar T, Palmquist A, Brånemark R, Hermansson L, Engqvist H, Thomsen P. Technique for preparation and characterization in cross-section of oral titanium implant surfaces using focused ion beam and transmission electron microscopy. J Biomed Mater Res A. 2008;87A:1003–9.
31. Dallas SL, Bonewald LF. Dynamics of the transition from osteoblast to osteocyte. Ann Ny Acad Sci. 2010;1192:437–43.
32. Bonewald LF. The amazing osteocyte. JBMR. 2011;26:229–38.
33. Robling AG, Bonewald LF. The osteocyte: New insights. Annu Rev Physiol. 2020;82:485–506.
34. Kubek DJ, Gattone VH, Allen MR. Methodological assessment of acid-etching for visualizing the osteocyte lacunar-canalicular networks using scanning electron microscopy. Microsc Res Techniq. 2010;73:182–6.
35. Shah FA, Wang X, Thomsen P, Grandfield K, Palmquist A. High-resolution visualization of the osteocyte lacuno-canalicular network juxtaposed to the surface of nanotextured titanium implants in human. ACS Biomater Sci Eng. 2015;1:305–13.
36. Sato M, Shah FA. Contributions of resin cast etching to visualising the osteocyte lacuno-canalicular network architecture in bone biology and tissue engineering. Calcif Tissue Int. 2023;112:525–542.
37. Shah FA, Johansson ML, Omar O, Simonsson H, Palmquist A, Thomsen P. Laser-modified surface enhances osseointegration and biomechanical anchorage of commercially pure titanium implants for bone-anchored hearing systems. PLOS One. 2016;11:e0157504.
38. Deering J, Chen J, Mahmoud D, Tang T, Lin Y, Fang Q, et al. Characterizing mineral ellipsoids in new bone formation at the interface of Ti6Al4V porous implants. bioRxiv. 2023;2023.01.20.524810.
39. Bonucci E. The locus of initial calcification in cartilage and bone. Clin Orthop Relat Res. 1971;78:108–39.
40. Midura RJ, Vasanji A, Su X, Wang A, Midura SB, Gorski JP. Calcospherulites isolated from the mineralization front of bone induce the mineralization of type I collagen. Bone. 2007;41:1005–16.
41. Addison WN, Nelea V, Chicatun F, Chien Y-C, Tran-Khanh N, Buschmann MD, et al. Extracellular matrix mineralization in murine MC3T3-E1 osteoblast cultures: An ultrastructural, compositional and comparative analysis with mouse bone. Bone. 2015;71:244–56.
42. Micheletti C, Hurley A, Gourrier A, Palmquist A, Tang T, Shah FA, et al. Bone mineral organization at the mesoscale: A review of mineral ellipsoids in bone and at bone interfaces. Acta Biomater. 2022;142:1–13.
43. McKee MD, Buss DJ, Reznikov N. Mineral tessellation in bone and the stenciling principle for extracellular matrix mineralization. J Struct Biol. 2022;214:107823.
44. Buss DJ, Kröger R, McKee MD, Reznikov N. Hierarchical organization of bone in three dimensions: A twist of twists. J Struct Biol X. 2022;6:100057.
45. Grandfield K, Vuong V, Schwarcz HP. Ultrastructure of bone: Hierarchical features from nanometer to micrometer scale revealed in focused ion beam sections in the TEM. Calcif Tissue Int. 2018;103:606–16.
46. Sennerby L, Ericson LE, Thomsen P, Lekholm U, Åstrand P. Structure of the bone-titanium interface in retrieved clinical oral implants. Clin Oral Impl Res. 1991;2:103–11.
47. Iezzi G, Scarano A, Mangano C, Cirotti B, Piattelli A. Histologic results from a human implant retrieved due to fracture 5 years after insertion in a sinus augmented with anorganic bovine bone. J Periodontol. 2008;79:192–8.
48. Shah FA, Johansson BR, Thomsen P, Palmquist A. Ultrastructural evaluation of shrinkage artefacts induced by fixatives and embedding resins on osteocyte processes and pericellular space dimensions. J Biomed Mater Res A. 2015;103:1565–76.

SUPPLEMENTARY

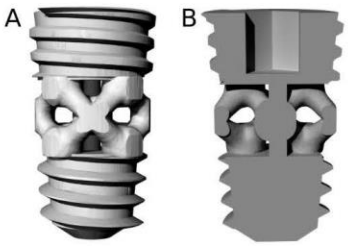

Figure S1. Renderings of implant design. A) 3D rendering of the implant design. B) Longitudinal cross-section of the implant.

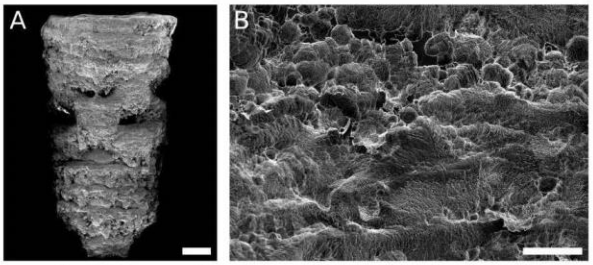

Figure S2. Implant surface topography after acid etching. A) Overview SE-SEM image of the implant after acid etching. B) Higher magnification SE-SEM image of the implant surface topography after acid etching. Scale bars are 500 µm in A and 50 µm in B.

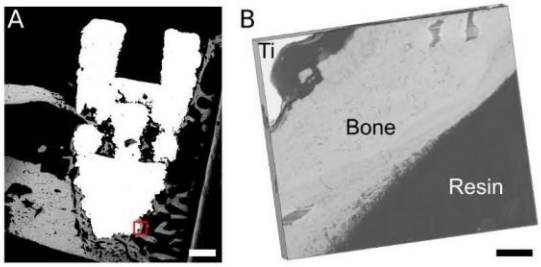

Figure S3. A) BSE-SEM overview image indicating the location of PFIB-SEM tomography acquisition (marked by the red rectangle). B) Visualization of the PFIB-SEM tomogram including resin and without false colouring, corresponding to Figure 3B-C. Scale bars are 500 µm in A and 10 µm in B.

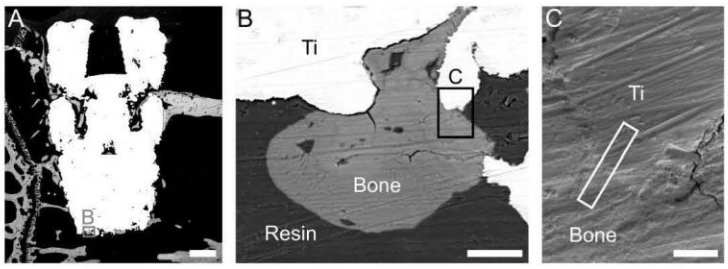

Figure S4. A) BSE-SEM overview image of the peri-implant space [Note: A is the same as Figure 2B, reproduced here to better show the site selection for STEM sample preparation]. B) BSE-SEM image of the area of bone-implant contact used for the preparation of the sample for STEM analysis. C) SE-SEM image indicating the location selected for STEM sample preparation by FIB *in situ* lift-out (marked by the white rectangle). Scale bars are 500 μm in A, 30 μm in B, and 5 μm in C.

Paper IV

Biomaterials Advances 134 (2022) 112688

Contents lists available at ScienceDirect

Biomaterials Advances

journal homepage: www.elsevier.com/locate/bioadv

PTH 1-34-functionalized bioactive glass improves peri-implant bone repair in orchiectomized rats: Microscale and ultrastructural evaluation

Pedro Henrique Silva Gomes-Ferreira [a,*], Chiara Micheletti [b], Paula Buzo Frigério [c], Fábio Roberto de Souza Batista [a], Naara Gabriela Monteiro [c], Odair Bim-júnior [d], Paulo Noronha Lisboa-Filho [d], Kathryn Grandfield [b,e], Roberta Okamoto [c,1]

[a] Department of Surgery and Integrated Clinic, São Paulo State University, Araçatuba Dental School, Araçatuba, SP, Brazil
[b] Department of Materials Science and Engineering, McMaster University, Hamilton, ON, Canada
[c] São Paulo State University, Araçatuba Dental School, Araçatuba, SP, Brazil
[d] Department of Physics, São Paulo State University, School of Sciences, Bauru, SP, Brazil
[e] School of Biomedical Engineering, McMaster University, Hamilton, ON, Canada

ARTICLE INFO

Keywords:
Osteoporosis
Bone regeneration
Parathyroid hormone
Dental implants
Bioactive glass
Local drug delivery

ABSTRACT

The objective of this work was to investigate the use of Biogran® functionalized with parathyroid hormone (PTH) 1–34 by sonochemistry for the local delivery of this anabolic agent to the implant site. The effects of Biogran® and topical administration of PTH 1–34 on peri-implant bone regeneration were evaluated from the microscale to ultrastructural levels in healthy (SHAM) and orchiectomized (ORQ). While some animals only received a titanium implant in their tibial metaphyses (CLOT group), in others the peri-implant defect was first filled with Biogran® either without or with PTH 1–34 functionalization (BG and BGPTH groups, respectively) prior to implant installation. Osseointegration was characterized from a biomechanical perspective by measuring the removal torque with the counter-torque technique. Micro-CT was used to evaluate the percentage of bone volume, trabecular thickness, number and separation, and bone-implant contact (BIC). Dynamics of new bone formation were assessed by measuring fluorochrome area, daily mineral apposition rate, and neoformed bone area using confocal laser microscopy. RT-PCR was performed to evaluate ALP and osteocalcin expression. The interface between newly formed bone and Biogran® was examined using scanning electron microscopy (SEM) and scanning transmission electron microscopy (STEM) at the micro-and nanoscale, respectively, while elemental analyses were completed in SEM with energy-dispersive X-ray spectroscopy (EDS). STEM imaging demonstrated the intimate attachment of bone to Biogran® (nanoscale level). Overall, the results suggest that the effectiveness of the topical administration of PTH 1–34 at the implant site seems enhanced in osteoporotic bone, promoting peri-implant bone regeneration to comparable levels in healthy conditions.

1. Introduction

Implant installation immediately after dental extraction is a common occurrence in deficient bone quality areas, such as dehiscences, fenestrations, and vertical and peri-implant defects, constituting a great part of the clinical conditions found in patients today [1]. In view of these situations, there is a need for improving bone reconstruction procedures to prepare or optimize the recipient bone through autogenous, xenogenous or alloplastic grafts [2].

Among alloplastic materials Biogran® (Biomet 3i, Palm Beach Gardens, Florida, USA) is a clinically available silica-based bioactive glass. Biogran® granules act as carriers for growth factors and serve as scaffold for bone formation [3,4]. Bioactive glasses have stood out as excellent osteoconductors, behaving superiorly to hydroxyapatite, as validated by the interaction between the biomaterial surface and adjacent bone tissue [5,6]. Biogran® has also been shown to be easy to manipulate and has displayed hemostatic properties, in addition to being more stable than hydroxyapatite in a bleeding site. Moreover, the silica content in bioactive glasses contributes further to their high bioactivity [7].

Not only the quantity, but also the quality of bone tissue is a determining factor for the proper integration of the dental implants [8–10]. In this context, when the bone exhibits a cortical and/or trabecular structure with lower density, the bone-implant interface is compromised [11,12], as it can be observed in osteoporosis [13,14]. Osteoporosis is a bone

* Corresponding author at: Rua José Bonifácio, 1193, 16015-050, Vila Mendonça, Aracatuba, Sao Paulo, Brazil.
E-mail address: pedroferreirabmf@gmail.com (P.H.S. Gomes-Ferreira).
[1] Roberta Okamoto is affiliated with research productivity scholarship (process: 306389/2017-7).

http://dx.doi.org/10.1016/j.msec.2022.112688
Received 15 August 2021; Received in revised form 20 January 2022; Accepted 27 January 2022
Available online 31 January 2022

metabolic disorder typically recognized as a significant health problem in women due to the depletion of estrogen supply in the post-menopausal phase, and affecting approximately 2/3 of this population [15,16]. However, osteoporosis is also regularly reported in men, with a higher incidence in individuals over 50 years of age [15–17].

Parathyroid hormone (PTH)-based medications are commonly indicated for severe osteoporosis, due to their anabolic properties able to increase bone mineral density [18]. In particular, PTH is an effective option for treating osteoporosis in men [18,19], and clinical studies have proved it to be successful at preventing vertebral and long bone fractures [20]. The use of topical PTH 1–34 has been tested in conjunction with titanium implants [20], showing that enough PTH was released locally from the implant surface to effectively influence the expression of osteoblastic genes, which suggests the potential efficacy of local delivery of PTH [21].

Metal ions used in scaffolds or processed in order to functionalize some surface showed osteoblastic and osteoclastic activity [22,23]. Zn-MS particles used in PLLA (Poly-L-lactic acid) scaffolds showed potential to improve mechanical properties and osteogenic activity [22]. Zinc silicate is also shown to be a promising additive to modify the osteogenic activity or even of other calcium phosphate ceramics (bone graft with low osteogenic activity and slow degradation rate) *via* macrophage immunomodulation [23].

Since the systemic use of PTH 1–34 is well described in the literature with positive outcomes on peri-implant bone regeneration and alveolar bone quality repair in rats [24,25]. In addition, previous work has shown that PTH 1–34 can be used to functionalize bioactive glass using sonochemistry [26]. This work aims to evaluate the effect of the local release of PTH 1–34 as functionalized to Biogran® by sonochemistry on peri-implant bone regeneration in osteoporotic conditions through analyses on calcified tissue, biomechanics, and the nanoscale ultrastructural evaluation of the bone-biomaterial interface formed in the reparation process.

2. Materials and methods

2.1. Animals

After approval by the Ethics Committee on the Use of Animals of the Araçatuba Dental School at UNESP (approval no. 00199/2017), 80 6-month-old male rats (Rattus novergicus albinus, Wistar) from the central vivarium of the Araçatuba Dental School at UNESP, weighing around 500 g, were used. The animals were randomly allocated in two groups (SHAM and ORQ), according to gonadectomy surgery. Rats assigned to the SHAM group were subjected to fictitious surgery, with exposure of the testicles only, while those in the ORQ group underwent bilateral orchiectomy.

Both ORQ and SHAM groups were further divided into three different subgroups: CLOT, receiving the implant only, without the use of Biogran®; BG, receiving Biogran® in the peri-implant defect, in addition to the implant; and BGPTH, receiving Biogran® functionalized with PTH 1–34, in addition to the implant (Table 1).

Prior to surgery, all the animals were kept in individual cages and fed a balanced diet (NUVILAB, Curitiba PR, Brazil) containing 1.4% Ca and 0.8% P, and water *ad libitum*.

2.2. Biomaterial, preparation and functionalization by sonochemistry

Biogran® (Biomet 3i, Palm Beach Gardens, Florida, USA) with a particle size of approximately 300 to 355 μm was used, this biomaterial is a silica-based bioactive glass, it has a osteoconductive characteristic, made of SiO_2(45 wt%), CaO (24.5 wt%), Na_2O (24.5 wt%) and P_2O_5 (6 wt%). The functionalization was performed using Biogran®, PTH 1–34 (Forteo®, Ely Lilly, Indianapolis, Indiana, USA), presented in liquid form in a concentration of 250 μg/ml in an injection pen with a cartridge of 3 ml, and Milli-Q® ultrapure water were mixed together by sonochemistry to obtain a homogeneous mixture and to decrease the particle size of the ceramic using the methodology described in thorough detail elsewhere [26]. Briefly, the above components were subjected to ultrasonic processing in a Sonics VCX-750 model, with 750 W of power and frequency of 20 kHz, with 3 pulses of 5 min (for a total 15 min of sonochemistry, which was previously shown to provide the best physiological response [25]) and variable amplitude fixed up to 40% of the nominal amplitude of the equipment (450 W/cm^2). In the synthesis chamber, the conditions were atmospheric air, whereas the container with the samples and the ultrasonic tip were cooled with an ice bath. For the BG group, a similar process was used but with Biogran® particles and Milli-Q® water only, without the addition of PTH 1–34. After sonochemistry the samples were subsequently dried in an oven at 60 °C, and no further thermal annealing treatment was carried out [26–28].

Table 1
Experimental groups according to the biomaterial experiment and test.

Groups	
CLOT	Group in which the peri-implant defect was created and an implant installed without the use of Biogran®.
BG	Group in which the peri-implant defect was created and an implant installed after filling the defect with Biogran®.
BGPTH	Group in which the peri-implant defect was created and implant installed after filling the defect with Biogran® functionalized with PTH 1–34.

After implantation of the biomaterial, a fraction of PHT molecules adsorbed on the outermost layers of glass particles will inevitably be released to the physiological environment. Another fraction of the drug will probably undergo sustained release as the bioactive glass dissolves *in situ*. It is known that when a surface-active silicate glass is immersed in body fluids, a sequence of inorganic stages leads to the partial dissolution of the glass, which is critical to the bone-bonding ability of these materials [29]. Furthermore, it is expected that the sonochemical treatment promotes an effective chemical bond between PTH (O) and the BG's surface (Si or P), as reported in the literature [30].

Otherwise, time-dependent release curves have also been reported with a drug release (in %) about of 50% after 30 h [31], in a similar behavior already reported by elsewhere [30].

2.3. Animal surgeries

2.3.1. Bilateral orchiectomy

After anesthesia with Coopazine (Xylazine-Coopers, Brasil, Ltd.) and Vetaset (injectable ketamine hydrochloride, Fort Dodge, Saúde Animal Ltd.), both scrotal sacs of the ORQ rats were incised to expose the testicles. Using hemostatic forceps, the spermatic funicular was presented, with concomitant individualization and ligation of the vas deferens and the vascular pedicle, and then sectioned. The testicles were removed and the surgical wound was sutured with polyglactín 910 4-0 (Ethicon, Johnson & Johnson, São José dos Campos, SP, Brazil). The SHAM group underwent the same procedure, but only the surgical exposure of the testicles was performed without their removal, in order to subject the animals in this group to the same surgical stress as the ORQ group [32]. The rats were kept in the Vivarium of the Basic Sciences Department of the Araçatuba Dental School at UNESP. This same surgical technique has already proved to be effective at inducing osteoporosis in other studies [24,25,33].

2.3.2. Peri-implant defect surgery and implant installation

Peri-implant defect surgery and implant installation occurred 30 days after orchiectomy and fictitious surgeries. The animals were fasted for 8 h prior to the surgical procedure and sedated by a combination of 50 mg/kg intramuscular ketamine (Vetaset, Fort Dodge Saúde Animal Ltd., Campinas, São Paulo, Brazil) and 5 mg/kg xylazine hydrochloride (Dopaser, Laboratorio Calier do Brasil Ltd., Osasco, São Paulo, Brazil), and they received mepivacaine hydrochloride (0.3 ml/kg, Scandicaíne 2% with adrenaline 1: 100,000, Septodont, France) as local anesthesia and for hemostasis of the operative field. After sedation, trichotomy was performed in the medial portion of the tibia and antisepsis was ensured with Polyvinyl Pyrrolidone Iodine (PVPI 10%, Riodeine Degermante, Rioquímica, São José do Rio Preto). A 1.5 cm long incision was made in

the region of the tibial metaphysis bilaterally with a blade number 15 (Feather Industries Ltda, Tokyo, Japan) and the bone was exposed.

Commercially pure grade IV titanium implants (Emfils Comércio Produtos Odontológicos) (Ø = 2 mm, L = 4 mm) with a surface treated by double acid etching were installed in the tibia after sterilization by gamma irradiation. A defect was created using the technique by Gomes-Ferreira et al. [26], *i.e.*, with a 1.3 mm diameter cutter on the two cortices, and a 2.0 mm, a pilot (2/3) and a 3.0 mm cutter on the upper cortex. In the CLOT group the implant was immediately inserted in the defect and locked in the lower cortex only. Conversely, implants in the BG and BGPTH groups were placed and locked into the lower cortex after the defect void was filled by Biogran® (with or without PTH functionalization). The volume of biomaterial used to fill the defect sites in the BG and BGPTH groups was computed from estimating the defect volume as a cylinder (L = 4 mm, radius = 3 mm cutter diameter/2, hence V = 28.27 mm^3), minus the volume of the implant estimated as a cylinder (L = 4 mm, radius = 2 mm, hence V = 12.57 mm^3). Therefore, a total of 15.7 mm^3 of Biogran® was inserted in the defect, which ensured contact with the implant throughout its length.

The relative mass concentration of PTH 1–34 and Biogran® in the BGPTH group was determined as described in [34], where 1 μg of PTH 1–34 was used for every 35.34 mm^3 of Biogran®. Therefore, a 15.7 mm^3 defect as used herein contains 0.44 μg of PTH 1–34, or about 2 μl.

A total of 128 implants were placed across all groups. Each animal received two implants, one in each tibial metaphysis. The tissues were sutured in planes using absorbable thread (Polygalactin 910 - Vycril 4.0, Ethicon, Johnson Prod., São José dos Campos, Brazil) with continuous stitches in the deep plane and with monofilament thread (Nylon 5.0, Ethicon, Johnson, São José dos Campos, Brazil) with interrupted points in the outermost plane.

In the immediate postoperative period, each animal received a single intramuscular dose of 0.2 ml of penicillin G-benzathine (Small Veterinary Pentabiotic, Fort Dodge Saúde Animal Ltd., Campinas, SP). The animals were kept in individual cages throughout the experiment with food and water *ad libitum*.

2.3.3. Implant and retrieval timeline

On the 30th day after ORQ and SHAM surgeries, surgery for the creation of bone defect and installation of the implants in the tibiae of the rats was performed. For elemental and ultrastructural analyses, euthanasia was performed 30 days after implant placement. For biomechanical, reverse transcriptase-polymerase chain reaction (RT-PCR), micro-computed X-ray tomography (micro-CT), and confocal laser microscopy analyses, 14 days after implant installation 20 mg/kg of the fluorochrome calcein was administered intramuscularly [35,36], and after another 28 days (*i.e.*, 42 days after implant placement) 20 mg/kg of the fluorochrome alizarin red was administered to each animal [35,36]. These animals were then euthanized at 60 days after implant placement (18 days after alizarin administration).

2.4. Biomechanical analysis

For biomechanical analysis, 8 animals from each group (CLOT, BG, BGPTH groups for both ORQ and SHAM) had the metaphyses of the left tibias reopened to expose the implants and perform removal torque. An implant mount (Conexão, São Paulo, Brazil) was adapted to the implant hexagon and a digital torque wrench was coupled to the implant mount. Counterclockwise motion was applied, increasing the reverse torque until rotation of the implant inside the bone tissue occurred, completely breaking the bone-implant interface. When the torque wrench registered the maximum torque peak for this break, expressed in Newton centimeters (N.cm), this value was noted and tabulated for further statistical evaluation.

2.5. RT-PCR

After removal torque experiments, bone tissue from the tibial region previously in contact with the implant was extracted to assess the genes associated with bone maturation at 60 days using RT-PCR. The tissue was rinsed with phosphate buffered saline (PBS), frozen in liquid nitrogen and stored at −80 °C prior to ribonucleic acid (RNA) extraction. The SV Total RNA Isolation System kit (Promega, Madison, Wisconsin, USA) was used for RNA extraction, followed by quantification, concentration and purity analyses.

Normalization of the total RNA concentration was performed, followed by the manufacture of complementary strands of deoxyribonucleic acid (cDNA) (Sigma-Aldrich, St. Louis, Missouri, USA). The expression of genes related to bone repair, *i.e.*, alkaline phosphatase (ALP) and osteocalcin (OC), was assessed by RT-PCR using the SybrGreen System method (Applied Biosystems, Foster City, California, USA). Taqman Universal PCR Master Mix was added to the plates containing the genes of interest. The reactions were repeated in quadruplicates and the cDNA volumes were calculated according to the quantification of the samples. The amplification reaction was performed, and the results analyzed based on the value of the cycle threshold (Ct), which allowed the quantitative analysis of the expression of genes of interest, as well as the related genes on the plate [24].

2.6. Micro-CT

Implants and surrounding bone from the right tibia (n = 8 per group) were retrieved and trimmed, fixed in a 10% buffered formalin solution (Analytical Reagents, Dinâmica Odonto-Hospitalar Ltd., Catanduva, SP, Brazil) for 48 h, rinsed under running water for 24 h, and then stored in 70% ethanol. Micro-CT was completed (SkyScan 1272 Bruker MicroCT, Aatselaar, Belgium) using 8 μm-thick cuts with a 90 kV X-ray beam, a 111 μA current, a 0.5 mm Al filter and a 0.4° rotation step. Images were recorded with a 2016 μm × 1344 μm resolution over 1 h and 38 min acquisition time. Data were reconstructed using the NRecon software (SkyScan, 2011; Version 1.6.6.0), applying a smoothing factor of 5, a correction of the artifact rings of 7, and a beam hardening correction equal to 40%. The Data Viewer software (SkyScan, Version 1.4.4 64-bit) was used to visualize the reconstructed volumes in the transversal, longitudinal and sagittal planes. The CT-Analyser (CTAn) software (SkyScan, 2012; Version 1.12.4.0) was used to determine the percentage of bone volume over total volume (BV/TV), the trabecular thickness (Tb.Th), trabecular separation (Tb.Sp) and trabecular number (Tb.N), in addition to the bone-implant contact (BIC) through the intersection surface (i.S) for 3D reconstruction by CTvox software (SkyScan, Version 2.7).

2.7. Preparation of calcified tissues

After micro-CT analysis, the samples were progressively dehydrated in ethanol (70%, 80%, 90% and 100%) changing the solution every 5 days in an orbital shaker every day for 4 h. At the end of dehydration, the pieces were immersed in a mixture of 100% alcohol and Techno Vit® light-curing resin (Kulzer GmbH, Hanau, Germany) in different concentrations, until only resin remained as an immersion medium, and the Technovit resin was light-cured. Embedded blocks were then cut along the medio-distal plane using a cutting system (Exakt Cutting System, Apparatebau, Gmbh, Hamburg, Germany) and polished using an established protocol until the cross-section was approximately 80 μm thick.

2.8. Confocal laser microscopy

Longitudinal cuts were obtained at the bone/implant interface region corresponding to the third, fourth and fifth turns of the implants. These sections were imaged by a Leica CTR 4000 CS SPE confocal laser microscope (Leica Microsystems, Heidelberg, Germany), using a 10× objective (original increase 100), to detect the fluorochromes calcein and alizarin red. The daily bone mineral apposition rate (MAR) and neoformed bone area (NBA) were calculated on the third thread on each side of the implant, following the method reported in [37].

The images were analyzed in ImageJ (National Institutes of Health, Bethesda, Maryland, USA) using the “freehand selection” tool to measure the area of the fluorochromes and the NBA. The “straight line” tool was

employed to complete 5 measurements from the outer margin of the calcein area towards the outer margin of the alizarin red area. The values obtained were then divided by 28 (time interval in days between the two injections of fluorochromes) in order to evaluate the MAR, as described in [38].

2.9. Elemental and ultrastructural analyses

The response of the biomaterial to the bone regeneration process in the peri-implant defect with or without functionalization with PTH 1–34 was evaluated within 30 days. For this purpose, 8 animals per group (ORQ - BG and BGPTH; and SHAM - BG and BGPTH) were submitted to the same surgeries previously mentioned, but with euthanasia time reduced to 30 days in order to assess the peak of bone neoformation before remodeling. These samples were embedded in Techno Vit® resin and cut in half by the EXAKT cutting system as described above before further preparation and ultrastructural analysis. It is important to note that the CLOT group, both SHAM and ORQ, was not included, since the objective of this analysis was to evaluate the bone-biomaterial interface with or without PTH 1–34 functionalization. The sample block was polished using 400 to 2400 grit silicon carbide paper to expose the cross section of the bone-biomaterial interface. The samples were fixed to SEM stubs with carbon tape, wrapped in aluminum tape, and then painted with nickel when necessary. Later, they were coated with a thin layer of carbon (~10 nm) to improve the conductivity in the SEM. The workflow of all electron microscopy characterizations at the bone-Biogran® interface is described in detail by Micheletti et al., [39] but the main steps are reported herein.

2.9.1. Scanning electron microscopy (SEM)

SEM imaging was completed by acquiring secondary (SE) and backscattered electron (BSE) images using a JEOL 6610LV (JEOL Ltd., Japan) and an FEI Magellan 400 XHR (ThermoFisher Scientific, Hillsboro, USA) SEMs operated at an acceleration voltage of 5 kV. Compositional contrast in BSE images allowed for the distinction between biomaterial and bone based on atomic number. The images were recorded in several enlargements around the implant for later selection of the best bone-biomaterial contact areas for the next stage of analyses.

2.9.2. Energy dispersive X-ray spectroscopy (EDS)

In the same sample, using an FEI Magellan 400 XHR SEM (ThermoFisher Scientific, Hillsboro, USA) the elemental analysis was determined by EDS operated at 10 kV. EDS data was collected using an 80 mm^2 X-Max detector (Oxford Instruments, Concord, MA, USA) and processed using AZtec software (Oxford Instruments, Concord, MA, USA). Elemental maps were obtained for Biogran® to search for compositional changes in Ca, P and Si and to generate line profiles for compositional changes across the biomaterial.

2.9.3. Focused ion beam (FIB) and scanning transmission electron microscopy (STEM)

After identifying regions of bone in contact with Biogran® particles with SEM, a dual beam focused ion beam (FIB) instrument (Zeiss NVision 40, Carl Zeiss AG, Oberkochen, Germany) was used to prepare electron transparent (100–200 nm thick) specimens for STEM analysis using an *in situ* lift-out protocol,[†] and shown step-by-step for the ORQ BG group in Fig. 1. The resultant average sample size extracted from the block was 10 μm × 6 μm, thus being large enough to analyze nano-osteoconduction.

STEM imaging was done in a Titan 80–300 instrument (ThermoFisher Scientific, Hillsboro, USA) operated at 300 kV with a high-angle annular dark field (HAADF) detector. In this form of image, the contrast is proportional to the atomic number, which allows us to record images without the use of heavy metal stains that alter bone chemistry.

2.10. Immunohistochemical analysis

Additional animals were used to perform the osteoclast evaluation through immunohistochemical analysis. The samples were reduced and fixed in 10% formaldehyde (Analytical Reagents, Dinâmica Odonto-Hospitalar Ltda, Catanduva, SP, Brazil) for 48 h, washed in running water for 24 h and demineralized in 10% EDTA. Then, the samples were dehydrated with a sequence of alcohols and diaphanized in xylol and then included in paraffin. Cuts with thickness of 5 μm were obtained.

The reaction was performed on four pieces (left tibias) per group, using the indirect immunoperoxidase method with an amplifier. To inhibit

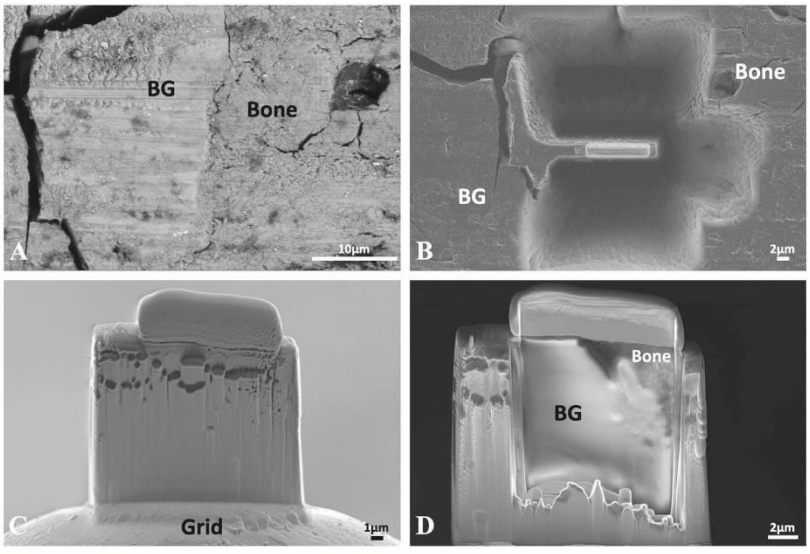

Fig. 1. The FIB lift-out procedure for preparing TEM samples illustrated for the ORQ BG group. A BSE-SEM image of the biomaterial (BG) and bone interface of interest for TEM sample preparation by FIB, including B trenches cut on both sides of the area of interest, protected by tungsten deposition; C the sample is attached to the TEM grid; D thinning of the sample by the ion beam.

endogenous peroxidase, 3% hydrogen peroxide (Merck Laboratories) was used. Antigen was retrieved by immersing the slices in citrate phosphate buffer, pH = 6, maintained in warm humidity, for 20 min. The non-specific reaction was blocked with bovine albumin (Sigma). The primary antibody used was against TRAP, whereas these polyclonal antibodies are produced in goats (Santa Crua Biotechnology). As the secondary antibody, rabbit anti-goat (Pierce Biotechnology) was used, and the amplifiers were avidin and biotin (Vector Laboratories) and chromogen to diaminobenzidine (Dako).

Immunolabeling analysis was performed through scores attribution, according to the area of positive presence of the proteins in the repairing tissue (interest area). For 25% of positive immunolabeling, it will be attributed the score 1; for 50% score 2; and for 75% score 3.

The objective of the immunostaining analysis was to characterize the osteoclastic activity in the different groups.

2.11. Statistical analyses

Statistical analyses were completed using the GraphPad Prism 8.1.1 software (GraphPadSoftware, La Jolla, USA). The analysis of homoscedasticity was performed by the Shapiro-Wilk test. One-way ANOVA was used to evaluate biomechanics, the parameters evaluated by micro-CT (BV/TV, Tb.Th, Tb.Sp, Tb.N, BIC), and MAR and NBA assessed by confocal laser microscopy regarding the measurement of overlapping fluorochromes, and when necessary, the Tukey's post-hoc test was applied. Two-way ANOVA was used to analyze the fluorochrome area. Significance level was set at $\alpha = 0.05$.

3. Results

The numerical values referring to the results of the present study are summarized in Table 2, and are described in more detail below.

3.1. Biomechanical analysis

The values of reverse torque obtained for each group are represented in Fig. 2. The maximum reverse torque necessary to remove the implants was the highest in SHAM BGPTH and SHAM BG groups with values of 9.6 N.cm and 8.2 N.cm respectively, followed by the ORQ BGPTH group with 6 N.cm. SHAM CLOT, ORQ BG and ORQ CLOT showed the lowest results with a reverse torque of 5.8 N.cm, 4.4 N.cm and 3 N.cm, respectively. However, the difference in reverse torque was not statistically significant for ORQ BGPTH with respect to SHAM BG ($p > 0.05$). On the contrary, the difference between SHAM BG and ORQ BG was statistically significant ($p < 0.05$).

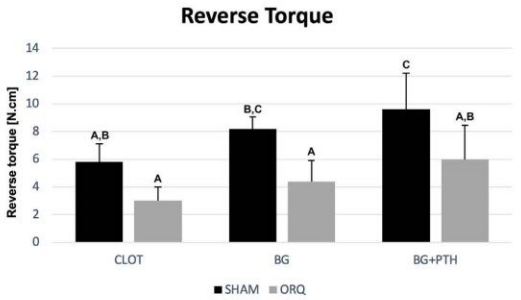

Fig. 2. Reverse torque values for the SHAM and ORQ groups evaluated for defects filled with clot only (CLOT), with Biogran® (BG) and Biogran® functionalized with PTH (BGPTH). Different letters denote statistical significance ($p < 0.05$).

3.2. Micro-CT

From the micro-CT measurements, the percentage of bone volume (BV/TV) (Fig. 3A) for the SHAM group was 64.40%, 60.22% and 29.79% for BGPTH, BG and CLOT groups, respectively. For the ORQ group, the highest bone percentage was present in the BGPTH group (60.32%), while the use of pure Biogran® (*i.e.* not functionalized with PTH) was able to form 50.37% of bone in the peri-implant defect, compared to the control ORQ CLOT group with only 27.57% BV/TV (SHAM and ORQ CLOT x SHAM and ORQ BG/BGPTH, one-way ANOVA, $p > 0.05$).

Regarding peri-implant bone trabeculae, trabecular thickness (Tb.Th) showed comparable results for all groups, with values ranging from 0.098 mm (ORQ CLOT) to 0.1133 mm (SHAM BGPTH), but without any statistical significance between groups (one-way ANOVA, $p > 0.05$) (Fig. 3B). Trabecular separation (Tb.Sp) displayed analogous values in the SHAM BGPTH (0.1 mm) SHAM BG (0.098 mm), ORQ BGPTH (0.1 mm) and ORQ BG (0.097 mm) groups, and a statistically significant (Tukey, $p < 0.05$) reduction in Tb.Sp was observed compared to the SHAM CLOT (0.1303 mm) and ORQ CLOT (0.135 mm) groups (Fig. 3C). As for the trabecular number (Tb.N), an average of 2.798/mm and 3.483/mm was obtained for the ORQ CLOT and SHAM CLOT groups, respectively, which was lower when compared to ORQ BG (5.345/mm), SHAM BG (5.45/mm), ORQ BGPTH (5.255/mm) and ORQ BG (5.651/mm) (Tukey, $p < 0.05$) (Fig. 3D).

As for the intersection between bone and implant, that is, the bone-implant contact (BIC), a larger three-dimensional contact area was identified for the BGPTH group for both SHAM (21.93 mm^2) and ORQ (18.93 mm^2) groups, but this difference was not statistically significant (Tukey, p

Table 2
Animal sample results: Control (SHAM) and orchiectomized rats (ORQ) - using clot (CLOT), Biogran® (BG) or Biogran® functionalized with PTH [1–34] (BGPTH) ± standard deviation (SD).

	SHAM			ORQ		
	CLOT	BG	BGPTH	CLOT	BG	BGPTH
Biomechanical	$n = 8$	$n = 8$	$n = 8$	$n = 8$	$n = 8$	$n = 8$
Reverse Torque	5.8 ± 1.3	8.2 ± 0.83	9.6 ± 2.6	3 ± 1	4.4 ± 1.51	6 ± 2.6
Bone structure	$n = 8$	$n = 8$	$n = 8$	$n = 8$	$n = 8$	$n = 8$
BV/TV (%)	29.79 ± 12.78	60.23 ± 5.78	64.33 ± 9.84	27.58 ± 2.01	50.38 ± 6.48	60.33 ± 5.48
Tb.Th (mm)	0.102 ± 0.019	0.110 ± 0.002	0.113 ± 0.009	0.098 ± 0.006	0.100 ± 0.009	0.107 ± 0.005
Tb.Sp (mm)	0.130 ± 0.015	0.098 ± 0.004	0.1 ± 0.014	0.135 ± 0.005	0.097 ± 0.008	0.100 ± 0.003
Tb.N (1/mm)	3.48 ± 1.39	5.45 ± 0.45	5.65 ± 0.53	2.79 ± 0.29	5.34 ± 0.48	5.25 ± 0.52
BIC - i.S (mm^2)	12.18 ± 1.08	15.67 ± 2.57	21.93 ± 1.85	10.79 ± 1.075	12.37 ± 2.99	18.93 ± 1.44
Bone dynamics	$n = 8$	$n = 8$	$n = 8$	$n = 8$	$n = 8$	$n = 8$
Fluorochrome (μm^2) Calcein/Alizarin	10,904 ± 1821	16,955 ± 4916	18,229 ± 6972	3178 ± 1900	100,068 ± 2097	13,949 ± 2258
MAR (μm/day)	1.67 ± 0.21	3.63 ± 0.28	3.94 ± 0.42	1.07 ± 0.19	2.48 ± 0.47	3.08 ± 0.32
NBA (μm^2)	8689 ± 3449	23,923 ± 3381	25,107 ± 4338	3299 ± 1163	15,953 ± 3841	21,194 ± 3280

BV/TV = percent bone volume; Tb.Th = trabecular thickness; Tb.N = trabecular number; Tb.Sp = trabecular separation; BIC = bone implant contact; i.S = intersection surface; MAR = mineral apposition rate; NBA = neoformed bone area.

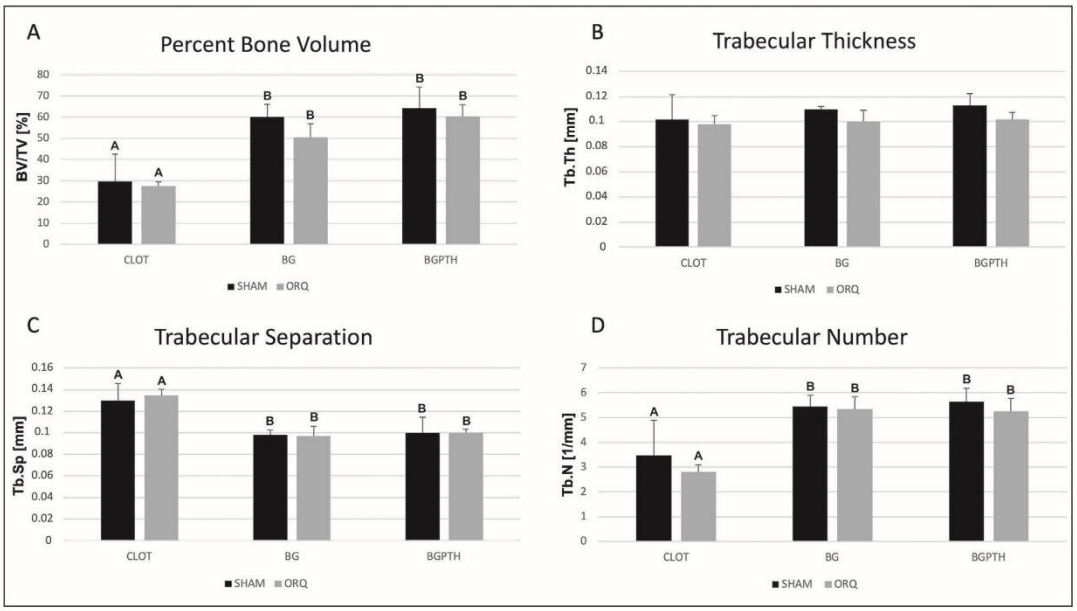

Fig. 3. Micro-CT analyses. A Percentage of bone volume (BV/TV). BG and BGPTH groups showed a higher BV/TV compared to CLOT group, both for SHAM and ORQ animals (different letters indicate $p < 0.05$); B Trabecular thickness (Tb.Th). All the groups displayed comparable values of Tb.Th (ANOVA, $p > 0.05$); C Trabecular separation (Tb.Sp). Higher values of Tb.Sp were obtained for SHAM CLOT and ORQ CLOT groups compared to SHAM BG, SHAM BGPTH, ORQ BG and ORQ BGPTH groups (different letters indicate $p < 0.05$); D Trabecular number (Tb.N). Lower values of Tb.N were observed for SHAM CLOT and ORQ CLOT groups compared to SHAM BG, SHAM BGPTH, ORQ BG and ORQ BGPTH groups (different letters indicate $p < 0.05$).

> 0.05). However, the difference in BIC in the ORQ BGPTH and SHAM BG groups was also not statistically significant (Tukey, $p > 0.05$), suggesting that the peri-implant defect of the osteoporotic animal filled with PTH-functionalized biomaterial had the same reparational behavior as the healthy animal treated with biomaterial only (Fig. 4). A representative three-dimensional rendering of the bone present around the implant is provided for each group in Fig. 5.

3.3. Confocal laser microscopy

The fluorochromes calcein (green) and alizarin (red) served to mark the calcium matrix, thus demonstrating the dynamics of peri-implant bone repair in all the experimental groups (Fig. 6). This allowed for assessment of bone dynamics, including total area, daily calcium depositions or mineral apposition rate (MAR), and neoformed bone area (NBA).

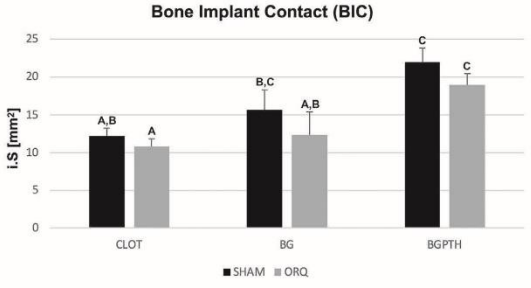

Fig. 4. Values of bone-implant contact (BIC) evaluated from micro-CT analysis. Different letters represent statistical significance ($p < 0.05$). There is no statistical difference between ORQ BGPTH and SHAM BG, suggesting PTH in ORQ has the same reparational capacity as healthy bone with biomaterial alone.

In the intragroup evaluation of the fluorochromes area in green and red, no statistically significant difference was found (two-way ANOVA, $p > 0.05$). In the intergroup comparison, the average of the results obtained showed the highest numerical result for the SHAM BGPTH group, being statistically significant in comparison with the other groups (Tukey, $p < 0.05$). SHAM BG and ORQ BGPTH displayed similar results in terms of fluorochromes area (Tukey, $p > 0.05$), indicating that the functionalization of Biogran® with PTH 1–34 in osteoporotic rats allowed for comparable repair of peri-implant defects as in healthy animals that received non-functionalized Biogran® (Fig. 7A). This was further supported by the evaluation of new bone formation, as the value of NBA for the ORQ BGPTH group was comparable to that of the SHAM BG and SHAM BGPTH groups (Tukey, $p > 0.05$) (Fig. 7B).

Daily mineral apposition ranged from 1.07 μm (ORQ CLOT) to 3.94 μm (SHAM BGPTH). The results (Fig. 7C) were: SHAM: 1.67 μm (CLOT), 3.62 μm (BG) and 3.94 μm (BGPTH); and for ORQ: 1.07 μm (CLOT), 2.48 μm (BG) and 3.08 μm (BGPTH). Similarly to fluorochrome area, topical PTH led to an increase in daily mineral apposition in osteoporotic animals (ORQ BGPTH group), showing no statistically significant difference when compared to SHAM BG (Tukey, $p < 0.05$).

3.4. RT-PCR

For all parameters evaluated with RT-PCR, the SHAM CLOT group was considered the standard, receiving a fixed value of 1, thus the other groups were evaluated with respect to this reference. The relative expression of ALP for the ORQ BG (0.808), SHAM BG (1.118) and SHAM BGPTH (1.451) groups did not show a statistically significant difference when

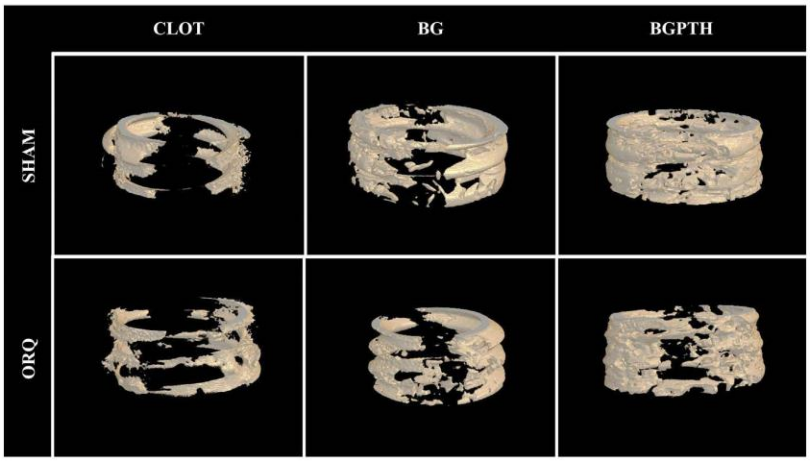

Fig. 5. Three-dimensional rendering of the bone formed around the implant threads in the different experimental groups obtained from micro-CT.

compared with SHAM CLOT (reference value 1.0). The ORQ CLOT group had the lowest value for ALP expression (0.33), which was statistically significant with respect to the SHAM CLOT group (Tukey, $p = 0.01$). The highest ALP expression was found for the ORQ BGPTH group (6.044), a result that was statistically significant compared to all the other groups (Tukey, $p < 0.05$) (Fig. 8A).

The relative expression of OC was similar for the SHAM CLOT (1.0), SHAM BG (1.283), SHAM BGPTH (1.706), ORQ BG (1.569) and ORQ BGPTH (1.489) groups, and no statistically significant difference between the groups was identified (ANOVA, $p > 0.05$). The ORQ CLOT group displayed the lowest value of OC expression, which was statistically significant compared to the ORQ BG, ORQ BGPTH and SHAM BGPTH groups (Tukey, $p < 0.05$) (Fig. 8B).

3.5. Elemental and ultrastructural analysis

3.5.1. SEM and elemental analysis by EDS

SEM images of the bone-Biogran® interface and EDS maps of Biogran® particles after 30 days *in vivo* revealed an uneven elemental distribution with Ca/P highly concentrated towards the particle exterior and a Si-rich core (Fig. 9). EDS analysis was performed on BG and BGPTH groups, with one representative map and extracted elemental profile given for SHAM (Fig. 10) and ORQ (Fig. 11) groups. While these images and elemental profiles are not compared statistically, there are some common observations to draw. The SHAM BG and BGPTH groups showed a very low (almost absent) amount of Si at the extremities, which were predominantly of Ca and P, and very high (approximately 3.5× more than Ca and P) amount in the central

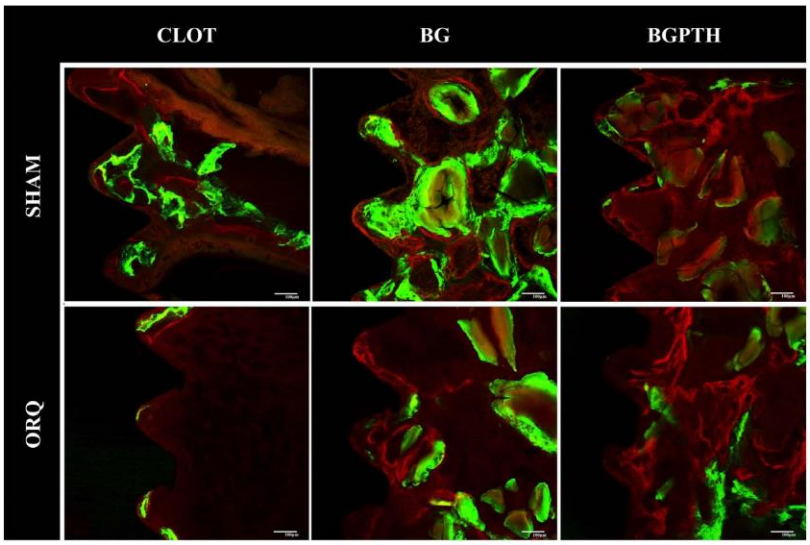

Fig. 6. Calcein (green) and alizarin (red) marking the calcium matrix, demonstrating the dynamics of the peri-implant bone of the experimental groups.

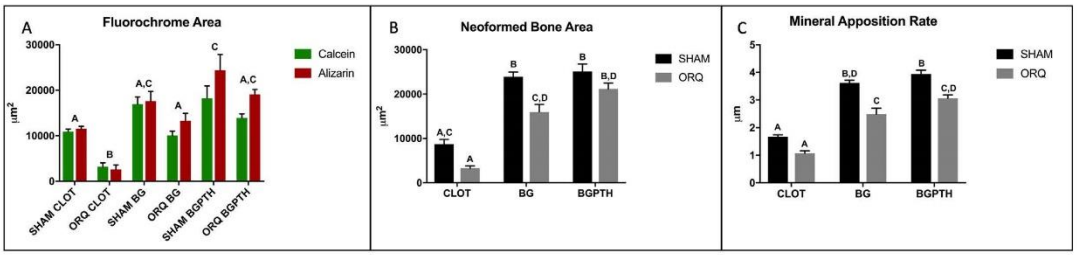

Fig. 7. Fluorochrome analyses across all groups: SHAM and ORQ in the different CLOT, BG and BGPTH groups. A Quantification of the fluorochrome area calcein (green) and alizarin (red), where SHAM BG shows similarity to ORQ BGPTH. B Values referring to neoformed bone area (NBA), where ORQ BGPTH shows no statistical difference from SHAM BG and SHAM BGPTH. C Values referring to the bone mineral apposition rate (MAR), which similar to fluorochrome area showed no difference between ORQ BGPTH and SHAM BG. Different letters denote statistical significance ($p < 0.05$).

region of the biomaterial. In addition, Si was present an average of 200 μm across each 300 μm particle imaged for both groups (Fig. 10B and D). Similarly, the ORQ groups showed amounts of Si in the interior nearly double when compared to Ca and P on the exterior (Fig. 11B and D). However, in the case of these 300 μm particles, the Si inside the particle extended only about 100 μm (Fig. 11B and D).

3.5.2. Scanning transmission electron microscopy

HAADF-STEM imaging showed the connection between bone and biomaterial at the nanoscale, allowing to understand whether there is a structural gradient or interfacial zone between the bone and the biomaterial. In all groups an intimate connection at the nanoscale level between newly formed bone and Biogran® was present (Figs. 12-15). Often, the interface,

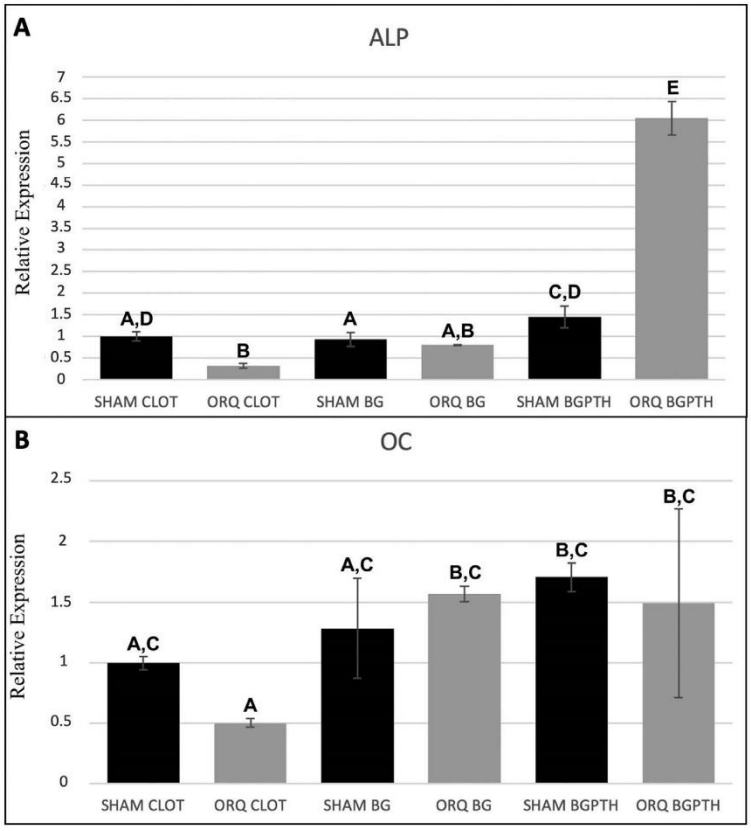

Fig. 8. Relative gene expression of ALP (A) and OC (B) in the period of 60 days in the CLOT, BG and BGPTH groups, both SHAM and ORQ. The highest relative expression of ALP was found for ORQ BGPTH, while OC expression was statistically lower in ORQ CLOT than both ORQ BG and ORQ BGPTH. Different letters indicate statistical significance ($p < 0.05$).

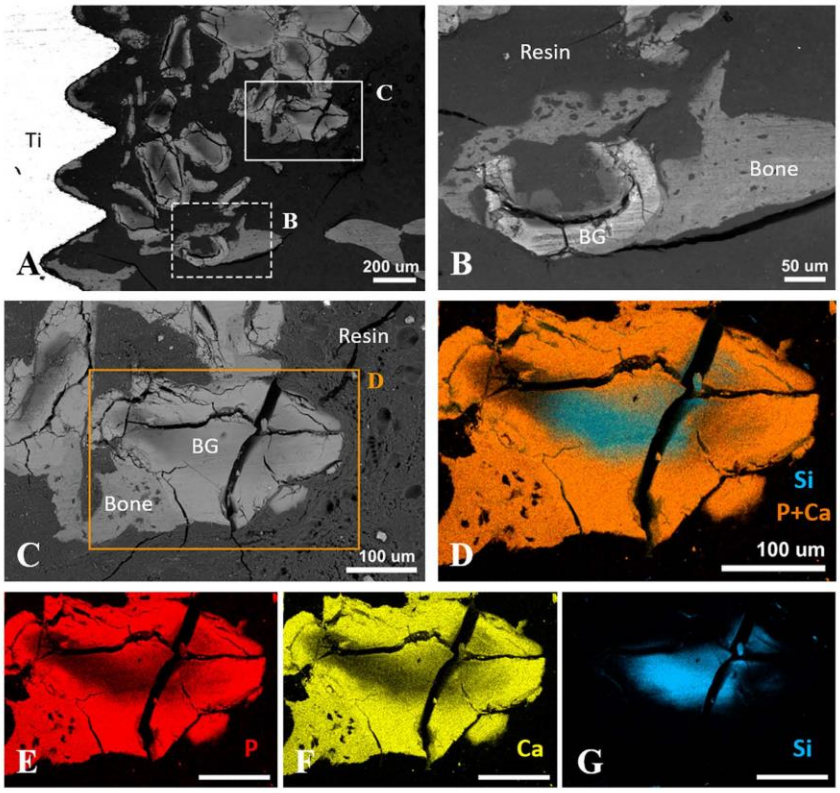

Fig. 9. A,B BSE-SEM image of the biomaterial and bone interface and C a representative Biogran® particle (BG) with D Elemental mapping by EDS showing a high exterior concentration of Ca and P (orange) and Si (blue) rich core. E,F,G Discrete elemental maps for P (red), Ca (yellow) and Si (blue) shown separately. Scale bar = 100 μm.

or better, the interphase, between bone and Biogran® appeared gradual and it ranged from 150 nm to up to 700 nm in thickness in the regions examined. In all samples, collagen fibres in the newly formed bone appeared to be laid down parallel to the Biogran® interface. In addition, new bone displayed a rather immature structure, as expected from the early retrieval time point (30 days). More organized collagen fibres could be distinguished in the ORQ groups, especially with PTH-functionalized Biogran®, for which the collagen banding pattern was more visible.

In the SHAM BG group (Fig. 12), an external dissolution/reprecipitation of the biomaterial was observed, which presented an average interphase of 150 nm. In addition, dissolution towards the inner part of the Biogran® particle, with almost total separation of a segment of the particle, was observed. Within this area, a greater dissolution zone of approximately 300 nm was found, in addition to an area resembling new bone formation (marked by *). Similarly, the SHAM BGPTH group (Fig. 13) showed an area of external dissolution/reprecipitation approximately 350 nm in width (Fig. 13D) and the same immature bone as the BG group, but with clear collagen banding at the interface. However, no area of internal dissolution of the biomaterial was noted in this individual particle.

For the ORQ BG group (Fig. 14), there was presence of bone that was still immature, but distinct mineral clusters were visible in some regions (Fig. 14B) while organized collagen fibrils, distinguishable due to their alignment in the plane of the image, were visible in other regions (Fig. 14D). As in other groups, the dissolution present was irregular and approximately 180 nm in width, and again without the presence of dissolution in internal cavities of the particle.

In the ORQ BGPTH group (Fig. 15), it was possible to observe a linear area in the most superficial portion of the particle with dissolution of the biomaterial underway up to approximately 770 nm in width (Fig. 15C). Underneath this, a greater dissolution area into a cavity towards the interior of the particle was visible. In this cavity showing 900 nm of dissolution (Fig. 15E), it was possible to observe the presence of an area with new bone formation (Fig. 15D,E,F marked by *). The bone juxtaposed to the exterior of the sample was in close contact with the particle and had distinct organized collagen bands visible, which were parallel to the biomaterial, suggesting greater bone organization. However, this could be simply related to the collagen fibrils being at an optimal orientation for imaging.

3.6. Immunohistochemical analysis

TRAP immunolabeling was performed in order to characterize osteoclastic activity during the peri-implant repair in the different conditions evaluated in the present study.

TRAP is a marker of an enzyme that is present in osteoclasts, during their activity. The images were captured in the area of medullary bone, the region of interest in the model of tibia's implants installation, exception on orchiectomy clot group when the image represents the cortical bone just in order to characterize the aspect of the osteoclasts in the activity, present in bone areas close to the implant.

One aspect that is observed is that in all of the groups evaluated in this study, there was a gap that was around the implant, causing an

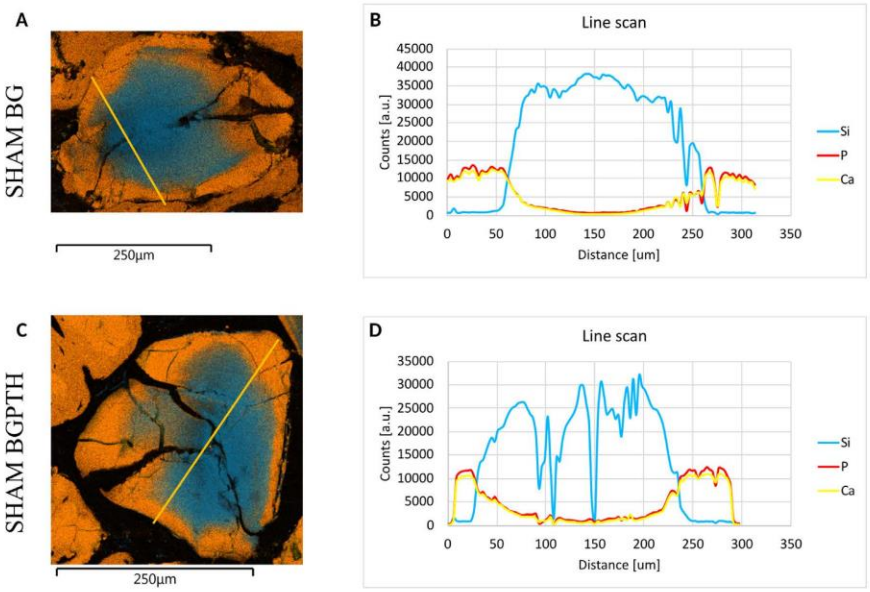

Fig. 10. A,C: Elemental maps of the biomaterial of the SHAM BG and BGPTH groups showing a predominance of Si (blue) inside the particle and Ca and P (orange) at the periphery; B,D: Elemental line profiles of the biomaterial particle showing a relative predominance of Si in the core, nearly 3.5× higher than Ca and P measured at the periphery.

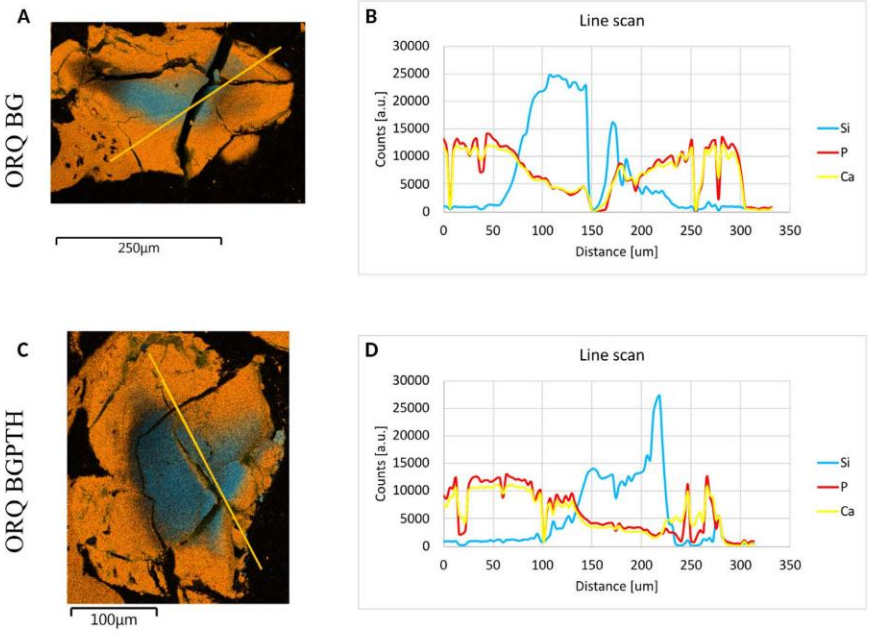

Fig. 11. A,C: Elemental maps of the biomaterial of the ORQ BG and BGPTH groups showing a predominance of Si (blue) inside the particle and Ca and P (orange) at the periphery; B,D: Elemental line profiles of the biomaterial particle showing a Si-rich core that spans only about 100 µm.

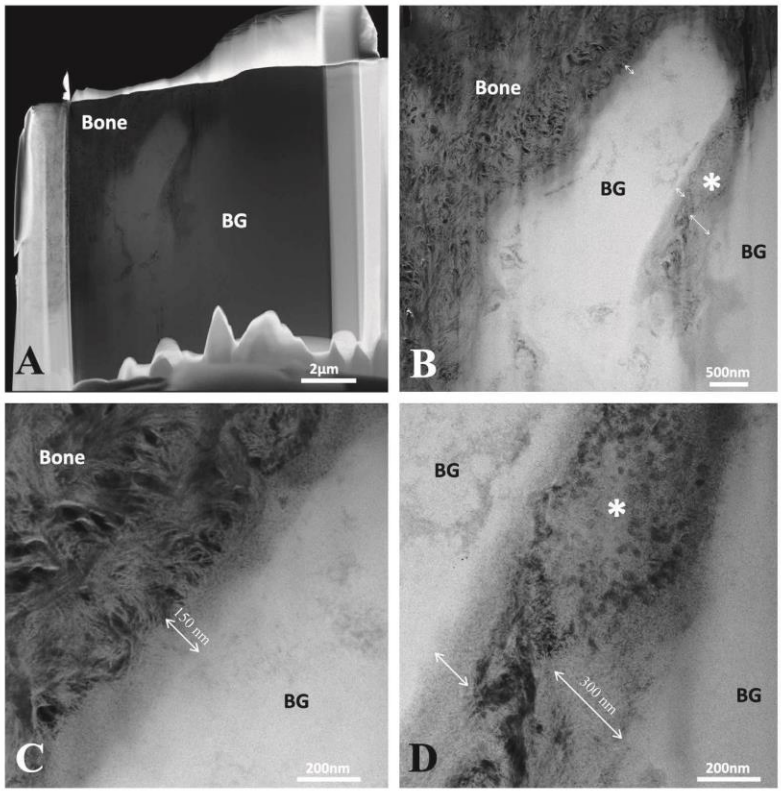

Fig. 12. Ultrastructural analyses from the SHAM BG group; A: Overview image of the entire sample as prepared in the FIB; B, C, D: STEM-HAADF images with different magnifications of the bone-biomaterial interface. A small cavity with bone ingrowth is noted in B and D by *,while the surface-active Ca/P layer is marked by double ended arrows in C and D. (BG = Biogran®; * = Region of new bone formation).

impairment of the adjusts of the implant in the preparation bed. In groups BG and BGPTH, the gap was filled for these biomaterials, in order to improve the adjustment between the implant and the preparation bed.

In SHAM group, it was observed that in the clot group, there isn't a the medullar region with a poor quantity of bone formed close to the implant's threads (negative area of the image), with discrete labeling for osteoclasts. When BG was used to fill the gap, it was observed that in the medullar region, bone was formed close to the implant's threads and a discrete to moderate labeling for osteoclasts was observed in the area. When PTH was added to BG, the formation of bone close to the implant's threads was also observed as well as a discrete to moderate positive labeling for osteoclasts.

When orchiectomy was performed in the animals what represents a challenge for the peri-implant repair process, it was possible to highlight that in the clot group, there was positive labeling for TRAP, in a discrete manner, but we consider that is a response for the osteopenia caused by the systemic condition. Note that the representation is for cortical bone, just in order to illustrate the aspect of the trap positive labeling and the aspect of the osteoclasts that are labeling in cortical bone, close to the implants. When BG was used to fill the gap, it was observed a discrete to moderate labeling of trap in osteoclasts and in BGPTH it was observed moderate labeling of osteoclasts (Fig. 16).

4. Discussion

Animals subjected to orchiectomy develop osteoporosis as a consequence of the sudden decrease in endogenous testosterone caused by this surgical procedure, as testosterone is directly related to bone formation. In addition, there are indications that aromatization of testosterone to estradiol plays an important role in the regulation of bone homeostasis in men [21,28,40]. Therefore, there will be a decrease in bone formation and a likely increase in bone resorption, ultimately leading to a rapid onset of osteoporosis after orchiectomy.

Biogran® is a commercially available bone graft used in dentistry [41, 42]. Previous work has reported the functionalization of Biogran® with Raloxifene®, a selective estrogen receptor modulator, using sonochemistry [5,28]. The sonochemical method relies on the phenomenon of acoustic cavitation, *i.e.*, the formation, growth and implosive collapse of bubbles in liquids with time in the order of microseconds, to mix two or more distinct substances [5]. Sonochemistry was chosen for the functionalization of the biomaterial proposed in the present work because it enables the modification of a wide variety of nanostructured materials from ultrasonic waves in a liquid medium, which cause chemical and physical transformations in the sample. Moreover, it is an economical and effective method to reduce and homogenize the size of particles due to the application of high pressures in a short time, inducing a rapid morphological change [28,43]. In this work, sonochemistry was used to homogenize Biogran® particles

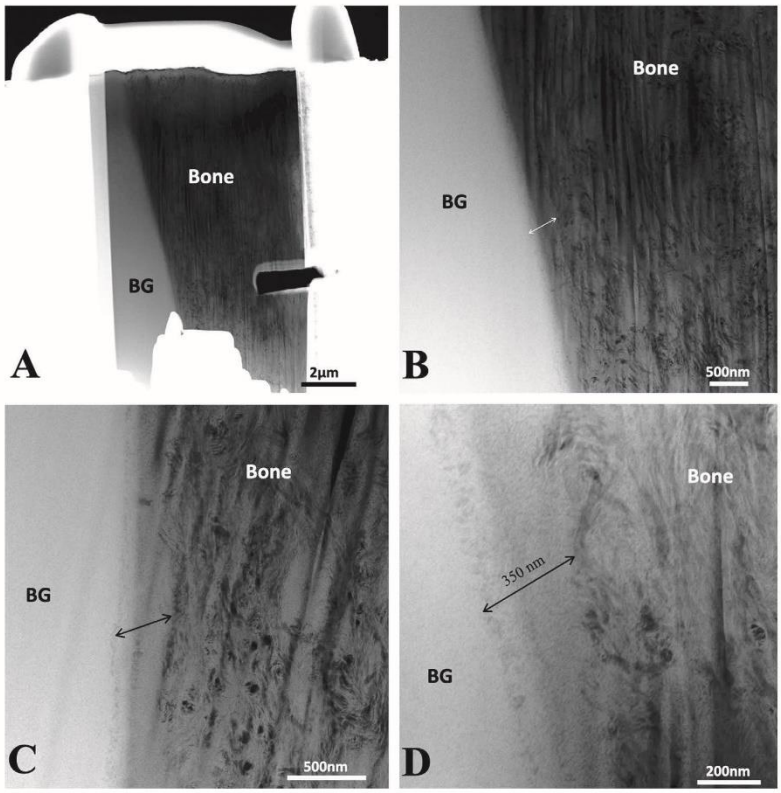

Fig. 13. Ultrastructural analyses from the SHAM BGPTH group; A: Overview image of the entire sample as prepared in the FIB; B, C, D: STEM-HAADF images with increasing magnifications of the bone-biomaterial interface. Double ended arrows mark the dissolution/reprecipitation bioactive layer visible on the surface. (BG = Biogran®).

and to functionalize them with PTH 1–34, an anabolic drug that acts directly on the WNT pathway, thereby signaling the formation of bone tissue [26]. Sonochemistry was carried out for 15 min, which was identified as an optimal time for the PTH functionalization of Biogran® in a previous study [26].

The implant/bone-graft/bone interface is a complex repair situation, which involves revascularization, graft incorporation and implant integration [44]. The combination of biomaterials as synthetic bone grafts with implants has been studied and used frequently in cases of post-exodontics peri-implant defects and bone fenestrations [44]. The osteoconductive properties of biomaterials and the physicochemical processes occurring *in vivo* after implantation are fundamental for bone repair. Biogran® is a silica-based bioactive glass, with demonstrated osteoconductivity, made of SiO_2(45 wt%), CaO (24.5 wt%), Na_2O (24.5 wt%) and P_2O_5 (6 wt%) [3]. After contact with body fluids, silica-rich bioactive glasses undergo an interfacial ion exchange, in which Si is rapidly released from the surface [illegible] and PO_4^{3-} from the material and external environment to form a gel of CaO–P_2O_5 on the silica-rich layer which then crystallizes with incorporation of hydroxyls and carbonates from solution and forms a surface layer of hydroxyapatite [45]. Such bioactive surface layers were noted herein on all groups by STEM imaging (Figs. 12-15). With increasing time, phagocytosing cells begin the resorption of these layers and, after this resorption, mesenchymal cells penetrate small ducts and adhere to the CaP layer formed more internally, where they are differentiated into osteoblasts and initiate the bone formation process inside the biomaterial even if there is no presence of previous bone at the site [3]. Indication of such internal formation of bone in Biogran® cavities was noted randomly in some samples, including SHAM BG and ORQ BGPTH, in Fig. 12 and Fig. 15.

The creation of a CaP-rich outer layer and a Si-rich core was shown in previous EDS line scans across Biogran® particles implanted in the edentulous jaws of beagle dogs [4]. In this study, EDS mapping of Biogran® verified the presence of a core richer in Si and an outer surface more concentrated in Ca and P. Notably, such distribution pattern of Ca, P and Si was analogous for particles functionalized by PTH 1–34 and for those implanted in osteoporotic animals, suggesting that neither the presence of PTH locally, nor the different metabolism in osteoporotic bone altered the characteristic interfacial ion exchange of Biogran® *in vivo*. However, for ORQ BG and ORQ BGPTH this process seemed to be slightly more accentuated and the ion exchange intensified since the layer of Ca and P in the periphery of the biomaterial was larger than that of Si inside the particle. Since only a few particles were probed herein, whether or not the rate of dissolution of Si into the surrounding environment is higher in ORQ groups requires further investigation, but it is plausible that local changes in pH would affect this rate.

This bioactive surface layer associated with Biogran® contributes to its osteoconduction and therefore, the quantity and quality of new bone formation surrounding an implant as well as its biomechanical strength when used in peri-implant bone graft applications. Biomechanical analysis of the bone-implant interface (Fig. 2) revealed that in each subgroup (CLOT, BG and BGPTH) smaller values of reverse removal torque were registered in the ORQ group than in the SHAM one, in turn indicating that the

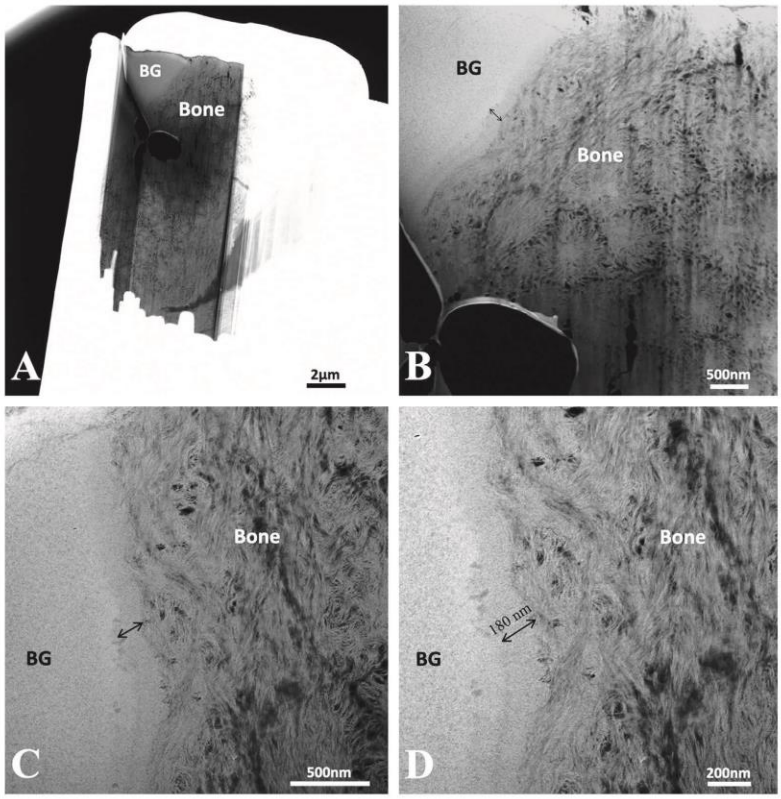

Fig. 14. Ultrastructural analyses from the ORQ BG group; A: Overview image of the entire sample as prepared in the FIB; B, C, D: STEM-HAADF images with different magnifications of a few regions at the bone-biomaterial interface. Double ended arrows mark the dissolution/reprecipitation bioactive layer visible on the surface. Under the label, "bone" in B, mineral clusters in newly deposited bone are visible, while C and D show alignment of collagen fibrils parallel to the interface, marked by collagen banding. (BG = Biogran®).

level of osseointegration was lower in the osteoporotic animals than in the healthy ones. Interestingly, no statistically significant difference in reverse torque was observed when comparing the healthy animal that received Biogran® only (SHAM BG) to the osteoporotic animal that received Biogran® functionalized with PTH 1–34 (ORQ BGPTH). This suggests that the topical application of PTH can improve the biomechanical stability of osseointegration in presence of osteoporosis, reaching a comparable level as that achieved using non-functionalized Biogran® in healthy skeletal conditions, which is promising for clinical dental applications.

This reverse torque result can be directly related to the results of BIC evaluated from micro-CT (Fig. 4 and Fig. 5), which shows that SHAM BG, SHAM BGPTH and ORQ BGPTH displayed the highest values of BIC, with no statistically significant difference among each other. This seems to indicate that, while the functionalization with PTH 1–34 does not have a significant effect in healthy animals, it plays a role when osteoporosis is present, as BIC was higher in the ORQ BGPTH group compared to ORQ BG. Similar results were found previously in the case of systemic administration of PTH 1–34 in orchiectomized rats, where an improvement in BIC was achieved compared to untreated animals, both osteoporotic and healthy [33].

Other micro-CT evaluation of the samples (Fig. 3) showed statistically significant differences in bone volume, trabecular separation and trabecular number only when comparing groups with biomaterial with or without functionalization (SHAM BG, SHAM BGPTH, ORQ BG, ORQ BGPTH) in relation to groups filled with clot only (SHAM-CLOT, ORQ-CLOT), indicating the reparative role that inclusion of the Biogran® itself plays on bone formation.

An aspect of fundamental importance to be evaluated is the osteoclastic activity present in the peri-implant repair in the proposed model. The cellular morphology present in osteoclasts in the SHAM group are mononucleated macrophages, different from the ORQ groups in which they have mature osteoclasts, probably due to orchiectomy showing greater cell recruitment. The ORQ CLOT group was represented by cortical bone to illustrate how osteoclasts were in this region. In the ORQ BG group, the labeling TRAP is in mononuclear cells, due to bone remodeling activity in which active resorption has already passed. In the BGPTH groups, active osteoclasts are observed apparently due to the local action of parathyroid hormone, contributing to a better turnover in the region, acting positively to maintain an active bone and consequently improving its quality.

Values of MAR (Fig. 7) confirmed the trend observed in the measurements of reverse torque, *i.e.*, that ORQ BGPTH group did not show any statistically significant difference compared to SHAM BG, in turn indicating that the PTH functionalization leads to a peri-implant repair process for osteoporotic bone analogous to that of healthy bone. The contribution of PTH in making the repair level for osteoporotic and healthy bone comparable was also noticed in the fluorochrome (calcein and alizarin) area and NBA analyses, since there was no statistically significant difference in the mean values for the ORQ BGPTH, SHAM BG and SHAM BGPTH groups. The data of calcium precipitation and NBA suggest that topical PTH 1–34

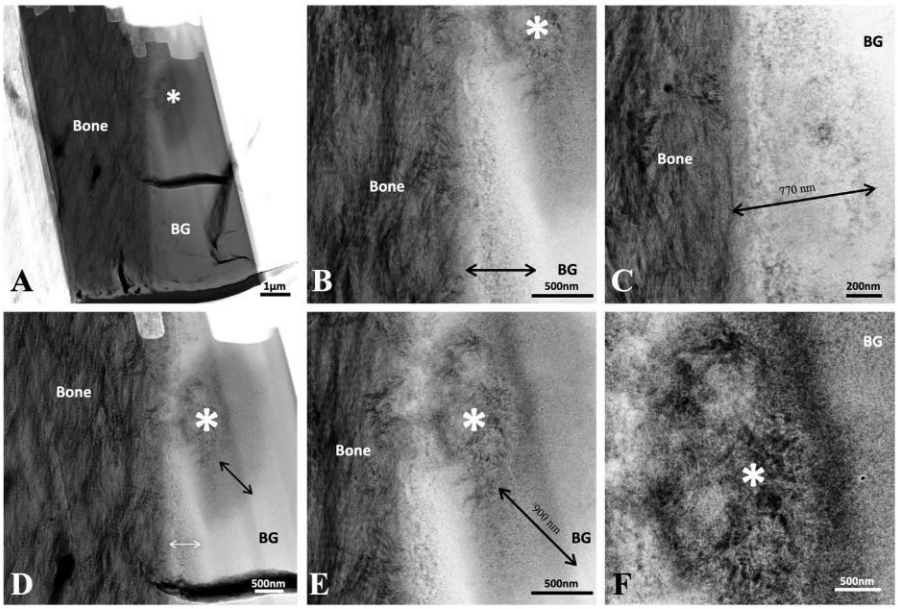

Fig. 15. Ultrastructural analyses from the ORQ BGPTH group; A: Overview image of the entire sample as prepared in the FIB; B, C: STEM-HAADF images with different magnifications of various regions along the bone-biomaterial interface, showing the bioactive surface layer marked by double ended arrows. D, E, F: STEM-HAADF images highlight an internal cavity where new bone ingrowth is noted by *, surrounded by a large dissolution/reprecipitation layer. (BG = Biogran®; * = Region of new bone formation).

contributes to making the process of new bone formation comparable in osteoporotic and healthy groups, while its effect in improving bone repair is not remarkable in healthy animals (SHAM BG and SHAM BGPTH). This is consistent with current clinical practices, where health individuals receive biomaterial only. This finding could be partly explained by RT-PCR results (Fig. 8), showing that the relative expression of ALP was much more elevated in the osteoporotic animals treated with functionalized Biogran® (ORQ BGPTH) compared to all the other groups, displaying a six-fold increase in ALP expression with respect to the reference group (SHAM CLOT). This may be indicative of a higher local bone activity, in turn facilitating mineral deposition in these animals. The higher expression of ALP in the ORQ BGPTH animals could also explain the higher level of bone organization visible in HAADF-STEM images of this group, as opposed to a rather immature structure observed in the other groups. HAADF-STEM imaging

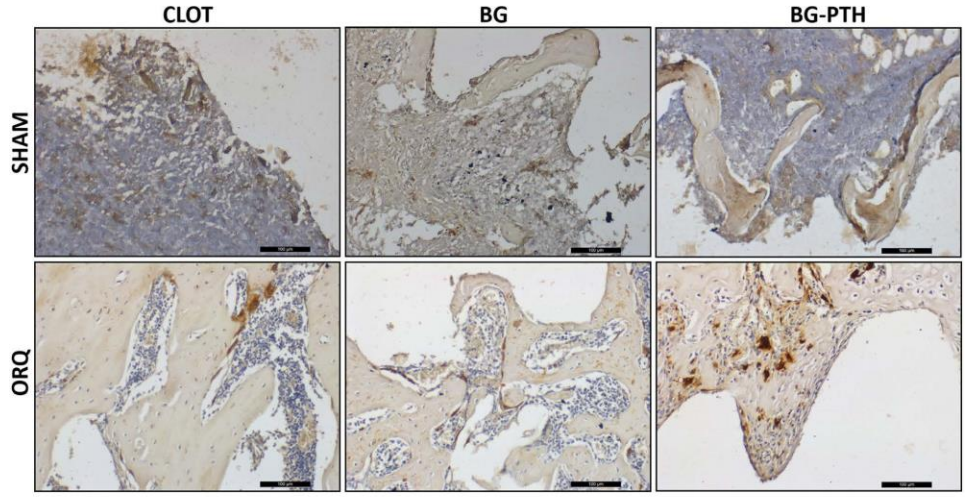

Fig. 16. Immunohistochemistry using proteins against TRAP. Immunolabeling of these proteins in SHAM and ORQ – CLOT, BG e BGPTH. Immunolabeling was defined as: mild; moderate and intense.

visualized the bone-Biogran® (without and with PTH 1–34) interface at the nanoscale, resolving the gradual layer where the biomaterial dissolves and apposition of Ca/P and subsequently new bone takes place. To our knowledge, this is the first time that the interfacial ion exchange process leading to bone repair in presence of Biogran® is visualized at the nanoscale. From this level of resolution of newly formed bone juxtaposed to Biogran®, it was possible to identify collagen fibrils oriented parallel to the interface, analogously to what observed for other ceramic biomaterials [46] or in case of titanium implants. Interestingly, a newly observed structure in bone, consisting of ellipsoidal mineral clusters [47], or circular features observed in cross-section called "rosettes" [48] are visible in both the ORQ groups. These clusters have been noted in early forming bone [49], as well as in fully developed, more mature bone of the human femoral neck [50]. To date, these have not been identified in osteoporotic bone, but are shown here to form after orchiectomy.

It is important to understand that the bone formation process around the biomaterial starts after the onset of the ion exchange of Ca/P and Si [3,51] at the biomaterial surface and cavities, and that PTH initiates cellular responses, one of which manifests in the activation of proteins from the extracellular matrix, such as ALP and OC expression. In the present work, ALP was expressed significantly more when topical PTH was used in orchiectomized rats (ORQ BGPTH) compared to the relative gene expression found in the other groups, which may lead the improvement in bone formation, since this protein is essential for the formation of quality bone tissue. The role of PTH in ALP expression *in vitro* has been well documented, where early osteoblast differentiation and ALP expression were improved with increasing PTH dose [50]. Similarly, in osteoporotic women receiving PTH systemically, all showed an increase in ALP expression over the first 6 months of treatment with PTH [52]. This correlation to *in vitro* and clinical systemic modes of delivery bolsters the unique findings herein that local delivery also impacts peri-implant bone repair.

5. Conclusion

Biogran® is a clinically available allograft used in the dental practice. For the first time, this work reports on the functionalization of Biogran® with PTH 1–34 using sonochemistry for local delivery in the peri-implant space. The local administration of this anabolic agent was shown to be beneficial for improving peri-implant bone repair in conditions of low bone quality and quantity, such as osteoporosis. This was confirmed in this study where orchiectomized rats that received Biogran® functionalized with PTH 1–34 showed similar results in terms of bone repair as healthy animals that received non-functionalized Biogran®. In particular, it appears that the topical action of PTH 1–34 led to an increased bone formation and local calcium precipitation, especially in orchiectomized animals. This can be attributed to the ability of PTH 1–34 to activate specific proteins in the extracellular matrix, in particular enhancing expression of ALP, which is fundamental for the formation of quality bone tissue. In view of these results, we conclude that it is essential to use biomaterials functionalized with PTH 1–34 to fill peri-implant defects in osteoporotic bone.

Declaration of competing interest

The authors declare that they have no known competing financial interests or personal relationships that could have appeared to influence the work reported in this paper.

Acknowledgments

Funding support is acknowledged from (FAPESP) for funding this work (process number: 2017/08187-3 and 2015/14688-0), CAPES (UNESP/CAPES/Print Project) Medens (implants used in the research), Multiuser laboratory of Araçatuba Dental School-UNESP and FINEP (FINEP/CT-INFRA – Covenant FINEP: 01.12.0530.00 PROINFRA 01/2011) and the Natural Science and Engineering Research Council of Canada (NSERC). RO is affiliated with the Research Productivity Scholarship (process no.: 306389/2017-7). Biogran sonochemistry and functionalization were carried out at the Advanced Materials Laboratory of the Centre for Research and Development of Functional Materials – Health Division – FAPESP (São Paulo, SP, Brazil), under direction of Prof. Paulo Noronha Lisboa-Filho. Electron microscopy work was completed at the Canadian Centre for Electron Microscopy (CCEM) at McMaster University.

References

[1] W.C. Stentz, B.L. Mealey, P.V. Nummikoski, J.C. Gunsolley, T.C. Waldrop, Effects of guided bone regeneration around commercially pure titanium and hydroxyapatite-coated dental implants. I. Radiographic analysis, J. Periodontol. 68 (3) (1997) 199–208.
[2] J.E. Davies, Understanding peri-implant endosseous healing, J. Dent. Educ. 67 (8) (2003) 932–949.
[3] E. Schepers, M. de Clercq, P. Ducheyne, R. Kempeneers, Bioactive glass particulate material as a filler for bone lesions, J. Oral Rehabil. 18 (5) (1991) 439–452.
[4] E.J. Schepers, P. Ducheyne, L. Barbier, S. Schepers, Bioactive glass particles of narrow size range: a new material for the repair of bone defects, Implant. Dent. 2 (3) (1993) 151–156.
[5] C. Chan, I. Thompson, P. Robinson, J. Wilson, L. Hench, Evaluation of Bioglass/dextran composite as a bone graft substitute, Int. J. Oral Maxillofac. Surg. 31 (1) (2002) 73–77.
[6] C.E. Misch, F. Dietsh, Bone-grafting materials in implant dentistry, Implant. Dent. 2 (3) (1993) 158–167.
[7] T. Furusawa, K. Mizunuma, Osteoconductive properties and efficacy of resorbable bioactive glass as a bone-grafting material, Implant. Dent. 6 (2) (1997) 93–101.
[8] K.C. Leung, T.W. Chow, P.Y. Wat, M.B. Comfort, Peri-implant bone loss: management of a patient, Int. J. Oral Maxillofac. Implants 16 (2) (2001) 273–277.
[9] F. Isidor, Influence of forces on peri-implant bone, Clin. Oral Implants Res. 17 (Suppl. 2) (2006) 8–18.
[10] L.F. Tabata, E.P. Rocha, V.A. Barão, W.G. Assunção, Platform switching: biomechanical evaluation using three-dimensional finite element analysis, Int. J. Oral Maxillofac. Implants 26 (3) (2011) 482–491.
[11] T. Shapurian, P.D. Damoulis, G.M. Reiser, T.J. Griffin, W.M. Rand, Quantitative evaluation of bone density using the hounsfield index, Int. J. Oral Maxillofac. Implants 21 (2) (2006) 290–297.
[12] N.A. Drage, R.M. Palmer, G. Blake, R. Wilson, F. Crane, I. Fogelman, A comparison of bone mineral density in the spine, hip and jaws of edentulous subjects, Clin. Oral Implants Res. 18 (4) (2007) 496–500.
[13] M. Yamazaki, T. Shirota, Y. Tokugawa, M. Motohashi, K. Ohno, K. Michi, et al., Bone reactions to titanium screw implants in ovariectomized animals, Oral Surg. Oral Med. Oral Pathol. Oral Radiol. Endod. 87 (4) (1999) 411–418.
[14] S. Ozawa, T. Ogawa, K. Iida, C. Sukotjo, H. Hasegawa, R.D. Nishimura, et al., Ovariectomy hinders the early stage of bone-implant integration: histomorphometric, biomechanical, and molecular analyses, Bone 30 (1) (2002) 137–143.
[15] S. Khosla, S. Amin, E. Orwoll, Osteoporosis in men, Endocr. Rev. 29 (4) (2008) 441–464.
[16] M.T. Drake, S. Khosla, Male osteoporosis, Endocrinol. Metab. Clin. N. Am. 41 (3) (2012) 629–641.
[17] A. Giusti, G. Bianchi, Treatment of primary osteoporosis in men, Clin. Interv. Aging 10 (2015) 105–115.
[18] R. Niimi, T. Kono, A. Nishihara, M. Hasegawa, A. Matsumine, T. Kono, et al., Analysis of daily teriparatide treatment for osteoporosis in men, Osteoporos. Int. 26 (4) (2015) 1303–1309.
[19] P. Farahmand, R. Spiegel, J.D. Ringe, Male osteoporosis, Z. Rheumatol. 75 (5) (2016) 459–465.
[20] J.S. Finkelstein, A. Hayes, J.L. Hunzelman, J.J. Wyland, H. Lee, R.M. Neer, The effects of parathyroid hormone, alendronate, or both in men with osteoporosis, N. Engl. J. Med. 349 (13) (2003) 1216–1226.
[21] D. Vanderschueren, L. Vandenput, S. Boonen, M.K. Lindberg, R. Bouillon, C. Ohlsson, Androgens and bone, Endocr. Rev. 25 (3) (2004) 389–425.
[22] G. Qian, L. Zhang, G. Wang, Z. Zhao, S. Peng, C. Shuai, 3D printed zn-doped mesoporous silica-incorporated poly-L-lactic acid scaffolds for bone repair, Int. J. Bioprint. 7 (2) (2021) 346.
[23] G. Qian, P. Fan, F. He, J. Ye, Novel strategy to accelerate bone regeneration of calcium phosphate cement by incorporating 3D plotted poly(lactic-co-glycolic acid) network and bioactive wollastonite, Adv. Healthc. Mater. 8 (9) (2019), e1801325.
[24] D. de Oliveira, Puttini I. de Oliveira, P.H. Silva Gomes-Ferreira, L.P. Palin, M.A. Matsumoto, R. Okamoto, Effect of intermittent teriparatide (PTH 1–34) on the alveolar healing process in orchiectomized rats, Clin. Oral Investig. 23 (5) (2019) 2313–2322.
[25] Puttini I. de Oliveira, P. Gomes-Ferreira, D. de Oliveira, J.S. Hassumi, P.Z. Gonçalves, R. Okamoto, Teriparatide improves alveolar bone modelling after tooth extraction in orchiectomized rats, Arch. Oral Biol. 102 (2019) 147–154.
[26] P.H.S. Gomes-Ferreira, P.N. Lisboa-Filho, A.C. da Silva, O. Bim-Júnior, F.R. de Souza Batista, A.C. Ervolino-Silva, et al., Sonochemical time standardization for bioactive materials used in periimplantar defects filling, Ultrason. Sonochem. 56 (2019) 437–446.
[27] A.A. Veis, N.N. Dabarakis, N.A. Parisis, A.T. Tsirlis, T.G. Karanikola, D.V. Printza, Bone regeneration around implants using spherical and granular forms of bioactive glass particles, Implant. Dent. 15 (4) (2006) 386–394.
[28] L.B. Arruda, M.O. Orlandi, P.N. Lisboa-Filho, Morphological modifications and surface amorphization in ZnO sonochemically treated nanoparticles, Ultrason. Sonochem. 20 (3) (2013) 799–804.
[29] A. Hoppe, N.S. Güldal, A.R. Boccaccini, A review of the biological response to ionic dissolution products from bioactive glasses and glass-ceramics, Biomaterials 32 (11) (2011) 2757–2774.

[30] A.M. El-Kady, M.M. Farag, Bioactive glass nanoparticles as a new delivery system for sustained 5-fluorouracil release: characterization and evaluation of drug release mechanism, J. Nanomater. 2015 (2015), 839207.
[31] X. Du, Z. Li, J. Xia, F. Zhang, Z. Wang, Facile sonochemistry-assisted assembly of the water-loving drug-loaded micro-organogel with thermo- and redox-sensitive behavior, Colloids Surf. A Physicochem. Eng. Asp. (2018) 561.
[32] A.R. Al-Shahat, M.A. Shalkh, R.A. Elmansy, K. Shehzad, Z.A. Kaimkhani, Prostatic assessment in rats after bilateral orchidectomy and calcitonin treatment, Endocr. Regul. 45 (1) (2011) 29–36.
[33] P.H.S. Gomes-Ferreira, D. de Oliveira, P.B. Frigério, F.R. de Souza Batista, K. Grandfield, R. Okamoto, Teriparatide improves microarchitectural characteristics of peri-implant bone in orchiectomized rats, Osteoporos. Int. 31 (9) (2020) 1807–1815.
[34] Z.S. Tao, W.S. Zhou, X.J. Wu, L. Wang, M. Yang, J.B. Xie, et al., Single-dose local administration of parathyroid hormone (1–34, PTH) with β-tricalcium phosphate/collagen (β-TCP/COL) enhances bone defect healing in ovariectomized rats, J. Bone Miner. Metab. 37 (1) (2019) 28–35.
[35] E.R. Luvizuto, S.S. Dias, T. Okamoto, R.C. Dornelles, R. Okamoto, Raloxifene therapy inhibits osteoclastogenesis during the alveolar healing process in rats, Arch. Oral Biol. 56 (10) (2011) 984–990.
[36] G. Ramalho-Ferreira, L.P. Faverani, F.B. Prado, I.R. Garcia Jr., R. Okamoto, Raloxifene enhances peri-implant bone healing in osteoporotic rats, Int. J. Oral Maxillofac. Surg. 44 (6) (2015) 798–805.
[37] C. Johansson, T. Albrektsson, Integration of screw implants in the rabbit: a 1-year follow-up of removal torque of titanium implants, Int. J. Oral Maxillofac. Implants 2 (2) (1987) 69–75.
[38] D.W. Dempster, J.E. Compston, M.K. Drezner, F.H. Glorieux, J.A. Kanis, H. Malluche, et al., Standardized nomenclature, symbols, and units for bone histomorphometry: a 2012 update of the report of the ASBMR histomorphometry nomenclature committee, J. Bone Miner. Res. 28 (1) (2013) 2–17.
[39] C. Micheletti, P.H.S. Gomes-Ferreira, T. Casagrande, P.N. Lisboa-Filho, R. Okamoto, K. Grandfield, From tissue retrieval to electron tomography: nanoscale characterization of the interface between bone and bioactive glass, J. R. Soc. Interface 18 (182) (2021) 20210181.
[40] J.M. Kaufman, B. Lapauw, S. Goemaere, Current and future treatments of osteoporosis in men, Best Pract. Res. Clin. Endocrinol. Metab. 28 (6) (2014) 871–884.
[41] F.A. Santos, M.T. Pochapski, M.C. Martins, E.G. Zenóbio, L.C. Spolidoro, E. Marcantonio Jr., Comparison of biomaterial implants in the dental socket: histological analysis in dogs, Clin. Implant. Dent. Relat. Res. 12 (1) (2010) 18–25.
[42] R.D.S. Pereira, J.D. Menezes, J.P. Bonardi, G.L. Griza, R. Okamoto, E. Hochuli-Vieira, Histomorphometric and immunohistochemical assessment of RUNX2 and VEGF of Biogran™ and autogenous bone graft in human maxillary sinus bone augmentation: a prospective and randomized study, Clin. Implant. Dent. Relat. Res. 19 (5) (2017) 867–875.
[43] T. Taghipour, G. Karimipour, M. Ghaedi, A. Asfaram, Mild synthesis of a Zn(II) metal organic polymer and its hybrid with activated carbon: application as antibacterial agent and in water treatment by using sonochemistry: optimization, kinetic and isotherm study, Ultrason. Sonochem. 41 (2018) 389–396.
[44] M. Sjöström, S. Lundgren, H. Nilson, L. Sennerby, Monitoring of implant stability in grafted bone using resonance frequency analysis. A clinical study from implant placement to 6 months of loading, Int. J. Oral Maxillofac. Surg. 34 (1) (2005) 45–51.
[45] J.R. Jones, Review of bioactive glass: from hench to hybrids, Acta Biomater. 9 (1) (2013) 4457–4486.
[46] K. Grandfield, A. Palmquist, F. Ericson, J. Malmström, L. Emanuelsson, C. Slotte, et al., Bone response to free-form fabricated hydroxyapatite and zirconia scaffolds: a transmission electron microscopy study in the human maxilla, Clin. Implant. Dent. Relat. Res. 14 (3) (2012) 461–469.
[47] D.M. Binkley, J. Deering, H. Yuan, A. Gourrier, K. Grandfield, Ellipsoidal mesoscale mineralization pattern in human cortical bone revealed in 3D by plasma focused ion beam serial sectioning, J. Struct. Biol. 212 (2) (2020), 107615.
[48] K. Grandfield, V. Vuong, H.P. Schwarcz, Ultrastructure of bone: hierarchical features from nanometer to micrometer scale revealed in focused ion beam sections in the TEM, Calcif. Tissue Int. 103 (6) (2018) 606–616.
[49] F.A. Shah, K. Ruscsák, A. Palmquist, Transformation of bone mineral morphology: from discrete marquise-shaped motifs to a continuous interwoven mesh, Bone Rep. 13 (2020), 100283.
[50] Q. Wang, T. Tang, D. Cooper, F. Elit, P. Fratzl, P. Guy, et al., Globular structure of the hypermineralized tissue in human femoral neck, J. Struct. Biol. 212 (2) (2020), 107606.
[51] R.E. Jung, G.A. Hälg, D.S. Thoma, C.H. Hämmerle, A randomized, controlled clinical trial to evaluate a new membrane for guided bone regeneration around dental implants, Clin. Oral Implants Res. 20 (2) (2009) 162–168.
[52] A. Blumsohn, F. Marin, T. Nickelsen, K. Brixen, G. Sigurdsson, J. González de la Vera, et al., Early changes in biochemical markers of bone turnover and their relationship with bone mineral density changes after 24 months of treatment with teriparatide, Osteoporos. Int. 22 (6) (2011) 1935–1946.

Paper V

INTERFACE

royalsocietypublishing.org/journal/rsif

Research

Cite this article: Micheletti C, Gomes-Ferreira PHS, Casagrande T, Lisboa-Filho PN, Okamoto R, Grandfield K. 2021 From tissue retrieval to electron tomography: nanoscale characterization of the interface between bone and bioactive glass. *J. R. Soc. Interface* **18**: 20210181. https://doi.org/10.1098/rsif.2021.0181

Received: 4 March 2021
Accepted: 16 August 2021

Subject Category:
Life Sciences–Engineering interface

Subject Areas:
biomaterials, biomedical engineering

Keywords:
Biogran, osseointegration, biointerphase, scanning transmission electron microscopy, electron tomography, focused ion beam

Author for correspondence:
Kathryn Grandfield
e-mail: kgrandfield@mcmaster.ca

Electronic supplementary material is available online at https://doi.org/10.6084/m9.figshare.c.5577686.

THE ROYAL SOCIETY PUBLISHING

From tissue retrieval to electron tomography: nanoscale characterization of the interface between bone and bioactive glass

Chiara Micheletti[1], Pedro Henrique Silva Gomes-Ferreira[4], Travis Casagrande[2], Paulo Noronha Lisboa-Filho[6], Roberta Okamoto[5,7] and Kathryn Grandfield[1,3]

[1]Department of Materials Science and Engineering, [2]Canadian Centre for Electron Microscopy, and [3]School of Biomedical Engineering, McMaster University, Hamilton, Ontario, Canada
[4]Department of Surgery and Integrated Clinic and [5]Department of Basic Sciences, São Paulo State University, Araçatuba Dental School, Araçatuba, São Paulo, Brazil
[6]Department of Physics, São Paulo State University, School of Sciences, Bauru, São Paulo, Brazil
[7]Research Productivity Scholarship (Process: 309408/2020-2), Araçatuba, São Paulo, Brazil

CM, 0000-0001-5823-6399; PHSG-F, 0000-0002-8936-3662; TC, 0000-0001-8044-192X; PNL-F, 0000-0002-7734-4069; RO, 0000-0002-6773-6966; KG, 0000-0002-0188-9580

The success of biomaterials for bone regeneration relies on many factors, among which osseointegration plays a key role. Biogran (BG) is a bioactive glass commonly employed as a bone graft in dental procedures. Despite its use in clinical practice, the capability of BG to promote osseointegration has never been resolved at the nanoscale. In this paper, we present the workflow for characterizing the interface between newly formed bone and BG in a pre-clinical rat model. Areas of bone–BG contact were first identified by backscattered electron imaging in a scanning electron microscope. A focused ion beam *in situ* lift-out protocol was employed to prepare ultrathin samples for transmission electron microscopy analysis. The bone–BG gradual interface, i.e. the biointerphase, was visualized at the nanoscale with unprecedented resolution thanks to scanning transmission electron microscopy. Finally, we present a method to view the bone–BG interface in three dimensions using electron tomography.

1. Introduction

Osseointegration, i.e. the direct contact between bone and implant surface, is a key requisite for the success of cementless bone implants [1]. *In vivo* studies using animal models are routinely performed to explore new implant biomaterials and novel approaches to improve osseointegration [2,3]. Retrieved implants are commonly examined at the microscale, usually by histology to assess tissue status and relevant cells, and often by microcomputed tomography (micro-CT) to quantify the bone–implant contact in three dimensions (3D) [4]. However, bone is a hierarchical tissue with features down to the nanoscale, hence it is fitting to use different tools to assess osseointegration across multiple length scales [5]. In particular, both native and new bone tissue forming at the interface with an implanted biomaterial have in the mineralized collagen fibril their nanoscopic building block [6,7]. Therefore, visualization of bone–implant interfaces at the nanoscale can reveal the exact arrangement of the organic (type I collagen [8]) and inorganic (hydroxyapatite [8]) nano-constituents of newly formed bone, in turn shedding light on the process of new bone formation around a biomaterial.

Since the 1980s, transmission electron microscopy (TEM) has been regularly used to visualize the bone–implant interface at the nanoscale [1,9,10]. The use of a convergent beam in scanning transmission electron microscopy (STEM) mode is often preferred to that of parallel illumination in conventional TEM when imaging bone interfaces. The interaction of the STEM electron probe with the sample results in scattering of the incident electron beam, which can then be collected when it emerges from the sample using a high-angle annular dark-field

(HAADF) detector [11]. HAADF-STEM imaging is particularly useful for resolving bone ultrastructure and interfaces since the contrast in the images depends on the atomic number Z, called Z-contrast or compositional contrast imaging [11]. Hence, heavier elements (e.g. bone mineral phase, metallic/ceramic biomaterials) can be easily distinguished from lighter ones (e.g. bone organic phase) as they appear brighter.

For several years, sample preparation of retrieved implants for (S)TEM characterization posed significant challenges, as samples, usually referred to as *lamellae*, need to be some 100–200 nm thick to be electron transparent, i.e. to ensure enough signal is collected to obtain a (S)TEM image. Significant enhancement in sample preparation was achieved with the use of dual-beam focused ion beam (FIB)–scanning electron microscopy (SEM) instruments. Applied for the first time to a bone–dental implant interface in 2005 [12], FIB rapidly became a prime tool to prepare electron transparent lamellae of bone interfaces for (S)TEM imaging with minimal sample disruption and with site-specificity in dual beam instruments [13–16].

(S)TEM images are two-dimensional (2D) projections of ultrathin but 3D samples, which results in the impossibility to locate specific features along the thickness of the sample. This can be an issue especially as bone nano-constituents, namely the mineralized collagen fibrils, are smaller than the lamella thickness and overlap each other in the 2D (S)TEM projection-based image. Thus, they cannot be truly represented and resolved [5]. High-resolution 3D imaging techniques, such as electron tomography (ET), can be used to overcome this limitation [17,18]. ET is based on the acquisition of (S)TEM images at different tilt angles, usually over a ±70° range, and then their back-projection or implementation of iterative algorithms to reconstruct a 3D volume representative of the sample [17]. ET carried out in HAADF-STEM mode has proved to be a powerful tool to investigate bone interfaces [19].

Hereinafter, we report on the nanoscale characterization of the interface between newly formed bone and Biogran (BG). BG is a commercially available bioactive glass commonly used in dental clinical practice as a synthetic bone graft [20]. While bioactivity of BG has been previously investigated at the microscale using scanning electron microscopy-energy dispersive X-ray spectroscopy (SEM-EDX) [21], to our knowledge, the bone-forming ability of BG, thus the bone–BG interface, has never been resolved at the nanoscale. Combining backscattered electron (BSE) imaging in SEM, FIB *in situ* lift-out, HAADF-STEM imaging and ET, we present a method to resolve the bone–BG interface at the nanoscale and evaluate the ultrastructure of newly formed bone on its surface.

2. Material and methods

2.1. Premise: peri-implant defect surgery and implant installation

Samples used to investigate the bone–BG interface were part of an *in vivo* study using male Wistar rats (unpublished work) conducted with institutional ethical approval (Process FOA no. 2017-00199). A total of 80 rats were used, but only one animal was considered for the characterization of the bone–BG interface presented herein. Trichotomy was performed in the medial portion of the right and left tibia of the animals previously sedated. Following the procedure developed by Gomes-Ferreira [22], a 15 mm-long incision was made in the left and right tibial metaphysis. After removal of soft tissue to expose the bone, milling was carried out with a 1.3 mm diameter spiral drill on both cortices, and a 2 mm, a pilot 2/3 (2.0 mm initial cut, followed by 3.0 mm cut) and a 3.0 mm milling cutter in the upper cortical and medullary portions of the tibia. The defect was filled with Biogran (Biomet 3i, Palm Beach Gardens, USA) in the form of irregular granules approximately 300–355 µm in size. Immediately after, a commercially pure grade IV titanium implant with surface treated by double acid attack was inserted in the cavity so that it contacted bone only in the lower and upper cortices. The tissues were then sutured in planes using absorbable thread (Polygalactin 910—Vycril 4.0, Ethicon, Johnson, São José dos Campos, Brazil) with continuous stitches in the deep plane and with monofilament thread (Nylon 5.0, Ethicon, Johnson, São José dos Campos, Brazil) with interrupted sutures in the outermost plane. Each animal received two implants, i.e. one in each tibial metaphysis.

The steps leading to the nanoscale characterization of the bone–BG interface are graphically summarized in figure 1. Each step illustrated in figure 1 is described in more detail in the following sections. The same sample was used for all characterization methods to ensure a correlative analytical workflow.

2.2. Sample retrieval and preparation

Thirty days after surgery and implant installation, the animals were euthanized by an overdose of inhaled anaesthetic (Halothane, Tanohalo, Cistália Produtos Químicos Farmacêuticos LTDA, Nova Itapira, Itapira, Brazil). This retrieval time point was selected in order to evaluate the peak of new bone formation prior to remodelling and the early stages of BG dissolution. The titanium implant and the surrounding tissue, including BG particles still present in the area, were retrieved. The samples were fixed in 10% formaldehyde (Analytical Reagents, Dinâmica Odonto-Hospitalar Ltda, Catanduva, Brazil) for 48 h, rinsed under running water for 24 h and dehydrated with a graded series of ethanol (70–80–90–100%). Samples were then embedded in resin (Technovit, Kulzer GmbH, Wehrheim, Germany) and divided in half along the long axis of the Ti implant using a cutting system (Exakt Apparatebau GmbH, Hamburg, Germany), and finally polished.

2.3. Microscale characterization: identification of interface

The embedded sample was mounted on a SEM aluminium stub by conductive carbon tape. The sample was wrapped tightly with aluminium tape leaving just the titanium implant and the area around exposed. Nickel paint was used to connect the titanium implant to the base of the aluminium stub. Finally, the sample was coated with a thin layer of carbon by thermal evaporation. Conductive tapes, paint and coating were used to minimize the risk of charging in the subsequent SEM imaging, as bone, BG and embedding resin are all non-conductive materials. The sample was imaged in BSE mode in a SEM instrument (FEI Magellan 400 XHR, ThermoFisher Scientific, Hillsboro, USA) operated at 5 kV.

2.4. Electron transparent lamella preparation

An *in situ* lift-out protocol was used to prepare an electron transparent lamella in a dual-beam FIB instrument (Zeiss NVision 40, Carl Zeiss AG, Oberkochen, Germany) with a 30 kV Ga ion column, a gas injection system and a micromanipulator (Kleindiek Nanotechnik GmbH, Reutlingen, Germany). The main steps of the lamella preparation are shown in figure 2. First, an approximately $12 \times 1.2\ \mu m^2$-wide region of interest (ROI) of new bone in close contact with BG was identified (figure 2*a*). The ROI was coated with a thin layer of, firstly, carbon, and, secondly, tungsten by

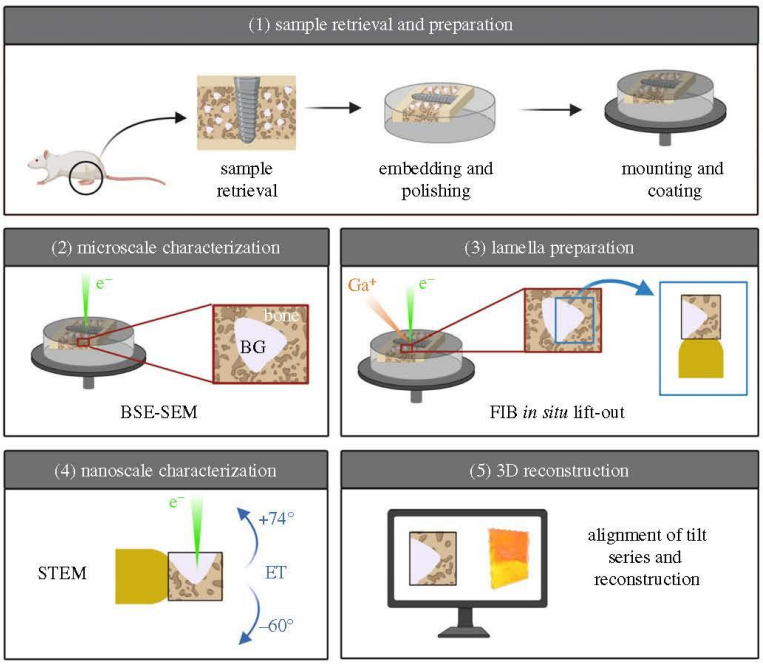

Figure 1. Workflow for the nanoscale characterization of the bone–BG interface. (1) Sample retrieval and preparation by resin embedding, polishing and mounting and coating for subsequent SEM. (2) Microscale characterization and identification of the interface by BSE imaging in SEM. (3) Electron transparent lamella preparation by FIB *in situ* lift-out. (4) Nanoscale characterization of the interface by STEM imaging and ET tilt-series acquisition. (5) 3D representation of the interface achieved using reconstruction algorithms. Created with BioRender.com.

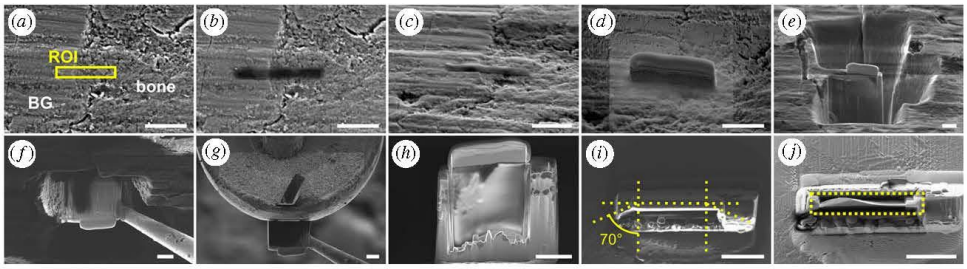

Figure 2. Sequence representing the main steps of the FIB *in situ* lift-out at the bone–BG interface. (*a*) Identification of the region of interest (ROI). (*b*) Carbon coating of ROI by electron beam deposition. (*c*) Tungsten coating of ROI by electron beam deposition. (*d*) Additional tungsten coating of ROI by ion beam deposition to a thickness of 2–3 µm. (*e*) Milling of trenches around ROI. (*f*) Attachment of micromanipulator. (*g*) Lift-out and attachment to TEM grid post. (*h*) Thinning (electron beam image). (*i*) Thinning of the sample and extra milling of the support sides falling within the ±70° STEM tilt range (shown before milling on the right and after milling on the left), marked in figure (ion beam image). (*j*) Final thinning to approximately 200 nm thick. The electron transparent lamella is in the region marked by the yellow dotted line. Scale bars are 5 µm.

electron beam deposition (figure 2*b*,*c*). Following this, a 3 µm-thick layer of tungsten was deposited over the same area by ion beam deposition (figure 2*d*). Afterwards, trapezoidal and rectangular trenches on three sides of the ROI were milled away with the Ga ion beam at 30 kV using progressively lower current (45, 27, 13 and 6.5 nA) as approaching the ROI (figure 2*e*). The micromanipulator was attached to the sample by a patch of W deposited by ion beam deposition (figure 2*f*). After cutting free the last side of the ROI, the lamella was lifted out and attached to the top post of a Cu grid by ion beam deposition of W (figure 2*g*). Subsequent thinning of the lamella to obtain an electron transparent sample (200–300 nm thick) was carried out at 30 kV in multiple steps using progressively lower currents equal to 150, 80 and 40 pA (figure 2*h*–*j*). Only an area 6 µm wide was thinned, leaving the lamella thicker on the sides for better support and to minimize warping. In order to reduce the extent of these support sides in the field of view, a region in the angular range of 70° from the orthogonal to the sample top view was cleared out to enable tilting to at least ±70° during tomography (figure 2*i*). This would allow one to maximize the width of the sample visible in STEM at high tilt angles, as the thicker sides would otherwise fall in the field of view, thus partially obstructing the image.

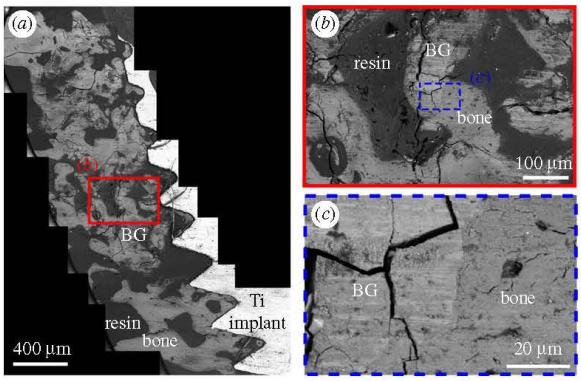

Figure 3. (*a*) BSE mosaic image of a retrieved sample, where remains of BG particles and regions of new bone formation can be identified (labelled in the image). (*b*) Zoomed in view of the region outlined in (*a*) showing new bone in contact with a BG particle. This area is further magnified in (*c*). BG particles can be distinguished from bone as they appear slightly brighter and they show more polishing marks and the presence of cracks running through them. Several BG particles appear cracked and excavated, as a consequence of BG dissolution and new bone formation occurring *in vivo*.

Lastly, to limit Ga ion implantation and amorphization damage, as well as to further thin the lamella, final beam polishing was carried out in two subsequent steps at 10 kV with a current of 80 pA, and 5 kV with a current of 60 pA.

2.5. Nanoscale characterization of the interface

Images of the electron transparent lamella were acquired with a HAADF detector in a STEM instrument (FEI Titan 80–300 LB, ThermoFisher Scientific, Hillsboro, USA) operated at 200 kV. The same STEM instrument was used to acquire the tilt-series for ET by mounting the lamella in a Fischione Model 2020 advanced tomography holder (Fischione Instruments, Export, USA). HAADF-STEM images for tomography were acquired at 300 kV. A linear single-axis tilt scheme was used, collecting images every 2° over an angular range going from −60° to +74° (electronic supplementary material, data S1).

2.6. Three-dimensional reconstruction of the interface

Reconstruction of the tilt-series was completed using Inspect 3D 4.1.2 (ThermoFisher Scientific, Hillsboro, USA). First, the 68 images recorded were aligned by cross-correlation of low-pass and high-pass filtered images. The aligned series was then reconstructed using a simultaneous iterative reconstruction technique (SIRT) with 25 iterations and applying a tilt axis correction in the x-direction (along the axis of the holder in the plane of the sample).

The reconstructed series was visualized in Avizo 9.2.0 (ThermoFisher Scientific, Hillsboro, USA). The (x, y, z) dimensions of the 3D reconstructed volume were obtained in Avizo when inputting the voxel size. The voxel size in the x- and y-directions (d_x and d_y, respectively) was assumed to be equal to the pixel size in the individual STEM images of the tilt-series, taking into account a two-fold binning applied in the reconstruction phase. The voxel size in z (d_z) was obtained by multiplying d_x by an elongation factor (e_{xz}) defined as follows from [23]:

$$e_{xz} = \sqrt{\frac{\alpha + \sin\alpha\cos\alpha}{\alpha - \sin\alpha\cos\alpha}},$$

where α is the maximum tilt angle expressed in rad units. As our tilt range was not symmetrical (−60° to +74°), we considered α as the mean value of the two extremes of the range. Therefore, the voxel size resulted to be equal to (1.46 nm, 1.46 nm, 2.01 nm) in (x, y, z). The 'orthogonal slices' (orthoslices) and volume rendering (Volren) modules available in Avizo were used for the visualization and analysis of the reconstructed electron tomogram in 2D and 3D, respectively.

3. Results and discussion

3.1. Sample retrieval and preparation

All the animals used in the study survived the implant installation surgery and were euthanized. A section of bone tissue around the implant site, including the Ti implant and BG particles still present in the area, was successfully retrieved and prepared for subsequent characterization. An example of a retrieved sample after embedding and preparation for SEM analysis is available in the electronic supplementary material (figure S1).

3.2. Microscale characterization: identification of interface

New bone growth around Ti implant and BG particles was first evaluated at the microscale acquiring BSE signal in SEM. A survey of the area around the implant site was carried out at low magnification (figure 3*a*). This enabled the identification of areas where the bone was growing in contact with BG particles (figure 3*b*,*c*). Said bone was identified as newly formed since it was not present in the region at the time of implant surgery and BG insertion. Subsequent ultrastructural analyses completed in STEM further confirmed the immature state of the tissue in contact with BG particles, as described later. BSE is a suitable imaging mode to characterize bone, as contrast arises from differences in composition [24], which easily distinguishes bone from the surrounding embed resin. On the contrary, topography-based contrast in secondary electron mode is unsuitable to discriminate between the materials of interest since both are polished flat. Bone and BG displayed a similar greyscale level in BSE images due to their similar composition rich in Ca and P. Bone regions could be identified due to the presence of some cells and their slightly darker appearance compared to BG particles. In addition, BG particles were characterized

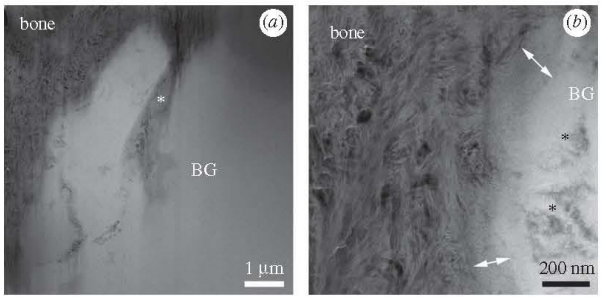

Figure 4. (*a*) Overview HAADF-STEM image of the electron transparent lamella where BG and bone regions can be distinguished. Bone ingrowth into a dissolving crevice in the BG is marked by the white star. (*b*) Bone–BG interface resolved at the nanoscale. The interfacial layer (marked by arrows) is around 120–200 nm in thickness, and appears to be gradual, formed both by the dissolution of BG and the generation of new bone. Areas of likely BG ongoing dissolution are indicated by black stars.

by cracks running through them, and by more evident polishing marks. The presence of excavated and cracked BG particles has been reported by previous microscale characterization of bioactive glass granules retrieved after implantation *in vivo* [21,25]. Cracking and excavation of the particles are compatible to the mechanism of BG dissolution and bone formation *in vivo* [21,26]. It is also possible the higher frequency of cracking occurred during sample retrieval, embedding and polishing, on the more brittle BG material [21]. In some instances, we observed contrast gradients within BG particles, which displayed a darker central region surrounded by a brighter layer. This is in agreement with previous SEM-EDX analysis revealing that ion exchange *in vivo* causes a redistribution of the BG elements, creating an outer shell depleted of Si and richer in Ca and P [21]. Based on how contrast is generated in BSE images [24], the central Si-rich region will appear darker than the outer layer with Ca and P, as Si has a lower atomic number.

Micro-CT is often included in the multiscale characterization of osseointegration, providing information at the microscale with a larger field of view than SEM, at the cost of lower resolution [4,5,27]. More recently, work has attempted to make a correlative use of micro-CT and electron microscopy-based analyses [28,29]. This was not applicable to the bone–BG interface here, given the similar contrast observed in BSE-SEM, which was used for identifying areas of bone in contact with BG for subsequent higher-resolution imaging. On the other hand, micro-CT is more easily implemented in the characterization of the bone–implant interface to materials such as titanium, that significantly differ from bone in terms of X-ray absorption [4,27].

3.3. Electron transparent lamella preparation

FIB *in situ* lift-out is a well-established method to preserve intact bone interfaces and bone structure, inducing less damage and artefacts compared to other techniques, such as ultramicrotomy [13,14]. For the first time, this technique was used to prepare a bone–BG interface. Even for this type of interface, the *in situ* lift-out protocol was confirmed as an ideal method for preparing an electron transparent lamella while preserving the interface and the sample structural features, as observed previously for other bone–biomaterial combinations [15,16,30]. BG and bone displayed different milling behaviour, with BG milling at a slower rate compared to bone, likely due to its lower porosity and

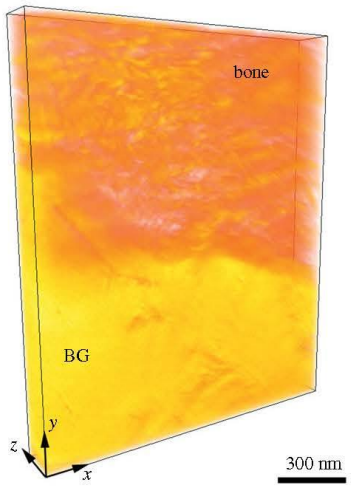

Figure 5. Volume rendering of the bone–BG interface. The volume is false-coloured such that the yellow and orange areas correspond to BG and bone, respectively. The dimensions of the volume are (1231 nm, 1494 nm, 161 nm) in (*x*, *y*, *z*). An approximate scale bar is added.

increased toughness and hardness compared to bone. In addition, although bone and BG have similar composition, rich in Ca and P, the absence of organic components in BG could also contribute to its slower milling rate compared to bone. To compensate for the different milling rate, sometimes areas made of BG were milled twice with respect to the adjacent bone to obtain a more even lamella thickness. Figure 4*a* represents a low magnification, overview image of the whole lamella acquired with a HAADF detector in a STEM instrument operated at 200 kV. This confirmed that the *in situ* lift-out protocol obtained an intact electron transparent lamella, with negligible curtaining artefacts, but some degree of bending, potentially caused by shrinkage of the embedding resin or damage to the organic components of bone induced by local thermal gradients during FIB milling and SEM imaging.

3.4. Nanoscale characterization of the interface

For the first time, the bone–BG interface was characterized at the nanoscale by HAADF-STEM imaging (figure 4). Although some early TEM studies showed osseointegrated

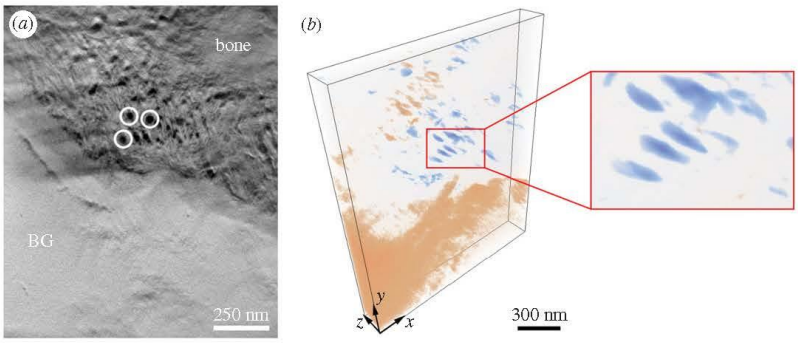

Figure 6. (*a*) Orthoslice representing the bone–BG interface in the *x*–*y* plane. The dark circles indicated in white correspond to collagen fibres. As these are oriented perpendicular to the plane of the page, they result to be parallel to the bone–BG interface. (*b*) Volume rendering of the bone–BG interface, where the colourmap and opacity were adjusted to segment the collagen fibres (blue). This allowed to better observe that collagen fibres were oriented parallel to the interface (inset), as suggested in (*a*). Pink regions correspond to BG and areas of higher mineralization in bone. The dimensions of the volume are (1231 nm, 1494 nm, 161 nm) in (*x*, *y*, *z*). An approximate scale bar is provided in (*b*).

BG particles in a rat femur [31], HAADF-STEM provided an unprecedented resolution of the bone–BG interface, not present in any other work. Thanks to the Z-contrast sensitivity of the HAADF detector [11], BG and bone were readily distinguishable as the higher atomic mass of BG caused more scattering of the electron beam, resulting in brighter intensity compared to bone. Not only did STEM confirm that bone was growing in close contact to BG as appeared from BSE imaging, but it made it possible to appreciate the gradual nature of the interface, or better, the interphase, formed both by the dissolution of BG and deposition of new bone (figure 4*b*). Such visualization of the interphase was not possible in previous work [31], as TEM imaging is not suitable to visualize compositional gradients, which instead can be clearly distinguished thanks to Z-contrast in HAADF-STEM. The presence of said interphase is compatible to the osteoconduction mechanism of BG *in vivo* [21]. As BG is exposed to body fluids, interfacial ion exchange leads to the formation of a Si-rich core and Ca/P-rich outer layer, which promotes the differentiation of primitive cells into osteoblasts [21,26]. The naturally formed biointerphase between BG and bone displayed varying thickness, from around 120 nm to 200 nm, due to the simultaneous dissolution of BG and reprecipitation of bone mineral at the interface [25]. Despite BG's current use in clinical practice, there is a lack of studies on its bioactive behaviour at the nanoscale. However, since bone formation begins at the nanoscale, the concept of osseointegration has evolved over time to become 'nano-osseointegration' [15,27,32]. This term emphasizes the value of high-resolution visualization of bone–biomaterial interfaces for a deeper understanding of the mechanisms behind bone growth and bone bonding, as well as of the changes occurring in the biomaterial *in vivo*. In the case of BG, nanoscale imaging enabled the resolution of the gradual biointerphase at its surface, not discernible with other techniques such as SEM. This was important to confirm its osteoconduction properties at the length scale where osseointegration begins. The HAADF-STEM characterization of nanoscale osseointegration of BG reported herein displayed similar results to what was previously shown for hydroxyapatite scaffolds [30]. Similar interfacial gradients and dissolution profiles have also been reported in TEM for other hydroxyapatite-based biomaterials, such as silicon-substituted hydroxyapatite [33], and carbonated hydroxyapatite [34]. TEM has also been used to characterize sub-micrometric particles of bioactive glass undergoing dissolution in simulated body fluid *in vitro* [35].

STEM imaging also resolved the nanoscale structure, i.e. the ultrastructure, of new bone forming in the vicinity of BG. Said ultrastructure is compatible to that of woven bone, as expected, since limited remodelling had presumably occurred given the early implant retrieval time point of 30 days.

3.5. Three-dimensional reconstruction of the interface

From the 68 HAADF-STEM images acquired at different tilt angles, an electron tomogram of around $1231 \times 1494 \times 161\ nm^3$ in volume was reconstructed and the tomogram is shown in figure 5 in coloured volume rendering. Inspection of 2D orthogonal slices throughout the reconstructed volume, one shown in figure 6*a*, confirmed that the bone–BG interface was continuous along the whole thickness of the sample, and not the result of feature overlap arising from 2D projections in STEM imaging. Visualization of individual orthoslices also enabled better identification of collagen fibres within newly formed bone. These were already distinguishable in HAADF-STEM images, but less clearly due to the overlapping of the mineral phase projected onto the same imaging plane. Analogously to what has been observed for other bone-interfacing materials [30,32,36], collagen fibres appeared to be aligned parallel to the interface with BG, as can be inferred from the dark circles oriented perpendicular to the plane of the page (figure 6*a*). This can be further assessed from the volume rendering in figure 6*b*, where the colourmap was selected to better highlight the collagen fibres. In the electronic supplementary material, we provide a video (electronic supplementary material, video S1) of the reconstructed 3D volume containing both the volume-rendered reconstruction and an animation slicing through the volume in the *z* (thickness) direction.

4. Conclusion

Resolving the bone–BG interface at the nanoscale can shed new light on the osseointegration process for this biomaterial. However, producing a thin intact interfacial sample is challenging via conventional preparation approaches, and usual

high-resolution imaging neglects to analyse the 3D nature of bone interphases with biomaterials.

The following workflow reported herein resolved the bone–BG interface at the nanoscale and in 3D. Specifically:

— BSE imaging identified areas of new bone contact with BG;
— FIB *in situ* lift-out obtained an electron transparent TEM sample, while preserving an intact BG–bone interface;
— HAADF-STEM unveiled the bone–BG interface with nanoscale resolution, revealing the gradual nature of the interface, a biointerphase and the presence of collagen fibres oriented parallel to the BG surface; and
— ET confirmed the organization of the interface and the ultrastructure of new bone in 3D, excluding structural artefacts that arise from the projection nature of 2D STEM images.

This workflow becomes especially relevant as a tool to assess the role of surface-modified BG or its use under different bone healing conditions, such as in compromised or pathological bone, in the future.

Ethics. The *in vivo* study was approved by the Ethics Committee on the Use of Animals (CEUA) at the São Paulo State University (Araçatuba, SP, Brazil) (Process FOA no. 2017-00199). A total of 80 male Wistar rats were employed in the study, but only one animal was used for the analyses reported in this paper. The study was conducted following the ARRIVE guidelines (Animal Research: Reporting of In Vivo Experiments) [37].

Data accessibility. The data used in this work are provided either in the paper or in the electronic supplementary material [38].

Authors' contributions. This paper has multiple authors and our individual contributions were as below: C.M.: conceptualization, investigation, methodology, writing—original draft; P.H.S.G.-F.: conceptualization, investigation, writing—review and editing; T.C.: methodology, writing—review and editing; P.N.L.-F.: conceptualization, funding acquisition, supervision, writing—review and editing; R.O.: conceptualization, funding acquisition, supervision, writing—review and editing; K.G.: conceptualization, funding acquisition, supervision, writing—review and editing.

Competing interests. We declare we have no competing interests.

Funding. This work was supported by CAPES (UNESP/CAPES/Print Project), the São Paulo Research Foundation (FAPESP) (process number: 2017/08187-3), the Natural Sciences and Engineering Research Council of Canada (NSERC) (RGPIN-2020-05722), the Ontario Ministry of Research, Science and Innovation (Early Researcher Award ER17-13-081) and the Canada Research Chairs Programme.

Acknowledgements. Microscopy was performed at the Canadian Centre for Electron Microscopy (CCEM) at McMaster University, a facility supported by the Natural Sciences and Engineering Research Council of Canada (NSERC) and other government agencies.

References

1. Albrektsson T, Brånemark P-I, Hansson H-A, Lindström J. 1981 Osseointegrated titanium implants: requirements for ensuring a long-lasting, direct bone-to-implant anchorage in man. *Acta Orthop. Scand.* **52**, 155–170. (doi:10.3109/17453678108991776)
2. Pearce A, Richards R, Milz S, Schneider E, Pearce S. 2007 Animal models for implant biomaterial research in bone: a review. *Eur. Cells Mater.* **13**, 1–10. (doi:10.22203/eCM.v013a01)
3. Wancket LM. 2015 Animal models for evaluation of bone implants and devices. *Vet. Pathol.* **52**, 842–850. (doi:10.1177/0300985815593124)
4. Binkley DM, Grandfield K. 2017 Advances in multiscale characterization techniques of bone and biomaterials interfaces. *ACS Biomater. Sci. Eng.* **4**, 3678–3690. (doi:10.1021/acsbiomaterials.7b00420)
5. Palmquist A. 2018 A multiscale analytical approach to evaluate osseointegration. *J. Mater. Sci. Mater. Med.* **29**, 60. (doi:10.1007/s10856-018-6068-y)
6. Reznikov N, Shahar R, Weiner S. 2014 Bone hierarchical structure in three dimensions. *Acta Biomater.* **10**, 3815–3826. (doi:10.1016/j.actbio.2014.05.024)
7. Shah FA, Thomsen P, Palmquist A. 2018 Osseointegration and current interpretations of the bone-implant interface. *Acta Biomater.* **84**, 1–15. (doi:10.1016/j.actbio.2018.11.018)
8. Clarke B. 2008 Normal bone anatomy and physiology. *Clin. J. Am. Soc. Nephrol.* **3**, S131–S139. (doi:10.2215/CJN.04151206)
9. Linder L, Albrektsson T, Branemark P-I, Hansson H-A, Ivarsson B, Jonsson U, Lundstrom I. 1983 Electron microscopic analysis of the bone-titanium interface. *Acta Orthop. Scand.* **54**, 45–52. (doi:10.3109/17453678308992868)
10. Tracy BM, Doremus RH. 1984 Direct electron microscopy studies of the bone–hydroxylapatite interface. *J. Biomed. Mater. Res.* **18**, 719–726. (doi:10.1002/jbm.820180702)
11. Carter CB, Williams DB (eds). 2016 *Imaging in STEM. Transmission electron microscopy diffraction, imaging and spectrometry*. New York, NY: Springer.
12. Giannuzzi LA, Giannuzzi NJ, Capuano MJ. 2005 FIB, SEM, and TEM of bone/dental implant interfaces. *Microsc. Microanal.* **11**, 998–999. (doi:10.1017/s1431927605508225)
13. Engqvist H, Botton GA, Couillard M, Mohammadi S, Malmström J, Emanuelsson L, Hermansson L, Phaneuf MW, Thomsen P. 2006 A novel tool for high-resolution transmission electron microscopy of intact interfaces between bone and metallic implants. *J. Biomed. Mater. Res. A* **78A**, 20–24. (doi:10.1002/jbm.a.30696)
14. Grandfield K, Engqvist H. 2012 Focused ion beam in the study of biomaterials and biological matter. *Adv. Mater. Sci. Eng.* **2012**, 841961. (doi:10.1155/2012/841961)
15. Palmquist A, Grandfield K, Norlindh B, Mattsson T, Brånemark R, Thomsen P. 2012 Bone–titanium oxide interface in humans revealed by transmission electron microscopy and electron tomography. *J. R. Soc. Interface* **9**, 396–400. (doi:10.1098/rsif.2011.0420)
16. Wang X, Shah FA, Palmquist A, Grandfield K. 2016 3D characterization of human nano-osseointegration by on-axis electron tomography without the missing wedge. *ACS Biomater. Sci. Eng.* **3**, 49–55. (doi:10.1021/acsbiomaterials.6b00519)
17. Ercius P, Alaidi O, Rames MJ, Ren G. 2015 Electron tomography: a three-dimensional analytic tool for hard and soft materials research. *Adv. Mater.* **27**, 5638–5663. (doi:10.1002/adma.201501015)
18. Frank J. 2006 *Electron tomography, methods for three-dimensional visualization of structures in the cell*. New York, NY: Springer.
19. Grandfield K, Palmquist A, Engqvist H. 2012 High-resolution three-dimensional probes of biomaterials and their interfaces. *Phil. Trans. R. Soc. A* **370**, 1337–1351. (doi:10.1098/rsta.2011.0253)
20. Furusawa T, Mizunuma K. 1997 Osteoconductive properties and efficacy of resorbable bioactive glass as a bone-grafting material. *Implant Dent.* **6**, 93–101. (doi:10.1097/00008505-199700620-00003)
21. Schepers E, Clercq MD, Ducheyene P, Kempeneers P. 1991 Bioactive glass particulate material as a filler for bone lesions. *J. Oral Rehabil.* **18**, 439–452. (doi:10.1111/j.1365-2842.1991.tb01689.x)
22. Gomes-Ferreira PHS *et al.* 2019 Sonochemical time standardization for bioactive materials used in perimplantar defects filling. *Ultrason. Sonochem.* **56**, 437–446. (doi:10.1016/j.ultsonch.2019.04.032)
23. Radermacher M. 1988 Three-dimensional reconstruction of single particles from random and nonrandom tilt series. *J. Electron Microsc. Tech.* **9**, 359–394. (doi:10.1002/jemt.1060090405)
24. Goldstein JI, Newbury DE, Michael JR, Ritchie NWM, Scott JHJ, Joy DC. 2018 *Scanning electron microscopy and X-ray microanalysis*. New York, NY: Springer.
25. Ducheyne P, Qiu Q. 1999 Bioactive ceramics: the effect of surface reactivity on bone formation and bone cell function. *Biomaterials* **20**, 2287–2303. (doi:10.1016/S0142-9612(99)00181-7)
26. Schepers EJG, Ducheyne P, Barbier L, Schepers S. 1993 Bioactive glass particles of narrow size range:

a new material for the repair of bone defects. *Implant Dent.* **2**, 151–156. (doi:10.1097/00008505-199309000-00025)
27. Grandfield K. 2015 Bone, implants, and their interfaces. *Phys. Today* **68**, 40–45. (doi:10.1063/PT.3.2748)
28. Karreman MA *et al.* 2017 Find your way with X-ray using microCT to correlate in vivo imaging with 3D electron microscopy. In *Methods in cell biology* (eds T Müller-Reichert, P Verkade), pp. 277–301. Cambridge, MA: Academic Press.
29. Starborg T, O'Sullivan JDB, Cameiro CM, Behnsen J, Else KJ, Grencis RK, Withers PJ. 2019 Experimental steering of electron microscopy studies using prior X-ray computed tomography. *Ultramicroscopy* **201**, 58–67. (doi:10.1016/j.ultramic.2019.03.002)
30. Grandfield K *et al.* 2012 Bone response to free-form fabricated hydroxyapatite and zirconia scaffolds: a transmission electron microscopy study in the human maxilla. *Clin. Implant Dent. Relat. Res.* **14**, 461–469. (doi:10.1111/j.1708-8208.2009.00270.x)
31. Hench LL, Paschall HA. 1973 Direct chemical bond of bioactive glass-ceramic materials to bone and muscle. *J. Biomed. Mater. Res.* **4**, 25–42. (doi:10.1002/jbm.820070304)
32. Grandfield K, Gustafsson S, Palmquist A. 2013 Where bone meets implant: the characterization of nano-osseointegration. *Nanoscale* **5**, 4302–4308. (doi:10.1039/c3nr00826f)
33. Porter AE, Patel N, Skepper JN, Best SM, Bonfield W. 2003 Comparison of in vivo dissolution processes in hydroxyapatite and silicon-substituted hydroxyapatite bioceramics. *Biomaterials* **24**, 4609–4620. (doi:10.1016/S0142-9612(03)00355-7)
34. Porter A, Patel N, Brooks R, Best S, Rushton N, Bonfield W. 2005 Effect of carbonate substitution on the ultrastructural characteristics of hydroxyapatite implants. *J. Mater. Sci. Mater. Med.* **16**, 899–907. (doi:10.1007/s10856-005-4424-1)
35. Labbaf S, Tsigkou O, Müller KH, Stevens MM, Porter AE, Jones JR. 2011 Spherical bioactive glass particles and their interaction with human mesenchymal stem cells in *vitro*. *Biomaterials* **32**, 1010–1018. (doi:10.1016/j.biomaterials.2010.08.082)
36. Grandfield K, Palmquist A, Engqvist H. 2013 Three-dimensional structure of laser-modified Ti6Al4 V and bone interface revealed with STEM tomography. *Ultramicroscopy* **127**, 48–52. (doi:10.1016/j.ultramic.2012.07.007)
37. Percie du Ser N *et al.* 2020 The ARRIVE guidelines 2.0: updated guidelines for reporting animal research. *PLoS Biol.* **18**, e3000410. (doi:10.1371/journal.pbio.3000410)
38. Micheletti C, Gomes-Ferreira PHS, Casagrande T, Lisboa-Filho PN, Okamoto R, Grandfield K. 2021 From tissue retrieval to electron tomography: nanoscale characterization of the interface between bone and bioactive glass. Figshare.

SUPPLEMENTARY

Figure S1. Sequence representing the preparation steps for SEM analysis of the sample retrieved from the *in vivo* study. The section of bone tissue, titanium implant and BG particles was first embedded in resin. The embedded sample was then secured on a SEM stub by carbon tape and wrapped with aluminum tape, and finally coated with carbon.

Data S1. Raw data (as acquired) of the tilt series used for the ET reconstruction (.mrc file).

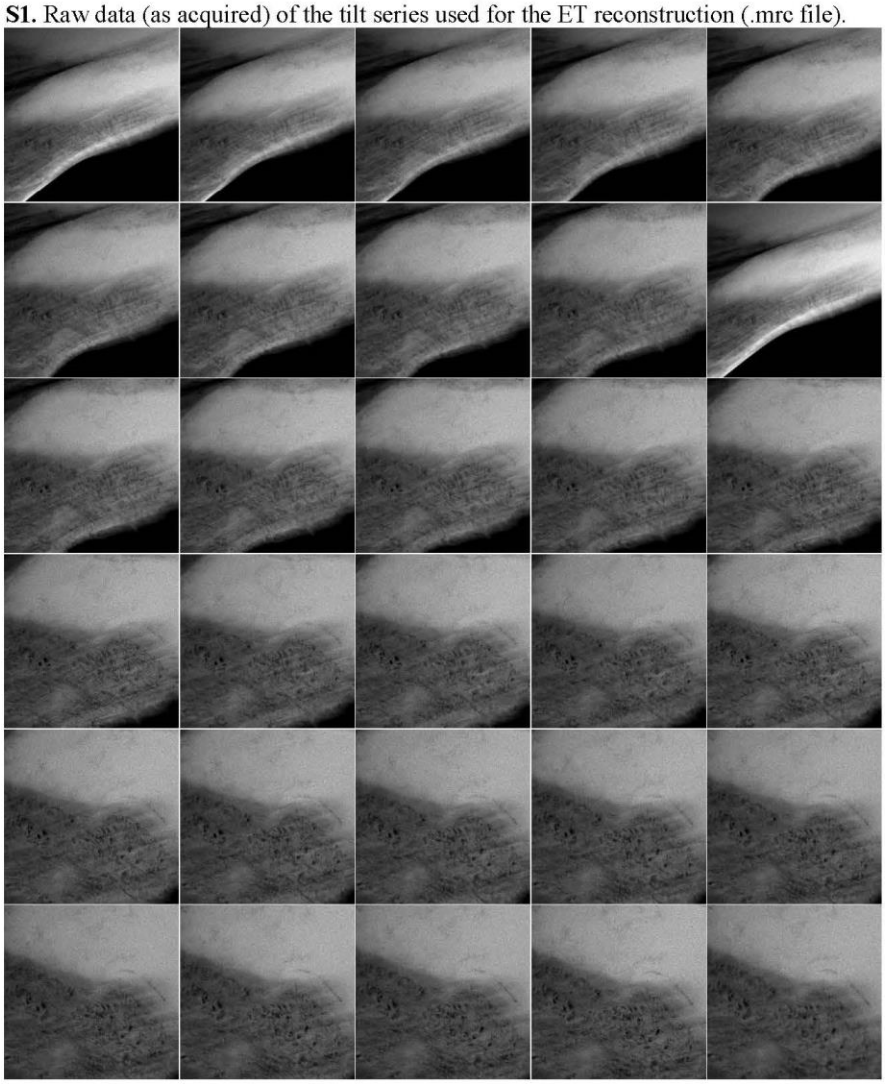

1/2

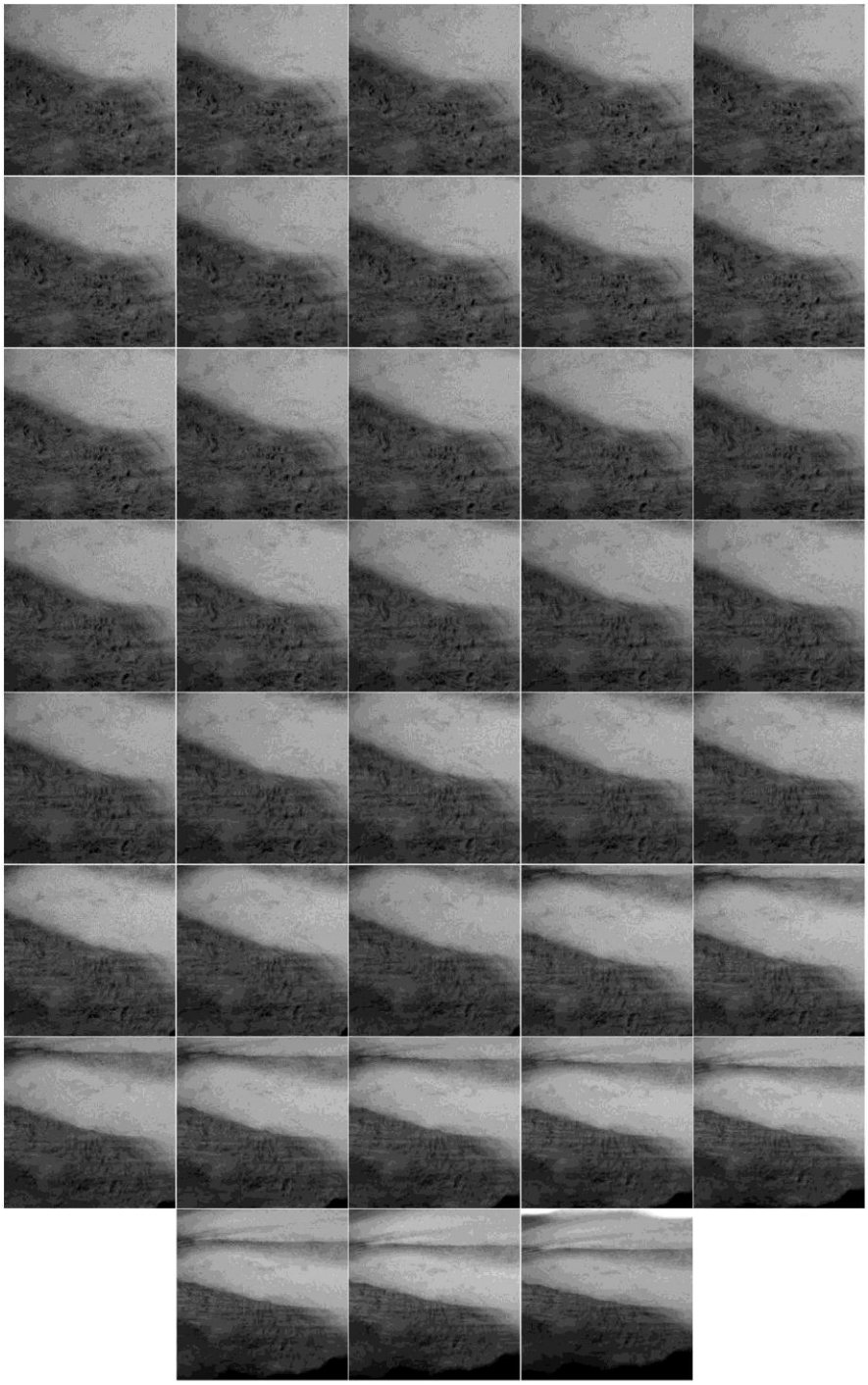

2/2

Paper VI

Preprint available in *bioRxiv*, DOI: 10.1101/2023.04.20.537681

Shedding light (... electrons) on human bone ultrastructure with correlative on-axis electron tomography and energy dispersive X-ray spectroscopy tomography

Chiara Micheletti[1,2], Furqan A. Shah[2], Anders Palmquist[2*], Kathryn Grandfield[1,3,4*]

[1] Department of Materials Science and Engineering, McMaster University, Canada
[2] Department of Biomaterials, Sahlgrenska Academy, University of Gothenburg, Sweden
[3] School of Biomedical Engineering, McMaster University, Canada
[4] Brockhouse Institute for Materials Research, McMaster University, Canada

* Corresponding authors:
Prof. Anders Palmquist, Department of Biomaterials, Sahlgrenska Academy, University of Gothenburg, Gothenburg, Sweden, e-mail: anders.palmquist@biomaterials.gu.se
Prof. Kathryn Grandfield, Department of Materials Science and Engineering, McMaster University, Hamilton, ON, Canada, e-mail: kgrandfield@mcmaster.ca

ABSTRACT

Mineralized collagen fibrils are the building block units of bone at the nanoscale. While it is known that collagen fibrils are mineralized both inside their gap zones (intra-fibrillar mineralization) and on their outer surfaces (extra-fibrillar mineralization), a clear visualization of this architecture in three dimensions (3D), combining structural and compositional information over large volumes, but without compromising the resolution, remains challenging. In this study, we demonstrate the use of on-axis Z-contrast electron tomography (ET) with correlative energy-dispersive X-ray spectroscopy (EDX) tomography to examine rod-shaped samples with a diameter up to 700 nm prepared from individual osteonal lamellae in the human femur. Our work mainly focuses on two aspects: i) low-contrast nanosized circular spaces ("holes") observed in sections of bone oriented perpendicular to the long axis of a long bone; and ii) extra-fibrillar mineral, especially in terms of morphology and spatial relationship with respect to intra-fibrillar mineral and collagen fibrils. From our analyses, it emerges quite clearly that most "holes" are cross-sectional views of collagen fibrils. While this had been postulated before, our 3D reconstructions and reslicing along meaningful two-dimensional (2D) cross-sections provide a direct visual confirmation. Extra-fibrillar mineral appears composed of thin plates that are interconnected and span over several collagen fibrils, confirming that mineralization is cross-fibrillar, at least for the extra-fibrillar phase. EDX tomography shows mineral signature (Ca and P) within the gap zones, but the signal appears weaker than that associated to the extra-fibrillar mineral, pointing towards the existence of dissimilarities between the two types of mineralization.

Keywords: collagen fibril; bone mineral; extra-fibrillar mineralization; cross-fibrillar mineralization; electron tomography; nanochannel

1. INTRODUCTION

At the nanoscale, bone is a composite whose two main components are type I collagen, a protein, and carbonated hydroxyapatite, a calcium-phosphate mineral [1]. Collagen molecules are quarter-staggered, creating overlap and gap zones which produce the characteristic 67 nm-periodic banding pattern seen in images of collagen fibrils [2,3]. In relation to collagen fibrils, mineralization is both intra-fibrillar, mainly in the gap zone [4], and extra-fibrillar (sometimes also referred to as inter-fibrillar), i.e., in the space outside or between the fibrils [5]. The presence of intra-fibrillar mineral in the gap zone is quite accepted, while extra-fibrillar mineral has received somewhat less attention, despite accounting for a significant fraction, if not even the majority, of the mineral phase according to some studies [6–11]. It has been proposed that the extra-fibrillar mineral is organized in stacks of four or more polycrystalline plates up to 200 nm in length, termed "mineral lamellae" [8–10,12]. Other studies identify mineralization as neither exclusively intra- or extra-fibrillar, but "cross-fibrillar", encompassing multiple collagen fibrils [13], and indicate that the morphology of mineral is acicular, forming a needle-like habit, and stacking into larger aggregates [14]. In general, neither the spatial and temporal relationship between intra- and extra-fibrillar, nor their exact organization with respect to each other and to the collagen fibrils are fully understood.

One factor that complicates this is the hierarchical and varying organization of bone based on anatomical location. At the nanoscale, different patterns in bone ultrastructure have been described based on the orientation of mineralized collagen fibrils with respect to the image plane, stemming from their organization within the tissue as a whole. In longitudinal sections, i.e., sections cut parallel to the collagen fibril long axis, the characteristic banding pattern of collagen is noted, confirming that collagen fibrils lie within the image plane [8,13,15]. This pattern has been termed as longitudinal or "filamentous motif" [13], given the presence of mineral structures, identified as mineral lamellae by Schwarcz [12], which are elongated along the fibril length. In transverse sections, i.e., sections cut perpendicular to the collagen fibril long axis, seemingly empty or low-contrast circular to elliptical regions some tens of nanometers in diameter are observed dispersed between high-contrast mineral that curves or wraps around them [8,13,15,16]. This overall pattern has been given several names: as it resembles lace [8], the term "lacy motif" was adopted in [13], while others have referred to this view by its dominant rosette-like features [15].

It is now fairly well accepted that the filamentous and lacy motifs are mutually orthogonal two-dimensional (2D) projections of the same three-dimensional (3D) arrays of mineralized collagen fibrils. Evidence of this stems not just from images of sections oriented parallel and perpendicular to the long axis of a long bone where collagen fibril orientation is mostly known [8,15], but also from images collected at ±45° tilt angles using sections cut at 45° to the long axis of bone [8], and from electron tomography [9,13,15]. However, the content of the low-contrast circular regions is still debated. Is it collagen fibrils cut in cross-section, or do these circles represent nano-porosity, possibly occupied by non-collagenous matter, within bone? Cressey et al. first noted these low-contrast nanosized spaces surrounded by mineral in fossil human bone and modern sheep bone, and referred to them as "pores", postulating that they are cross-sections of collagen fibrils [16]. Jantou et al., reinforced this theory when observing similar features in perpendicular sections of ivory dentin from elephant tusk [17]. This view was then adopted by more researchers in the bone field [8–10,12,15]. Grandfield et al. also noted nanosized circular features around and within mineral-rich rosettes, later to be interpreted in 3D as mineral ellipsoids [18], also suggesting that they correspond to collagen fibrils in cross-section [15]. Reznikov et al. disputed this interpretation, observing that the "lens-shaped", "electron-transparent voids" typical of the lacy pattern do not match collagen fibrils in either size or distribution [13], while others proposed these are "unmineralized spaces" located within the collagen fibrils themselves and likely contain macromolecules [19]. While the studies cited so far are dominated by the use of transmission electron microscopy (TEM) and scanning TEM (STEM), similar structures have also been described by focused ion beam-scanning electron

microscopy (FIB-SEM) tomography in the form of "nanochannels", which are postulated to be involved in ion transport [20–22]. Nanochannels were found to be most abundant at the periphery of circular mineral-rich areas that have a columnar shape in 3D [21], which most likely represent the same features termed mineral ellipsoids by other authors [18,23].

One of the challenges with identifying the contents of these spaces, as well as the organization and morphology of the mineral phase, in the studies to date is the limitations of electron microscopy imaging techniques. TEM has been the primary tool to investigate bone ultrastructure with nanoscale resolution [24]. While powerful, this tool is constrained with respect to the volume that can be analyzed, as TEM samples need to be electron transparent, usually <100 to 200 nm-thick. Moreover, S/TEM images are 2D projections, hence features along the sample thickness result overlapped in the final image. This limitation can be overcome by electron tomography (ET), where S/TEM images are collected over a range of tilt angles, and reconstructed by special algorithms to produce a 3D representation of the sample [25]. However, due to the holder geometry and spatial constraints within the sample chamber, the tilt range is typically restricted to ±70°, originating artifacts in the reconstruction due to a wedge-shaped unsampled region, the so-called "missing wedge" [25]. A more advanced type of ET, termed on-axis ET, uses specialized holders and rod-shaped samples to tilt over a ±90° range, or even allow for full 360° rotation, removing reconstruction artifacts due to the missing wedge in conventional ET [26,27]. Previous work on a bone-implant interface has demonstrated that on-axis ET can be effectively applied to the study of bone interfaces, leading to reconstructions with superior fidelity when high tilt ranges are used [28]. On-axis ET has also been combined with electron energy loss spectroscopy (EELS) tomography to correlate structural and compositional information, focusing on the chemical gradients at the bone-implant interface [29]. However, in both these studies [28,29], detailed analysis of bone nanoscale architecture was hindered by the more inconsistent orientation of collagen fibrils in bone formed around an implant placed in the maxilla, where collagen fibril organization reflects the complex loading patterns. On the other hand, distinct organizational motifs can be typically recognized in long bones such as the femur [8,13,15,30] and would be a more suitable candidate to investigate bone ultrastructure. To our knowledge, no work has combined ET with corresponding 3D analytical techniques, such as EELS or energy-dispersive X-ray (EDX) tomography, to simultaneously probe bone ultrastructure and composition.

As bone contains a significant amount of crystalline material in its mineral phase, ET is typically acquired in STEM mode to fulfill the so-called projection requirement [31]. This tomography mode is also known as Z-contrast tomography, as the contrast in images acquired with high-angle annular dark-field (HAADF) detectors in STEM strongly depends on composition, hence on the atomic number (Z). While ET provides 3D information with nanoscale resolution, the volume analyzed is still limited. Other electron microscopy techniques such as FIB-SEM can indeed examine larger volumes of material via a sequential slice and imaging protocol, but the trade-off is a loss in spatial resolution due to the probe size and a minimum slice thickness, perhaps at best 5-10 nm [32].

Herein, we combine on-axis Z-contrast ET of rod-shaped human bone samples, prepared from osteonal lamellae in the femoral cortex, with EDX tomography to gain more insights on the nature of the low-contrast regions characteristic of the lacy motif. By removing missing wedge artifacts and correlating spatial and compositional information with high resolution, we expose the contents of these regions. Hereinafter, we will refer to them as "holes" as in [8], leaving the quotation mark to reflect their low-contrast appearance and the debate on whether they are vacant or not. We also examine intra-fibrillar mineralization, as well as extra-fibrillar mineral morphology and its spatial organization with respect to collagen fibrils. This work applies a new methodology to correlate structural and compositional information to examine healthy human bone ultrastructure, which could be further expanded to the study of pathologies that alter bone nanoscale architecture.

2. MATERIALS AND METHODS

2.1. Sample preparation

2.1.1. Bone sample

A sample of human femur from a 68-year-old male, without any known bone disease, obtained freshly-frozen, was fixed upon thawing in a solution of 4% glutaraldehyde in a 0.1 M cacodylate buffer for 7 days, and cut to obtain a transverse (i.e., perpendicular to the long axis of the femur) section of cortical bone using a slow speed diamond saw (IsoMet™, Buehler, IL, USA) under hydrated conditions (Figure S1A). The section was dehydrated in ethanol (70%, 80%, 90%, 95%, 100%) and embedded in Embed812 resin (Electron Microscopy Sciences, PA, USA). A detailed embedding protocol for mineralized bone samples is provided in [18]. The sample was polished (400, 800, 1200, and 2400 grit emery paper, followed by polishing cloth with a 50 nm diamond suspension), mounted on an Al stub with C and Ag tape, and coated with C (~10-20 nm thickness). The sample was obtained with institutional ethical approval (HIREB No. 12–085-T, McMaster University, ON, Canada).

2.1.2. Site selection

Regions of interest (ROIs) for preparation of electron transparent samples for STEM imaging and ET were selected based on backscattered electron (BSE) images acquired in a SEM instrument (JEOL 6610LV, JEOL, MA, USA) operated at 10-15 kV (Figure S1B-C). ROIs for the rod-shaped samples were selected within a single osteonal lamella. These samples are numbered as *i* and *ii* hereinafter. ROIs for wedge-shaped samples were selected in three different orientations orthogonal to each other: sample *iii*, parallel to the osteonal axis and along an individual osteonal lamella; sample *iv*, parallel to the osteonal axis and across an osteonal lamella, i.e., centered on an individual lamella but crossing two inter-lamellar boundaries; sample *v*, perpendicular to the osteonal axis. Each sample was prepared in a different osteon, except samples *ii* and *v*. For a better understanding of the ROIs locations, please refer to the schematic in Figure S1D-K.

2.1.3. Preparation of rod-shaped samples for ET

Two rod-shaped samples for ET experiments (samples *i* and *ii*) were prepared by *in situ* lift-out followed by annular milling in a dual-beam FIB instrument (Zeiss NVision 40 and Zeiss Crossbeam 350, Carl Zeiss AG, Germany) equipped with a 30 kV Ga^+ ion column following published protocols [33]. Briefly, after depositing a layer of W over a previously selected 3 × 3 μm^2 ROI, trenches were milled around the ROI at 30 kV with currents in the 6.5-65 nA range (lower values when approaching the ROI). The sample was attached to the micromanipulator, lifted-out and attached to a 1 mm cartridge for an on-axis rotation tomography holder (Model 2050, Fischione Instruments, PA, USA). The sample was milled with annular milling patterns at 30 kV and progressively lower currents (80-100 pA, 40-50 pA).

2.1.4. Preparation of wedge-shaped samples

Wedge-shaped samples for STEM experiments (samples *iii-v*) were prepared in a dual-beam FIB instrument (Zeiss NVision 40, Carl Zeiss AG, Germany) equipped with a 30 kV Ga^+ ion column.

Samples parallel to the osteonal axis. Samples *iii* and *iv* were prepared by *in situ* lift-out following published protocols [34]. Briefly, after depositing a layer of W over a previously selected 12 × 2 μm^2 ROI, trenches were milled around the ROI at 30 kV with currents in the 6.5-45 nA range (lower values when approaching the ROI). The sample was attached to the micromanipulator, lifted-out and attached to a Cu grid. In each sample, three ~2 µm-wide windows were thinned to electron transparency at 30 kV and progressively lower currents (150, 80, and 40 pA), leaving thicker supports in between. Final beam polishing was completed at 5 kV and 60 pA to limit Ga^+ implantation and amorphization damage.

Sample perpendicular to the osteonal axis. To avoid re-mounting the bone sample, sample *v* was prepared following a *plan-view* lift-out protocol similar to [35]. A layer of W was deposited over a previously selected 15 × 15 μm^2 ROI. Trenches were milled around the ROI at 30 kV with currents in the 6.5-45 nA range (lower values when

approaching the ROI). The sample was attached to the micromanipulator, lifted-out, and attached to a Cu grid mounted horizontally in a specialized stub with two pins located at 90° from each other (this holder is described in [33]). The stub was removed from the holder, rotated by 90°, and repositioned in a standard holder so that the Cu grid was now oriented vertically, as in conventional *in situ* lift-outs. The sample was thinned to electron transparency as described above for the samples *iii* and *iv*.

2.2. STEM imaging and on-axis ET

STEM imaging and ET experiments of the rod-shaped samples *i* and ii were completed in a S/TEM instrument (Talos 200X, Thermo Fisher Scientific, MA, USA) equipped with four in-column silicon drift detectors (Super-X detector) and operated at 200 kV. The same instrument was used to acquire STEM images of wedge-shaped samples *iv* and *v*, while STEM images of sample *iii* were acquired in a Titan 80-300 LB (Thermo Fisher Scientific, MA, USA) operated at 200 kV. For on-axis ET, an on-axis rotation tomography holder (Model 2050, Fischione Instruments, PA, USA) was used. ET was completed using the STEM Tomography application in Velox (Thermo Fisher Scientific, MA, USA), acquiring multiple signals simultaneously (HAADF-STEM and BF-STEM, HAADF-STEM and EDX) with automated focusing and image shifting based on the HAADF-STEM image. In each rod-shaped sample, two tilt series were acquired in two different locations (marked by rectangles in Figure 1). In sample *i*, two tilt series were acquired over a ±90° range, completely removing missing wedge artifacts, while in sample *ii* the tilt range was restricted to a ±85° range to simplify acquisition and reconstruction. A summary of acquisition conditions is reported in Table 1. In all samples, EDX maps of Ca, P, C, and N were acquired over 10 frames with a 50 µm dwell time per pixel and smoothing to denoise (Gaussian blur with $\sigma = 2$; 5-7 pixel average). Background-subtracted maps were generated automatically in the Velox software and recorded at each tilt step.

2.3. Data reconstruction, visualization, and analysis

All the tilt series were aligned by cross-correlation, followed by manual adjustment of the tilt axis shift, and reconstructed using a simultaneous iterative reconstruction technique (SIRT) with 25 iterations in Inspect 3D (Thermo Fisher Scientific, MA, USA). BF-STEM and EDX tilt series were aligned based on the HAADF-STEM tilt series. The reconstructed electron tomograms were visualized and analyzed in Dragonfly (Object Research Systems, QC, Canada), as described below.

Analysis of the "holes". "Holes" (dark in HAADF-STEM and bright in BF-STEM reconstructed slices) were segmented as follows: 1) a ROI containing both these features and the background (i.e., the region around the rod-shaped sample included in the field of view of the detector) was segmented using the "Define range" operation; 2) another ROI was created by inverting the ROI

Table 1. ET acquisition conditions for the regions examined in the rod-shaped samples *i* and *ii*.

Sample	*Region*	*Tilt range*	*Tilt step*	*Signal collected*	*Pixel size*
i	*a*	±90°	2°	HAADF-STEM	0.73 nm
				BF-STEM	0.73 nm
	b	±90°	5°	HAADF-STEM	2.05 nm
				EDX	4.10 nm
ii	*a*	±85°	5°	HAADF-STEM	1.05 nm
				EDX	4.20 nm
	b	±85°	5°	HAADF-STEM	0.74 nm
				EDX	2.97 nm

in point 1 (note: this ROI mostly corresponds to mineralized regions); 3) the ROI in point 2 was filled using the "Fill inner areas" operation (applied in 2D in x, y, and z); 4) a ROI was created by a Boolean intersection operation between the ROIs in points 1 and 3 to isolate the dark (in HAADF-STEM)/bright (in BF-STEM) features contained within the sample (i.e., the "holes"). This was necessary to separate the "holes" from the background. The ROI in point 4 was further refined using the "Process islands" operation to remove mislabeled voxels. The size of the "holes" was evaluated by applying the "Volume thickness map" operation to the ROI in point 4. The ROI in point 4 was split in separate ROIs using the "Connected components – Multi ROI (6-connected)" operation. Intensity profiles along specific features were extracted using the "Ruler" tool. The distance between local minima and maxima in the intensity profile was evaluated with the function "argrelextrema" in the "scipy.signal" library in Python 3.8.10. The average distance between peaks was evaluated as the arithmetic mean between the average distance between local minima and maxima.

Analysis of mineral. A "coarse" segmentation of the mineral phase based on grey-levels was performed using the "Define range" operation. This ROI was split in separate ROIs using the "Connected components – Multi ROI (6-connected)" operation. Some representative mineral structures (3-5 in each tomogram) were manually segmented in the reconstructed slices with the "Brush" tool with local Otsu thresholding, selecting the upper Otsu range only. In tomograms *i-a/b* and *ii-a*, mineral structures were assumed to be oriented with their length predominantly within the xy planes and their width in the yz planes (refer to Figure S1 for coordinate system convention). For these samples, variation in mineral length and thickness was evaluated with the "Slice analysis" module by computing the perimeter (2p) and thickness (t) of the segmented feature in each xy slice, and estimating the length (l) by subtracting the thickness from the semi-perimeter (l = p - t). The width was estimated by multiplying the number of xy slices where the feature was segmented by the voxel size in z. In tomogram *ii-b*, mineral structures were assumed to be oriented with their width predominantly within the xy planes and their length in the xz planes (refer to Figure S1 for coordinate system convention). For these samples, variation in mineral width and thickness was evaluated with the "Slice analysis" module by computing the perimeter (2p) and thickness (t) of the segmented feature in each xy slice, and estimating the width (w) by subtracting the thickness from the semi-perimeter (w = p - t). The length was estimated by multiplying the number of xy slices where the feature was segmented by the voxel size in z.

Analysis of EDX maps. EDX tomograms of Ca, P, C, and N were segmented to select the most intense signal only (for each element independently). A Boolean intersection operation was applied between the segmented EDX signal for each element and the segmented "holes" to quantify the content (expressed as number of voxels) of each element within the segmented "holes" only.

2.4. Simulation of ion beam-sample interaction

Implantation of Ga^+ in bone during FIB sample preparation was simulated using the SRIM (Stopping and Range of Ions in Matter) software [36]. Bone was considered as a compound of 70 wt% mineral (hydroxyapatite) and 30 wt% organic (type I collagen) [37]. The mineral phase was approximated as made of 47.8 wt% Ca and 22.2 wt% P, considering a Ca/P atomic ratio of 1.67 for hydroxyapatite [38]. The organic phase was approximated as solely composed of C. Bone density was set equal to 1.8 g/cm^3 [39].

2.5. Estimation of X-ray absorption

Absorption of X-rays during EDX tomography experiments was estimated considering the following attenuation law [40]:

$$I=I_0 e^{-\rho L\left(\frac{\mu}{\rho}\right)} \quad (1)$$

where I/I_0 is the fraction of X-rays not absorbed, L is the path length, ρ is the density of the material, and the ratio μ/ρ represents the mass attenuation coefficient of the material at a certain energy [40]. A maximum path length (L) of 700 nm was considered, since this corresponds to the maximum diameter of the rod-shaped samples in the regions where EDX tomography was

completed. Bone density (ρ) was set equal to 1.8 g/cm^3 [39], as in the simulation of ion beam-sample interaction. The mass attenuation coefficient (μ/ρ) was considered to be equal to 3.781 × 10^3 cm^2/g, which is the tabulated value for cortical bone at 1 keV [41]. This is the tabulated value closest to that of the lowest X-ray energy for the elements we mapped with EDX tomography (C Kα = 0.277 keV).

3. RESULTS AND DISCUSSION

3.1. Collagen fibril orientation in rod-shaped samples

Two quasi-cylindrical, slightly conical samples (Figure 1) were obtained by FIB annular milling. The samples, referred to as *i* and *ii*, have a diameter ranging from approximately 200-300 nm at the top to 700 nm at the bottom, and a length that retained electron transparency of 8 μm and 4 μm for *i* and *ii*, respectively. Sample *i* presents collagen banding perpendicular to the long axis of the rod irrespective of the tilt angle, confirming collagen fibrils laying roughly in-plane at all tilts and co-aligned with the long axis of the rod (Figure 1A-E). The trace of some mineral ellipsoids is faintly distinguishable (Figure 1C, black dotted line), though a full ellipsoid was not captured. On the other hand, in sample *ii*, two different motifs are visible (Figure 1F-J). While a more disorganized region is distinguishable in the top half of the sample (Figure 1G), this disappears upon tilting and in-plane collagen fibrils can be noted instead (Figure 1I). An area with a mineral-rich rosette-like pattern dominates the bottom half of the sample with collagen fibrils appearing out-of-plane (Figure 1H) at some angles, then in-plane at other angles (Figure 1J). The banding patterns are nearly orthogonal to one another in the upper and lower regions, and this juncture likely represents that the boundary between two lamellae was crossed along the length of sample *ii*.

For comparison to conventional wedge-shaped TEM samples, sample *i* well corresponds to the longitudinal motif of in-plane collagen in sample *iii* (Figure S2A-B). Conversely, the more inconsistent and angle-dependent orientation of the collagen fibrils in sample *ii* resembles the patterns observed in samples *iv* and *v* (Figure S2C-F), with transitions from longitudinal to lacy motif, hence indicating variations in fibril organization within the osteonal lamella selected for sample *ii* preparation.

3.2. What are the "holes"?

Co-locating "holes" with collagen banding.

Electron tomograms were acquired in the boxed regions shown in Figures 1B (tomogram *i-a*), C (tomogram *i-b*), G (tomogram *ii-a*), and H (tomogram *ii-b*). For tomograms *i-b* and *ii-a/b* we simultaneously acquired EDX maps for C and N as markers of the organic phase, and Ca and P as markers of the mineral phase.

Electron tomograms give accurate 3D volumes that can be resliced in any orientation. By reslicing, the reconstructions clearly confirmed the correspondence between the longitudinal and lacy motifs in mutually orthogonal planes. Specifically, in Figure 2, the banding pattern is present in the reconstructed slices in both xy and yz planes, while "holes" are visible in the xz plane instead, corresponding to similar 2D S/TEM images from either longitudinal or lacy motifs (Figure 2D,F). The reciprocity between "holes" and collagen fibrils is probed in more detail in Figure 3, where the banding pattern is noted in the reconstructed xy and yz slices in correspondence to a specific "hole" marked by a box in the xz plane (Figure 3B-E). The intensity profile extracted in the regions marked by the rectangles in Figures 3C and D confirms the presence of a periodic variation in grey-levels, with an average distance between the peaks in the profile of 66.5 nm and 58.5 nm in panels C and D, respectively (Figure 3F), quite close to the expected 67 nm for D-spacing in collagen fibrils. Another example of collagen banding pattern orthogonal to the "holes" is presented in Figure S3.

The clear correspondence between banding pattern and "holes" in mutually orthogonal views enforces that the "holes" are indeed filled with collagen fibrils that are seen in cross-section. This is especially apparent in the tomograms acquired in sample *i* (Figure 1B-

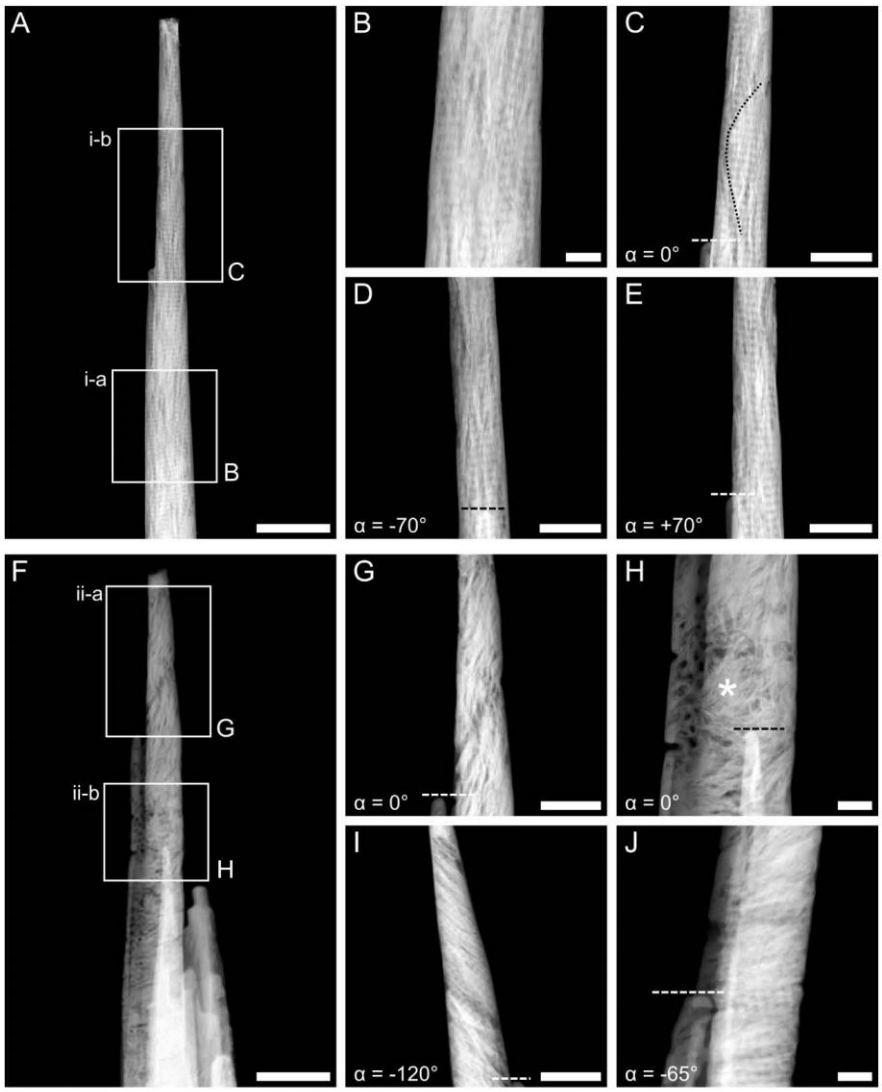

Figure 1. HAADF-STEM images of rod-shaped samples. A) Overview image of the rod-shaped sample *i*. B-C) Higher magnification images where the tilt series *i-a* (B) and *i-b* (C) were acquired. In sample *i*, collagen banding is visible throughout the length of the sample and at different tilt angles (α). An incomplete mineral ellipsoid can also be noted in C, where its boundary is marked by the black dotted line. D-E) Images acquired in the same region as C but tilted to -70° (D) and +70° (E). F) Overview image of the rod-shaped sample *ii*. G-H) Higher magnification images where the tilt series *ii-a* (G) and *ii-b* (H) were acquired. In sample *ii*, collagen is present both out-of-plane (G-H) and in-plane (I-J) based on the tilt angle. A mineral-rich region resembling a rosette surrounded by circular dark features can be noted in H (marked by *). I) Collagen banding is more apparent when imaging the region in G at a tilt angle equal to -120°. J) Collagen banding is present instead of the rosette in H when imaging at a different tilt angle (-65°). The dotted lines in C-E and G-J mark the same feature seen at different tilt angles for ease of interpretation. Please note that, given the cylindrical geometry of the samples and the rotation holder used, the tilt angle α represents a relative and not absolute reference. Scale bars are 1 μm in A and F, 200 nm in B, H, and J, and 500 nm in C, D, E, G, and I.

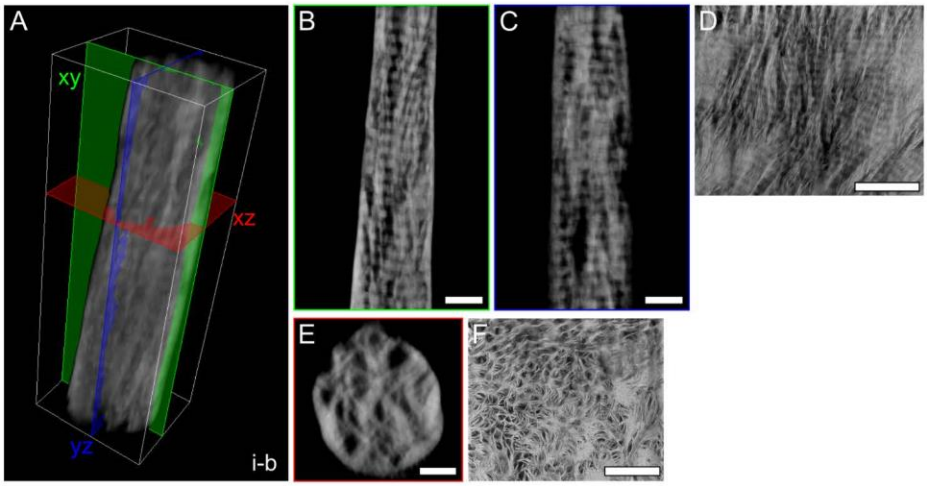

Figure 2. Banding pattern and "holes" are seen in mutually orthogonal views. A) 3D reconstruction of tomogram *i-b*, where three mutually orthogonal planes are marked (xy: green; yz: blue; xz: red). B) A representative reconstructed slice in the xy plane, corresponding to the green plane in A. C) A representative reconstructed slice in the yz plane, corresponding to the blue plane in A. D) Longitudinal motif shown in a HAADF-STEM image of the wedge-shaped sample *iii*, prepared parallel to the osteonal axis within a single lamella such that collagen fibrils are in the image plane. This motif is analogous to that of B and C. E) A representative reconstructed slice in the xz plane corresponding to the red plane in A, showing dark circular features or "holes". F) HAADF-STEM image of the wedge-shaped sample *v* (prepared perpendicular to the osteonal axis), where the presence of "holes" and encircling mineral is analogous to the view in E. Scale bars are 200 nm in B, C, D, and F, and 100 nm in E. A scale bar is not provided in A as the 3D representation is not an orthographic projection; the dimensions (x, y, z) of the white box are 555.55 × 1611.30 × 457.15 nm^3.

C), due to the optimal orientation of the banding pattern with respect the long axis of the sample. Yet, it follows that if collagen indeed fills the "holes", the cross-sectional views should differ in a gap versus an overlap zone in a mineralized sample, assuming that at least some of the mineral is located in the gap zone (intra-fibrillar). To further demonstrate this, we extracted xz slices within gap and overlap zones from an area where the banding pattern is well resolved over several bands, especially when adjusting the grey-level range to better encompass low-contrast elements (Figure 4). When examining the cross-sections in the xz plane, it becomes evident that the darkest (blackest) "holes" are cross-sectional views of overlap zones, hence explaining the nature of their low-contrast appearance, while the gap zones have some matter and a brighter grey-level detected (Figure 4D).

In summary, as the banding pattern is the dominant motif in the xy and yz planes of our ET reconstructions, it seems natural to conclude that most "holes" in the lacy motif (xz plane) are cross-sections of collagen fibrils, confirming what was first proposed by Cressey et al. [16] and supported by other authors [8–10,12,15,17]. If this was not the case, more areas devoid of collagen fibrils, i.e., without any clear banding pattern and pure black, should be apparent in the xy/yz planes. Some of these areas were indeed noted (Figure S4A-C), but in a very limited amount, which could not then explain the extensive presence of "holes" in the xz view. In the locations where the banding pattern cannot be resolved, it cannot be truly determined whether collagen fibrils are indeed present but cross-sectioned along a plane that makes the banding less evident, or if they correspond to true nano-porosity or areas where non-collagenous elements are located. Recent work by Macías-Sánchez et al. in similar cross-sectional views of mineralizing turkey leg tendon proposed that unmineralized spaces exist within collagen fibrils and macromolecules are likely contained therein [19].

Why do "holes" appear empty in most S/TEM images?

In ET reconstructions, most "holes" in the xz plane correspond to the banding pattern in

the xy plane. However, in previous works, "holes" seemed largely empty in S/TEM images of conventional wedge-shaped TEM samples. This vacant appearance of the "holes" in the lacy motif has been previously attributed to the preferential erosion of the organic phase by the ion beam during sample preparation [8]. In EELS experiments in ivory dentin, Jantou et al. observed that t/λ (relative thickness) was never equal to zero in the "holes", indicating that they are not empty [42]. Furthermore, Lee et al. showed also by EELS that the "holes" were rich in C and N [43]. To confirm the hypothesis of ion erosion, we simulated the interaction between Ga^+ ion and bone, which yielded an implantation depth up to nearly 50 nm at 30 kV. Hence, ion erosion justifies the vacant nature of "holes" in wedge-shaped samples that only have a 100-200 nm thickness, considering that thinning to electron transparency is typically performed on both sides of the sample. Conversely, the ion beam cannot erode the collagen fibrils in central regions of the thicker 300-700 nm rod-shaped samples shown here. Ion erosion could explain the lack of banding pattern in correspondence with some "holes" located near the outer surface of the rod-shaped samples presented herein (Figure S4A,D), but overall the larger thickness of the samples ensures that collagen was not eroded away, enabling its clear visualization in planes orthogonal to the "holes". This confirms that nearly all "holes" seen in so-called lacy or rosette motifs of bone are indeed collagen fibrils in cross-section.

Size and organization of the "holes" in 3D.

The size and arrangement of the "holes" were comprehensively analyzed in 3D after segmenting the tomograms based on grey-levels, which included those "holes" that appear rather low-contrast in xz slices. While "holes" display a circular/elliptical shape in S/TEM images of the lacy motif and in the reconstructed xz slices in tomograms *i-a/b* (and in well-oriented cross-sections in tomogram *ii-a*), their visualization in 3D reveals that they are elongated rod-like features mainly aligned perpendicular to the banding pattern. This is yet another similarity with and evidence of them being collagen fibrils. Therefore, segmentation of low-contrast "holes" likely captures fragments of mineralized collagen fibrils less masked by the brighter contrast of the mineral phase.

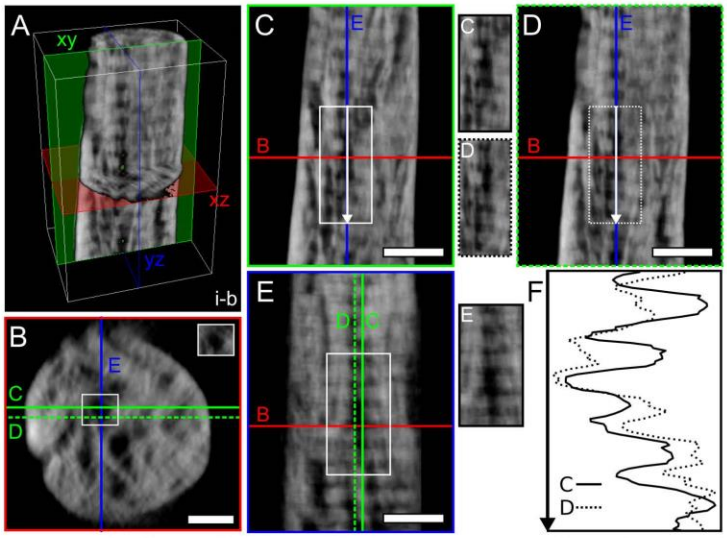

Figure 3. Co-localization of "holes" and banding pattern. A) 3D rendering of a section of tomogram *i-b*. B) A representative reconstructed slice in the xz plane where "holes" can be noted, originating a pattern similar to the lacy motif. The "hole" marked by the white rectangle was examined in the two planes orthogonal to xz (red), i.e., xy (green) and yz (blue). C) Slice in the xy plane corresponding to the solid green line in B. D) Slice in the xy plane corresponding to the dashed green line in B. The xy slices in C and D are 22.55 nm away from each other in the z direction. E) Slice in the yz plane corresponding to the blue line in B. F) The intensity profile extracted from 350 nm-long lines marked by arrows in C and D confirms the presence of collagen banding pattern (average distance between minima and maxima equal to 66.5 nm and 58.5 nm in C and D, respectively). An unmarked image of the regions marked by rectangles in C, D, and E is provided next to each panel. Scale bars are 100 nm in B, and 200 nm in C, D, and E. A scale bar is not provided in A as the 3D representation is not an orthographic projection; the dimensions (x, y, z) of the white box are 555.55 × 865.10 × 457.15 nm^3.

The size of the segmented "holes" was evaluated using the "Volume thickness map"

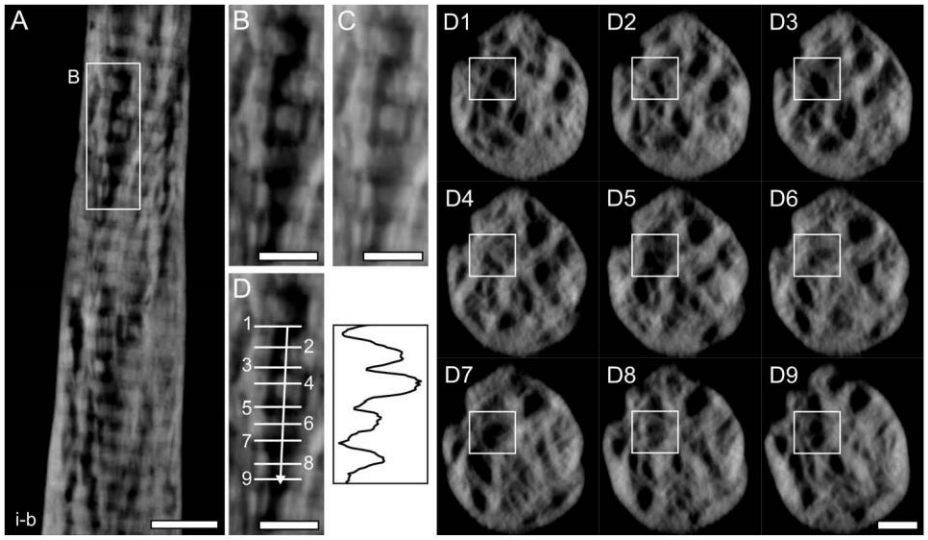

Figure 4. Dark "holes" are cross-sections of overlap zones. A) A representative reconstructed slice in the xy plane in tomogram *i-b*. B) Banding pattern can be noted, but is obscured by the low contrast in some regions. C) The banding pattern is more noticeable when grey-levels are adjusted to include lower values. D) Different cross-sections (xz plane) are examined in gap (even numbers) and overlap (odd numbers) zones in the xy plane. "Holes" are mostly visible when cross-sectioning along the overlap regions (the "hole" marked in D1-9 corresponds to the region shown in the xy plane in D). The histogram profile extracted along the white arrow in D confirms the presence of periodicity (61-66 nm). Scale bars are 200 nm in A, and 100 nm in B, C, and D.

operation in the Dragonfly software, yielding an average diameter of 22.9 ± 4.6 nm over the four tomograms (Figure 5A, Figure S5, Table S1). Specifically, the average diameter is in the 22.9-26.4 nm range in tomograms *i-b* and *ii-a/b*, but is reduced to 16.4 nm in tomogram *i-a*. At a closer inspection, it appears that a higher number of smaller features below 10 nm are captured in the segmented "holes" in tomogram *i-a* (Figure S5). Overall, the size of the segmented "holes" does not correspond to what is commonly indicated for mineralized collagen fibrils, i.e., 80-120 nm [1,44,45]. On the other hand, "holes" in out-of-plane S/TEM images of bone have also been described as 20-50 nm in size [8,12,13,15]. Mineralized collagen fibrils with diameters as small as 30 nm have been reported using atom probe tomography [46]. Sample preparation artifacts such as shrinkage (up to 27% [47]) or fibrils cross-sectioned along planes not perfectly perpendicular to their long axis could also explain our smaller measurements. Hence, considering the co-localization of "holes" and banding pattern in mutually orthogonal slices, it appears inaccurate to rule out that "holes" are cross-sections of collagen fibrils solely based on size considerations.

Interestingly, the average diameter of "holes" in our segmentations is well within the 10-50 nm range reported for nanochannels [20–22]. However, some discrepancies also exist. Most nanochannels in bone have a certain degree of interconnectivity (3-4 nodes) [21] and are micrometres in length [22]. On the other hand, our connectivity analysis of the segmented "holes" using the "Connected components – Multi-ROI" operation in the Dragonfly software, which splits the segmented ROI in multiple ROIs based on their degree of connection, revealed that "holes" are mostly disconnected from each other (Figure 5B-C, Figure S6). Additionally, no segmented "holes" extending over the entire sample length are present. Conversely, most appear rather short, with a length of at most ~500 nm in the longest continuous segments. Overall, more evidence indicates that "holes" are collagen fibrils, rather than other hole-like features like nanochannels. However, it is possible that some regions we noted where the banding pattern is not present do indeed correspond to nanochannels.

In the region of tomogram *i-b* where a partial mineral ellipsoid can be seen (Figure 1C in

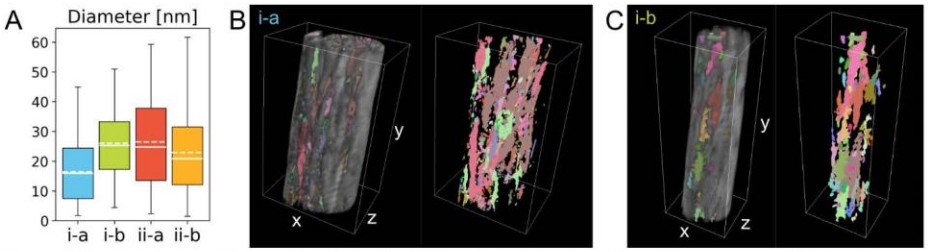

Figure 5. Size and connectivity of the "holes". A) Box plot of the diameter of the segmented "holes" in each tomogram. Each box represents 25-75% of the data, while the capped lines indicate the entire range of the data. Median and mean values are marked by solid and dashed lines, respectively. B) 3D rendering of tomogram *i-a* with the segmented "holes", shown in different colours to represent their disconnected nature. C) Similar visualization as B for tomogram *i-b*. A scale bar is not provided in B and C as the 3D representation is not an orthographic projection; the dimensions (x, y, z) of the white box are 879.65 × 1416.20 × 620.50 nm^3 in B, and 555.55 × 1611.30 × 457.15 nm^3 in C.

HAADF-STEM), not many segmented "holes" are present within the ellipsoid, but they seem most abundant around its periphery (Figure S7). This is probably due to the mineral-rich nature of the ellipsoids, especially in their core [30], which obscures low-contrast elements, resulting in fewer dark "holes" being detected within. Similarly, "holes" (already interpreted as collagen fibrils in that study) were mostly noted on the periphery of rosettes in 2D HAADF-STEM images [15]. On the other hand, the lower mineral content in between ellipsoids, likely due to the accumulation of mineral inhibitors [48], makes the "holes" (i.e., the collagen fibrils) more noticeable in the images due to contrast effects. By analogy, since both nanochannels [21] and unmineralized spaces [19] are noted at the periphery of ellipsoids (called spherulites in [19]), it is indeed possible that at least some of these features do indeed correspond to cross-sections of collagen fibrils.

Correlative 3D compositional information with EDX tomography.

We completed correlative HAADF-STEM and EDX tomography experiments to confirm whether "holes" are rich in organic components, namely C and N. Unfortunately, the spatial distribution of C and N does not provide resolutive information in this regard, as the maps appear quite noisy for these light elements. C and N seem more abundant in close proximity to the holes (Figure S8A-B). A few instances of C and N within the "holes" are noted (Figure S8C-D), but it cannot be excluded that this spatial correspondence arises as an artifact due to noise. We segmented EDX maps and performed a Boolean intersection operation with the segmented "holes". This showed that most "holes" are empty, although the presence of C and N in the segmented "holes" is considerably higher than that of Ca and P (Table S2). The lack of signal collected in most "holes" should be regarded as a technical limitation rather than true vacancy. In fact, as the lowest-contrast "holes" were the ones segmented and used in the Boolean intersection, this indicates that they may not contain enough matter to generate a strong EDX signal. If the "holes" were indeed empty pores, it would still be expected to collect C signal from the infiltrated embedding resin. Even if "holes" hosted non-collagenous organic substances, e.g., macromolecular complexes [19], C and N signals should still be detected. On the other hand, compositional information obtained from EELS experiments point towards the presence of C and N within the "holes" [42,43], corroborating their correspondence to collagen fibrils. Some additional technical considerations on EDX tomography in our work are provided in greater detail in Section 3.4.

3.3. Towards a better understanding of intra- and extra-fibrillar mineralization

Extra-fibrillar mineral is cross-fibrillar.

Collagen fibrils are mostly in register across the entire volume in the tomograms where the banding pattern is visible in individual reconstructed slices (tomograms *i-a*/*b* and *ii-a*). Extra-fibrillar mineral, i.e., the phase not located within the gap zones, appears mostly aligned with collagen fibrils in tomograms *i-*

a/b and *ii-a*, with mineral structures elongated along the direction of the collagen fibrils (Figure 6). We performed a "coarse" segmentation of the mineral phase based on grey-levels, followed by identification of disconnected sub-components. This showed that the segmented mineral regions are mostly interconnected, as in all tomograms the "Connected components – Multi-ROI" operation identifies a multi-ROI where a sub-ROI has significantly more voxels than the others (Table S3). This analysis also confirms the "cross-fibrillar mineralization" model proposed by Reznikov et al., where mineral aggregates form a continuous mineral phase extending beyond a single fibril, hence spanning adjacent fibrils [13]. The mineral phase encompassed in our segmentation appears to be mostly extra-fibrillar, since some intra-fibrillar mineral was excluded as the contrast in the corresponding gap zones was lower than our segmentation threshold (grey-level based). Therefore, in our reconstructions, the cross-fibrillar nature of the mineral can be accurately confirmed for the extra-fibrillar component.

Extra-fibrillar mineral is made of thin plates.

In the complex scenario of fully mineralized tissues like mature bone, segmentation of individual mineral structures is not straightforward. In our reconstructions, some fine mineral structures were sometimes visible, but hard to isolate as they often seemed to fuse together (Figure 6A). In the extra-fibrillar mineral, a few of these structures appearing as one individual entity were manually segmented in each tomogram to offer some insights into their shape and size (Figure 6B, Table S4). Mineral structures in tomograms *i-a/b* and *ii-a* have a very similar length in the order of ~100 nm. Mineral length appears smaller in tomogram *ii-b*, but this can be attributed to limitations in the segmentation of individual features given the high density of mineral throughout the tomogram, where small mineral structures appear extensively merged into bigger aggregates. The width of mineral plates is around 33-43 nm in tomograms *i-a/b* and *ii-b*, but smaller for tomogram *ii-a* (14 nm), while the plate thickness is in the 5-9 nm range. These values are in alignment with those found in the literature for 2D TEM measurements, typically in the order of 30-70 nm in length, 15-50 nm in width, and 5-10 nm in thickness [8,49–52], as well as for 3D measurements in early tomography studies (40-170 × 30-35 × 4-6 nm^3) [53]. Additionally, the mineral we segmented appears to be extra-fibrillar, for which larger dimensions have been measured, with lengths up to 90-200 nm [6,8].

Over the years, varying size and shape have been reported for bone mineral. Discrepancies in mineral size can be mostly attributed to different techniques and/or sample preparation. For example, measurements from atomic force microscopy (AFM) yielded shorter crystals compared to TEM [54]. Mineral shape has also been often debated since early applications of TEM in bone research. While pioneering TEM analyses by Robinson showed the mineral to be plate-shaped ("tabular") [49], others later proposed that the mineral is needle/rod-shaped [55]. This theory was disputed by others when imaging TEM samples at different tilt angles, concluding that the needle-shaped appearance was a misinterpretation arising from plates seen edge-on [56,57]. Using small-angle X-ray scattering, Fratzl et al. reconciled these views suggesting that mineral shape varies in different species, with human bone being more plate-shaped [58]. Later studies based on both TEM and AFM have consistently reported plate-shaped mineral [8,52,54,59], although the hypothesis of a needle-like habit has more recently resurfaced [13]. Our analyses overall support that the mineral is in the shape of thin plates, given the aspect ratio between the three dimensions (length/thickness, width/thickness, length/width). The plate morphology of the mineral is especially apparent when considering its shape in 3D and in distinct orthogonal planes (Figure 6C), further proving the advantages of 3D ET, especially on-axis tomography without artifacts, over 2D projection S/TEM images where edge-on views could lead to false interpretation of plates as needles.

Are extra-fibrillar plates made of even smaller components?

Given resolution limits and the small size of bone mineral, it is indeed possible that the segmented features correspond to aggregates of smaller sub-structures (e.g., platelets and/or needles), but their boundaries cannot

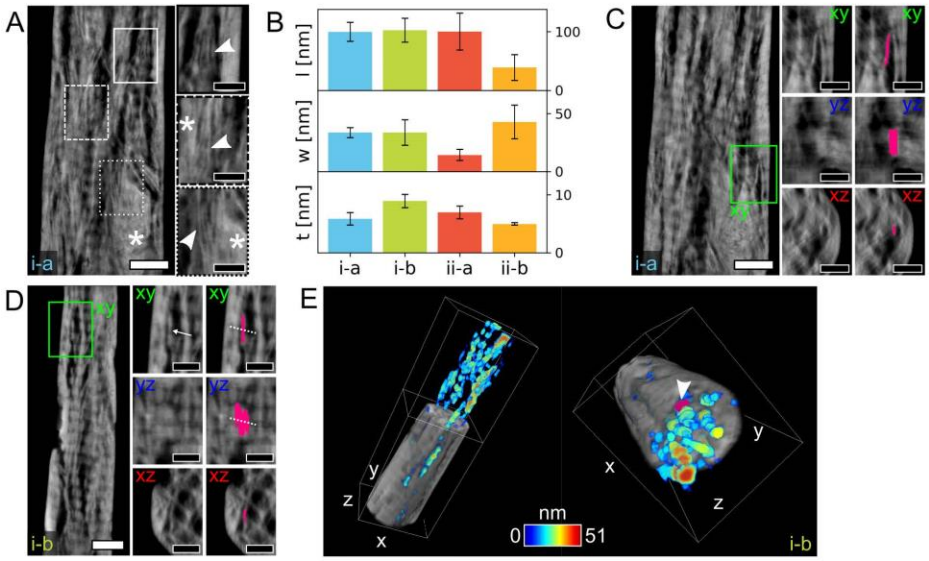

Figure 6. Representative examples of mineral plates. A) A representative reconstructed slice in the xy plane in tomogram *i-a* where both fine mineral structures (magnified in the insets, indicated by arrowheads) and larger aggregates (marked by *) are visible. B) Bar plots of average values of mineral length (l, top plot), width (w, middle plot), and thickness (t, bottom plot) for some representative mineral plates segmented in the four tomograms. C) An example of a mineral plate segmented in tomogram *i-a* (bright pink). Its plate-shape is confirmed by the cross-sectional view in the yz plane. In the xz plane, the mineral plate wraps around a "hole". D) An example of mineral plate(s) segmented in tomogram *i-b* (bright pink). As the collagen banding pattern likely modulates the grey-levels in the entire slice, it is difficult to establish whether the segmented feature is a single plate or it is made of smaller plates fused together, especially when considering the cross-sectional view in yz (the potential boundary between sub-components is marked by the white arrow and dashed lines). In the xz plane, the mineral plate wraps around a "hole". E) 3D renderings of tomogram *i-b* cropped to better show the segmented "holes" (heat map represents size). In the orientation on the right side, a mineral plate (same as in D) on the outside of a segmented "hole", wrapping around it, can be noted (arrowhead). Scale bars are 200 nm in the overview images in A, C, and D, and 100 nm in their insets. A scale bar is not provided in E as the 3D representation is not an orthographic projection; the dimensions (x, y, z) of the white box are 555.55 × 1611.30 × 457.15 nm^3.

be resolved, making them appear as one single feature. Similar challenges in identifying individual mineral structures have been reported in analyses of human trabecular bone [52]. Mineral structures (therein interpreted as needles) merging into larger aggregates were observed in human cortical bone, suggesting that bone mineral itself is a hierarchical assembly [13]. Early ET work also showed that mineral crystals fuse in a coplanar way to form large platelets [53], although it is worth noting that this study and several others dealing with collagen-mineral relationships in bone (where "bone" indicates a family of materials, and not just skeletal tissue) focused on the mineralized turkey tendon, which is a somewhat simplified system where collagen fibrils are well aligned with each other. Some authors also pointed out the existence of two populations of mineral structures in bone, i.e., small and large mineral components, with the large ones possibly being aggregates of small mineralites [54].

Interestingly, we noted some mineral plates presenting variation in grey-levels along their length (Figure 6D). This could indicate that they are composed of sub-structures, or, alternatively, this could be a modulation of the *Z*-contrast over the entire image due to the superimposition of the collagen banding pattern, as previously suggested [9,12]. For example, mineral plates splaying multiple bands, such as that shown in Figure 6D, were noted, but it remains difficult to establish whether they represent: i) the same purely extra-fibrillar entity (in agreement with [9,12]); ii) intra-fibrillar mineral growing in the inter-fibrillar space (as proposed in early ET studies by Landis et al. [53]); or iii) two distinct extra-fibrillar structures fused into one, in which case the distinction of different sub-

components is irrelevant. Clearly, the direct visualization of bone mineral in fully mineralized bone is technically challenging, especially compared to simpler models like the mineralized turkey tendon. As bone mineral is the smallest biogenic crystal known, an even higher resolution is needed to clearly resolve mineral plates in ET, but this would inevitably reduce the volume analyzed, both in terms of field of view and sample thickness constraints.

Spatial relationship between extra-fibrillar mineral and "holes".

In tomograms *i-a/b*, some individual mineral plates appear surrounding the "holes" in the xz plane (Figure 6C-D). Given the evidence that "holes" are cross-sections of collagen fibrils, the presence of extra-fibrillar mineral wrapped around the fibril exterior yields a spatial relationship similar to the ultrastructural model described by Schwarcz [12]. This is even more noticeable in 3D, such as in Figure 6E, confirming the extra-fibrillar nature of the segmented mineral plate, which can be seen located on the outer surface of a segmented "hole" (i.e., collagen fibril).

Intra- and extra-fibrillar mineralization in EDX tomography.

In reconstructed EDX maps, Ca and P are located in correspondence with both extra- and intra-fibrillar mineral (Figure 7A-B). These signals are more intense for the extra-fibrillar mineral, but they can also be detected within the gap zones, confirming intra-fibrillar mineralization (Figure 7C). This corroborates the contrast in the reconstructed HAADF signal, where extra-fibrillar mineral often appears brighter, while some gap zones display a lower contrast. Reconstructed EDX maps showing stronger Ca/P signal for the extra-fibrillar mineral are analogous to 2D STEM-EDX maps reported by McNally et al. [8]. While EDX tomography seems limited in the analysis of the organic phase, with low detection of C and N, it emerges as a viable tool to examine the mineral phase in 3D and reconstructed 2D slices.

Not only does the intra-fibrillar mineral display a lower contrast (and Ca/P content) than the extra-fibrillar, but also the grey-level in each gap zone appears rather uniform. In other words, no individual mineral plates can be discerned in the intrafibrillar spaces, conversely to the extra-fibrillar mineral for which thin plates are observed. Some authors have proposed that the intra-fibrillar mineral is more amorphous [11,46], which would

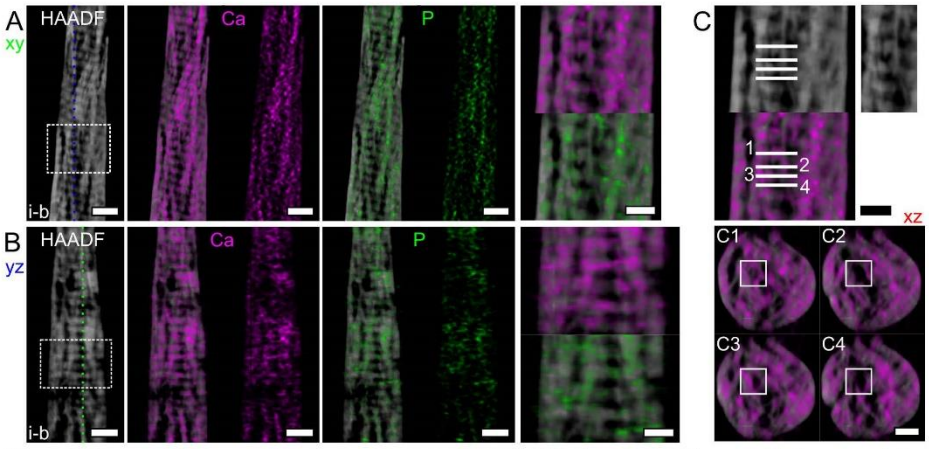

Figure 7. Representative examples of reconstructed HAADF-STEM slices and EDX maps. A) A representative reconstructed slice in the xy plane in tomogram *i-b* for the HAADF signal and EDX maps of Ca (magenta) and P (green) with and without the underlying HAADF slice. B) A representative reconstructed slice in the yz plane in tomogram *i-b* for the HAADF signal and EDX maps of Ca and P with and without the underlying HAADF slice. In both A and B, a magnified version of the area marked by the dashed rectangle is provided, where mineral can be seen both as extra- and intra-fibrillar. C) Different cross-sections (xz plane) are examined in gap (odd numbers) and overlap (even numbers) zones in the xy plane. From the reconstructed EDX maps of Ca in these different xz planes, intra-fibrillar mineralization, i.e., mineral in the gap zones, is evident. An unmarked version of the fibril examined is provided to the right of the HAADF slice in C, and marked by the rectangle in C1-4. Scale bars are 200 nm in A and B, and 100 nm in C and in the magnified areas corresponding to the dashed rectangles in B.

explain why individual crystals were not identified within the gap zones of our ET reconstructions. If intra- and extra-fibrillar mineral phases differ in crystalline structure, such a distinct property would challenge the inter-connection between these two phases.

3.4. Some technical considerations

HAADF-STEM ET has been applied to the study of bone ultrastructure [9,13,15,30] and various bone-biomaterial interfaces [28,29,60–62]. In sample *i-a*, we also acquired a tilt series in BF-STEM mode at the same time as the HAADF-STEM mode acquisition (Figure S9). Previous work has demonstrated both experimentally and by simulations that STEM tomograms of thick biological specimens (600 nm-1 µm) have a greater spatial resolution when acquired with a BF detector compared to a HAADF detector [63]. Our two rod-shaped samples (*i* and *ii*) have a diameter up to 700 nm, which is much thicker than conventional electron transparent wedge-shaped samples (100-200 nm). When comparing HAADF-STEM and BF-STEM tomography reconstructions, some features appear better resolved in the latter (Figure S9), suggesting that the BF detector may be more suitable for our thicker samples as reported in [63], even though differences are not striking. However, some artifacts (i.e., bright dots in the xy and yz planes and bright streaks in the xz plane) are present in the BF-STEM tomogram, deteriorating its overall quality (Figure S9). These artifacts were not present in the acquired nor aligned tilt series, but only in the individual reconstructed slices, implying that they originated during the SIRT reconstruction in the Inspect 3D software. It is possible that they are due to software computational assumptions related to the BF-STEM detector, or that the projection requirement is not entirely fulfilled, as incoherent image conditions for crystalline materials also depend on the BF detector semi-angle [63,64]. Therefore, in-depth analyses were performed only on HAADF-STEM tomograms.

EDX tomography is usually limited by a low signal-to-noise ratio (SNR), which requires long dwell times and/or high beam current to increase the dose, with the risk of inducing damage in the sample [65]. The S/TEM instrument used in this study (Talos 200X, Thermo Fisher Scientific) is equipped with a Super X-detector made of four separate silicon drift detectors, which allows for greater signal collection over a wider range of tilt angles compared to single detectors [40,66,67]. Additionally, the use of rotation tomography holders (in this work the Model 2050 by Fischione) eliminates X-ray collection issues related to the shadowing of the EDX detector [67]. Nonetheless, the spatial resolution in our EDX maps, especially for lighter elements like C and N, is not high enough to resolve the composition of some features of interest, such as the "holes". Despite the not-so-optimal SNR, we kept a short acquisition time (~2 min per map) to limit beam damage, which in fact was not visible during tilt series acquisition. It is also possible that the SNR was limited by X-ray absorption effects due to the large sample thickness. Based on our calculations using Eq. (1), up to nearly 40% X-rays could have been absorbed in the thicker parts of the sample (700 nm), especially for the lighter elements (C and N). More detailed simulations are needed to precisely quantify the fraction of X-rays absorbed and their path through the bone samples. In alternative to EDX, EELS tomography can be combined with HAADF-STEM tomography to correlate compositional and spatial information, as already demonstrated for bone-implant interfaces [29]. Greater spatial resolution is typically achieved in EELS than EDX [68], but as the signal collected in EELS is dependent on that transmitted through the sample, our thick samples were not suitable for this analysis.

Although on-axis ET requires specialized holders and rod-shaped samples, the advantages in the field of bone studies are not limited only to the removal of missing wedge artifacts. Using rod-shaped samples that were thicker than conventional wedge-shaped samples, we were able to collect more of the structural and compositional information contained in the sample thickness (z direction, considering xy as the image plane). This came at the cost of reduced information along the sample width (x direction), as the rod-shaped samples occupy only a limited portion of the field of view in the image plane (xy plane). However, the cylindrical, although slightly conical, shape of samples *i* and *ii* retains a near constant thickness at all tilts, unlike wedge-shaped samples, and its geometry

better matches that of the features of interest present in bone at the nanoscale, i.e., the mineralized collagen fibrils. Collagen fibrils are reported to be oval-shaped in cross-section [44] and are routinely represented as rods [1,14]. At higher levels, fibrils organize themselves in bundles, which are described as cylindrical [1,14]. At the mesoscale, mineral aggregates are geometrically approximated in the shape of an ellipsoid [18,23,30], which is a solid of revolution.

4. CONCLUSIONS

Bone ultrastructure is challenging to assess with high resolution, elemental clarity, and over meaningful 3D volumes. In this work, we present a new method to characterize human bone ultrastructure and composition by correlating on-axis Z-contrast ET and EDX tomography in the TEM. Rod-shaped samples, with a diameter up to 700 nm, provided a larger sample thickness than conventional wedge-shaped TEM samples, as well as a geometry consistent with features of interest, such as mineralized collagen fibrils. Moreover, rotation of the rod-shaped samples on their long axis in on-axis ET removes missing wedge artifacts in the reconstructions. The segmentation of low-contrast spaces, the "holes", debated to be some form of nano-porosity (eventually housing some non-collagenous organics) or collagen fibrils viewed in cross-section, revealed that they are rod-shaped with a diameter of ~23 nm and are disconnected from each other. When examining mutually orthogonal planes in the reconstructions, collagen banding pattern is mostly seen in correspondence with the "holes", supporting that these are cross-sectional views of collagen fibrils, especially along the overlap zones. 3D EDX confirmed both extra- and intra-fibrillar mineralization, but a clear understanding of their spatial relationship remains challenging. Extra-fibrillar mineral appears plate-shaped and richer in Ca and P than the intra-fibrillar mineral, with larger interconnected aggregates splaying multiple collagen fibrils. In this sense, the definition of an individual mineralized collagen fibril should perhaps be revisited, given the increasing evidence of extra-fibrillar mineral organized in a cross-fibrillar fashion.

ACKNOWLEDGEMENTS

This study was supported by funds awarded to KG from the Natural Sciences and Engineering Research Council of Canada (NSERC) (grant no. RGPIN-2020-05722), the Ontario Ministry of Research, Innovation and Science (Early Researcher Award ER17-13-081), and the Canada Research Chairs Program from whom KG holds the Tier II Chair in Microscopy of Biomaterials and Biointerfaces. Scholarship support is acknowledged from the Ontario Graduate Scholarship and the Blanceflor Foundation for CM. Electron microscopy experiments were performed at the Canadian Centre for Electron Microscopy (CCEM) at McMaster University (ON, Canada), a facility supported by NSERC and other government agencies. Funding support is also acknowledged from the Adlerbertska Foundation, the Kungliga Vetenskaps-och Vitterhets-Samhället i Göteborg, and the Svenska Sällskapet för Medicinsk Forskning (SSMF) for FAS, and from the Swedish Research Council (grant no. 2020-04715) and the Swedish state under the agreement between the Swedish government and the county councils, the ALF agreement (ALFGBG-725641), for AP. The Area of Advance Materials at Chalmers and at the Department of Biomaterials (University of Gothenburg) within the Strategic Research Area initiative launched by the Swedish government, and the Hjalmar Svensson Foundation are also acknowledged. The authors are thankful to Cheryl Quenneville for providing the bone sample, Dakota M. Binkley for the preparation of the bone sample, and Travis Casagrande for the preparation of the FIB samples.

AUTHOR CONTRIBUTIONS

Conceptualization: All authors. **Formal analysis:** Chiara Micheletti. **Methodology**: Chiara Micheletti. **Investigation:** Chiara Micheletti. **Visualization:** Chiara Micheletti. **Supervision:** Furqan A. Shah, Anders Palmquist, Kathryn Grandfield. **Funding acquisition:** Kathryn Grandfield. **Writing – original draft:** Chiara Micheletti. **Writing – review and editing:** All authors.

CONFLICT OF INTEREST

The authors declare no conflicts of interest.

DATA AVAILABILITY STATEMENT

Data are provided in the main manuscript or in Supplementary Information.

REFERENCES

1. Reznikov N, Shahar R, Weiner S. Bone hierarchical structure in three dimensions. Acta Biomater. 2014;10:3815–26.
2. Hodge AJ, Petruska JA. Recent studies with the electron microscope on ordered aggregates of the tropocollagen macromolecule. In: Ramachandran GN, editor. Aspects of protein structure. New York, NY: Academic Press; 1963. p. 289–300.
3. Orgel JPRO, Irving TC, Miller A, Wess TJ. Microfibrillar structure of type I collagen in situ. Proc Natl Acad Sci USA. 2006;103:9001–5.
4. Weiner S, Traub W. Organization of hydroxyapatite crystals within collagen fibrils. Febs Lett. 1986;206:262–6.
5. Landis WJ, Hodgens KJ, Song MJ, Arena J, Kiyonaga S, Marko M, et al. Mineralization of collagen may occur on fibril surfaces: Evidence from conventional and high-voltage electron microscopy and three-dimensional imaging. J Struct Biol. 1996;117:24–35.
6. Lees S, Prostak KS, Ingle VK, Kjoller K. The loci of mineral in turkey leg tendon as seen by atomic force microscope and electron microscopy. Calcif Tissue Int. 1994;55:180–9.
7. Alexander B, Daulton TL, Genin GM, Lipner J, Pasteris JD, Wopenka B, et al. The nanometre-scale physiology of bone: Steric modelling and scanning transmission electron microscopy of collagen–mineral structure. J R Soc Interface. 2012;9:1774–86.
8. McNally EA, Schwarcz HP, Botton GA, Arsenault AL. A model for the ultrastructure of bone based on electron microscopy of ion-milled sections. PLOS One. 2012;7:e29258.
9. McNally E, Nan F, Botton GA, Schwarcz HP. Scanning transmission electron microscopic tomography of cortical bone using Z-contrast imaging. Micron. 2013;49:46–53.
10. Schwarcz HP, McNally EA, Botton GA. Dark-field transmission electron microscopy of cortical bone reveals details of extrafibrillar crystals. J Struct Biol. 2014;188:240–8.
11. Schwarcz HP, Binkley DM, Luo L, Grandfield K. A search for apatite crystals in the gap zone of collagen fibrils in bone using dark-field illumination. Bone. 2020;135:115304.
12. Schwarcz HP. The ultrastructure of bone as revealed in electron microscopy of ion-milled sections. Semin Cell Dev Biol. 2015;46:44–50.
13. Reznikov N, Bilton M, Lari L, Stevens MM, Kröger R. Fractal-like hierarchical organization of bone begins at the nanoscale. Science. 2018;360:eaao2189.
14. Buss DJ, Kröger R, McKee MD, Reznikov N. Hierarchical organization of bone in three dimensions: A twist of twists. J Struct Biol X. 2022;6:100057.
15. Grandfield K, Vuong V, Schwarcz HP. Ultrastructure of bone: Hierarchical features from nanometer to micrometer scale revealed in focused ion beam sections in the TEM. Calcif Tissue Int. 2018;103:606–16.
16. Cressey BA, Cressey G. A model for the composite nanostructure of bone suggested by high-resolution transmission electron microscopy. Mineral Mag. 2003;67:1171–82.
17. Jantou V, Turmaine M, West GD, Horton MA, McComb DW. Focused ion beam milling and ultramicrotomy of mineralised ivory dentine for analytical transmission electron microscopy. Micron. 2009;40:495–501.
18. Binkley DM, Deering J, Yuan H, Gourrier A, Grandfield K. Ellipsoidal mesoscale mineralization pattern in human cortical bone revealed in 3D by plasma focused ion beam serial sectioning. J Struct Biol. 2020;212:107615.
19. Macías-Sánchez E, Tarakina NV, Ivanov D, Blouin S, Berzlanovich AM, Fratzl P. Spherulitic crystal growth drives mineral deposition patterns in collagen-based materials. Adv Funct Mater. 2022;32:2200504.
20. Zou Z, Tang T, Macías-Sánchez E, Sviben S, Landis WJ, Bertinetti L, et al. Three-dimensional structural interrelations between cells, extracellular matrix, and mineral in normally mineralizing avian leg tendon. Proc Natl Acad Sci USA. 2020;117:14102–9.
21. Tang T, Landis W, Raguin E, Werner P, Bertinetti L, Dean M, et al. A 3D network of nanochannels for possible ion and molecule transit in mineralizing bone and cartilage. Adv Nanobiomed Res. 2022;2:2100162.
22. Tang T, Landis W, Blouin S, Bertinetti L, Hartmann MA, Berzlanovich A, et al. Subcanalicular nanochannel volume is inversely correlated with calcium content in human cortical bone. J Bone Miner Res. 2023;38:313–25.
23. Buss DJ, Reznikov N, McKee MD. Crossfibrillar mineral tessellation in normal and Hyp mouse bone as revealed by 3D FIB-SEM microscopy. J Struct Biol. 2020;212:107603.
24. Georgiadis M, Müller R, Schneider P. Techniques to assess bone ultrastructure organization: Orientation and arrangement of mineralized collagen fibrils. J R Soc Interface. 2016;13:20160088.
25. Ercius P, Alaidi O, Rames MJ, Ren G. Electron tomography: A three-dimensional analytic tool for hard and soft materials research. Adv Mater. 2015;27:5638–63.
26. Kawase N, Kato M, Nishioka H, Jinnai H. Transmission electron microtomography without the "missing wedge" for quantitative structural analysis. Ultramicroscopy. 2007;107:8–15.
27. Biermans E, Molina L, Batenburg KJ, Bals S, Tendeloo GV. Measuring porosity at the nanoscale by quantitative electron tomography. Nano Lett. 2010;10:5014–9.
28. Wang X, Shah FA, Palmquist A, Grandfield K. 3D characterization of human nano-osseointegration by on-axis electron tomography without the missing wedge. ACS Biomater Sci Eng. 2017;3:49–55.
29. Wang X, Langelier B, Shah FA, Korinek A, Bugnet M, Hitchcock AP, et al. Biomineralization at titanium revealed by correlative 4D tomographic and spectroscopic methods. Adv Mater Interfaces. 2018;5:1800262.
30. Micheletti C, Hurley A, Gourrier A, Palmquist A, Tang T, Shah FA, et al. Bone mineral organization at the mesoscale: A review of mineral ellipsoids in bone and at bone interface. Acta Biomater. 2022;142:1–13.
31. Midgley PA, Weyland M. 3D electron microscopy in the physical sciences: The development of Z-contrast and EFTEM tomography. Ultramicroscopy. 2003;96:413–31.
32. Mobus G, Inkson BJ. Nanoscale tomography in materials science. Mater Today. 2007;10:18–25.
33. Huang J, Wang X, Grandfield K. FIB preparation of bone-implant interfaces for correlative on-axis rotation electron tomography and atom probe tomography. Microsc Microanal. 2014;20:352–3.
34. Jarmar T, Palmquist A, Brånemark R, Hermansson L, Engqvist H, Thomsen P. Technique for preparation and characterization in cross-section of oral titanium implant surfaces using focused ion beam and transmission electron microscopy. J Biomed Mater Res A. 2008;87A:1003–9.
35. Li C, Habler G, Baldwin LC, Abart R. An improved FIB sample preparation technique for site-specific plan-view specimens: A new cutting geometry. Ultramicroscopy. 2018;184:310–7.
36. Ziegler JF, Ziegler MD, Biersack JP. SRIM – The stopping and range of ions in matter (2010). Nucl Instrum Methods Phys Res B. 2010;268:1818–23.

37. Skinner HCW. Biominerals. Mineral Mag. 2005;69:621–41.
38. Gordon LM, Tran L, Joester D. Atom probe tomography of apatites and bone-type mineralized tissues. ACS Nano. 2012;6:10667–75.
39. Evans FG. Mechanical properties and histology of cortical bone from younger and older men. Anat Rec. 1976;185:1–11.
40. Slater TJA, Janssen A, Camargo PHC, Burke MG, Zaluzec NJ, Haigh SJ. STEM-EDX tomography of bimetallic nanoparticles: A methodological investigation. Ultramicroscopy. 2016;162:61–73.
41. Hubbell JH, Seltzer SM, editors. X-ray mass attenuation coefficients, NIST standard reference database 126. Gaithersburg, MD: National Institute of Standards and Technology; 2004.
42. Jantou-Morris V, Horton MA, McComb DW. The nano-morphological relationships between apatite crystals and collagen fibrils in ivory dentine. Biomaterials. 2010;31:5275–86.
43. Lee BEJ, Luo L, Grandfield K, Andrei CM, Schwarcz HP. Identification of collagen fibrils in cross sections of bone by electron energy loss spectroscopy (EELS). Micron. 2019;124:102706.
44. Weiner S, Arad T, Sabanay I, Traub W. Rotated plywood structure of primary lamellar bone in the rat: Orientations of the collagen fibril arrays. Bone. 1997;20:509–14.
45. Fratzl P, Weinkamer R. Nature's hierarchical materials. Progr Mater Sci. 2007;52:1263–334.
46. Lee BEJ, Langelier B, Grandfield K. Visualization of collagen-mineral arrangement using atom probe tomography. Adv Biology. 2021;5:2100657.
47. Kadler KE, Holmes DF, Trotter JA, Chapman JA. Collagen fibril formation. Biochem J. 1996;316:1–11.
48. McKee MD, Buss DJ, Reznikov N. Mineral tessellation in bone and the stenciling principle for extracellular matrix mineralization. J Struct Biol. 2022;214:107823.
49. Robinson RA. An electron-microscopic study of the crystalline inorganic component of bone and its relationship to the organic matrix. J Bone Joint Surg Am. 1952;34-A:389–435.
50. Weiner S, Price PA. Disaggregation of bone into crystals. Calcif Tissue Int. 1986;39:365–75.
51. Ziv V, Weiner S. Bone crystal sizes: A comparison of transmission electron microscopic and X-ray diffraction line width broadening techniques. Connect Tissue Res. 1994;30:165–75.
52. Rubin MA, Jasiuk I, Taylor J, Rubin J, Ganey T, Apkarian RP. TEM analysis of the nanostructure of normal and osteoporotic human trabecular bone. Bone. 2003;33:270–82.
53. Landis WJ, Song MJ, Leith A, McEwen L, McEwen BF. Mineral and organic matrix interaction in normally calcifying tendon visualized in 3D by HV EM tomography and graphic image reconstruction. J Struct Biol. 1993;110:39–54.
54. Eppell SJ, Tong W, Katz JL, Kuhn L, Glimcher MJ. Shape and size of isolated bone mineralites measured using atomic force microscopy. J Orthopaed Res. 2001;19:1027–34.
55. Fernandez-Morán H, Engström A. Electron microscopy and X-ray diffraction of bone. Biochim Biophys Acta. 1957;23:260–4.
56. Bocciarelli DS. Morphology of crystallites in bone. Calcif Tissue Res. 1970;5:261–9.
57. Johansen E, Parks HF. Electron microscopic observations on the three-dimensional morphology of apatite crystallites of human dentine and bone. J Cell Biol. 1960;7:743–6.
58. Fratzl P, Schreiber S, Klaushofer K. Bone mineralization as studied by small-angle X-ray scattering. Connect Tissue Res. 1996;34:247–54.
59. Tong W, Glimcher MJ, Katz JL, Kuhn L, Eppell SJ. Size and shape of mineralites in young bovine bone measured by atomic force microscopy. Calcif Tissue Int. 2003;72:592–8.
60. Grandfield K, McNally EA, Palmquist A, Botton GA, Thomsen P, Engqvist H. Visualizing biointerfaces in three dimensions: Electron tomography of the bone-hydroxyapatite interface. J R Soc Interface. 2010;7:1497–501.
61. Palmquist A, Grandfield K, Norlindh B, Mattsson T, Brånemark R, Thomsen P. Bone-titanium oxide interface in humans revealed by transmission electron microscopy and electron tomography. J R Soc Interface. 2012;9:396–400.
62. Micheletti C, Gomes-Ferreira PHS, Casagrande T, Lisboa-Filho PN, Okamoto R, Grandfield K. From tissue retrieval to electron tomography: Nanoscale characterization of the interface between bone and bioactive glass. J R Soc Interface. 2021;18:20210181.
63. Sousa AA, Hohmann-Marriott MF, Zhang G, Leapman RD. Monte Carlo electron-trajectory simulations in bright-field and dark-field STEM: Implications for tomography of thick biological sections. Ultramicroscopy. 2009;109:213–21.
64. Ercius P, Weyland M, Muller DA, Gignac LM. Three-dimensional imaging of nanovoids in copper interconnects using incoherent bright field tomography. Appl Phys Lett. 2006;88:243116.
65. Collins SM, Midgley PA. Progress and opportunities in EELS and EDS tomography. Ultramicroscopy. 2017;180:133–41.
66. Genc A, Kovarik L, Gu M, Cheng H, Plachinda P, Pullan L, et al. XEDS STEM tomography for 3D chemical characterization of nanoscale particles. Ultramicroscopy. 2013;131:24–32.
67. Lepinay K, Lorut F, Pantel R, Epicier T. Chemical 3D tomography of 28 nm high K metal gate transistor: STEM XEDS experimental method and results. Micron. 2013;47:43–9.
68. Titchmarsh JM. Comparison of high spatial resolution in EDX and EELS analysis. Ultramicroscopy. 1989;28:347–51.

SUPPLEMENTARY

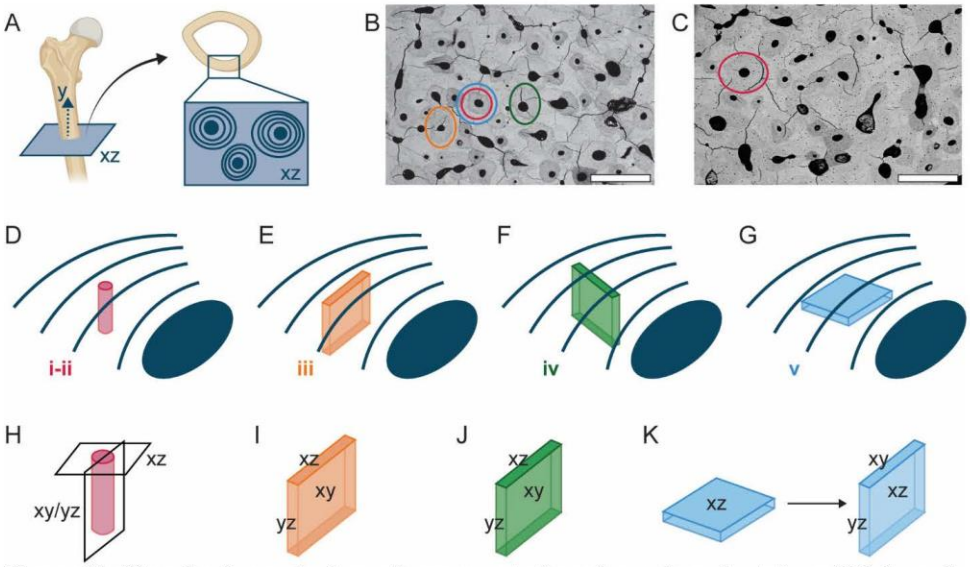

Figure S1. Site selection and schematic representation of samples orientation. A) Schematic representing the orientation of the "bulk" bone sample relative to the long axis of the femur. B-C) BSE-SEM images with circular marks around the osteons from which the samples were prepared. D-G) Orientation of both rod- (*i* and *ii* in D) and wedge-shaped (*iii* in E; *iv* in F; *v* in G) samples in relation to the osteonal axis and osteonal lamellae (the blue circle represents the Haversian canal, and the blue curved lines the inter-lamellar boundaries). H-K) Representation of the coordinate system convention used in the manuscript. The image plane in STEM corresponds to the xy plane, except for sample *v* where it corresponds to xz instead, as the sample was rotated during the *plan-view* FIB lift-out. Please note that given the cylindrical geometry of the rod-shaped samples, the definition of xy and yz planes is arbitrary, and depends on the insertion of the sample post in the holder and in the S/TEM instrument. In this case, the xy plane in the tomography reconstructions corresponds to the imaging plane during the tilt series acquisition. Scale bars are 500 µm in B and C. [Note: the drawings are not to scale, and the exact location of the samples from the Haversian canal is only indicative].

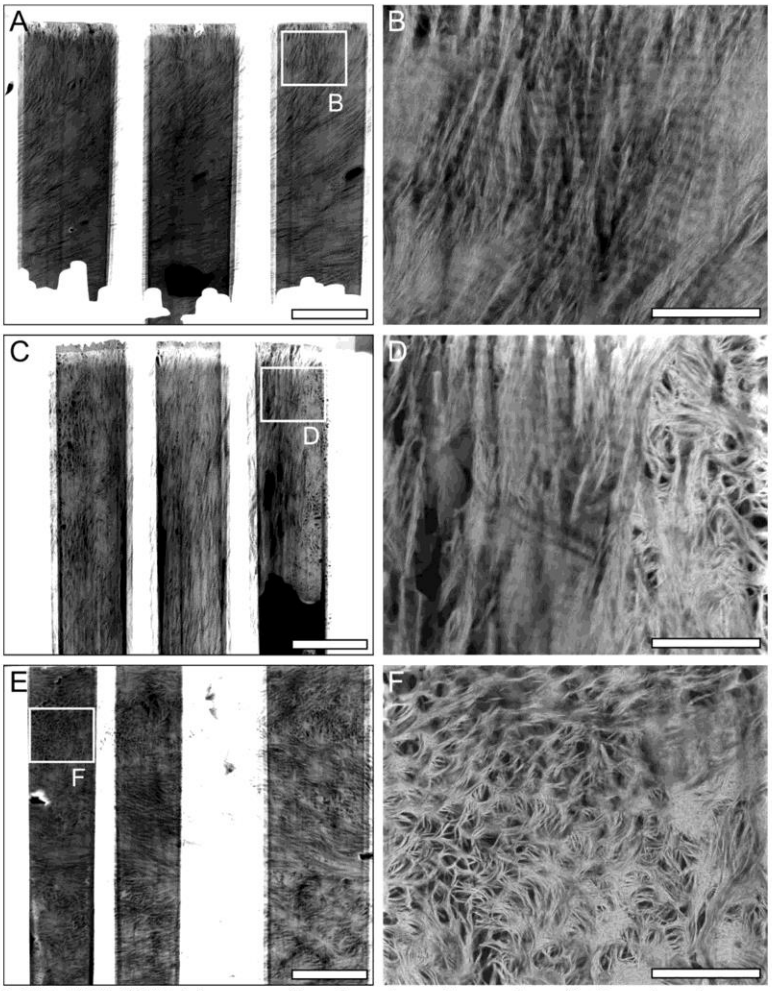

Figure S2. HAADF-STEM images of wedge-shaped samples. A) Overview image of wedge-shaped sample *iii*, where the characteristic banding pattern of in-plane collagen is predominant. B) Higher magnification view of the banding pattern. C) Overview image of wedge-shaped sample *iv*, where both longitudinal and lacy motifs are present. D) Higher magnification image showing the transition in orientation of collagen fibrils from in-plane (left side) to out-of-plane (right side). E) Overview image of wedge-shaped sample *v*, where collagen fibrils are mostly out-of-plane. F) Higher magnification image where "rosettes" and "holes" can be seen. Scale bars are 2 μm in A, C, and E, and 500 nm in B, D, and F. [Note: Figures S2A and S2F are also reported in the manuscript as Figures 2D and 2F, respectively].

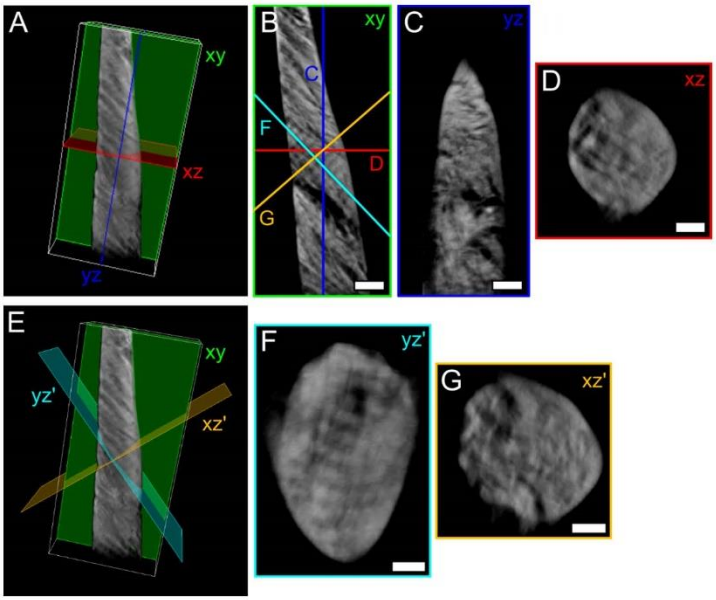

Figure S3. Correspondence between longitudinal and lacy motifs. A) 3D rendering of tomogram *ii-a*, showing three representative orthogonal planes, corresponding to xy (green), yz (blue), and xz (red), defined as per the coordinate system adopted in this work. B) A representative reconstructed slice in the xy plane where banding pattern is visible. C) Reconstructed slice in the yz plane corresponding to the blue line in A and B. Mineral-rich areas are present, but the banding pattern is not distinguishable. D) Reconstructed slice in the xz plane corresponding to the red line in A and B. E) 3D rendering of tomogram *ii-a*, showing three representative orthogonal planes, where yz' (cyan) and xz' (orange) are oriented perpendicular and parallel, respectively, to the banding pattern. F) Reconstructed slice corresponding to the cyan line in B and E, oriented perpendicular to the banding pattern, i.e., parallel to the collagen fibrils. The banding pattern is now clearly distinguishable, as opposed to C. G) Reconstructed slice corresponding to the orange line in B and E, oriented parallel to the banding pattern, i.e., perpendicular to the collagen fibrils. In both D and G, mineral-rich regions and "holes" can be observed. Scale bars are 200 nm in B, C, and F, and 100 nm in D and G. A scale bar is not provided in A and E as the 3D representation is not an orthographic projection; the dimensions (x, y, z) of the white box are 916.65 × 1943.55 × 579.60 nm^3 in both A and E.

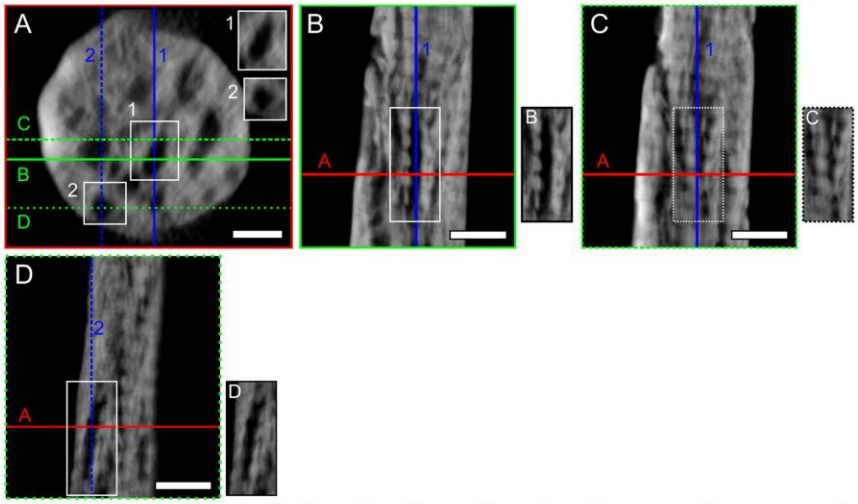

Figure S4. Examples of "holes" where banding pattern is not apparent in cross-section. A) A representative reconstructed slice in the xz plane in tomogram *i-b*. The "holes" marked by the white rectangles numbered "1" and "2" were examined in the xy planes shown in B/C and D, respectively. B) Reconstructed slice in the xy plane corresponding to the solid green line in A. The banding pattern is not clearly distinguishable within the "hole" (numbered "1" in A), but mostly around it. C) Reconstructed slice in the xy plane corresponding to the dashed green line in A. The banding pattern is more distinguishable than in B. The xy slices in B and C are 39.95 nm away from each other in the z direction. D) Reconstructed slice in the xy plane corresponding to the dotted green line in A. Collagen banding is barely visible, but the collagen fibrils could have been eroded by ion milling as this "hole" (numbered "2" in A) is approximately 13-15 nm away from the sample outer surface. An unmarked image of the regions marked by rectangles in B, C, and D is provided next to each panel. Scale bars are 100 nm in A, and 200 nm in B, C, and D.

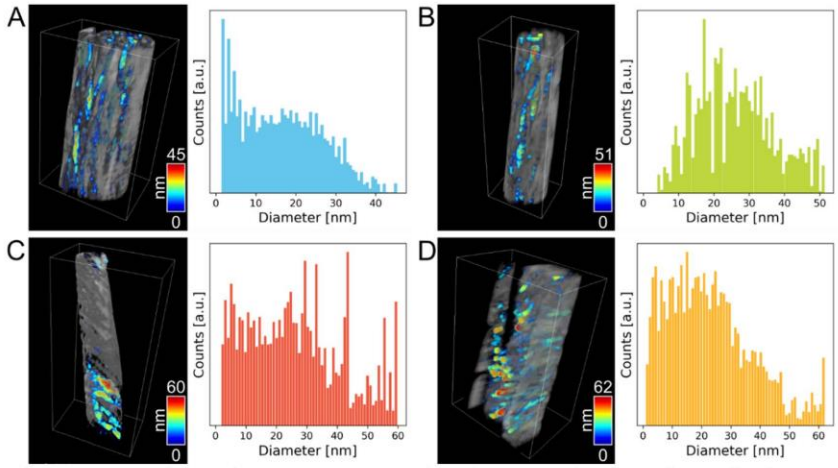

Figure S5. 3D renderings of the tomograms with size analysis of the "holes". The segmented "holes" are colour-coded based on size, and the distribution of the measured values is provided in the histogram: A) tomogram *i-a*; B) tomogram *i-b*; C) tomogram *ii-a*; D) tomogram *ii-b*. A scale bar is not provided as the 3D representation is not an orthographic projection; the dimensions (x, y, z) of the white box are 879.65 × 1416.20 × 620.50 nm^3 in A, 555.55 × 1611.30 × 457.15 nm^3 in B, 916.65 × 1943.55 × 579.60 nm^3 in C, and 1010.10 × 1515.52 × 704.48 nm^3 in D.

Table S1. Mean, median, minimum, and maximum "hole" size measured in each tomogram with the "Volume thickness map" operation in the Dragonfly software.

Tomogram	*Mean [nm]*	*Median [nm]*	*Minimum [nm]*	*Maximum [nm]*
i-a	16.4	15.9	1.8	45.0
i-b	26.0	25.3	4.4	51.0
ii-a	26.4	24.5	2.3	59.3
ii-b	22.9	20.9	1.5	61.6
Average	**22.9 ± 4.6**	**21.7 ± 4.3**	**2.5 ± 1.3**	**54.2 ± 7.7**

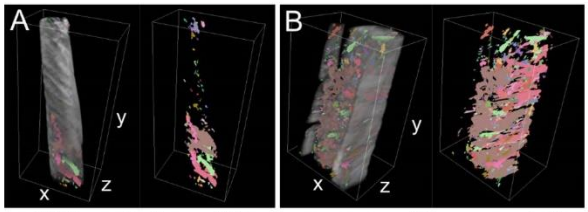

Figure S6. Additional 3D renderings of the tomograms with segmentation of the "holes". A) 3D rendering of tomogram *ii-a* with the segmented "holes", shown in different colours to represent their disconnected nature. B) Similar visualization as A for tomogram *ii-b*. A scale bar is not provided as the 3D representation is not an orthographic projection; the dimensions (x, y, z) of the white box are 916.65 × 1943.55 × 579.60 nm^3 in A, and 1010.10 × 1515.52 × 704.48 nm^3 in B.

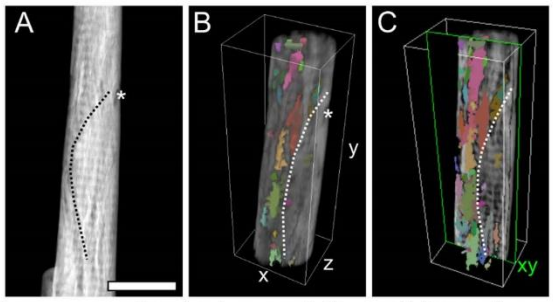

Figure S7. "Holes" are more abundant around the periphery of a mineral ellipsoid. A) HAADF-STEM image where the contour of a partial mineral ellipsoid (oriented longitudinally with respect to the long axis of the sample) is marked (black dotted line). B) 3D rendering of tomogram *i-b*, where the same mineral ellipsoid contour in A is marked by the white dotted line. For ease of comparison between A and B, a landmark is indicated by *. C) 3D rendering of tomogram *i-b* sliced along a representative xy plane where it becomes clearer that most segmented "holes" lie outside the mineral ellipsoid (contour marked by the white dotted line). Scale bar is 500 nm in A. A scale bar is not provided in B and C as the 3D representation is not an orthographic projection; the dimensions (x, y, z) of the white box are 555.55 × 1611.30 × 457.15 nm^3. [Note: Figures S7A and S7B are also reported in the manuscript as Figures 1C and 5C, respectively].

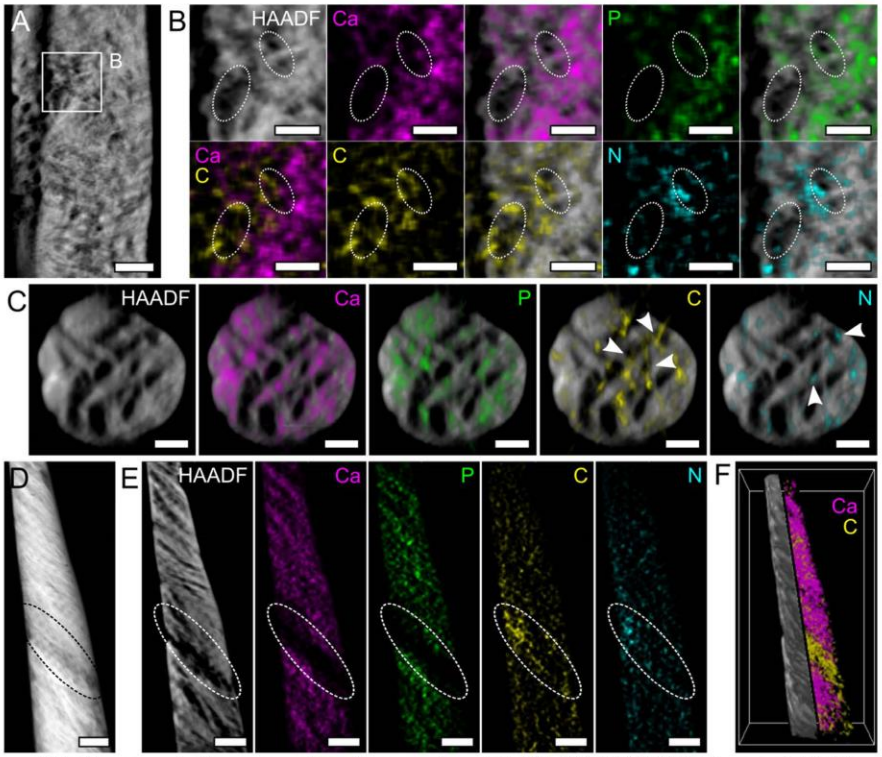

Figure S8. Representative examples of reconstructed HAADF-STEM slices and EDX maps. A) A representative reconstructed HAADF-STEM slice in the xy plane in tomogram *ii-b*. B) Reconstructed EDX maps (with and without underlying HAADF-STEM reconstructed slice) corresponding to the area marked by the white square in A. In the areas where the "holes" are, Ca (magenta) and P (green) are mostly absent, while C (yellow) and N (cyan) signals appear more intense (e.g., regions circled by the white dotted lines). C) A representative reconstructed HAADF-STEM slice and EDX maps in the xz plane in tomogram *i-b*. While Ca and P are not detected within the "holes", C and N seem co-localized with some of them (arrowheads). D) HAADF-STEM image where tomogram *ii-a* was acquired. E) Reconstructed HAADF-STEM slice and EDX maps in the xy plane in tomogram *ii-a*. A region where faint banding pattern is present in the HAADF-STEM image in D and in the HAADF-STEM reconstructed slice appears depleted in Ca and P, but enriched in C and N. F) 3D rendering of HAADF-STEM and Ca/C signals on the left and right halves, respectively. Scale bars are 200 nm in A, D, and E, and 100 nm in B and C. A scale bar is not provided in F as the 3D representation is not an orthographic projection; the dimensions (x, y, z) of the white box are 919.8 × 1869.0 × 579.6 nm^3. [Note: Figure S8D is also reported in the manuscript as Figure 1J, and it is cropped and duplicated here for ease of comparison with Figure S8E].

Table S2. Amount of Ca, P, C, and N contained within the segmented "holes", expressed as the number of voxels of each element with respect to the total number of voxels of the segmented "holes".

Tomogram	*Ca [% voxels]*	*P [% voxels]*	*C [% voxels]*	*N [% voxels]*
i-b	1.40	3.00	13.26	12.90
ii-a	0.02	0.12	10.08	16.37
ii-b	0.69	2.48	14.87	13.21

Table S3. Voxels labelled in the largest and second largest ROIs identified using the "Connected component – Multi-ROI" operation in the Dragonfly software applied to the segmentation of the mineral phase, and fraction of the largest ROI compared to the total number of voxels segmented for the entire mineral ROI.

Tomogram	*Largest ROI [no. voxels]*	*Second largest ROI [no. voxels]*	*Fraction of largest ROI with respect to total ROI [%]*
i-a	363,894,609	102,645	99.5
i-b	8,952,638	17,824	99.5
ii-a	87,083,428	94,695	99.4
ii-b	609,949,549	114,003	99.9

Table S4. Length, width, and thickness of mineral plates segmented in each tomogram.

Tomogram	*Length [nm]*	*Width [nm]*	*Thickness [nm]*
i-a	81.9	40.2	5.3
	118.6	28.5	7.5
	92.6	31.4	5.2
	90.6	33.6	6.3
	115.2	34.3	4.9
Average	**99.8 ± 16.2**	**33.6 ± 4.3**	**5.8 ± 1.1**
i-b	86.1	28.7	8.9
	96.5	41	10.5
	100.9	24.6	7.6
	137.1	24.6	8.1
	90.7	49.2	9.6
Average	**102.3 ± 20.3**	**33.6 ± 11.0**	**8.9 ± 1.1**
ii-a	111.7	11.6	5.7
	64.4	20.0	7.3
	123.8	11.6	7.9
Average	**100.0 ± 31.4**	**14.4 ± 4.8**	**7.0 ± 1.1**
ii-b	64.4	53.5	5.1
	27.4	48.8	5.1
	25.2	26.3	4.7
Average	**39.0 ± 22.0**	**42.9 ± 14.5**	**4.7 ± 0.2**

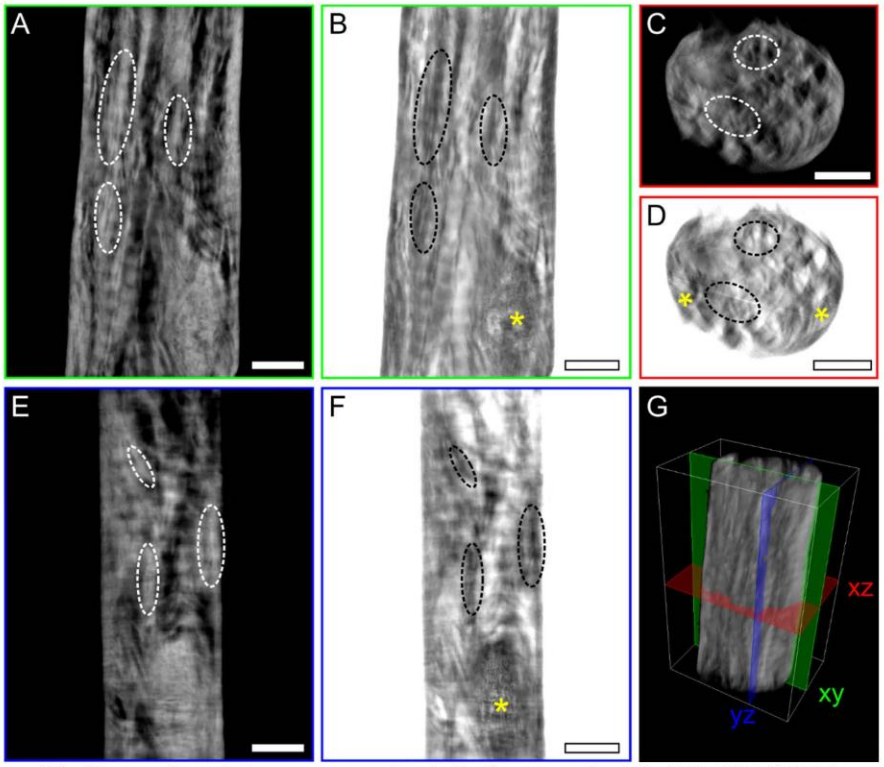

Figure S9. Comparison between reconstructed slices acquired in HAADF-STEM *vs.* BF-STEM mode. A-B) A representative reconstructed slice in the xy plane (green) acquired in HAADF-STEM (A) and BF-STEM (B) mode. C-D) A representative reconstructed slice in the xz plane (red) acquired in HAADF-STEM (C) and BF-STEM (D) mode. E-F) A representative reconstructed slice in the yz plane (blue) acquired in HAADF-STEM (E) and BF-STEM (F) mode. Although differences are not striking, mineral structures appear overall less blurred and better distinguishable from the background in all planes in BF-STEM mode. Some examples are marked by the dotted ovals. Artifacts are present in the BF-STEM reconstruction in the form of bright dots in the xy and yz planes and bright streaks in the xz plane (regions marked by the yellow *). G) 3D rendering of the HAADF-STEM tomogram showing the position of the three representative slices in A-F. Scale bars are 200 nm in A-F. A scale bar is not provided in G as the 3D representation is not an orthographic projection; the dimensions (x, y, z) of the white box are 879.65 × 1416.2 × 620.5 nm^3.